REVIEW

Chalcogenide passivation of III–V semiconductor surfaces

V. N. Bessolov and M. V. Lebedev

A. F. Ioffe Physicotechnical Institute, Russian Academy of Sciences, 194021 St. Petersburg, Russia

(Submitted June 9, 1998; accepted for publication June 10, 1998)
Fiz. Tekh. Poluprovodn. **32**, 1281–1299 (November 1998)

Experimental studies of chalcogenide passivation (by sulfur and selenium atoms) of III–V semiconductor surfaces are analyzed. The characteristic features of chemical-bond formation, the atomic structure, and the electronic properties of III–V semiconductor surfaces coated with chalcogenide atoms are examined. Advances in recent years in the application of chalcogenide passivation in semiconductor technology and trends and prospects for further development of this direction are discussed. © *1998 American Institute of Physics.* [S1063-7826(98)00111-2]

1. INTRODUCTION

III–V Semiconductors are now widely used to produce fast electronic and high-power microwave devices as well as infrared- and visible-range optoelectronic devices. In semiconductor electronics the active regions of devices have been steadily decreasing in recent years. As a result, surfaces and interfaces have a larger influence on device characteristics.

In the ideal case a surface or interface is a sharp barrier making it possible to delimit clearly the interior regions or to establish the outer boundaries of devices. Most III–V semiconductor surfaces are characterized by a high density of surface states in the band gap. This results in rigid pinning of the Fermi level, whose position at the surface is essentially independent of the nature of the adsorbed atoms. This circumstance has a negative effect on the operation of many micro- and optoelectronic devices, impeding full disclosure of the high potentials of these semiconductors.

To eliminate the undesirable effect of the surface on device properties, the direction called ''passivation'' is being actively developed in technology. In this direction, different surface-treatment methods involving the deposition of different coatings on surfaces are being developed. Semiconductor surface passivation technology must solve three problems:[1] First, it must prevent a semiconductor from reacting with the atmosphere during the entire lifetime of the semiconductor device (chemical passivation); second, it must eliminate interfacial states from the band gap and prevent their formation (electrical passivation); and, third, it must provide an adequate barrier to prevent the semiconductor electrons from being lost in the passivating layer. The term ''passivation'' signifies that a semiconductor surface becomes less chemically active and in the process fewer active recombination centers form on the surface and (or) these centers themselves become less active.

Work on passivation of III–V semiconductor surfaces is following mainly two directions. The first one is deposition of relatively thick (thickness ranging from several tens of nanometers to several microns) insulator layers. In this process, a semiconductor–insulator heterojunction, whose properties depend largely on the density of states at the interface, which in turn depends on the method used to produce this heterojunction and to prepare the semiconductor surface, is formed. This direction includes passivation by the native oxide layer, obtained by methods such as thermal or plasma oxidation, anodization, and recently epitaxy, as well as passivation by a layer of a foreign insulator. The second direction is modification of the atomic structure of the surface by foreign atoms which changes the electronic structure of the semiconductor surface. This method is often used to prepare a surface for subsequent deposition of an insulator material. This direction includes passivation by group V–VII atoms. In this review article we shall not dwell on questions concerning passivation technology using thick insulator layers and modification by group-V and -VII atoms. The reader can find the required information in the literature.[2–7]

Chalcogenide passivation (modification by sulfur or selenium atoms) enables both chemical and electronic passivation of a surface and is therefore a promising method in III–V semiconductor technology. On the one hand, chalcogenide passivation makes it possible to decrease substantially the density of surface states in the band gap, to decrease the surface recombination velocity and, as a result, to improve many characteristic features of diverse devices. On the other hand, it makes it possible to slow down considerably the oxidation of a semiconductor surface in the atmosphere. The development of this method started in the mid-1980s, and there are now more than 500 papers on chalcogenide passivation and interaction of sulfur and selenium atoms with III–V semiconductor surfaces. The obvious progress made in improving the characteristics of semiconductor devices and the enormous interest shown in this problem by investigators from many countries have motivated the present review article, which examines the physicochemical aspects of chalcogenide passivation of III–V semiconductors and devices based on them.

 © 1998 American Institute of Physics

2. CHARACTERISTIC FEATURES OF CHALCOGENIDE PASSIVATION TECHNOLOGY

2.1. Passivation from solutions

Broad development of chalcogenide passivation was initiated by Sandroff *et al.*,[8] who proposed a method for improving the characteristics of AlGaAs/GaAs bipolar transistors. In their variant of the method, an aqueous solution of sodium sulfide ($Na_2S{:}9H_2O$) with concentration 0.5–1.0 M was deposited on a semiconductor structure, after which the structure was spun in a centrifuge at 5000 rpm for 60 s (spin-on method).

Aqueous solutions of another inorganic sulfide — ammonium sulfide $(NH_2)_2S$, which is most often used even today — were first used in Ref. 9. Almost simultaneously, Fan *et al.*[10] employed aqueous solutions of ammonium sulfide to which 6% excess sulfur was added. After passivation, the structures were washed with deionized water and dried in a dry nitrogen flow. Such treatment, in contrast to passivation in sodium sulfide solutions, did not leave any visible film on the semiconductor surface.

In Ref. 11 P_2S_5/NH_4OH solutions were used to passivate a GaAs surface. Treatment in such solutions made it possible to improve the stability of the luminescence properties after holding a sulfidized semiconductor in air for ten days than treatment in a sodium sulfide solution. Later, $P_2S_5/(NH_4)_2S$ solutions were used.[12,13] Such a solution made it possible to obtain passivated GaAs, whose photoluminescence intensity was much higher than that of the GaAs control sample, passivated in pure $(NH_4)_2S$, and was likewise characterized by a higher stability. The characteristics of Al– and Au–GaAs Schottky barriers, prepared using a semiconductor sulfidized in a $P_2S_5/(NH_4)_2S$ solution, were likewise noticeably better.

Later, GaAs surfaces were passivated in aqueous solutions of K_2Se as well as in the solutions $Na_2S+RuCl_3$,[14] Na_2Se/NH_4OH,[15] SeS_2,[16] S_2Cl_2,[17] and Se/NH_4OH.[18] To increase the effectiveness of passivation it was suggested that sulfide treatment be performed in aqueous solutions with the semiconductor illuminated by white light while heating the solution.[19] In addition to inorganic sulfides and selenides, complicated sulfide-containing organic compounds were also used for GaAs surface passivation: thiols dissolved in nonaqueous solvents[20,21] and $[CH_3(CH_2)_{17}]_2NCSSNa$.[22] Such treatment made it possible to obtain a GaAs surface no worse than that obtained by passivation in sodium sulfide solutions. The surface was characterized by high stability against heating and standing in the atmosphere.

The technology of sulfide passivation from solutions advanced further after electrochemical deposition of sulfides on a semiconductor surface came into use. This method was first used to sulfidize InSb to improve the quality of MIS structures.[23] Both aqueous solutions of ammonium sulfide and solutions of sodium sulfide in ethylene glycol ahve been used for such passivation.[24,25] Electrochemical sulfide passivation has made it possible to obtain a relatively thick sulfide coating on a GaAs surface, such that the properties of GaAs are not degraded by intense laser radiation,[26] and has found practical application for improving the characteristics of AlGaInP-based laser diodes.[25]

Another promising direction of sulfide passivation is sulfidizing in alcohol solutions. Sodium sulfide and ammonium sulfide solutions in ethanol, isopropanol, butanol, and tretbutanol have been used. In Refs. 27 and 28 it was shown that decreasing the permittivity of the solvent greatly increases the photoluminescence intensity of sulfidized GaAs, which did not decrease even after the semiconductor was irradiated for 0.5 h with intense laser light. In addition, passivation in alcohol solutions of sodium sulfide has made it possible to increase considerably the threshold of catastrophic optical degradation of InGaAs/AlGaAs lasers.[29,30]

2.2. Passivation from the gas phase

The interaction of III–V semiconductor surfaces with chalcogenide atoms adsorbed from the gas phase has been actively studied since the end of the 1970s. Initially, freshly prepared semiconductor surfaces placed in a ultrahigh vacuum were the objects of investigation. In Ref. 31 the adsorption of various molecules, including H_2S, on a freshly cleaved (110) GaAs surface was studied. In Ref. 32 adsorption of H_2S on the surface of strongly doped *n*-GaAs (100), grown immediately prior to the experiment by molecular-beam epitaxy, was investigated.

In Ref. 33 a special preparation of a GaAs surface, covered with a layer of the native oxide, was used for depositing sulfur and selenium from the gas phase. Accordingly, GaAs was immersed in a freshly prepared solution $H_2SO_4:H_2O_2:H_2O$ (4:1:1) to remove mechanical damage on the surface. The semiconductor was then immediately placed in a ultrahigh-vacuum chamber. X-ray photoelectron spectroscopy of the surface showed that a thin (8–10 Å) oxide layer remained on the surface after such treatment. In Ref. 33 this layer was removed by heating the semiconductor up to 550 °C under vacuum conditions. The semiconductor surface cleaned in this manner was placed in a vacuum at room temperature near an open quartz cell, which was filled with highly pure sulfur or selenium. The sulfur and selenium were evaporated by heating the cell. Sysoev *et al.*[34] conducted heterovalent substitution of surface arsenic with selenium atoms in order to produce an insulating coating on a GaAs surface. The experiments were performed in preevacuated cells. The substrate temperature was maintained above the selenium temperature, which determined the selenium partial pressure.

In Ref. 35 sulfidization of both GaAs (100) and InP (100) was performed. Chemically polished semiconductor wafers were annealed in a hydrogen atmosphere at 550 °C (GaAs) or 300 °C (InP). Sulfidization was performed without contact with air. A H_2S/H_2 mixture, obtained by decomposition of copper sulfide in hydrogen, was used as the sulfidizing gas. The chemical potential of sulfur in the gas was monitored by varying the decomposition temperature. In Ref. 36 thermal sulfidization was used. It was perforemd in a hydrogen sulfide atmosphere by repeated cycles of holding GaAs at a low temperature (90–95 K) followed by heating to 600 K.

In Ref. 37 a plasma method was suggested to be used for passivation of an InP surface. A corona discharge was produced in a hydrogen sulfide flow. As a result, relatively thick (140–350 Å) sulfide layers were obtained on the semiconductor surface. Later, a similar method was also used for passivation of GaAs.[38] In Ref. 39, a mixture consisting of atomic hydrogen and hydrogen sulfide molecules, was decomposed by means of a microwave discharge, which resulted in the production of atomic sulfur that was adsorbed on the GaAs surface at 60–70 °C. As a result of such treatment, the sulfur was bonded exclusively with gallium atoms.

In Refs. 40 and 41 sulfur adsorption on a GaAs surface was performed using a solid-state electrochemical source $Ag/AgI/Ag_2S/Pt$, from which molecular sulfur S_2 effluxed. In Ref. 42 polyphenyl–sulfide, which was deposited on a substrate by vacuum sputtering, was used for passivation of GaAs.

In Ref. 43 irradiation of the semiconductor with an ArF excimer laser under ultrahigh-vacuum conditions was used as a means to prepare a GaAs surface for gaseous passivation. This was followed immediately by sulfide treatment of the semiconductor, also during irradiation with this laser in a H_2S/H_2 atmosphere. Surface preparation and treatment were both conducted at room temperature. A photostimulated process was also used in Ref. 44, where a capsule containing an allotropic modification of sulfur S_8 was used as the source of sulfur and an UV mercury lamp was used as the light source.

3. FORMATION OF CHEMICAL BONDS ON III–V SEMICONDUCTOR SURFACES DURING CHALCOGENIDE PASSIVATION

3.1. Mechanism for the formation of a passivating coating

We shall examine sulfide passivation as an example of the formation of a passivating coating. In the passivation process the semiconductor is placed in contact with a sulfide-containing solution or gas for a certain time. The process leading to the formation of a passivating coating on III–V semiconductor surfaces can be conventionally divided into two stages. At the first stage the oxide layer is removed from the surface (Fig. 1). This layer consists of a mixture of different phases of oxides of the semiconductor components, several tens of angstroms thick. During sulfidization in solutions (specifically, in aqueous and alcohol solutions of inorganic sulfides and in solutions containing sulfur monochloride) the oxide layer is etched directly by the passivating solution. In the case of sulfidization from the gas phase, additional surface preparation measures must be taken in order to deposit a passivating coating — for example, high-temperature annealing ($T>600$ °C) in an ultrahigh vacuum[33] or UV radiation.[43]

The chemical reaction leading to the formation of a sulfide coating from solutions of inorganic sulfides can be written in the general form[45,46]

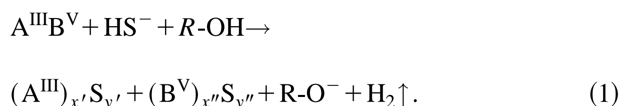

$$A^{III}B^{V}+HS^{-}+R\text{-}OH\rightarrow (A^{III})_{x'}S_{y'}+(B^{V})_{x''}S_{y''}+R\text{-}O^{-}+H_2\uparrow. \quad (1)$$

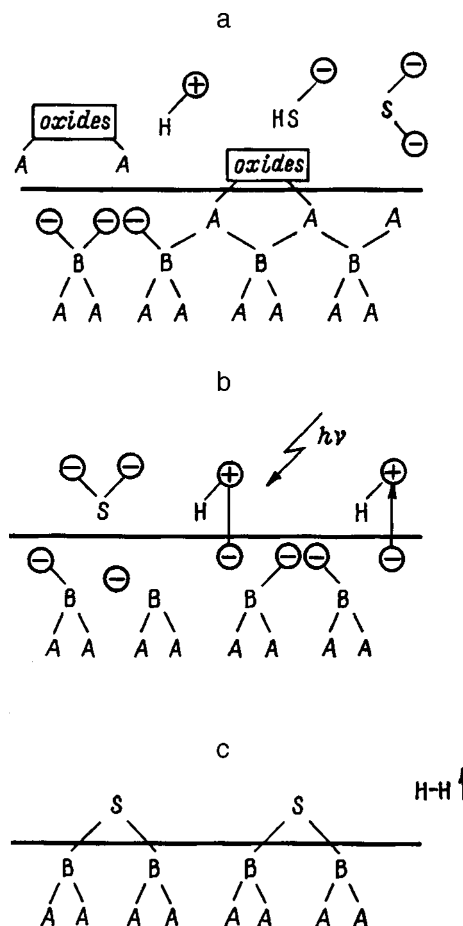

FIG. 1. Schematic diagram of the processes occurring during the formation of a sulfide passivating coating: a — Rupture of bonds between III and V atoms, removal of oxide layer, and dissociation of HS^- ions; b — transfer of electrons from the semiconductor into the solution; c — formation of chemical bonds between semiconductor and sulfur atoms.

Here R is either a hydrogen atom (for aqueous solutions) or an alkyl group (for alcohol solutions). In general, the stoichiometric coefficients $x'(x'')$ and $y'(y'')$ can assume values from 1 to 5 (for example, GaS, In_2S_3, and Sb_2S_5) and, as a rule, after sulfidization a mixture of different sulfides (and also oxosulfides[24]) is present on the surface.

Since the degree of oxidation of the semiconductor components and of the hydrogen ion changes in the course of the sulfidization reaction (the semiconductor oxidizes and hydrogen is reduced), this reaction, an oxidation-reduction reaction, can be written in the form of two half-reactions:[45]

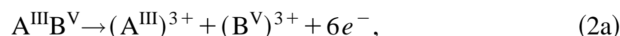

$$A^{III}B^{V}\rightarrow (A^{III})^{3+}+(B^{V})^{3+}+6e^{-}, \quad (2a)$$

$$6H^{+}+6e^{-}\rightarrow 3H_2\uparrow. \quad (2b)$$

We shall examine in greater detail the physical processes occurring during the oxidation-reduction reaction. Each atom in the crystal lattice of zinc blende possesses four bonds, each of which is formed by two electrons. At the same time, each A^{III} or B^{V} atom in the sulfide compound formed on the surface forms three chemical bonds.[47] This means that in the sulfidization process one bond becomes extraneous and to form a passivating coating (Fig. 1c) the electrons localized on this bond must either enter the solution or recombine with

a hole (Fig. 1a). Absorption of light with photon energy greater than the band gap of the semiconductor (Fig. 1b) can serve as the source of energy required to transfer an electron into the conduction band or to the level of a surface state. The outflow of electrons into the solution (entry of holes into the semiconductor) can occur via either the conduction band of the semiconductor (valence band) or the levels of surface states.

Since the reaction forming a sulfide coating is a photoelectrochemical reaction, the rate of formation of a passivating coating on the surface of a *n*-type semiconductor should be much higher than on the surface of a *p*-type semiconductor. In addition, the formation rate of a passivating coating should increase with increasing treatment temperature, light intensity incident on the semiconductor/electrolyte interface, and concentration of sulfur atoms in the solution and with decreasing pH of the solution (the fact that a decrease of the pH below a certain limit can stop etching of the oxide layer must be taken into account).

In Ref. 48 it was observed that in the process of sulfidization of GaAs the position of the surface Fermi level changes, and the rate of motion of the Fermi level in *n*-GaAs is always much higher than in *p*-GaAs. Activation of the sulfidization process by illumination of a semiconductor/electrolyte interface was demonstrated in Ref. 49 for the example of sulfidization of InAlAs in aqueous solutions of ammonium sulfide. Moreover, it should be noted that etching of an oxide layer and formation of a sulfide coating on a semiconductor surface are more efficient in solutions of a sulfide of a strong base (for example, Na_2S) than in solutions of a sulfide of a weak base [for example, $(NH_4)_2S$].[46]

3.2. Chemical bonds on a passivated surface

3.2.1. Gallium arsenide

The natural oxide on a GaAs surface is an amorphous mixture of oxides. X-ray photoelectron spectroscopy of a GaAs surface coated with a natural oxide layer revealed the presence of elemental arsenic and the oxides As_2O, AsO, As_2O_3, Ga_2O, GaO, and Ga_2O_3 on the surface,[50] in agreement with the diagram of phase equilibrium in the system Ga–As–O.[51]

3.2.1.1. GaAs/S

Sulfidization of a surface in solutions results in an appreciable decrease and often complete vanishing of the oxide layer,[52–55] and oxides are more actively removed as the permittivity of the sulfide solution decreases.[28,46] In the process, however, physisorbed oxygen (aqueous) and carbon remain on the surface. Sulfidization from the gas phase requires preliminary treatment of the semiconductor surface to remove the oxide layer.[33,43,56]

X-ray photoelectron spectra show that after a GaAs surface is held in sulfur vapor the As3*d* peak acquires components with a chemical shift (Δ) of about 2 eV (which corresponds to the chemical shift characteristic of the compound As_2S_3) and the Ga3*d* peak is broadened by a small amount as a result of the appearance of gallium sulfides on the surface.[33] The sulfide layer was estimated to be about 5 Å thick. Holding GaAs in the mixture H_2S/H_2 resulted in sulfur adsorption on the surface, arsenic depletion of the surface, and gallium enrichment in an approximately 10-Å-thick layer.[35]

Modern x-ray photoelectron spectroscopy data on sulfidized GaAs surfaces attest to the presence of various Ga and As sulfides on the surface and, in addition, a large quantity of elemental arsenic remains on the surface (here, mainly the spectral lines Ga3*d* and As3*d* are investigated; the low binding energy makes these lines accessible for investigation by the most surface-sensitive synchrotron radiation with photon energy of about 100 eV). Most often, As–S bonds with a 1.7 to 2.0-eV chemical shift (which corresponds to the compound As_4S_4) and Ga–S bonds with a 0.6–0.7 eV chemical shift (corresponding to the compound Ga_2S) are observed on the surface.[53,55] These bonds have been observed with sulfidization both in Na_2S,[53] $(NH_4)_2S$,[55] and P_2S_5 (Ref. 13) solutions and in gases, for example, H_2S (Ref. 57), or in a molecular sulfur flow.[58] In addition, if the sulfidization was performed at temperatures close to room temperature, the number of As–S bonds was always greater than the number of Ga–S bonds. This attests to the fact that surface arsenic atoms are chemically very active.

In the case of sulfidization in ammonium sulfide solutions, besides these components, an As–S component with a 2.5-eV chemical shift[56] and a Ga–S component with a 1.7-eV chemical shift[55,56] have been observed. Detailed quantitative investigations of chemical bonds on GaAs surfaces sulfidized in different solutions made it possible to identify other gallium and arsenic sulfides also.[59,60] In the case of sulfidization of a surface in an atomic sulfur flow[39] all adsorbed sulfur is bonded with surface gallium atoms only. Surface passivation by a H_2S plasma[61] and in a H_2S atmosphere under the action of ArF excimer laser radiation[43] led to the appearance of only a small number of As–S bonds on the surface, while Ga–S bonds were not observed, and passivation in thiol solutions did not lead at all to the appearance of sulfides on the semiconductor surface, although the photoluminescence intensity did increase.[20]

Sulfidization of a GaAs surface by hydrogen sulfide at low temperature ($T = 150$ K) leads to adsorption of sulfur on arsenic atoms, while sulfidization at high temperatures (280–450 °C) results in adsorption of sulfur on gallium atoms.[62] Sulfidization from the gas phase (holding at room temperature in a H_2S atmosphere followed by annealing at 400 °C) removes the surface arsenic atoms and results in the formation of a GaS_x sulfide phase.[63]

Bonds with a large chemical shift have been observed in the case of electrochemical passivation of a GaAs surface:[26] Ga–S bonds with chemical shifts 1.65 eV and 3.25 eV and As–S bonds with shifts 1.8 and 3.5 eV.

Cleaving a GaAs(110) surface in alcohol solutions of sodium sulfide resulted in the formation of only Ga–S bonds on the surface.[64] At the same time, a large number of As–S bonds was observed on the surface in the case of sulfidization of a GaAs (110) surface in an aqueous solution of sodium sulfide.[65]

Sulfidization of a AlGaAs (110) surface in ammonium sulfide solutions, just as in the case of a GaAs surface, re-

sulted in a decrease in the quantity of oxides on the surface and the formation of sulfides on the surface. In addition, in layers with a high aluminum content ($X=0.78$) the sulfur was bonded predominantly with aluminum atoms.[66]

Annealing of a sulfidized surface in ultrahigh vacuum results in a substantial redistribution of the chemical bonds on the semiconductor surface. When a sulfidized gallium arsenide surface is heated, sulfur transfers from arsenic to gallium atoms,[67] and at 360 °C the As–S bonds vanish completely[56,58,67] and only Ga–S bonds remain on the surface, while the total amount of sulfur on the surface remains virtually constant. This shows that Ga–S bonds are more stable than As–S bonds, which agrees well with data on the heat of formation of these sulfides.

It should be noted that the bonds with a large chemical shift (As–S,$\Delta=2.5$ eV and Ga–S, $\Delta=1.7$ eV), observed in Refs. 55 and 56, are less stable against heating than the ordinary bonds As–S ($\Delta=1.8$ eV) and Ga–S ($\Delta=0.7$ eV).

Desorption of sulfur from a GaAs surface starts at higher temperatures ($T>580$ °C). The desorption temperature T_D is different for faces with different orientations and correlates well with the coordination number of sulfur on semiconductor surface as well as with the Ga–S binding energy calculated in Refs. 68 and 69 : $T_D(111)A<T_D(100)<T_D(111)B$.[67] For the (111)A and (111)B faces, a predesorption state was observed at temperatures 50 °C below the desorption temperature: A Ga–S component appears in the x-ray photoelectron spectra at even lower energy, attesting to electron transfer from Ga to S immediately preceding desorption of sulfur.[67] We also note that two sulfide components have been identified in the Ga3*d* spectra of a (111)A face sulfidized by a molecular beam and annealed at temperatures above 360 °C: One is associated with sulfur built into the skin layer of GaAs at the location of arsenic atoms and the other is associated with sulfur adsorbed on the surface.[70]

Desorption of sulfur from a sulfidized GaAs surface also occurs as a result of exposure to vacuum-UV radiation.[71] In this case, the sulfur is desorbed in the form of neutral molecules and the amount of elemental arsenic on the surface increases.

The thickness of the sulfide coating estimated from the x-ray photoelectron spectra was, as a rule, 0.5–2.0 monolayers, but an approximately 15-Å thick sulfide coating was obtained by electrochemical passivation.[26] The thickness of a sulfide coating on a surface depends on the orientation and, just as the desorption temperature, correlates with the Ga–S bond energy.[72]

3.2.1.2. GaAs/Se

In one of the first studies of the chemical bonds on a GaAs surface treated in solutions of sodium selenide in ammonium hydroxide, selenium on the surface was manifested at least in three different forms: selenates (Se^{4+}), elemental selenium (Se^0), and selenides (Se^{2-}).[15] After such a surface was treated in sodium sulfide solutions, the bulk selenium was removed, and the chemisorbed selenium in all its forms remained unchanged. Therefore, the GaAs–Se surface bonds are stronger than GaAs–S bonds. As a aresult of room-temperature treatment, selenium bonded with arsenic and after heating selenium bonds with gallium were formed. It has also been observed[73] that, in contrast to a sulfide coating, prolonged washing of a semiconductor with water does not remove a selenium coating.

Treatment of a surface in a solution of selenium sulfide[16] had the effect that selenium was present on the surface only in the form of selenides, specifically, As_2Se_3. A small quantity of sulfur has also been observed in the x-ray photoelectron spectra, although the bonds in which sulfur participated could not be identified. It has also been noted that As_2Se_3 remains stable upon heating to 300 °C. In addition, such treatment resulted in virtually complete removal of the oxide layer from the semiconductor surface. The native oxide layer has also been removed by using other selenium solutions, specifically, Se/NH_4OH.[18]

The temperature at which a surface is treated by a molecular selenium beam determines the chemical composition of the GaAs surface.[74] Treatment at room temperature led to the formation of only As–Se bonds, while treatment at 550 °C led to the formation of only Ga–Se bonds. Just as in the case of sulfidization, as temperature increases, selenium transfers from arsenic to gallium, but the activation energy of this process is appreciably higher than for the case of sulfidization. After GaAs is treated with a molecular selenium beam at high temperatures, for which there are no As–Se bonds on the surface, the Se3*d* peak decomposed into two components:[75] One was due to selenium absorbed on the surface and the other was due to selenium occupying arsenic sites in the volume of the semiconductor near the surface. It was also observed that the amount of arsenic on the surface decreases after treatment with selenium. The penetration depth of selenium in the skin layer of GaAs depends on the orientation of the semiconductor surface.[74] This dependence in turn was correlated with the temperature at which selenium desorbs from the surface: The lower the desorption temperature, the deeper selenium penetrates into the volume of the semiconductor. The orientation dependence of the selenium desorption temperature is the same as the dependence of the sulfur desorption temperature, but selenium desorbs at higher temperatures than sulfur. Substitution of selenium for arsenic in the skin layer about 5 monolayers thick has also been observed accompanying treatment of the surface in a H_2Se flow,[76], but in this work the components due to the chemical bonds Ga–Se and As–Se were absent in the x-ray photoelectron spectra, although a Se3*d* peak was observed.

3.2.1.3. Oxidation of a passivated GaAs surface

Since the passivation effect degrades with time when a surface is allowed to stand in the atmosphere, the oxidation of a sulfidized semiconductor surface and the accompanying change in the chemical bonds on the surface were studied extensively. Experimental studies of the oxidation of a GaAs surface sulfidized in a $(NH_4)_2S$ solution showed that neither allowing a surface to stand in oxygen in the dark nor illumination of the surface with light in vacuum influences the chemical bonds on a sulfidized surface.[53] At the same time,

even a 40-min holding period in oxygen (at 200 Torr) in the presence of illumination produced appreciable oxidation of the surface, the x-ray photoelectron spectra became the same as for presulfidization GaAs coated with the native oxide layer. Moreover, it has been observed[72] that a passivated GaAs surface oxidizes more slowly than a surface immediately extracted from the epitaxial system after growth, and it has also been shown that the rate of oxidation of a sulfidized surface depends strongly on the orientation of the surface [the (100) surface oxidized most rapidly] and that gallium oxidizes more rapidly than arsenic. The slower oxidation of a sulfidized surface as compared with a nonsulfidized surface has also been observed in Ref. 77.

In an investigation of the degradation of a selenium coating, it was observed that the selenium bonds are more stable against photooxidation than bonds with sulfur.[15,16] Investigation of different stages of oxidation in the atmosphere of a GaAs surface modified by a molecular selenium beam showed that first oxygen is physisorbed and then rapid oxidation of gallium occurs (in several minutes). Just as on a sulfidized surface, arsenic oxidizes much more slowly (after a 1-h holding period), and in the process the oxide As_2O_3 forms first and then transforms into As_2O_5. Selenium oxidizes even more slowly.[78] First, a peak due to the appearance of a bulk selenium layer on the surface appears in the decomposition of the photoelectron spectrum (after a 16-min holding period). Selenium oxide appears only after the surface is allowed to stand in the atmosphere for 3 h.

3.2.2. Indium phosphide

The structure of the native oxide layer on an InP surface differs from the structure of the oxide on a GaAs surface. X-ray photoelectron spectroscopy of an InP surface coated with a native oxide layer shows that primarily In_2O_3 is present on the surface and there are only small traces of $InPO_3$ and $InPO_4$,[79] even though the oxide $InPO_4$ is in thermodynamic equilibrium with the InP surface.[51] The $InPO_4$ content increased with thermal and photostimulated oxidation of the surface. In contrast to GaAs, on whose surface elemental arsenic is almost always observed, elemental phosphorus has not been observed on an InP surface.

Sulfidization in solutions (both sodium sulfide and ammonium sulfide) results in removal of the native oxide layer and, as a rule, the formation of a sulfide coating, which consists only of In–S bonds, on the surface.[80–84] The absence of P–S bonds was attributed to the good solubility of phosphorus sulfides in water[81] (in contrast to arsenic sulfides, which are present in large quantities on the surface of GaAs sulfidized from solutions). Virtually complete removal of physisorbed carbon was also observed.[84]

X-ray photoelectron spectroscopy using measurements which are more surface-sensitive made it possible to investigate in detail the chemical bonds on an InP surface sulfidized from solutions. It has been observed[85] that sulfur is present on the surface in at least four chemical states, which are manifested in the decomposition of the peak S2*p* in the form of four components with energies 161.3, 162.1, 163.1, and 168.4 eV, respectively. These components were attributed to indium monosulfide (In–S bond), indium and phosphorus polysulfide (compound of the type $InPO_4$), elemental sulfur, and sulfur oxide, respectively. Similar components (except for the latter, which is associated with oxide) have been observed in Refs. 86 and 87. In those studies, however, the first two components were identified with sulfur which replaces phosphorus in the second subsurface monolayer and with sulfur adsorbed on the surface (sulfur bonded with In atoms).

Washing with water an InP surface sulfidized from solution completely removed elemental sulfur and sulfur oxide from the surface.[88] Annealing of a sulfidized surface at 125 °C in an ultrahigh vacuum did not change much the shape of the S2*p* line,[86] while after annealing at 250 °C the component due to elemental sulfur vanishes, and after annealing at 320 °C the bonds characteristic of polysulfides vanished on the surface and only the In–S bonds remained.[86,88] Desorption of sulfur from the surface occurs at 460 °C.[89,90]

The chemical bonds formed on an InP surface during sulfidization in the gas phase are, in general, similar to the bonds formed during sulfidization from solutions;[86] the only difference is that the P–S bonds are more pronounced.[91–93] Moreover, the presence of physisorbed sulfides has been observed,[93] and in a number of cases (for example, when cleaving the crystal in a H_2S/H_2 atmosphere) only physisorbed sulfides were present on the surface. It should be noted that annealing (200 °C) converts physisorbed sulfur into chemisorbed sulfur.

Mass-spectrometric investigations of desorption from an InP surface sulfidized in the gas phase have shown[94] that when the surface is annealed at 300 °C hydrogen, sulfur, HS, and H_2S desorb from the surface. As temperature increases to 400 °C, phosphorus also starts to leave the surface.

3.2.3. Indium arsenide and solid solutions based on it

According to a thermodynamic analysis,[51] the composition of the native oxide layer on an InAs surface should be similar to that of the native oxide layer on a GaAs surface, i.e., it should contain both elemental arsenic and various indium and arsenic oxides.

Sulfidization of an InAs surface in solutions results in etching of the oxide layer and the appearance of adsorbed sulfur on the surface.[95,96] Sulfur is present on the surface in three different states,[95] which are similar to the states of sulfur on a sulfidized InP surface:[86] monosulfides, polysulfides, and elemental sulfur. Moreover, after sulfidization the amount of elemental arsenic on an InAs (111)B surface decreases.[96]

Sulfidization of an InAlAs surface in ammonium sulfide solutions also removes the native oxide layer, decreases the amount of elemental arsenic on the surface,[49,97] and leads to the appearance of In–S, Al–S, and As–S bonds. In addition, it has been observed that the surface becomes enriched with indium and, correspondingly, with depleted aluminum.[49] When a sulfidized surface is annealed in vacuum, the composition of the surface depends on the annealing temperature.[97] Investigation of a surface as the temperature is raised has shown that at $T=300$ °C As–S bonds vanish

from the surface and the thickness of the sulfide coating decreases. Further, at $T=400$ °C the In–S bonds vanish and the thickness of the sulfide coating again decreases. Finally, at $T=600$ °C the Al–S bonds vanish and sulfur is no longer detected on the surface.

Chemical bonds on an InGaAs surface sulfidized in a hydrogen sulfide atmosphere were studied in Ref. 98. It was found that such passivation removes a thin oxide layer that arises when the sample is transported from the growth chamber used in molecular epitaxy into the analytical chamber of the photoelectronic spectrometer.

3.2.4. Gallium phosphide

There are very few studies in which chemical bonds on sulfidized GaP surfaces were investigated. Nonetheless, it has been shown[99] that, just as for other III–V semiconductors, sulfidization of gallium phosphide in solutions removes the oxide layer from the surface and forms a thin (approximately 1 monolayer thick) sulfide coating on it.

Sulfur on GaP (100) and (111) surfaces bonds only with gallium atoms. Sulfur bonds with phosphorus have not been observed with sulfidization from either solutions[99,100] or the gas phase.[101] We note that two components with energies 161.9 and 163.2 eV, which correspond to two different states of sulfur on a GaP (001) surface, have been identified in the spectra of the S2*p* line of GaP sulfidized by hydrogen sulfide.[101]

In the case of hydrogen-sulfide sulfidization of a GaP (110) surface prepared by cleaving a crystal in vacuum,[102] P–S bonds appeared on the surface, but these bonds were unstable and vanished from the surface even with heating up to 50 °C. For a longer holding period in hydrogen sulfide Ga–S bonds appeared on the surface. These bonds stabilized the P–S bonds that remained on the surface even after annealing at 200 °C.

4. ATOMIC STRUCTURE AND ELECTRONIC PROPERTIES OF III–V SEMICONDUCTOR SURFACES COATED WITH CHALCOGEN ATOMS

4.1. Atomic structure of a surface coated with chalcogen atoms

4.1.1. Gallium arsenide

Treatment of a GaAs (100) surface in sulfide solutions leads to the appearance of an amorphous sulfur layer on the surface. This layer has been observed by direct investigation of electron diffraction by the sulfidized surface[103,104] and by indirect investigations — reflection anisotropy[105] and work function[106] spectra. A number of investigations have shown that beneath this sulfur layer there is present an ordered sulfide coating with (1×1) structure, where each sulfur atom is bonded with an arsenic atom.[103,105,107]

Annealing of a GaAs (100) surface sulfidized in solution led to the removal of an amorphous sulfur layer and to the formation of a (2×1) dimer structure on the surface.[103,105,107,108] Dimers forming a (2×1) structure are thought to consist of two sulfur atoms bonded both with one another and with lower-lying arsenic atoms.[53] It was noted in Ref. 104, however,that the existence of such dimers should lead to undesirable accumulation of charge on the surface and, correspondingly, make it impossible to explain the passivating effect of a sulfide coating. For this reason, an alternative model was proposed for the dimer structure of a surface,[104] according to which each dimer consists of a Ga atom and a S atom which are bonded with lower-lying Ga atoms. This model is supported by the fact that annealing removes virtually all As–S bonds from the surface, leaving only Ga–S bonds, and by the circumstance that there should be no charge accumulation on such a surface. Moreover, the possibility for the existence of arsenic dimers on the surface has also been discussed.[109]

Annealing of a surface at $T>600$ °C resulted in the removal of sulfur from the semiconductor surface and to the formation of a (4×1) structure with excess gallium.[108]

Different configurations of S–Ga bonds have been observed on GaAs surfaces of different orientations which were sulfidized from a solution of ammonium sulfide and annealed at 500 °C.[110] Sulfur atoms on a (111)A surface are located 2.27 Å directly above gallium atoms. Sulfur on a (100) surface is bonded with two gallium atoms in a bridge configuration; the distance between the sulfur and gallium atoms is 2.31 Å. Finally, sulfur on a (111)B surface replaces the upper arsenic atom and is located 2.34 Å from each of the three nearest gallium atoms.

A (2×6) structure has been observed when a pure GaAs 100) surface was treated in sulfur vapor.[111] This structure appeared after a sulfidized surface with (2×1) structure was annealed up to 370 °C. The (2×6) structure formed as a result of desorption of As atoms from the surface, leaving only S–S dimers on the surface.

Diffusion (1×1) reconstruction appears when a pure GaAs (111)A or GaAs (111)B surface with (2×2) reconstruction is sulfidized in sulfur vapor at room temperature.[70] As the temperature is raised, this reconstruction becomes increasingly more pronounced. As sulfur desorbs from a GaAs (111)A surface, the initial (2×2) reconstruction is restored, and when sulfur desorbs from a GaAs (111)B surface a (1×1) reconstruction characteristic of a sulfidized surface remains.

Selenium on a GaAs (100) surface, just like sulfur, forms a (2×1) structure after annealing.[112] As selenium is deposited on a pure GaAs 100) surface, the (4×6) structure of the surface changes gradually from (4×6) to (4×3) and then to (2×3), and finally a stable (2×1) surface is obtained.[113]

4.1.2. Indium phosphide

The atomic structure of a sulfidized InP surface is fundamentally different from that of a sulfidized GaAs surface. An InP 100) surface sulfidized in a solution of ammonium sulfide possesses (1×1) structure, which remains even after the surface is allowed to stand for three days in air.[84] Sulfur forms a bridge bond with two surface indium atoms in the direction [011] with an In–S–In angle of 100°.[114] It has been shown by dynamic low-energy electron diffraction[115] that the distance between the layer of sulfur adatoms and the semiconductor surface is 1.445 Å, i.e. somewhat less than the

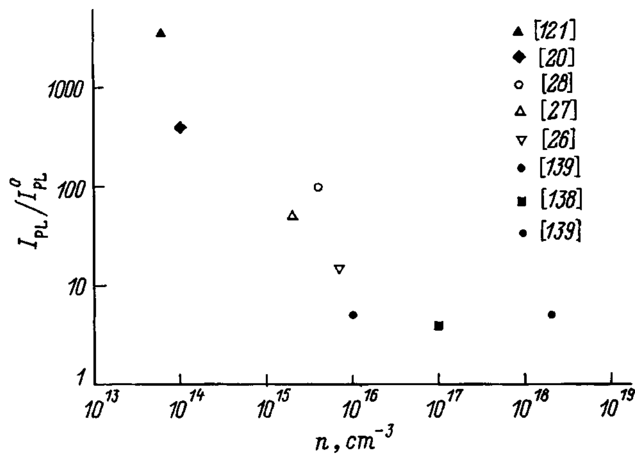

FIG. 2. Increase in the intensity I_{PL} of photoluminescence of GaAs passivated in aqueous sulfide solutions relative to the intensity I^0_{PL} of the photoluminescence of nonpassivated GaAs as a function of the degree n of doping of the semiconductor according to data from various studies (the references are indicated).

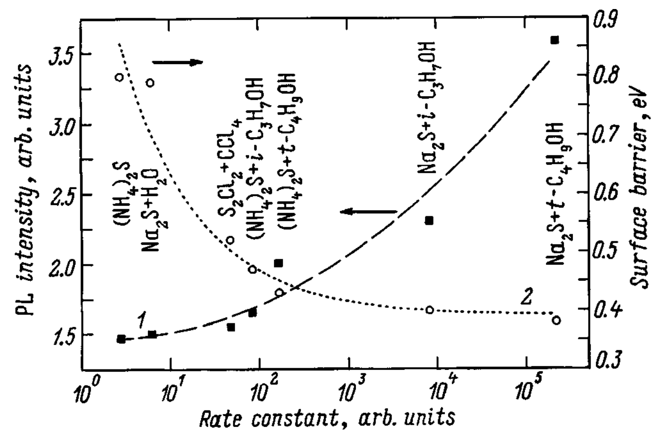

FIG. 3. Increase of the photoluminescence (PL) intensity relative to the intensity of a nonsulfidized semiconductor (*1*) and height of the surface barrier (*2*) of n-GaAs ($n=1\times10^{18}$ cm^{-3}) passivated in different solutions as a function of the rate constant of the reaction forming a sulfide coating.

interplanar distance in bulk InP, and both sulfur adatoms and surface indium atoms have sp^3 hybridization and are bonded with one another by covalent bonds.

Theoretical analysis[116] has shown that the lowest energy sulfidized InP (100) surface is a surface with (2×2) reconstruction, where the sulfur atoms are displaced from positions characteristic of bridge bonds and thereby form long and short dimers that belong to two different atomic planes. It was shown subsequently[117,118] that several stable structures with (2×2) reconstruction can exist on a sulfidized InP (100) surface. The experimental results obtained in Refs. 116 –118 by Raman and photoemission spectroscopies are consistent with the theoretical calculations.

A study of the structure of a sulfidized InP(110) surface showed[119,120] that the sulfide coating has a (1×1) structure, and sulfur occupies the location that phosphorus would occupy in the next monolayer after the surface. The deviation of the sulfur position from the ideal phosphorus position was 0.04 Å in the $(00\bar{1})$ direction, 0.02 Å in the $(\bar{1}10)$ direction, and 0.10 Å in a direction normal to the surface.

4.2. Electronic properties of a surface coated with chalcogen atoms

An appreciable increase in the photoluminescence intensity of a semiconductor,[121] resulting from a large decrease in the nonradiative surface recombination velocity, which is equal to the nonradiative recombination velocity on an ideal GaAs/AlGaAs heterojunction,[122] was observed even in the first studies of the passivation of a GaAs surface in sulfide solutions. The increase in the photoluminescence intensity of GaAs after sulfidization depends largely on the degree of doping of the semiconductor (Fig. 2) and on the rate constant of the reaction that forms a sulfide coating during sulfidization (i.e., on the thickness of the sulfide coating formed per unit time divided by the sulfur concentration in the solution) (Fig. 3),[123,124] as well as on the conditions of subsequent annealing.[125] Electronic passivation of a GaAs (100) surface becomes more efficient as the rate constant of the reaction forming a sulfide coating in aqueous and alcohol solutions of sodium or ammonium sulfides increases.[46] The decrease in the surface recombination rate after the surface is treated with chalcogen atoms was attributed to a decrease in the density of surface states in the band gap of the semiconductor and to a change in the surface bending of bands of the semiconductor.

4.2.1. Effect of chalcogen atoms on surface states in the band gap in III–V semiconductors

Two peaks due to surface states are observed in the band gap in the spectrum obtained for the surface states of n-GaAs by analyzing the dark capacitance–voltage characteristics of metal–insulator–GaAs structures: one 0.6 eV from the conduction-band bottom and the other 0.3–0.5 eV from the valence-band top.[10,126] The density of states in these peaks is about 10^{13} $cm^{-2}\cdot$ eV^{-1}. Treatment in an aqueous solution of ammonium sulfide decreases the density of surface states near the center of the band gap by approximately an order of magnitude. It was shown at the same time[127] that such treatment causes the height of the Schottky barrier on a sulfidized GaAs surface to depend on the work function of the metal used for preparing the barrier contact. This also attests to a decrease in the density of surface states in the band gap as a result of sulfide treatment. It was noted that sulfidization in aqueous solutions leads primarily to a decrease in the density of deep surface traps, while the density of shallow surface traps even increases slightly.[128]

Theoretical investigations of the sulfidized surfaces GaAs (001) — (1×1),[68] GaAs (001) — (2×1),[129,130] and GaAs (111)[69] have shown that adsorption of sulfur results in the surface states being shifted out of the band gap of the semiconductor (especially with formation of Ga–S bonds). Later, analysis of other possible atomic structures on a GaAs (001) surface[131] established that the adsorption of sulfur increases the surface band gap, i.e., the gap between the highest filled and lowest vacant surface states.

Sulfidization of an InP (100) surface prior to deposition of an insulator made it possible to decrease the density of states at the InP/insulator boundary by two orders of magni-

tude. The density of surface states on such a heterojunction has been estimated as 7×10^{9} $cm^{2}\cdot eV^{-1}$ (Ref. 132). The metal–insulator–semiconductor structures produced by sulfide treatment had hysteresis-free capacitance–voltage characteristics, essentially with no frequency dispersion in the range from 10 kHz to 5 MHz.

Investigation of the photoluminescence of lightly doped InP at liquid-helium temperatures showed that sulfide passivation decreases the radiative recombination via surface states.[133] Treatment of an InP (100) surface (with carrier density $n=4\times10^{16}$ cm^{-3}) in an aqueous solution of sodium sulfide tripled the room-temperature photoluminescence intensity of the semiconductor.[134] The photoluminescence intensity of InP (100) ($n=3\times10^{18}$ cm^{-3}), treated in a aqueous solution of ammonium sulfide, at liquid-nitrogen temperature quadrupled and subsequent annealing increased the photoluminescence intensity ninefold over that of a semiconductor with a nonsulfidized surface.[135]

4.2.2. Effect of chalcogen atoms on band bending at the surface in III–V semiconductors and position of the energy levels at the surface

The band bending at the surface and the position of the energy levels at the surface (surface Fermi level, ionization energy, and electron affinity) are the most important parameters characterizing the electronic structure of a semiconductor. Since band bending is one of the factors responsible for surface recombination, it is not surprising that investigations of the electronic structure of passivated semiconductors have focused on investigations of the surface barrier and the position where the Fermi level is pinned at the surface.

In previous studies of sulfidized semiconductors the surface barrier was investigated mainly by indirect methods. Even in one of the first studies of sulfide passivation of GaAs,[136] it was established that in *n*-GaAs the band bending at the surface decreased when a sodium sulfide layer was deposited on the surface. Raman spectroscopy of a sulfidized semiconductor showed that the intensity of the peak due to scattering by longitudinal optical (LO) phonons is lower than for a nonsulfidized semiconductor. Since the peak associated with LO phonons is due to a depleted region on the semiconductor surface, the intensity of the peak (measured as the ratio to the intensity of the peak associated with scattering by a paired phonon–plasmon mode in the volume of the semiconductor on free carriers) characterizes the depth of the depleted region of the semiconductor. The sulfidization-induced decrease in the intensity of the peak associated with LO phonons attests to a decrease in the depth of the depleted region. Assuming that sulfidization does not result in the accumulation of excess charge on the surface, and using data on the barrier height for nonsulfidized *n*-GaAs, which were obtained by photoemission investigations in Ref. 137 ($\phi_0=0.78$ eV), the authors of Ref. 136 calculated the surface barrier of sulfidized GaAs ($n=1\times10^{18}$ cm^{-3}) to be 0.48 eV.

However, it was shown later, first by measuring the surface conductivity[138,139] and then by photoemission measurements,[54–56] that sulfidization of GaAs (100) in aqueous solutions of sodium sulfide or ammonium sulfide does not change the band bending at the surface and the position of the Fermi level at the surface. Annealing of a sulfidized *n*-GaAs surface at about 360 °C decreased the surface band bending by 0.3 eV.[55,56] Investigation of the position of the surface Fermi level in *p*-GaAs by anisotropic reflection showed[125] that the observed shift in the direction of the conduction band by 0.8 eV as a result of vacuum annealing at 270 °C is due to desorption of a passivating coating that possess negative charge. Further annealing results in the formation of dimers on the surface and causes the Fermi level to return approximately to its initial position.

Sulfidization of a *n*-GaAs (100) surface from the gas phase, specifically, in a sulfur flow from an electrochemical cell, decreased even at room temperature the band bending by 0.2 eV, which decreased by another 0.3 eV as a result of annealing at 360 °C.[56] Additionally, the observed decrease in the surface band bending after annealing depends on the reconstruction of the initial *n*-GaAs (100) surface:[58] The surface band bending at the surface with c (2×8) reconstruction sulfidized by a sulfur flow does not change on annealing even to 500 °C, while for the initial surface with (4×1) reconstruction and sulfidized in a similar manner the surface band bending decreases as a result of annealing to 500 °C by 0.3 eV. Upon annealing to 570 °C, i.e., to complete desorption of sulfur from the surface, the Fermi level returns to its initial position in the nonsulfidized semiconductor.

In the case of sulfur adsorption from the gas phase on a *n*-GaAs (111) surface, the band bending at the surface and, correspondingly, the position of the Fermi level at the surface change in a different manner.[70] The Fermi level on a pure GaAs (111)A surface lies 0.45 eV above the valence-band top, and room-temperature sulfur adsorption shifts it by 0.2 eV in the direction of the conduction band. Annealing up to 450 °C shifts the Fermi level by 0.1 eV, so that the resulting decrease of the band bending is 0.3 eV, while the Fermi level becomes pinned near the center of the band gap. Annealing of a sulfidized GaAs (111)A surface up to complete desorption of sulfur from the surface returns the Fermi level to its initial position characteristic of the nonsulfidized semiconductor. The Fermi level on a pure GaAs (111)B surface lies 1.0 eV above the valence-band top and the adsorption of sulfur at room temperature shifts it by 0.1 eV in the direction of the conduction band. However, subsequent annealing shifts the Fermi level by 0.3 eV in the opposite direction, so that the Fermi level is pinned near the center of the band gap.

Investigation of sulfur adsorption on *n*- and *p*-type GaAs (110) surfaces cleaved in vacuum[40] showed that as the holding time of the surface in a sulfur flow increased, the Fermi level on the *n*-GaAs (110) and *p*-GaAs (110) surfaces shifted from a position coinciding with the position in the interior of the semiconductor to a position shifted by approximately 0.35 eV from the valence-band top. Further holding in the sulfur flow has the effect that the Fermi level in both *n*- and *p*-GaAs (110) is pinned in a position 0.85 eV above the valence-band top. At the same time, the ionization energy of the semiconductor increases by 0.92 eV.

Other methods of sulfidizing GaAs also change the position of the surface energy levels. Specifically, sulfidization of *n*-GaAs (100) in alcohol solutions of inorganic sulfides

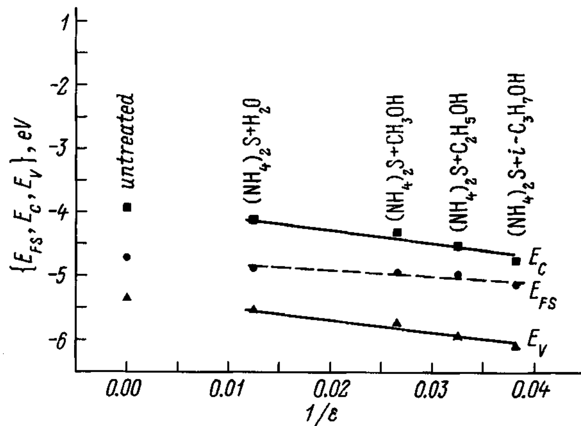

FIG. 4. Position of the surface Fermi level E_{FS}, conduction-band edge E_C, and valence-band edge E_V with respect to the vacuum level for n-GaAs(100) ($n=1\times10^{18}$ cm^{-3}), nonsulfidized and sulfidized in different solutions as a function of the reciprocal of the dielectric constant ε of the sulfide solution.

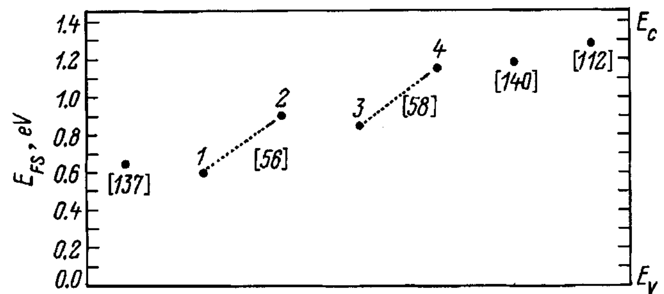

FIG. 5. Position of the surface Fermi level E_{FS} relative to the conduction-band edge E_C and the valence-band edge E_V of n-GaAs(100) with different chalcogenide passivations according to data from various studies: Ref. 137 — untreated surface; Ref. 56 — treatment in aqueous sulfide solutions (*1*) and annealing at 360 °C (*2*); Ref. 58 — treatment in S_2 flow (*3*) and annealing at 500 °C (*4*); Ref. 140 — treatment in the solution $(NH_4)_2S$ + t-C_4H_9OH; Ref. 112 — treatment in a Se_2 flow.

(sodium or ammonium sulfides) decreases the surface band bending,[124,140,141] and the shift of the surface Fermi level increases as the dielectric constant of the sulfide solution and the rate constant of the reaction forming the sulfide coating decreases (Fig. 3). In the process, the ionization energy of the semiconductor increases. The increase was accelerated with decreasing dielectric constant of the solution[142] (Fig. 4). For example, for sulfidization of n-GaAs (100) in an aqueous solution of ammonium sulfide the Fermi level remained essentially in place and the ionization energy increased by 0.2 eV, while with sulfidization in a solution of ammonium sulfide in isopropyl or tret-butyl alcohol the Fermi level shifted by 0.53 eV in the direction of the conduction band[140,141] and the ionization energy increased by 0.75 eV.

Treatment of a GaAs (100) surface with selenium atoms also changed the surface band bending. It has been shown that band bending at a n-GaAs (100) surface decreases to 0.1–0.15 eV as a result of treatment in aqueous solutions containing Se[15] and as a result of holding of an atomically pure, nonoxidized n-GaAs (100) surface in H_2Se at 425 °C (Ref. 76) and in a Se_2 flow.[112] The position of the Fermi level relative to the edges of the semiconductor bands, which is characteristic of different n-GaAs (100) surfaces covered with chalcogen atoms, is shown in Fig. 5.

Sulfidization of InP (100) changes the position of the Fermi level at the surface relative to the band edges of the semiconductor. It has been shown[93] that treatment of a p-InP (100) surface in the gas mixture H_2S/H_2S_n at room temperature pins the Fermi level in a position 0.5–0.6 eV above the valence-band top. Annealing of this surface shifts the Fermi level in the direction of the conduction band, and an increase of annealing temperature increases the shift. Thus, at an annealing temperature of 300 °C the Fermi level is pinned in a position 0.9–1.2 eV above the valence-band top; i.e., inversion of the conduction type is observed at the semiconductor surface. Further annealing (at 400 °C) shifts the Fermi level back to its initial position. The same type of treatment of a n-InP(100) surface does not change the position of the Fermi level (which is pinned 1.2 eV above the valence-band top) even after annealing.

Inversion of conduction type of the p-InP (100) surface has been observed when the surface was held in H_2S at room temperature[91] and in H_2S plasma,[92] and also in the case of sulfidization in an aqueous solution of ammonium sulfide.[86,143] It should be noted that in the case of sulfidization of n-InP (100) in an aqueous solution of ammonium sulfide, the Fermi level shifts by 0.1 eV in the direction of the valence band.[86,143]

It has recently been shown that adsorption of selenium on an atomically pure InAs (100) surface shifts the surface Fermi level by 0.4 eV, which is pinned in a position 0.5 eV above the conduction-band bottom; i.e., anomalously high band bending is observed at the surface.[144]

5. APPLICATION OF CHALCOGENIDE PASSIVATION IN SEMICONDUCTOR TECHNOLOGY

5.1. Passivation of semiconductor devices

5.1.1. Bipolar transistors

Bipolar transistors based on GaAs/AlGaAs heterostructures are widely used in high-frequency analog and digital integrated circuits. To increase the working frequency and decrease the power requirements, devices must be made as small as possible. However, because of the high surface recombination velocity characteristic of GaAs, a substantial fraction of the electrons injected into the base is lost, which results in a sharp decrease in gain as device size decreases. For this reason, to obtain small working devices surface recombination must be reduced substantially.

Passivation with chalcogen atoms was first used to improve the characteristics of a GaAs/AlGaAs bipolar transistor.[8] Treatment of the transistor in an aqueous solution of sodium sulfide increased the current gain sixtyfold at low collector currents. It was shown subsequently[145] that such passivation considerably improves the ideality of the emitter junction (passivation decreases the nonideality coefficient n from 1.7 to 1.03). This made it possible to obtain high current gain with higher collector currents.

Later, to improve passivation stability, after sulfidization in ammonium polysulfide solutions a GaAs/AlGaAs bipolar transistor was covered with a layer of either As_2S_3 (Ref.

146) or SiN_x.[147] Such treatment appreciably decreased the base current at low collector currents and increased the gain. In addition, these characteristics of the transistor remained stable for at least several months.

Another application of sulfide passivation for bipolar transistors is suppression of the dependence of the current gain on the emitter size.[148] Treatment of a GaAs/AlGaAs bipolar transistor in an ammonium sulfide solution not only increases the gain but also makes it virtually independent of the emitter size for dimensions ranging from 12×12 to $4\times4\ \mu m^2$.

5.1.2. Devices based on Schottky barriers and MIS structures

The properties of surfaces and interfaces are among the most important factors which are taken into account in the design of field-effect transistors. The corresponding parameters are the Schottky barrier height in Schottky-barrier field-effect transistors, the position of the Fermi level at the surface, and the density of surface and interfacial states in MIS transistors. The possibility of producing states of inversion, depletion, and enrichment with a transition through a flat-band state, as well as the possibility of shifting the surface potential from its equilibrium value by applying a voltage to the gate,are also of interest.

Sulfide or selenide treatment of a semiconductor prior to the formation of a Schottky barrier substantially decreases the leakage currents in metal–semiconductor structures.[12,149–152] Other achievements were a considerable increase of the barrier height in Au/*n*-InGaAs structures,[149] an increase in the photosensitivity of Al/*p*-GaP (Ref. 99) and Au–AlGaAsSb (Ref. 150) Schottky diodes, and a decrease in the density of interfacial states in Au–*n*-GaAs and Au–*n*-InGaP Schottky contacts.[153] In addition, it has been shown that the characteristics of GaAs-based, high-power, field-effect transistors are substantially improved by treatment in an ammonium sulfide solution.[154] In particular, the leakage currents between the gate and drain decreased considerably (by a factor of 15) and the breakdown voltage between the source and drain doubled.

The high density of surface states in the band gap, characteristic of real III–V semiconductor surfaces, leads to rigid pinning of the Fermi level at the surface. This prevents control of the surface barrier and therefore makes it difficult to produce such devices based on these semiconductors. Sulfidization of *n*- and *p*-GaAs surfaces in ammonium sulfide solutions decreases the density of surface states in the band gap of the semiconductor, and this in turn leads to less rigid pinning of the Fermi level at the surface and hence the barrier height becomes dependent on the work function of the metal.[127,155] The same dependence has been obtained for *n*-GaAs pretreated in selenium vapor.[156] Later, the dependence of the barrier height on the work function of metals was also observed for other passivated III–V semiconductors: InP, GaP, AlGaAs,[157] AlGaAsSb,[150] and InGaP.[158]

The large decrease produced in the electron density of states of a semiconductor by chalcogenide passivation made it possible to use this method in MIS structure technology. In Refs. 10 and 159 a substantial decrease of the density of states was achieved at a $GaAs/SiO_x$ interface (to $1.2\times10^{11}\ cm^{-2}\cdot\ eV^{-1}$) after GaAs treatment in a solution of ammonium sulfide and the thermal stability of the semiconductor/insulator boundary was increased. Treatment of GaAs in selenium vapor prior to deposition of SiO_2 made it possible to produce MIS diodes with a low-frequency dispersion of the capacitance for any bias.[160] Sulfide passivation has also been used to improve the high-frequency characteristics of GaAs-based MIS structures.[161]

Besides simple passivation, a relatively thick (about 300 Å) sulfide coating grown by plasma technology has been used as a subgate insulator on an InP surface.[37] The result was a substantial decrease in the leakage currents and density of interfacial states. Moreover, in these structures it was possible to obtain both depletion and enrichment regimes, as well as a hysteresis-free capacitance–voltage characteristic at room temperature. Subsequently, sulfide passivation made it possible to improve the electrical characteristics and thermal stability of InP-based MIS diodes.[162] Treatment of a *n*-InP surface with gas-phase polysulfides prior to deposition of the insulator made it possible to produce diodes in which an inversion regime was realized.[163]

5.1.3. Semiconductor p–n structures

The decrease in the surface recombination velocity due to chalcogenide passivation has made it possible to improve substantially the characteristics of *p–n* structure phototransducers. Even in large-area GaAs homostructures ($0.25\ cm^2$), after treatment in sodium sulfide and ammonium sulfide solutions the edge recombination current decreased threefold and the shunting leakages in the presence of a small forward bias virtually vanished.[9] Similar results were later obtained on even larger-area structures (up to $16\ cm^2$).[164]

Sulfide passivation of GaAs homostructure solar cells with thin emitters (several hundreds of nanometers) considerably increased the photocurrent, improved the photosensitivity, especially in the short-wavelength region of the spectrum (for example, the photosensitivity at 400 nm of a diode with a 600-nm-thick emitter was 4.5 times higher after passivation), and decreased the saturation current.[14] These effects are attributable to a passivation-induced decrease in the surface recombination velocity from 5×10^6 to 10^3 cm/s. Subsequently, it was shown that the short-wavelength photosensitivity can be increased in AlGaAs-based *p–n* heterostructures with a relatively thick (several microns) emitter.[165]

Sulfide passivation appreciably improves the dark current in mesadiodes based on GaAlSb,[166] InAsSb,[167] and GaSb/GaInAsSb/GaAlAsSb[168] and increases the photosensitivity, the external quantum yield, and the detection power of InAsPSb/InAs infrared photodetectors.[169]

5.1.4. Semiconductor lasers

Sulfide passivation has been used to improve the quality of a buried interface during the fabrication of AlGaAs/GaAs heterolasers. Passivation of an AlGaAs/GaAs mesastrip laser

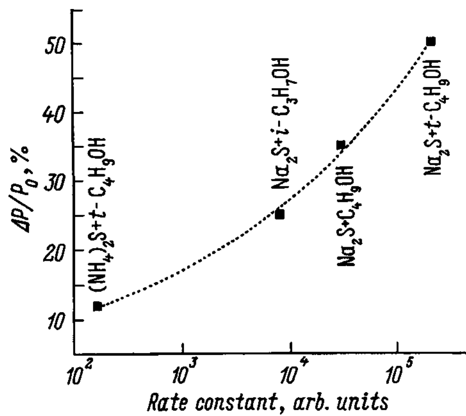

FIG. 6. Increase of the threshold for catastrophic optical degradation of SQW-InGaAs/AlGaAs (3 μm × 800 μm, 300 K) laser diodes[29,30] with passivation in different sulfide solutions as a function of the rate constant of the reaction forming the sulfide coating. $\Delta P/P_0$ — Relative change in the threshold power of the laser.

structure in an ammonium sulfide solution prior to burying with an AlGaAs layer decreases threefold the threshold current of such lasers.[170,171]

Treatment of microdisk-shaped AlGaAs/GaAs structures in ammonium sulfide solutions has made it possible to obtain lasing in these structures.[172,173] In addition, coating of the sulfidized structures with a SiN_x layer made it possible to decrease the degradation of these lasers considerably and correspondingly to increase their service life.

Treatment of InGaAsP lasers in an aqueous solution of ammonium sulfide makes these lasers much more reliable with respect to voltage overloading,[174] and passivation of InGaAsP/InP mirrors (at wavelength $\lambda = 1.55$ μm) in an alcohol solution of sodium sulfide strongly decreases the low-frequency noise in these devices (by 30 dB at 1 kHz).[175] The threshold of catastrophic optical degradation of AlGaInP lasers ($\lambda = 0.67$ μm) has been increased by 25% by electrochemical sulfide passivation.[25] Passivation of the mirrors of high-power InGaAs/AlGaAs ($\lambda = 0.98$ μm) lasers in alcohol solutions of sodium sulfide made it possible to increase their threshold for catastrophic optical degradation by 25–50%,[29,30] and the increase in the threshold of catastrophic optical degradation depends on the rate constant of the reaction forming the sulfide coating (Fig. 6), which correlates with the increase in the photoluminescence intensity of sulfidized GaAs (Fig. 3). Treatment of similar lasers in aqueous solutions of ammonium sulfide increased the threshold for catastrophic optical degradation by 10–20%.[176]

5.2. Application of chalcogenide passivation in the technology for burying structures

To fabricate many modern semiconductor devices, such as lasers or devices with quantum wires, it is often necessary to bury different semiconductor structure which have been subjected to different technological procedures. The burying operation must allow performing multistep technological processing (etching, annealing, photolithography, and so on) with the structure removed from the growth chamber, and then continuing epitaxial growth with the structure returned into the growth chamber. Such a process opens up the possibility of producing many new devices if the interface obtained by burying is of acceptable quality.

In GaAs and other III–V semiconductors it is difficult to perform high-quality burying because of the high density of surface states on a surface held under ordinary room conditions. Chalcogenide passivation of GaAs, first, removes the native oxide layer from the surface and, second, decreases the density of surface states. For this reason it is promising for preparing a surface for the burying operation.

Burying a GaAs surface, treated in an ammonium sulfide solution, with a GaAs layer ($n = 2 \times 10^{16}$ cm^{-3}) by molecular-beam epitaxy gave a high-quality interface, although a small accumulation of donors as a result of imbedding of residual sulfur atoms was observed on it. The accumulation decreases with increasing epitaxy .[177] On the other hand, imbedding of residual sulfur atoms is accompanied by compensation of interfacial carbon and oxygen impurities, which makes it possible to decrease the contact resistance of the heterojunction.[178] Burying a GaAs layer, treated in sodium selenide solutions, with GaAs and $Al_{0.5}Ga_{0.5}As$ layers in the process of molecular-beam epitaxy leads to the formation of a layer consisting of selenides and selenates on it.[179] A (1×1) reconstruction was observed on a selenium-treated surface, indicating that the quantity of residual oxides is very small. Transmission electron microscopy showed that the interface obtained after burying is atomically sharp and defect-free. Photoluminescence investigations showed that the intensity of the photoluminescence of a buried AlGaAs/GaAs structure is virtually identical to that of a AlGaAs/GaAs structure grown in a single process without interruption of the growth process. This shows that burying a GaAs surface modified with selenium atoms gives an interface of high electronic quality.

For epitaxy from organometallic compounds, the semiconductor surface can be prepared by chemical gas etching in a reactor immediately prior to burial. However, such etching is undesirable for burying structures with thin layers. In particular, a carrier density peak at the forming interface can radically change the form of the potential in the device. It is therefore very important to obtain a good interface without etching.

An appreciable improvement of interface quality accompanying InP epitaxy has been obtained by treating the surface in an ammonium sulfide solution before final burial in epitaxy from organometallic compounds.[180] It was found that in a nonsulfidized sample the carrier density in the interfacial layer is approximately three orders of magnitude higher than in the surrounding layers, while in a sulfidized sample the carrier density at the interface is 5×10^{15} cm^{-3}, which corresponds to the density in the growing layers.

Chalcogenide passivation makes it possible to bury layers of solid solutions containing aluminum. Ordinarily, this process encounters serious difficulties because of the high rate of oxidation of the layers. In Ref. 171, an $Al_{0.3}Ga_{0.7}As$ mesa structure was buried by an $Al_{0.1}Ga_{0.9}As$ layer by epitaxy from organometallic compounds. This made it possible to decrease considerably the interfacial recombination velocity on the walls of the mesa structure and produce low-

threshold lasers. Subsequently,[181] $Al_xGa_{1-x}As$ layers with high aluminum content $(0.3<x<0.8)$, held in air for 1 day and then treated in a sulfide solution, were buried by liquid-phase epitaxy.

An interesting experiment was performed in Ref. 182, where GaAs microcrystals were grown on a GaAlAs surface covered with selenium atoms. The average size of the microcrystals obtained was 45 nm; the deviation from the average size did not exceed 12%. The distance between the microcrystals was about 200 nm. It should be noted that passivation in an ammonium sulfide solution has been used for GaAlAs surface preparation (before loading the surface into a molecular-beam epitaxy chamber for deposition of a thin selenium coating and for GaAs epitaxy).

Chalcogenide passivation has also been used to prepare GaAs and InP surfaces for epitaxial growth on them of wide-gap semiconductors and insulator layers, specifically, GaF_2 and BaF_2 (Refs. 183 and 184), as well as ZnS and ZnSe (Ref. 185).

5.3. Degradation of passivated structures

For many applications of passivation the most important question is to ensure long-time stability of the improved electronic properties of passivated heterojunctions and devices. Even in the first successful application of sulfide passivation to improve the characteristics of a GaAs/AlGaAs bipolar transistor,[8] high gain was observed for several days after sulfidization. However, the photoluminescence characteristics of GaAs passivated in an aqueous solution of sodium sulfide degraded when exposed to radiation for 0.5 h.[139] These results agree with the conclusion drawn in Ref. 53 that photooxidation is the main mechanism leading to the degradation of the properties of a sulfide coating.

A high stability of the properties of a passivated GaAs surface has been achieved by electrochemical passivation[26] and passivation in alcohol solutions.[28] The photoluminescence properties of a surface sulfidized by these methods remain stable even under the action of intense laser radiation, and laser mirrors become more stable against catastrophic optical degradation. Another method of increasing the stability of the properties of passivated devices is shielding of the passivated surface with an insulator layer. For example, microdisk-shaped GaAs/AlGaAs laser structures sulfidized in an aqueous solution of ammonium sulfide emitted for 2 min before completely degrading, while emission remained stable for the entire period of investigation (about 2 h) when the surface of these layers was protected with a SiN_x layer.[173]

Other semiconductors are characterized by the higher degree of stability of the properties of the sulfide coating. For example, the photoluminescence characteristics of InP sulfidized in aqueous solutions of sodium sulfide essentially did not degrade under the action of the exciting radiation from a He–Ne laser.[134] The characteristics of a GaAsSb photodiode treated in an aqueous solution of ammonium sulfide remained stable for one year after sulfidization without the surface being protected by an insulator layer.[166]

6. CONCLUSIONS

Experimental study of the chemical and electronic passivation of III–V semiconductor surfaces by chalcogen atoms that has been recently conducted undoubtedly provides both a deeper understanding of the surface properties of semiconductors and promotes further advancement of semiconductor technology. However, much remains unclear in this field.

What paths exist for further advances in this direction?

In the first place, the possibilities of controlling the surface properties of III–V semiconductors must be clarified. Today our knowledge of the properties of semiconductor surfaces modified by foreign atoms does not permit obtaining surfaces with a prescribed electronic structure, i.e., with the desirable band bending and density of surface states. At the same time, the chemical state of an atom prior to adsorption can largely determine the electronic structure of the surface, and therefore it is important to determine the systematic features underlying the chemical processes that effect the electronic properties of surfaces.

Second, further advancement of chalcogenide passivation is impossible without better experimental methods for studying the atomic and electronic structure to clarify the interrelation of chemical processes and the effectiveness of electronic passivation of III–V semiconductor surfaces.

Finally, new applications of chalcogenide passivation in semiconductor electronics will stimulate further investigations of the interaction of III–V semiconductor surfaces with chalcogen atoms.

We wish to express our deep appreciation to B. V. Tsarenkov under whose guidance we started our work. We also wish to thank P. S. Kop'ev for support.

The original studies of the authors mentioned in this review article were supported by the Russian Fund for Fundamental Research, the Soros Fund, and the Volkswagen Foundation. The authors express their deep appreciation to these organizations.

[1] A. M. Green and W. E. Spicer, J. Vac. Sci. Technol. A **11**, 1061 (1993).
[2] D. L. Lile, *Technologies for Optoelectronics,* SPIE **869**, 107 (1987).
[3] P. Viktorovitch, Rev. Phys. Appl. **25**, 895 (1990).
[4] P. Viktorovitch, M. Gendry, S. K. Krawczyk, F. Krafft, P. Abraham, A. Bekkaoni, and Y. Monteil, Appl. Phys. Lett. **58**, 2387 (1991).
[5] M. Kasu, T. Makimoto, and N. Kobayashi, Appl. Phys. Lett. **68**, 955 (1996).
[6] P. R. Varekamp, M. C. Håkansson, J. Kanski, D. K. Shuh, M. Björkquist, M. Gothelid, W. C. Simpson, U. O. Karlsson, and Y. A. Yarmoff, Phys. Rev. B **54**, 2101 (1996).
[7] M. Passlack, M. Hong, J. P. Mannaerts, R. L. Opila, S. N. G. Chu, N. Moriya, F. Ren, and J. R. Kwo, IEEE Trans. Electron Devices **44**, 214 (1997).
[8] C. J. Sandroff, R. N. Nottenburg, J.-C. Bischoff, and R. Bhat, Appl. Phys. Lett. **51**, 33 (1987).
[9] M. S. Carpenter, M. R. Melloch, M. S. Lundstrom, and S. P. Tobin, Appl. Phys. Lett. **52**, 2157 (1988).
[10] J.-F. Fan, H. Oigawa, and Y. Nannichi, Jpn. J. Appl. Phys. **27**, L1331 (1988).
[11] H. H. Lee, R. J. Racicot, and S. H. Lee, Appl. Phys. Lett. **54**, 724 (1989).
[12] K. C. Hwang and S. S. Li, J. Appl. Phys. **67**, 2162 (1990).
[13] Y. Wang, Y. Darici, and P. H. Holloway, J. Appl. Phys. **71**, 2746 (1992).
[14] M. G. Mauk, S. Xu, D. J. Arent, R. P. Mertens, and G. Borghs, Appl. Phys. Lett. **54**, 213 (1989).

[15] C. J. Sandroff, M. S. Hegde, L. A. Farrow, R. Bhat, J. P. Harbison, and C. C. Chang, J. Appl. Phys. **67**, 586 (1990).
[16] B. A. Kuruvilla, G. V. Ghaisas, A. Datta, S. Banerjee, and S. K. Kulkarni, J. Appl. Phys. **73**, 4384 (1993).
[17] Z. S. Li, W. Z. Cai, R. Z. Su, G. S. Dong, D. M. Huang, X. M. Ding, X. Y. Hou, and X. Wang, Appl. Phys. Lett. **64**, 3425 (1994).
[18] K. Tsuchiya, M. Sakata, A. Funyu, and H. Ikoma, Jpn. J. Appl. Phys. **34**, 5926 (1995).
[19] A. S. Weling, K. K. Kamath, and P. R. Vaya, Thin Solid Films **215**, 179 (1992).
[20] S. R. Lunt, G. N. Ryba, P. G. Santangelo, and N. S. Lewis, J. Appl. Phys. **70**, 7449 (1991).
[21] J. F. Dorsten, J. E. Maslar, and P. W. Bohn, Appl. Phys. Lett. **66**, 1755 (1995).
[22] K. Asai, T. Miyashita, K. Ishigure, and S. Fukatsu, J. Appl. Phys. **77**, 1582 (1995).
[23] S. Weiguo, Appl. Phys. A **52**, 75 (1991).
[24] J. Yota and V. A. Burrows, J. Vac. Sci. Technol. A **11**, 1083 (1993).
[25] A. J. Howard, C. I. H. Ashby, J. A. Lott, R. P. Schneider, and R. F. Corless, J. Vac. Sci. Technol. A **12**, 1063 (1994).
[26] X. Y. Hou, W. Z. Cai, Z. Q. He, P. H. Hao, Z. S. Li, X. M. Ding, and X. Wang, Appl. Phys. Lett. **60**, 2252 (1992).
[27] V. N. Bessolov, A. F. Ivankov, E. V. Konenkova, and M. V. Lebedev, Pis'ma Zh. Tekh. Fiz. **21**, 46 (1995) [Tech. Phys. Lett. **21**, 20 (1995)].
[28] V. N. Bessolov, E. V. Konenkova, and M. V. Lebedev, J. Vac. Sci. Technol. B **14**, 2761 (1996).
[29] V. N. Bessolov, M. V. Lebedev, Yu. M. Shernyakov, and B. V. Tsarenkov, Pis'ma Zh. Tekh. Fiz. **21**, 53 (1995) [Tech. Phys. Lett. **21**, 561 (1995)].
[30] V. N. Bessolov, M. V. Lebedev, Yu. M. Shernyakov, and B. V. Tsarenkov, Mater. Sci. Eng., B **44**, 380 (1997).
[31] M. Liehr and H. Luth, J. Vac. Sci. Technol. **16**, 1200 (1979).
[32] J. Massies, F. Dezaly, and N. T. Linh, J. Vac. Sci. Technol. **17**, 1134 (1980).
[33] J. R. Waldrop, J. Vac. Sci. Technol. B **3**, 1197 (1985).
[34] B. I. Sysoev, V. F. Antyushkin, V. D. Strygin, and V. N. Morgunov, Zh. Tekh. Fiz. **56**, 913 (1986) [Sov. Phys. Tech. Phys. **31**, 554 (1986)].
[35] N. Barbouth, Y. Berthier, J. Oudar, J.-M. Moison, and M. Bensoussan, J. Electrochem. Soc. **133**, 1663 (1986).
[36] M. G. Nooney, V. Liberman, and R. M. Martin, J. Vac. Sci. Technol. A **13**, 1837 (1995).
[37] P. Klopfenstein, G. Bastide, M. Rouzeyre, M. Gendry, and J. Durand, J. Appl. Phys. **63**, 150 (1988).
[38] J. S. Herman and F. L. Terry Jr., Appl. Phys. Lett. **60**, 716 (1992).
[39] G. Y. Gu, E. A. Ogryzlo, P. C. Wong, M. Y. Zhou, and K. A. R. Mitchell, J. Appl. Phys. **72**, 762 (1992).
[40] L. Koenders, M. Blomacher, and W. Mönch, J. Vac. Sci. Technol. B **6**, 1416 (1988).
[41] L. Roberts, G. Hughes, B. Fennema, and M. Carbery, J. Vac. Sci. Technol. B **10**, 1862 (1992).
[42] R. S. Bhide, S. V. Bhoraskar, and V. J. Rao, J. Appl. Phys. **72**, 1464 (1992).
[43] N. Yoshida, S. Chichibu, T. Akane, M. Totsuka, H. Uji, S. Matsumoto, and H. Higuchi, Appl. Phys. Lett. **63**, 3035 (1993).
[44] K. R. Zavadil, C. I. H. Ashby, A. J. Howard, and B. E. Hammons, J. Vac. Sci. Technol. A **12**, 1045 (1994).
[45] V. N. Bessolov, M. V. Lebedev, E. B. Novikov, and B. V. Tsarenkov, J. Vac. Sci. Technol. B **11**, 10 (1993).
[46] V. N. Bessolov, E. V. Konenkova, and M. V. Lebedev, Mater. Sci. Eng., B **44**, 376 (1997).
[47] A. F. Wells, *Structural Inorganic Chemistry* (Clarendon Press, Oxford, 1986).
[48] V. L. Berkovits, V. N. Bessolov, T. V. L'vova, E. B. Novikov, V. I. Safarov, R. V. Khasieva, and B. V. Tsarenkov, J. Appl. Phys. **70**, 3707 (1991).
[49] J. L. Leclercq, E. Bergignat, and G. Hollinger, Semicond. Sci. Technol. **10**, 95 (1995).
[50] T. Ishikawa and H. Ikoma, Jpn. J. Appl. Phys. **31**, 3981 (1992).
[51] N. N. Berchenko and Yu. V. Medvedev, Usp. Khim. **63**, 655 (1994).
[52] M. S. Carpenter, M. R. Melloch, B. A. Cowans, Z. Dardas, and W. N. Delgass, J. Vac. Sci. Technol. B **7**, 845 (1989).
[53] C. J. Sandroff, M. S. Hegde, and C. C. Chang, J. Vac. Sci. Technol. B **7**, 841 (1989).
[54] C. J. Spindt, R. S. Besser, R. Cao, K. Miyano, C. R. Helms, and W. E. Spicer, J. Vac. Sci. Technol. A **7**, 2466 (1989).
[55] H. Sugahara, M. Oshima, H. Oigawa, H. Shigekawa, and Y. Nannichi, J. Appl. Phys. **69**, 4349 (1991).
[56] H. Sugahara, M. Oshima, R. Klauser, H. Oigawa, and Y. Nannichi, Surf. Sci. **242**, 335 (1991).
[57] J. Shin, K. M. Geib, and C. W. Wilmsen, J. Vac. Sci. Technol. B **9**, 2337 (1991).
[58] P. Moriarty, B. Murphy, L. Roberts, A. A. Cafolla, G. Hughes, L. Koenders, and P. Bailey, Phys. Rev. B **50**, 14237 (1994).
[59] K. Sato, M. Sakata, and H. Ikoma, Jpn. J. Appl. Phys. **32**, 3354 (1993).
[60] M. Sakata and H. Ikoma, Jpn. J. Appl. Phys. **33**, 3813 (1994).
[61] J. S. Herman and F. L. Terry Jr., J. Vac. Sci. Technol. A **11**, 1094 (1993).
[62] W. Ranke, J. Finster, and H. J. Kuhr, Surf. Sci. **187**, 112 (1987).
[63] T. Tiedje, K. M. Colbow, D. Rogers, Z. Fu, and W. Eberhardt, J. Vac. Sci. Technol. B **7**, 837 (1989).
[64] V. N. Bessolov, E. V. Konenkova, and M. V. Lebedev, J. Vac. Sci. Technol. B **15**, 876 (1997).
[65] E. A. Miller and G. L. Richmond, J. Phys. Chem. B **101**, 2669 (1997).
[66] H. Ohno, H. Kawanishi, Y. Akagi, Y. Nakajima, and T. Hijikata, Jpn. J. Appl. Phys. **29**, 2473 (1990).
[67] T. Scimeca, Y. Muramatsu, M. Oshima, H. Oigawa, and Y. Nannichi, Phys. Rev. B **44**, 12 927 (1991).
[68] T. Ohno and K. Shiraishi, Phys. Rev. B **2**, 11 194 (1990).
[69] T. Ohno, Phys. Rev. B **44**, 6306 (1991).
[70] B. Murphy, P. Moriarty, L. Roberts, T. Cafolla, G. Hughes, L. Koenders, and P. Bailey, Surf. Sci. **317**, 73 (1994).
[71] Y. Takakuwa, M. Niwano, S. Fujita, Y. Takeda, and N. Miyamoto, Appl. Phys. Lett. **58**, 1635 (1991).
[72] M. Oshima, T. Scimeca, Y. Watanabe, H. Oigawa, and Y. Hannichi, Jpn. J. Appl. Phys. **32**, 518 (1993).
[73] F. S. Turco, C. J. Sandroff, M. S. Hedge, and M. C. Tamargo, J. Vac. Sci. Technol. B **8**, 856 (1990).
[74] T. Scimeca, Y. Watanabe, R. Berrigan, and M. Oshima, Phys. Rev. B **46**, 10201 (1992).
[75] S. Takatani, T. Kikawa, and M. Nakazawa, Phys. Rev. B **45**, 8498 (1992).
[76] S. A. Chambers and V. S. Sundaraman, Appl. Phys. Lett. **57**, 2342 (1990).
[77] K. Sato and H. Ikoma, Jpn. J. Appl. Phys. **32**, 921 (1993).
[78] T. Scimeca, Y. Watanabe, F. Maeda, R. Berrigan, and M. Oshima, J. Vac. Sci. Technol. B **12**, 3090 (1994).
[79] N. Shibata and H. Ikoma, Jpn. J. Appl. Phys. **31**, 3976 (1992).
[80] C. W. Wilmsen, K. M. Geib, J. Shin, R. Iyer, D. L. Lile, and J. J. Pouch, J. Vac. Sci. Technol. B **7**, 851 (1989).
[81] W. M. Lau, S. Jin, and X.-W Wu, and S. Ingrey, J. Vac. Sci. Technol. B **8**, 848 (1990).
[82] C. S. Sundararaman, S. Poulin, J. F. Currie, and R. Leonelli, Can. J. Phys. **69**, 329 (1991).
[83] W. M. Lau, R. W. M. Kwok, and S. Ingrey, Surf. Sci. **271**, 579 (1992).
[84] Y. Tao, A. Yelon, E. Sacher, Z. H. Lu, and M. J. Graham, Appl. Phys. Lett. **60**, 2669 (1992).
[85] F. Maeda, Y. Watanabe, and M. Oshima, Appl. Phys. Lett. **62**, 297 (1993).
[86] T. Chasse, H. Peisert, P. Streubel, and R. Szargan, Surf. Sci. **331–333** , 434 (1995).
[87] Y. Fukuda, Y. Suzuki, N. Sanada, S. Sasaki, and T. Ohsawa, J. Appl. Phys. **76**, 3059 (1994).
[88] S. Maeyama, M. Sugiyama, S. Heun, and M. Oshima, J. Electron. Mater. **25**, 593 (1996).
[89] G. W. Anderson, M. C. Hanf, P. R. Norton, Z. H. Lu, and M. J. Graham, Appl. Phys. Lett. **65**, 171 (1994).
[90] M. Sugiyama, N. Yabumoto, S. Maeyama, and M. Oshima, Jpn. J. Appl. Phys. **34**, L1588 (1995).
[91] A. J. Nelson, S. Frigo, and R. Rosenberg, J. Appl. Phys. **71**, 6086 (1992).
[92] A. J. Nelson, S. Frigo, and R. Rosenberg, J. Vac. Sci. Technol. A **11**, 1022 (1993).
[93] R. W. M. Kwok and W. M. Lau, J. Vac. Sci. Technol. A **10**, 2515 (1992).
[94] R. W. M. Kwok, G. Gin, B. K. L. So, K. C. Hui, L. Hwang, W. M. Lau, C. C. Hsu, and D. Landheer, J. Vac. Sci. Technol. A **13**, 652 (1995).
[95] Yu. G. Galitsin, V. G. Mansurov, V. I. Poshevnev, R. A. Sokolov, and N. A. Valisheva, Poverkhnost'. Fizika, Khimiya, Mekhanika, No. 5, 108 (1992).
[96] Yu. A. Kudryavtsev, E. B. Novikov, N. M. Stus', and E. I. Chaĭkina, Fiz. Tekh. Poluprovodn. **26**, 1742 (1992) [Sov. Phys. Semicond. **26**, 975 (1992)].

[97] N. Yoshida, M. Totsuka, J. Ito, and S. Matsumoto, Jpn. J. Appl. Phys. **33**, 1248 (1994).
[98] L. Geelhaar, R. A. Bartynski, F. Ren, M. Schnoes, and D. N. Buckley, J. Appl. Phys. **80**, 3076 (1996).
[99] L. Jedral, H. E. Ruda, R. Sodhi, H. Ma, and L. Mannik, Can. J. Phys. **70**, 1050 (1992).
[100] Z. H. Lu and M. J. Graham, J. Appl. Phys. **75**, 7567 (1994).
[101] Y. Fukuda, N. Sanada, M. Kuroda, and Y. Suzuki, Appl. Phys. Lett. **61**, 955 (1992).
[102] E. Dudzik, R. Whittle, C. Muller, I. T. McGovern, C. Nowak, A. Markl, A. Hempelmann, D. R. T. Zahn, A. Cafolla, and W. Braun, Surf. Sci. **307–309**, 223 (1994).
[103] H. Hirayama, Y. Matsumoto, H. Oigawa, and Y. Nannichi, Appl. Phys. Lett. **54**, 2565 (1989).
[104] X.-S. Wang and W. H. Weinberg, J. Appl. Phys. **75**, 2715 (1994).
[105] V. L. Berkovits and D. Paget, Appl. Phys. Lett. **61**, 1835 (1992).
[106] V. N. Bessolov, A. F. Ivankov, and M. V. Lebedev, J. Vac. Sci. Technol. B **13**, 1018 (1995).
[107] N. Yokoi, M. Taketani, H. Andoh, and M. Takai, Jpn. J. Appl. Phys. **33**, 7130 (1994).
[108] X.-S. Wang, K. W. Self, R. Maboudian, V. Bressler-Hill, and W. H. Weinberg, J. Vac. Sci. Technol. A **11**, 1089 (1993).
[109] D. Paget, J. E. Bonnet, V. L. Berkovits, P. Chiaradia, and J. Avila, Phys. Rev. B **53**, 4604 (1996).
[110] S. Maeyama, M. Sugiyama, and M. Oshima, Surf. Sci. **357–358**, 527 (1996).
[111] S. Tsukamoto and N. Koguchi, Jpn. J. Appl. Phys. **33**, L1185 (1994).
[112] M. D. Pashley and D. Li, J. Vac. Sci. Technol. A **12**, 1848 (1994).
[113] Y. Haga, S. Miwa, and E. Morita, Appl. Surf. Sci. **107**, 58 (1996).
[114] Z. H. Lu, M. J. Graham, X. H. Feng, and B. X. Yang, Appl. Phys. Lett. **60**, 2773 (1992).
[115] O. L. Warren, G. W. Anderson, M. C. Hauf, K. Griffits, and P. R. Norton, Phys. Rev. B **52**, 2959 (1995).
[116] J.-M. Jin, M. W. C. Dharma-wardana, D. J. Lockwood, G. C. Aers, Z. H. Lu, and L. J. Lewis, Phys. Rev. Lett. **75**, 878 (1995).
[117] Z. Tian, M. W. C. Dharma-wardana, Z. H. Lu, A. Cao, and L. J. Lewis, Phys. Rev. B **55**, 5376 (1997).
[118] M. W. C. Dharma-wardana, Z. Tian, Z. H. Lu, and L. J. Lewis, Phys. Rev. B **56**, 10526 (1997).
[119] E. Dudzik, A. Leslie, E. O'Toole, I. T. McGovern, A. Pachett, D. R. T. Zahn, J. Lüdecke, D. P. Woodruff, and B. C. C. Cowie, J. Phys.: Condens. Matter **8**, 15 (1996).
[120] E. Dudzik, A. Leslie, E. O'Toole, I. T. McGovern, A. Pachett, and D. R. T. Zahn, Appl. Surf. Sci. **104–105**, 101 (1996).
[121] B. J. Skromme, C. J. Sandroff, E. Yablonovich, and T. J. Gmitter, Appl. Phys. Lett. **51**, 2022 (1987).
[122] E. Yablonovitch, C. J. Sandroff, R. Bhat, and T. Gmitter, Appl. Phys. Lett. **51**, 439 (1987).
[123] V. N. Bessolov, E. V. Konenkova, and M. V. Lebedev, Pis'ma Zh. Tekh. Fiz. **22**, 37 (1996) [Tech. Phys. Lett. **22**, 749 (1996)].
[124] V. N. Bessolov, M. V. Lebedev, N.-M. Binh, M. Friedrich, and D. R. T. Zahn, Semicond. Sci. Technol. **13**, 611 (1998).
[125] D. Paget, A. O. Gusev, and V. L. Berkovits, Phys. Rev. B **53**, 4615 (1996).
[126] D. Liu, T. Zhang, R. A. LaRue, J. S. Harris, and T. W. Sigmon, Appl. Phys. Lett. **53**, 1059 (1988).
[127] J.-F. Fan, H. Oigawa, and Y. Nannichi, Jpn. J. Appl. Phys. **27**, L2125 (1988).
[128] E. V. Venger, S. I. Kirillova, V. I. Primachenko, and V. A. Chernobaĭ, Poverkhnost'. Rentgenovskie, Sinkhrotronnye i Neĭtronnye Issledovaniya, No. 12, 59 (1996).
[129] S.-F. Ren and Y.-C. Chang, Phys. Rev. B **41**, 7705 (1990).
[130] K. N. Ow and X. W. Wang, Phys. Rev. B **54**, 17 661 (1996).
[131] J. Guo-Ping and H. E. Ruda, J. Appl. Phys. **79**, 3758 (1996).
[132] H. Ishimura, K. Sasaki, and H. Tokuda, Inst. Phys. Conf. Ser. **106**, 405 (1990).
[133] I. K. Hau, D. H. Woo, H. J. Kim, E. K. Kim, J. I. Lee, S. H. Kim, K. N. Kang, H. Lim, and H. L. Park, J. Appl. Phys. **80**, 4052 (1996).
[134] T. K. Paul and D. N. Bose, J. Appl. Phys. **70**, 7387 (1991).
[135] W. D. Chen, X. Q. Li, L. H. Duan, X. L. Xie, and Y. D. Cai, Appl. Surf. Sci. **100–101**, 592 (1996).
[136] L. A. Farrow, C. J. Sandroff, and M. C. Tamargo, Appl. Phys. Lett. **51**, 1931 (1987).
[137] G. P. Schwartz and G. J. Gualtieri, J. Electrochem. Soc. **133**, 1266 (1986).
[138] R. S. Besser and C. R. Helms, Appl. Phys. Lett. **52**, 1707 (1988).
[139] H. Hasegawa, H. Ishii, T. Sawada, T. Saitoh, S. Konishi, Y. Liu, and H. Ohno, J. Vac. Sci. Technol. B **6**, 1184 (1988).
[140] V. N. Bessolov, M. V. Lebedev, and D. R. T. Zahn, J. Appl. Phys. **82**, 2640 (1997).
[141] V. N. Bessolov, E. V. Konenkova, M. V. Lebedev, and D. R. T. Zahn, Fiz. Tekh. Poluprovodn. **31**, 1350 (1997) [Semiconductors **31**, 1164 (1997)].
[142] V. N. Bessolov, M. V. Lebedev, A. F. Ivankov, W. Bauhofer, and D. R. T. Zahn, Appl. Surf. Sci. **133**, 17 (1998).
[143] T. Chasse, A. Chasse, H. Peisert, and P. Streubel, Appl. Phys. A **65**, 543 (1997).
[144] Y. Watanabe and F. Maeda, Appl. Surf. Sci. **117–118**, 735 (1997).
[145] R. N. Nottenburg, C. J. Sandroff, D. A. Humphrey, T. H. Hollenbeck, and R. Bhat, Appl. Phys. Lett. **52**, 218 (1988).
[146] H. L. Chuang, M. S. Carpenter, M. R. Melloch, M. S. Lundstrom, E. Yablonovitch, and T. J. Gmitter, Appl. Phys. Lett. **57**, 2113 (1990).
[147] A. Kapila, V. Malhotra, L. H. Camnitz, K. L. Seaward, and D. Mars, J. Vac. Sci. Technol. B **13**, 10 (1995).
[148] S. Shikata, H. Okada, and H. Hayashi, J. Appl. Phys. **69**, 2717 (1991).
[149] K. C. Hwang, S. S. Li, C. Park, and T. J. Anderson, J. Appl. Phys. **67**, 6571 (1990).
[150] A. Y. Polyakov, M. Stam, A. G. Milnes, A. E. Bochkarev, and S. J. Pearton, J. Appl. Phys. **71**, 4411 (1992).
[151] H. Xu, S. Belkouch, C. Aktik, and W. Rasmussen, Appl. Phys. Lett. **66**, 2125 (1995).
[152] B. Rotelli, L. Tarricone, E. Gombia, R. Mosca, and M. Perotin, J. Appl. Phys. **81**, 1813 (1997).
[153] C. R. Moon, B.-D. Choe, S. D. Kwon, and H. Lim, J. Appl. Phys. **81**, 2904 (1997).
[154] J.-L. Lee, D. Kim, S. J. Maeng, H. H. Park, J. Y. Kang, and Y. T. Lee, J. Appl. Phys. **73**, 3539 (1993).
[155] M. S. Carpenter, M. R. Melloch, and T. E. Dungan, Appl. Phys. Lett. **53**, 66 (1988).
[156] B. I. Sysoev, V. D. Strygin, and G. I. Kotov, Pis'ma Zh. Tekh. Fiz. **16**, 22 (1990) [Sov. Tech. Phys. Lett. **16**, 332 (1990)].
[157] H. Oigawa, J.-F. Fan, Y. Nannichi, H. Sugahara, and M. Oshima, Jpn. J. Appl. Phys. **30**, L322 (1991).
[158] Y. K. Kim, S. Kim, J. M. Seo, S. Ahn, K. J. Kim, T.-H. Kang, and B. Kim, J. Vac. Sci. Technol. A **15**, 1124 (1997).
[159] J.-F. Fan, Y. Kurata, and Y. Nannichi, Jpn. J. Appl. Phys. **28**, L2255 (1989).
[160] T. Kikawa, S. Takatani, and Y. Tezen, Appl. Phys. Lett. **60**, 2785 (1992).
[161] L. J. Huang, K. Rajesh, W. M. Lau, S. Ingrey, D. Landheer, J.-P. Noel, and Z. H. Lu, J. Vac. Sci. Technol. A **13**, 792 (1995).
[162] G. Eftekhari, J. Vac. Sci. Technol. B **12**, 3214 (1994).
[163] D. Landheer, G. H. Yousefi, J. B. Webb, R. W. M. Kwok, and W. M. Lau, J. Appl. Phys. **75**, 3516 (1994).
[164] P. D. DeMoulin, S. P. Tobin, M. S. Lundstrom, M. S. Carpenter, and M. R. Melloch, IEEE Electron Device Lett. **EDL-9**, 368 (1988).
[165] E. B. Novikov, R. V. Khasieva, and G. A. Shakiashvili, Fiz. Tekh. Poluprovodn. **24**, 1276 (1990) [Sov. Phys. Semicond. **24**, 802 (1990)].
[166] M. Pérotin, P. Coudray, A. Etcheberry, L. Gouskov, C. Debiemme-Chouvy, and H. Luquet, Mater. Sci. Eng., B **28**, 374 (1994).
[167] X. Y. Gong, T. Yamaguchi, H. Kan, T. Makino, K. Oshimo, M. Aoyama, M. Kumagawa, and N. L. Rowell, Appl. Surf. Sci. **113–114**, 388 (1997).
[168] I. A. Andreev, E. V. Kunitsyna, V. M. Lantratov, T. V. L'vova, M. P. Mikhaĭlova, and Yu. P. Yakovlev, Fiz. Tekh. Poluprovodn. **31**, 653 (1997) [Semiconductors **31**, 556 (1997)].
[169] X. Y. Gong, T. Yamaguchi, H. Kan, T. Makino, T. Iida, T. Kato, M. Aoyama, Y. Suzuki, N. Sanada, Y. Fukuda, and M. Kumagawa, Jpn. J. Appl. Phys. **37**, 55 (1998).
[170] T. Tamanuki, F. Koyama, and K. Iga, Jpn. J. Appl. Phys. **30**, 499 (1991).
[171] T. Tamanuki, F. Koyama, and K. Iga, Jpn. J. Appl. Phys. **31**, 3292 (1992).
[172] W. S. Hobson, U. Mohideen, S. J. Pearton, R. E. Slusher, and F. Ren, Electron. Lett. **29**, 2199 (1993).
[173] W. S. Hobson, F. Ren, U. Mohideen, R. E. Slusher, M. Lamont Schnoes, and S. J. Pearton, J. Vac. Sci. Technol. A **13**, 642 (1995).
[174] L. F. DeChiaro and C. J. Sandroff, IEEE Trans. Electron Devices **ED-39**, 561 (1992).
[175] R. Hakimi and M.-C. Amann, Semicond. Sci. Technol. **12**, 778 (1997).

[176] G. Beister, J. Maege, D. Gutsche, G. Erbert, J. Sebastian, K. Vogel, M. Weyers, J. Wurfl, and O. P. Daga, Appl. Phys. Lett. **68**, 2467 (1996).
[177] M. R. Melloch, M. S. Carpenter, D. E. Dungan, D. Li, and N. Otsuka, Appl. Phys. Lett. **56**, 1064 (1990).
[178] N. Furuhata and Y. Shiraishi, Jpn. J. Appl. Phys. **37**, 10 (1998).
[179] F. S. Turco, C. J. Sandroff, D. M. Hwang, T. S. Ravi, and M. C. Tamargo, J. Appl. Phys. **68**, 1038 (1990).
[180] Y. Miyamoto, H. Hirayama, T. Suemasu, Y. Miyake, and S. Arai, Jpn. J. Appl. Phys. **30**, L672 (1991).
[181] V. L. Berkovits, V. M. Lantratov, T. V. L'vova, G. A. Shakiashvili, V. P. Ulin, and D. Paget, Appl. Phys. Lett. **63**, 970 (1993).
[182] T. Chikyow and N. Koguchi, Appl. Phys. Lett. **61**, 2431 (1992).
[183] L. S. Hung, G. H. Braunstein, and L. A. Bosworth, Appl. Phys. Lett. **60**, 201 (1992).
[184] S. Omori, H. Ishii, and Y. Nihei, Surf. Sci. **121–122**, 241 (1997).
[185] Y. H. Wu, T. Toyoda, Y. Kawakami, S. Fujita, and S. Fujita, Jpn. J. Appl. Phys. **29**, L144 (1990).

Translated by M. E. Alferieff

ATOMIC STRUCTURE AND NON-ELECTRONIC PROPERTIES OF SEMICONDUCTORS

Scanning electron microscopy of long-wavelength laser structures

V. A. Solov'ev, M. P. Mikhaĭlova, K. D. Moiseev, M. V. Stepanov, V. V. Sherstnev, and Yu. P. Yakovlev

A. F. Ioffe Physicotechnical Institute, Russian Academy of Sciences, 194021 St. Petersburg, Russia
(Submitted March 3, 1998; accepted for publication March 4, 1998)
Fiz. Tekh. Poluprovodn. **32**, 1300–1305 (November 1998)

New possibilities of scanning electron microscopy, using secondary- and reflected-electron signals, for determining the position of heteroboundaries in long-wavelength laser structures are reported. The formation of the indicated signals in structures of mid-infrared-range lasers of a new type based on type-II GaInAsSb/InGaAsSb heterostructures as well as in the conventional InAsSb/InAsSbP heterostructures is analyzed. The observed characteristic features of the formation of secondary- and reflected-electron signals in these structures as compared with the well-studied AlGaAs/GaAs structures are explained. The results obtained are necessary for accurate determination of an important laser parameter — the position of the p–n junction. It is shown that it is best to use the reflected-electron signal. © *1998 American Institute of Physics.* [S1063-7826(98)00211-7]

The great interest in mid-infrared (IR) range ($3-5\ \mu$m) diode lasers based on narrow-gap III–V semiconductor compounds is due to the fact that the absorption bands of many industrial and natural gases lie in this spectral range. Infrared lasers operating at room temperature are very important for problems of laser diode spectroscopy, laser ranging, and ecological monitoring.[1] However, until now the maximum working temperature of conventional diode heterolasers based on InAs and its solid solutions has not exceeded 180–200 K in the pulsed regime, while for GaInSb/InAs superlattice based injection lasers grown by molecular-beam epitaxy a temperature of 250 K has been achieved.[2,3] New and unconventional approaches to producing mid-IR lasers using type-II heterojunctions and quantum-well structures based on the system GaSb/InAs/AlSb have also been proposed in recent years. Radiative recombination in such structures is due primarily to indirect (tunneling) optical transitions at the type-II heterojunction and radiation arises near the interface.[2–6] Thus a new tunneling-injection laser structure, produced by the liquid-phase epitaxy, with a GaInAsSb/InGaAsSb broken-gap type-II p–n heterojunction in the active region has been proposed and implemented in Ref. 7 . This laser structure operated in the pulsed mode up to $T=205$ K. Thus, both conventional and unconventional long-wavelength lasers based on narrow-gap III–V compounds still cannot operate at room temperature. The so-called quantum-cascade unipolar lasers proposed by Capasso *et al.* are the only exception.[8] Thus, the development of room-temperature lasers for definite wavelengths, 5.2 and 8 μm, has been reported.[9] However, the technology and construction of such lasers are quite complicated.

Further improvement of the characteristics of mid-IR lasers grown by liquid-phase epitaxy (lower threshold current, higher working temperature) requires the development of better multilayer laser structures with high-quality heterojunctions and low carrier-leakage currents. In turn, this requires the development of diagnostic methods, specifically, methods for monitoring the parameters of the internal geometry of a structure (thickness of the epitaxial layers, sharpness of heterojunctions, position of the p–n junction, and others). The latter parameter is especially important, since it strongly influences the threshold current in injection heterolasers.

Scanning electron microscopy (SEM) is widely used for investigation of semiconductor lasers, including lasers based on submicron heterostructures.[10] Because of the possibility of detecting a variety of signals simultaneously — secondary electrons, reflected electrons, current induced by the electronic probe, microcathodoluminescence, and others[11] — they possess high spatial resolution and high information content. For example, secondary- or reflected-electron signals make it possible to identify and measure the thickness of layers with different chemical compositions. Computer simulation of the reflected-electron signal makes it possible to lower the limit of the measurable layer thickness right down to several nanometers.[12] The induced-current signal can be used effectively to determine the position of a p–n junction in semiconductor structures.[13]

An attempt to use conventional scanning electron microscopy approaches to investigate laser structures based on the narrow-gap semiconductors GaSb and InAs and their solid solutions encounters a number of problems. Specifically, as a rule, such structures possess substantial leakage currents at close to room temperatures, which in most cases makes it impossible to detect at a given temperature the current signal induced in them by the electron probe. To overcome this problem we have proposed[14] that the measurements be performed at low temperatures, close to the liquid-

 © 1998 American Institute of Physics

nitrogen temperature. Another problem is the following. In contrast to homogeneous *p–n* structures, where it is sufficient to know the depth of the *p–n* junction, i.e., its distance from the surface, in the case of multilayer heterostructures it becomes important to determine accurately the position of the *p–n* junction relative to definite heterojunctions. For this purpose, simultaneous detection of induced-current and reflected-electron signals (or induced-current and secondary-electron signals) is most often used in SEM. Then, to interpret correctly the experimentally obtained profiles of a specific signal it is necessary to study the formation of the signals for the heterostructure under investigation. The formation of a reflected-electron signal for AlGaAs/GaAs heterostructures, which are widely used in optoelectronics, has been investigated in detail.[12,15] We know of no similar investigations of heterostructures based on narrow-gap GaSb/InAs semiconductors. As will be shown below, the problem of identifying and accurately determining the position of heterojunctions in such structures by means of SEM is nontrivial.

In summary, our objective in the present work is to investigate the characteristic features of the formation of secondary- and reflected-electron signals in laser structures, both new structures based on type-II GaInAsSb/InGaAsSb heterojunctions and in the conventional InAsSb/InAsSbP double heterostructures, especially since these signals are also used to measure the thicknesses of layers with different chemical compositions.

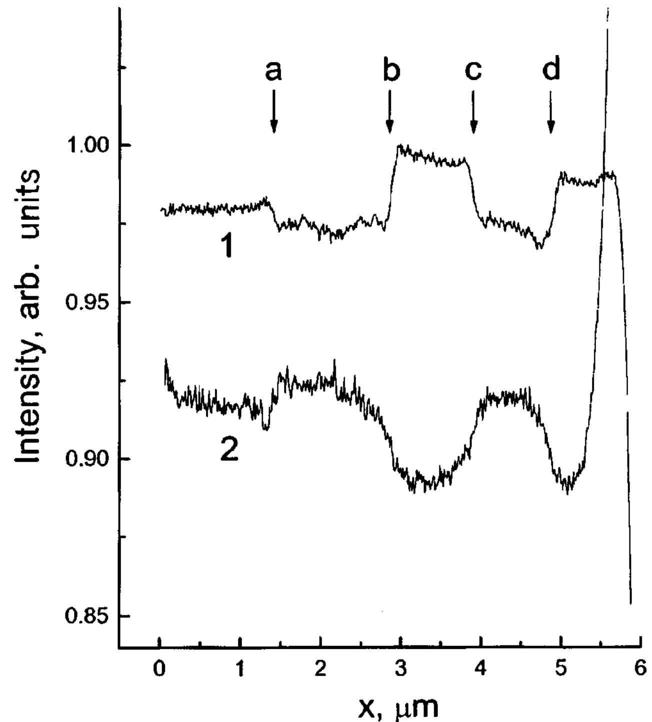

FIG. 1. Linear profiles of the reflected-electron (*1*) and secondary-electron (*2*) signals for a MK-539 structure (type A). The letters mark the heterojunctions: a — InAs(substrate)/$Ga_{0.83}InAsSb_{0.78}$; b, d — $Ga_{0.83}InAsSb_{0.78}$/$Ga_{0.17}InAsSb_{0.2}$; c — $Ga_{0.17}InAsSb_{0.2}$/$Ga_{0.83}InAsSb_{0.78}$.

SAMPLES AND MEASUREMENT PROCEDURE

Heterostructures based on the quaternary solid solutions $Ga_{0.83}In_{0.17}As_{0.22}Sb_{0.78}$ and $Ga_{0.17}In_{0.83}As_{0.8}Sb_{0.2}$ (type-A structure), whose compositions are close to GaSb and InAs, respectively, as well as double heterostructures based on the solid solutions $InAsSb_{0.15}P_{0.30}$ and $InAsSb_{0.04}$ (type-B structures) were investigated. All structures were grown by liquid-phase epitaxy on InAs (100) substrates. Some type-A structures contain, in addition, the solid solution $InAsSb_{0.12}P_{0.26}$ as the first cover layer.

The linear profiles of the secondary- and reflected-electron signals were measured by scanning the electron probe over a cleavage surface of the experimental sample in a direction perpendicular to the epitaxial layers. The characteristic features of the formation of secondary- and reflected-electron signals were studied on freshly cleaved structures before contacts were deposited on them; in addition, close-to-crystallographic cleavage surfaces with the minimal number of defects were chosen for this. The experiments were performed on an automated setup based on a CamScan Series 4-88 DV100 scanning electron microscope. In our experiments the accelerating voltage was $U=10-15$ kV and the probe current was $I_b=(1-5)\times 10^{-10}$ A. The signal-to-noise ratio was increased by analog filtering of the detected signals and by repeated (20–100) linear scanning of the electron probe over a chosen section of the sample followed by averaging of the data.

FORMATION OF SECONDARY- AND REFLECTED-ELECTRON SIGNALS

Type A structures (based on $Ga_{0.83}InAsSb_{0.78}$/$Ga_{0.17}InAsSb_{0.2}$ heterojunctions).

A characteristic feature of structures of this type is that the average atomic numbers (Z) for neighboring epitaxial layers differ very little (for GaSb and InAs compounds they are simply identical). As is well known, the reflected-electron yield for individual chemical elements is proportional to Z.[11] Thus, in the reflected-electron regime there should be no contrast between epitaxial layers with different compositions. However, contrast is observed experimentally in both the secondary- and reflected-electron regimes (Fig. 1).

It was established that contrast is unstable in the secondary-electron regime. For a single scan of a section which has not been irradiated beforehand, strong contrast with sign opposite to that in the reflected-electron regime is observed (compare curves 1 and 2 in Fig. 2). For multiple scanning it decreases, changes sign, and becomes similar to the contrast in the reflected-electron regime (Fig. 2, curve *3*).

Such behavior is explained by the formation of a contamination film on the cleavage surface during irradiation of the surface by an electron beam.[11] As this film grows, the difference in the yield of the secondary electrons themselves, i.e., the electrons produced by scattering of the primary electrons, for layers with different composition is lost. Such secondary electrons leave a thin (~10 nm) surface region and their number in the irradiated structure will be determined mainly by the material of the contamination film and not the

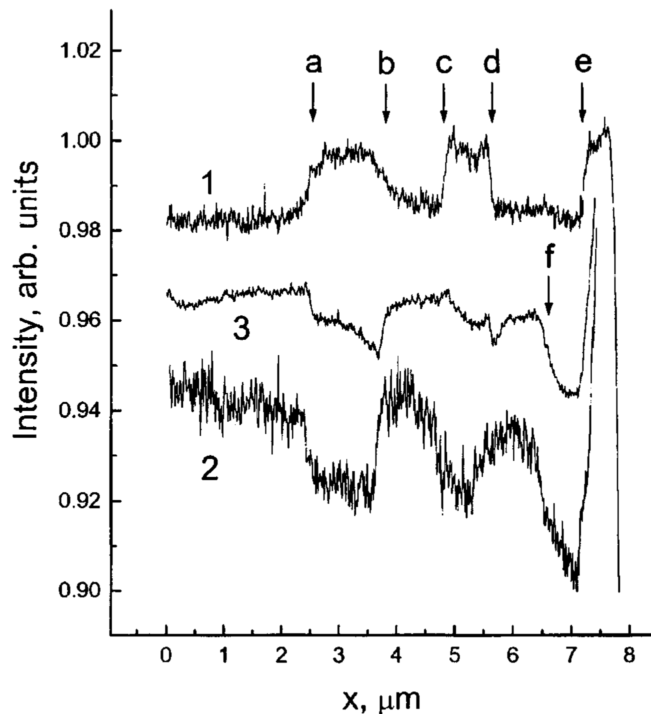

FIG. 2. Linear profiles of reflected-electron (*1*) and secondary-electron (*2, 3*) signals obtained by single (*2*) and fiftyfold (*3*) scanning for a MK-542 structure (type A). The letters mark the heterojunctions: a — InAs(substrate)/$InAsSb_{0.12}P_{0.26}$; b — $InAsSb_{0.12}P_{0.26}$/$Ga_{0.83}InAsSb_{0.78}$; c, e — $Ga_{0.83}InAsSb_{0.78}$/$Ga_{0.17}InAsSb_{0.2}$; d — $Ga_{0.17}InAsSb_{0.2}$/$Ga_{0.83}InAsSb_{0.78}$; f — p-$Ga_{0.83}InAsSb_{0.78}$/n-$Ga_{0.83}InAsSb_{0.78}$.

epitaxial layers. Therefore, the fraction of secondary electrons, produced by the reflected electrons,[11] and the contrast associated with them increase in the irradiated section.

A so-called voltage–contrast, due to the presence of regions with different types of doping in the structure (transition f in Fig. 2), is also observed in the secondary-electron regime. This contrast can be used to determine the position of the p–n junction, but only if the p–n junction is separated from the heterojunctions by at least ~0.5 μm. Otherwise, the voltage–contrast is strongly distorted and can vanish completely under the influence of the contrast associated with the variation of the chemical composition at a heterojunction. For example, in the structure shown in Fig. 1 (transition *d*) the p–n junction coincides with the heterojunction and the voltage–contrast is suppressed.

In contrast to the secondary-electron regime, the profile of the signal in the reflected-electron regime remains essentially unchanged with repeated scanning of the cleavage surface of the experimental structure. As one can see from Figs. 1 and 2, the reflected-electron yield for layers with composition close to InAs is higher than the reflected-electron yield for layers with composition close to GaSb. Here, the reflected-electron signal varies nonmonotonically when heterostructures of this type are scanned. The linear reflected-electron profiles, similarly to AlGaAs/GaAs heterostructures,[12] have a maximum and minimum intensity on different sides of the interface, although they are less pronounced. The observed feature is due to the anisotropy of the reflected-electron energy spectrum at a heterojunction. This effect appears because of the fact that near a heterojunction some of the reflected electrons produced in material with one value of Z move toward the surface through neighboring material where the value of Z and correspondingly the stopping power for electrons are different. For a sharp heterojunction the coordinate of the maximum of the derivative of the reflected-electron signal corresponds to the position of this heterojunction (by a sharp heterojunction we mean a heterojunction with a wide transitional region much smaller than the diameter of the electron beam, i.e., less than 10 nm (Ref. 15).

To make an accurate determination of the position of heterojunctions in type-A structures, the reflected-electron regime should be used. It is more stable than the secondary-electron regime, simpler to interpret, and gives sharper intensity differentials at the interfaces (compare the secondary- and reflected-electron profiles for the heterojunctions a,b,c, and d in Fig. 1 and c,d, and e in Fig. 2). It should be noted that the reflected-electron contrast in the structures investigated is quite low and does not exceed 1.5 rel. %. For comparison, in $Al_{0.4}Ga_{0.6}As$/GaAs structures it equals 5 rel. %. Therefore, the quality of the cleavage surface must be much higher. To eliminate artifacts and to make an accurate determination of the positions of heterojunctions, the investigations should be performed on fresh, high-quality cleavage surfaces, which should be close to an ideal crystallographic plane and defect-free.

Type-B structures (based on $InAsSb_{0.15}P_{0.3}$/$InAsSb_{0.04}$ heterojunctions).

In type-B structures the difference in the average atomic numbers between neighboring epitaxial layers is also small. As a result, the contrast in the reflect-electron regime is weak (less than 1.5 rel.%). Just as for

type-A structures, the contrast in the secondary-electron regime for type-B structures is not constant, and for a single scan the sign of the contrast is opposite to that observed in the reflected-electron regime (Fig. 3). The reflected-electron yield for InAsSbP layers is greater than for InAs or InAsSb. However, the profile of the reflected-electron signal obtained on sharp InAsSbP/InAsSb (or InAsSbP/InAs) heterojunctions differs substantially from the reflected-electron profiles for the GaInAsSb/InGaAsSb (Fig. 1) and AlGaAs/GaAs[15] systems and has the form of a zig-zag curve (Fig. 4).

To explain the observed features we shall make a comparative analysis of the formation of the reflected-electron signal for the systems mentioned above. In the case that the electron beam approaches a AlGaAs/GaAs heterojunction on the GaAs side (where the average atomic number is larger and correspondingly the reflected-electron yield is higher than in AlGaAs), the intensity of the reflected-electron signal increases. This occurs because some of the reflected electrons produced in GaAs move toward the surface through AlGaAs, where the rate of energy loss of electrons is less than in GaAs, while the detector signal is determined not only by the number but also the energy of the reflected electrons.[15]

The picture is exactly the opposite for the system InAsSbP/InAsSb in the situation similar to that examined

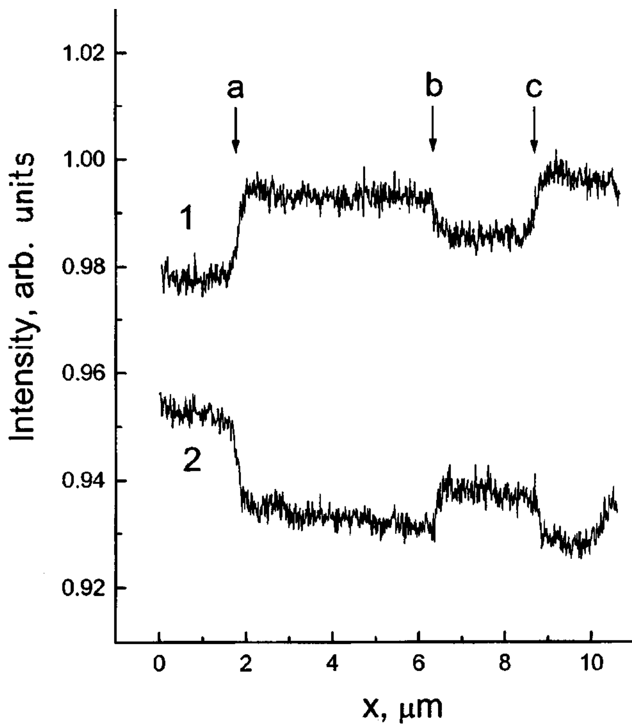

FIG. 3. Linear profiles of reflected-electron (*1*) and secondary-electron (*2*) signals for a S202 structure (type B). The letters mark the heterojunctions: a — InAs(substrate)/$InAsSb_{0.15}P_{0.30}$; b — $InAsSb_{0.15}P_{0.30}$/$InAsSb_{0.04}$; c — $InAsSb_{0.04}$/$InAsSb_{0.15}P_{0.30}$.

above. As the electron probe moves over the layer of the solid solution InAsSbP, where the reflected-electron yield is greater than in InAsSb, at first the reflected-electron signal drops off gradually as the probe approaches the interface

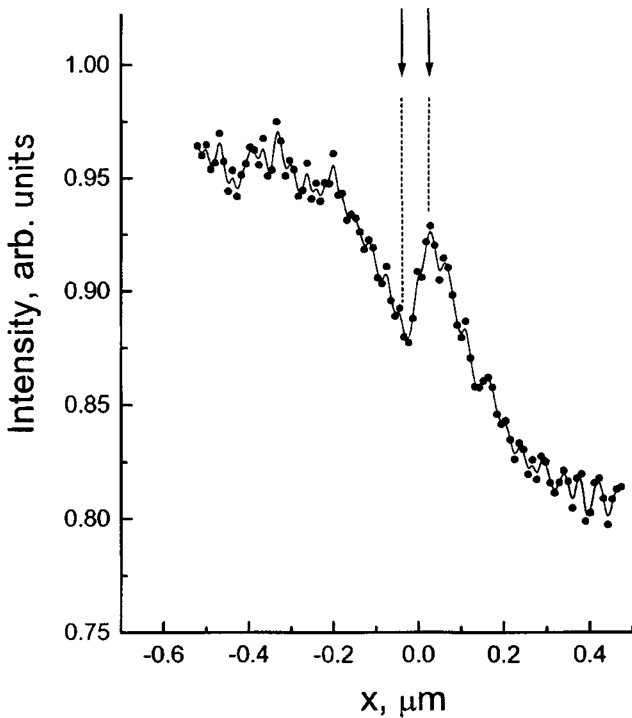

FIG. 4. Linear profile of the reflected-electron signal near an $InAsSb_{0.15}P_{0.30}$/$InAsSb_{0.04}$ heterojunction marked by the letter b in Fig. 3.

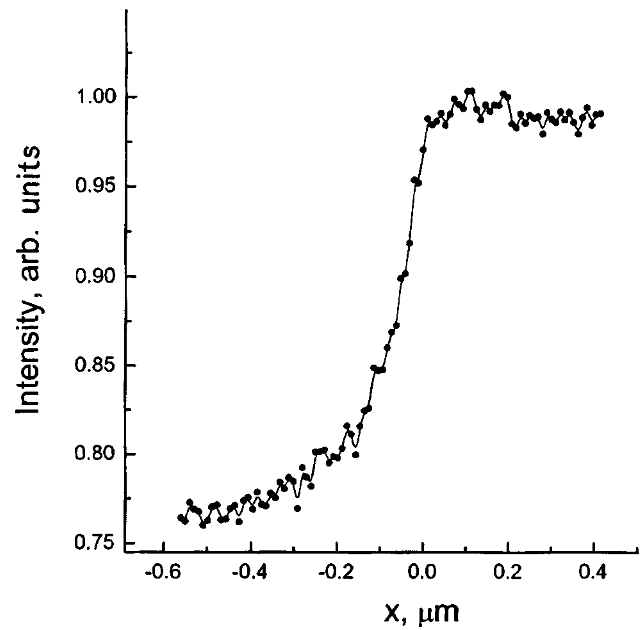

FIG. 5. Linear profile of the reflected-electron signal near an InAs(substrate)/$InAsSb_{0.15}P_{0.30}$ heterojunction marked by the letter a in Fig. 3.

(left side of the reflected-electron profile in Fig. 4). This attests to the fact that the rate of energy losses by electrons in InAsSb is higher than in InAsSbP. A section where the reflected-electron signal increases sharply is present next to the heterojunction (the section is marked by arrows in Fig. 4). This section corresponds to the transmission of the electron beam, which has a Gaussian profile along the cross section and is characterized by probe diameter $\sim 30-40$ nm for the currents used in the experiments $I_b=(1-5)\times 10^{-10}$ A, through the interface. As is well known, the entire reflected-electron flux consists of the truly reflected electrons, which are produced as a result of the direct scattering of primary electrons next to the point of incidence of the electron beam, and reflected electrons whose yield is determined by multiple scattering, while the generation region constitutes ~ 1 μm.[12] Therefore, the jump observed in the reflected-electron signal at the heterojunction attests to an increase in the number of truly reflected electrons at the transition from the InAsSbP to the InAsSb layer. Thus, despite the fact that the total reflected-electron yield is higher in InAsSbP than in InAsSb, the fraction of truly reflected electrons in the total reflected-electron flux is less than for InAsSb. Of course, all arguments and conclusions are also valid for InAsSbP/InAs heterojunctions.

It should be noted that the zig-zag form of the reflected-electron profile with a jump at the heterojunction is characteristic of abrupt interfaces (with a less than 10-nm-wide transitional region). The less abrupt the heterojunction, the smaller and flatter is the jump in the reflected-electron signal. This jump is completely absent (Fig. 5) for smooth (diffused) heterojunctions with a transitional region greater than 100 nm wide.

In Ref. 16 the reflected-electron signal was used to reconstruct the profiles of asymmetric diffused CdHgTe/CdTe heterojunctions. It was shown there that the distortion-induced effects similar to those observed in AlGaAs/GaAs (in the form of minima and maxima of the reflected-electron signal near the heterojunction) vanish on the side of the layer with a diffusion composition profile. It can be asserted on the basis of these results that the heterojunction in Fig. 5 is also asymmetric, and that the diffusion profile is located on the InAsSbP layer side.

CONCLUSIONS

In summary, in the present paper the possibilities of using scanning electron microscopy in the secondary- and reflected-electron signal regimes to solve the problem of determining the positions of the heteroboundaries in long-wavelength laser structures were studied. The formation of the indicated signals in mid-IR laser structures of a new type based on type-II GaInAsSb/InGaAsSb heterojunctions and in conventional InAsSb/InAsSbP heterostructures was analyzed. The characteristic features observed in the formation of secondary- and reflected-electron signals in these structures, as compared with the well-studied AlGaAs/GaAs structures, were explained. It was shown that it is preferable to use the reflected-electron signal.

This work was supported in part by the Russian Ministry of Science as part of the program ''Physics of Solid-State Nanostructures'' (Project No. 96-1010), the Russian Fund for Fundamental Research (Project No. 96-02-17841a), and the EC INCO program (Contract IC15-CT97-0802).

[1] T. N. Danilova, O. G. Ershov, A. N. Imenkov, M. V. Stepanov, V. V. Sherstnev, and Yu. P. Yakovlev, Fiz. Tekh. Poluprovodn. **30**, 1265 (1995) [Semiconductors **30**, 667 (1995)].
[2] H. K. Choi, G. W. Turner, and Z. L. Liau, Appl. Phys. Lett. **65**, 2251 (1995).
[3] D. H. Show, R. H. Miles, T. C. Hasenberg, A. R. Cost, Y.-H. Zang, H. L. Dunlap, and L. West, Appl. Phys. Lett. **64**, 3700 (1995).
[4] J. Faist, F. Capasso, C. Sirtori, D. L. Sivco, J. N. Baillargeon, A. L. Hutchinson, S. N. G. Chu, and A. J. Cho, Appl. Phys. Lett. **68**, 3680 (1996).
[5] A. I. Nadezhdinski and A. M. Prokhorov, Proc. SPIE **1724**, 2 (1992).
[6] K. D. Moiseev, M. P. Mikhaĭlova, O. G. Ershov, and Yu. P. Yakovlev, Fiz. Tekh. Poluprovodn. **30**, 399 (1996) [Semiconductors **30**, 223 (1996)].
[7] K. D. Moiseev, M. P. Mikhaĭlova, O. G. Ershov, and Yu. P. Yakovlev, Pis'ma Zh. Tekh. Fiz. **23**, 55 (1997) [Tech. Phys. Lett. **23**, 151 (1997)].
[8] J. Faist, F. Capasso, D. L. Sivco, C. Sirtori, A. Hutchinson, and A. Cho, Science **264**, 553 (1994).
[9] J. Faist, C. Sirtori, F. Capasso, D. L. Sivco, J. Baillargeon, A. Hutchinson, S.-N. Chu, and A. Cho, in *CLEO-96*, Anaheim, California, Lune 2–7, 1996, CPD9-2.
[10] S. G. Konnikov, in *Semiconductor Heterostructures*, edited by Z. I. Alferov, CRC Press, 1990 (Mir, Moscow, 1989).
[11] J. I. Goldstein *et al.*, *Scanning Electron Microscopy and X-Ray Microanalysis* (Plenum Press, N. Y., 1981; Mir, Moscow, 1984, Vol. 1).
[12] V. A. Solov'ev, S. A. Solov'ev, and V. E. Umanksiĭ, Izv. Akad. Nauk SSSR, Ser. Fiz. **54**, 232 (1990).
[13] S. G. Konnikov, V. A. Solov'ev, V. E. Umanskiĭ, A. A. Khusainov, V. M. Chistyakov, and I. N. Yassievich, Fiz. Tekh. Poluprovodn. **21**, 1648 (1987) [Sov. Phys. Semicond. **21**, 997 (1987)].
[14] V. A. Solov'ev, M. V. Stepanov, V. V. Sherstnev, and Yu. P. Yakovlev, Pis'ma Zh. Tekh. Fiz. **23**, 54 (1997) [Tech. Phys. Lett. **23**, 233 (1997)].
[15] L. A. Bakaleĭnikov, S. G. Konnikov, V. A. Solov'ev, and V. E. Umanskiĭ, Izv. Akad. Nauk SSSR, Ser. Fiz. **51**, 458 (1987).
[16] A. Konkol, P. R. Wilshow, and G. R. Booker, Ultramicroscopy **55**, 183 (1994).

Translated by M. E. Alferieff

Formation of Se_2 quasimolecules in selenium-doped silicon

A. A. Taskin and E. G. Tishkovskiĭ

Institute of Semiconductor Physics, Siberian Branch of the Russian Academy of Sciences, 630090 Novosibirsk, Russia

(Submitted March 16, 1998; accepted for publication April 23, 1998)
Fiz. Tekh. Poluprovodn. **32**, 1306–1312 (November 1998)

The kinetics of the formation of impurity complexes associated with selenium is investigated. The stationary density of complexes is obtained as a function of temperature and the density of selenium atoms that occupy silicon lattice sites. It is established that in the process of interconversions of electrically active complexes in the temperature range 670–1000 °C the total number of atoms participating in complex-forming reactions remains unchanged at any point of the spatial distribution of the impurity. The kinetics of accumulation of centers with ionization energy 0.2 eV is satisfactorily described by a scheme of quasichemical reactions leading to the formation and decomposition of Se_2 quasimolecules. In the ideal, strongly dilute solution approximation the binding energy of a Se_2 quasimolecule is 1.35 eV. © *1998 American Institute of Physics.* [S1063-7826(98)00311-1]

INTRODUCTION

The behavior of dopants in silicon at high concentrations is characterized by the existence of the so-called ''solubility limit,'' usually taken to mean the maximum density of impurity atoms occupying substitution positions.[1,2] A variety of characteristic features in the redistribution of dopants have been observed near this density level,[3–7] specifically, the formation of impurity complexes — quasimolecules consisting of several close-lying impurity atoms.

In the case of the main dopants (B, P, As, Sb) in silicon, the low ionization energies make it difficult to observe directly levels associated with impurity complexes. Moreover, the density of these impurities in substitution solutions can be so high that possible distortions of the band structure, including also the formation of an impurity band,[8] must be taken into account in the transport phenomena, which makes the interpretation of the electrical measurements must less reliable.

In this respect, selenium dissolved in silicon is distinguished by the comparatively low limiting density in substitution positions [not greater than 1×10^{17} cm^{-3} (Ref. 9)]. As follows from theoretical estimates[10,11] and experimental data[12] obtained thus far, isolated selenium atoms occupy predominantly sites in the silicon lattice and in this position they are doubly charged donors with ionization energies of 0.3 and 0.59 eV. It is also known that when silicon is doped with selenium, centers with ionization energy 0.2 eV are formed, and in a number of cases centers with even lower ionization energies (of the order of 0.1 eV) are also formed.[13,14] The nature of these centers has not been definitively established, although in the literature it has been repeatedly hypothesized that isolated selenium atoms can combine to form more complicated complexes. Specifically, the formation of a center with ionization energy 0.2 eV is associated with the formation of a Se_2 quasimolecule consisting of two interacting selenium atoms that occupy neighboring lattice sites.[15,16]

Experimental data, which are still lacking, on the kinetics of accumulation of centers associated with selenium and data on the temperature dependences of their stationary densities would shed light on the nature of these complexes and would make it possible to use selenium-doped silicon to study complex-formation of charged impurities at close to maximum densities. A difference of the order of 0.1 eV in the ionization energies of the centers associated with selenium atoms in silicon will make it possible to determine reliably the contribution of each center to the electrical properties of the samples.

Our objective in the present work is to determine the composition of impurity complexes associated with selenium by investigating the kinetics of their formation and by determining the dependences of the density of the complexes on the temperature and the density of isolated selenium atoms occupying lattice sites.

EXPERIMENT

Silicon was doped by implantation of 125-keV selenium ions in the dose range 100–400 $\mu C/cm^2$ in a KDB-20 silicon wafer. The initial diffusion profiles of the selenium distribution were formed by heat treatment at 1200 °C for 6, 24, or 76 h in a nitrogen atmosphere.

The formation of complexes associated with selenium atoms was investigated in the initial samples prepared in this manner by means of heat treatment in the range 550 –1000 °C. The temperature interval and duration of the heat treatments were chosen so that the diffusion distribution of selenium atoms produced beforehand in the initial samples would not change much.

The spatial distribution of electrically active centers was monitored by measuring the temperature dependences of the Hall voltage and the electrical conductivity with successive etching off of silicon layers. The etching was performed in a $HF:HNO_3$ (1:20) solution. The backside of a sample was

 © 1998 American Institute of Physics

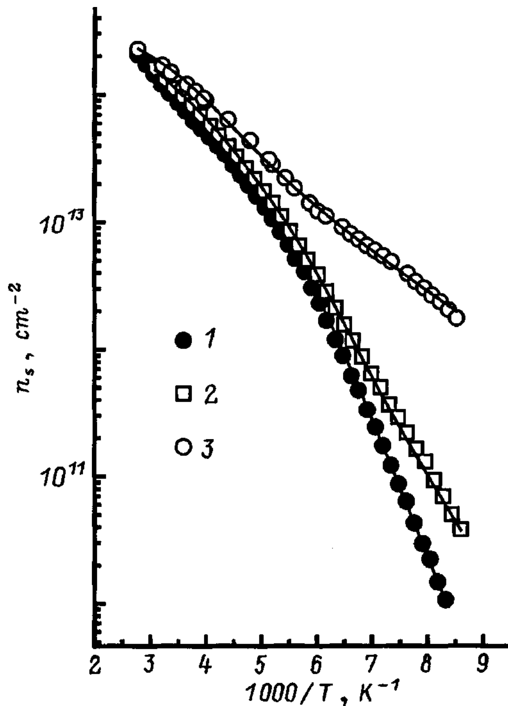

FIG. 1. Temperature dependences of the in-layer electron density after heat treatments in the temperature range 680–1200 °C. Implantation dose: 400 μC/cm^2. Heat-treatment regimes: *1* — Diffusion spreading at 1200 °C, 6 s; *2* — diffusion spreading 900 °C, 4 h; *3* — diffusion spreading 680 °C, 4 h.

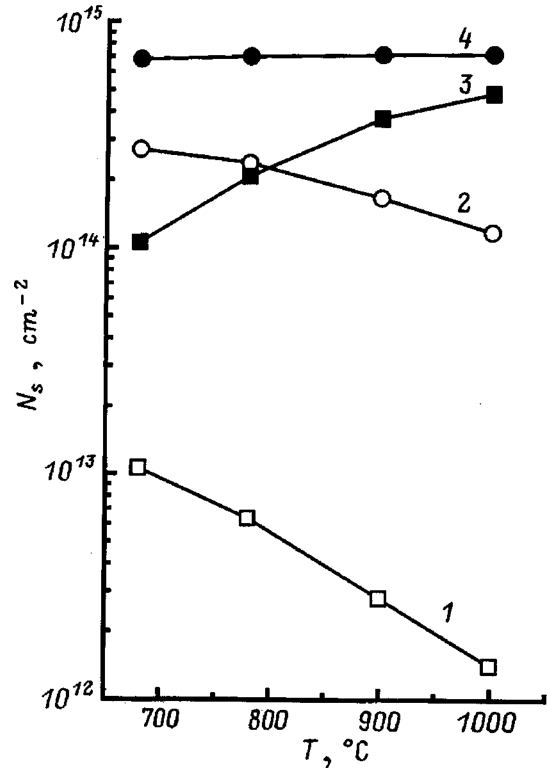

FIG. 2. Variation of the stationary in-layer density of the observed centers as a function of heat-treatment temperature in a series of samples with maximum implantation dose 400 μC/cm^2 (diffusion spreading 1200 °C, 6 h): *1* — C_3 centers, *2* — C_2 centers, *3* — C_1 centers, *4* — $Ns_1+2\times Ns_2+3\times Ns_3$.

coated with chemically stable lacquer, and the thickness of the etched-off layer (as a rule, not less than 10–15 μm) was determined from the change in the sample thickness to within ± 0.5 μm.

The densities of electrically active centers and their microscopic parameters (ionization energy, degeneracy factor, and so on) were determined by measuring the temperature dependences of the Hall voltage and the electrical conductivity in the range 80–370 K. The magnetic field intensity was 2500 G.

The parameters of the centers were determined by solving an optimization problem — searching for the minimum discrepancy between the experimental and computed temperature dependences of not only the in-layer densities but also the mobilities of the free charge carriers, with allowance for the scattering by lattice phonons and by charged and neutral impurities. The nonuniformity of the spatial distribution of the electrically active centers in a doped layer was taken into account when calculating the temperature dependences of the in-layer density and mobility.[14,17]

EXPERIMENTAL RESULTS

The typical temperature dependences of the in-layer conduction-electron density after heat treatment at temperatures in the range 680–1200 °C are shown in Fig. 1. The best agreement between the experimental dependences (points in Fig. 1 and the computed dependences (solid lines in Fig. 1) for all measured samples is obtained for the same set of microparameters (ionization energies and degeneracy factors) that characterize the electrically active centers. The computed values of the ionization energies of donor centers C_1, C_2, and C_3, which correspond to a transition from a neutral state of the donor into a singly charged state, are 0.30, 0.20, and 0.13 eV, respectively, which agrees well with the existing experimental data.[13]

The contribution of each of these centers (the total number of centers in a sample per unit area) to the experimental curves depends on the heat-treatment temperature, as shown in Fig. 2 for one series of samples.

A complete set of analogous data obtained in the implantation dose range 100–400 μC/cm^2 shows that the following are characteristic of all series which we investigated:

The total number of C_1 centers decreases and at the same time the number of C_2 and C_3 centers increases as the initial heat-treatment temperature 1200 °C decreases to lower subsequent heat-treatment temperatures.

At any temperature the quantity

$$Ns_1+2\times Ns_2+3\times Ns_3=Ns_0\approx \text{const}, \tag{1}$$

to within 10–15%. Here Ns_1 is the total amount of C_1 centers (atoms/cm^2), and Ns_2 and Ns_3 are the numbers of C_2 and C_3 centers, respectively.

The repeated short-time (no longer than 5 min) annealing at 1200 °C of the samples which have undergone low-temperature treatments restores the temperature dependences of the Hall voltage and the electrical conductivity and therefore restores the initial relative numbers of observed donor centers.

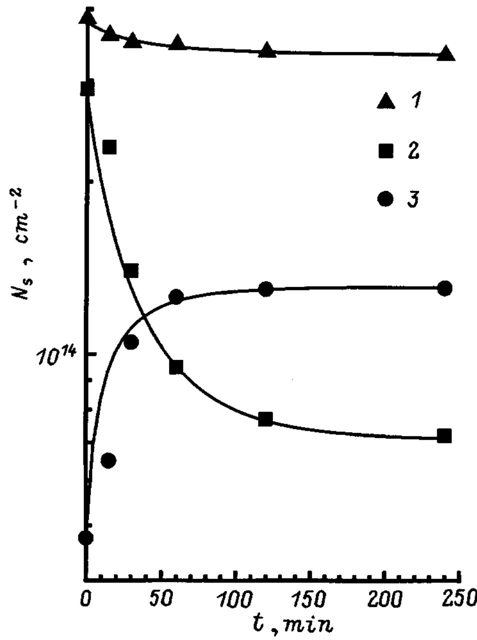

FIG. 3. Kinetics of intertransformations of C_1 and C_2 centers in selenium-doped layers at 670 °C: 1 $-Ns_1+2\times Ns_2$, 2 — C_1 centers, 3 – C_2 centers. Implantation dose: 200 μC/cm^2: diffusion spreading regime — 1200 °C, 6 h.

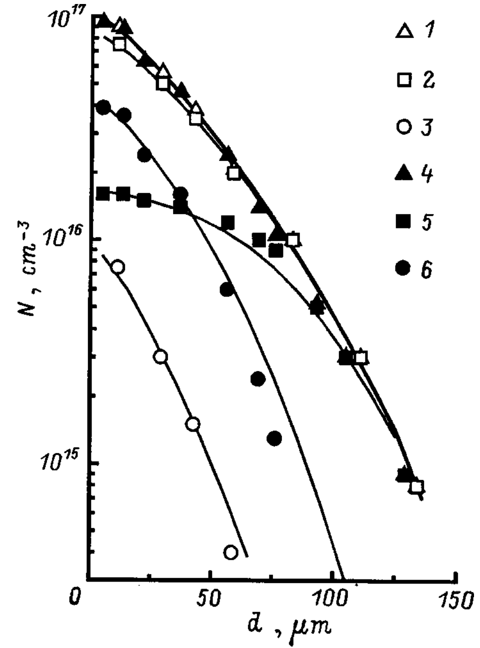

FIG. 4. Profiles of the spatial distribution of the centers in the initial sample (*1* — initial total density of centers ($N_1+2\times N_2$), *2* — initial density N_1 of C_1 centers, *3* — initial density N_2 of C_2 centers) and after annealing at $T=670$ °C for 1 h (*4* — total density of centers ($N_1+2\times N_2$), *5* — density N_1 of C_1 centers, *6* — density N_2 of C_2 centers). Implantation dose: 200 μC/cm^2. Diffusion spreading regime — 1200 °C, 6 h. The solid lines are the computed curves.

In the course of the intertransformations noted above, the relative contribution of C_3 centers to the Hall dependences depends on the implantation dose used for the initial doping. Under fixed diffusion spreading conditions, the dose decreases with decreasing contribution. This made it possible to investigate the kinetics of intertransformations of only two centers — C_1 and C_2, using for this a series of samples which were initially doped at an implantation dose not exceeding 200 μC/cm^2. For the C_1 and C_2 centers observed in this case (Fig. 3), a relation similar to Eq. (1) holds approximately at any moment in time:

$$Ns_1+2\times Ns_2=Ns_0\approx \text{const}, \tag{2}$$

where in the course of heat treatment the distribution of the centers becomes close to stationary (in the case at hand at 670 °C in 4 h).

To determine the relative densities (in atoms/cm^3) with the formation of the observed complexes, successive etching was used to obtain profiles of their spatial distribution in the initial samples from different series as well as for a number of stages of low-temperature treatments.

The initial distribution profiles of the centers and the profiles obtained after heat treatment at 670 °C for 1 h for the samples from one series ($D=200$ μC/cm^2, $T=1200\,°$C ,and $t=6$ h) are compared in Fig. 4.

It is obvious that despite the mutual changes in the densities of the C_1 and C_2 centers as a result of annealing a relation of the type (2) holds, within the limits of the experimental error, at each point of the spatial distribution:

$$N_1(x)+2\times N_2(x)=N_0(x), \tag{3}$$

where $N_1(x)$ is the density of C_1 centers, $N_2(x)$ is the density of C_2 centers, and x is the distance from the sample surface.

It is also important to note that the spatial distribution $N_0(x)$ does not change appreciably during the entire duration of low-temperature treatments.

DISCUSSION

Since the relations (1) and (2) hold at any moment in time and at all temperatures in the range investigated, it is logical to assume that the conserved quantity Ns_0 in these expressions is the total number of selenium atoms in the sample, while Ns_1 corresponds to the number of single selenium atoms, and Ns_2 and Ns_3 correspond to the number of complexes consisting of two and three, respectively, selenium atoms.

Then the process leading to the redistribution of selenium atoms between the states which we observed can be associated with the following scheme of quasichemical reactions leading to the formation and decomposition of the corresponding complexes:

$$\mathrm{Se}+\mathrm{Se}\underset{\beta}{\overset{\alpha}{\Leftrightarrow}}\mathrm{Se}_2, \tag{4}$$

$$\mathrm{Se}+\mathrm{Se}_2\underset{\beta_1}{\overset{\alpha_1}{\Leftrightarrow}}\mathrm{Se}_3, \tag{5}$$

where α, α_1, β, and β_1 are phenomenological constants that account for the rates of the forward and reverse reactions and do not depend on the reagent densities. The scheme (4)–(5) presupposes successive attachment of the mobile compo-

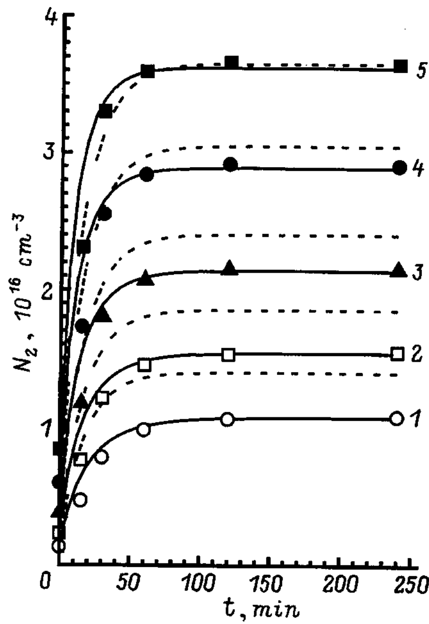

FIG. 5. Experimental (dots) and computed (solid lines) dependences of the density of Se_2 quasimolecules versus time during heat treatment at 670 °C on different sections of the impurity profile with different selenium densities (in 10^{16}, cm^{-3}): *1* — 3.5, *2* — 4.7, *3* — 6.2, *4* — 8.0, *5* — 9.7. The dashed curves were calculated for the monomolecular reaction forming SeY.

nent — selenium atoms occupying lattice sites. The reactions (4) and (5) are written in a reversible form, since, as noted above, short-time heat treatment at 1200 °C returns the impurity subsystem under study into the initial state. Moreover, taking into account the decomposition ensures for the scheme (4)–(5) the existence of stationary states in accordance with the experimental data (Figs. 3 and 5).

In the case where the C_2 centers are predominantly formed, the stationary state is provided by only the reaction (4). The corresponding kinetic equation in the combinatorial kinetics approximation[18] has the form

$$\frac{\partial N_1(x,t)}{\partial t}=D\frac{\partial^2 N_1(x,t)}{\partial x^2}-2(\alpha N_1^2(x,t)-\beta N_2(x,t)), \tag{6}$$

$$\frac{\partial N_2(x,t)}{\partial t}=\alpha N_1^2(x,t)-\beta N_2(x,t), \tag{7}$$

$$N_1(x,t=0)=N_1^0(x), \tag{8}$$

$$N_2(x,t=0)=N_2^0(x), \tag{9}$$

where $N_1(x,t)$ is the density of isolated selenium atoms occupying substitution positions, $N_2(x,t)$ is the density of the quasimolecules Se_2 consisting of two interacting selenium atoms, α is the probability of an elementary event of formation of a Se_2 quasimolecule per unit time, the so-called rate constant of the reaction; β is the rate constant of the reaction by which Se_2 quasimolecules decompose; and $N_1^0(x)$ and $N_2^0(x)$ are the corresponding densities in the initial profile of the impurity. Moreover, from Eq. (3) follows a limit on the reagent densities:

$$N_1(x,t)+2\cdot N_2(x,t)=N_0(x). \tag{10}$$

As follows from the experimental data (Fig. 4) and estimates made using the known values of the diffusion coefficient of selenium in silicon,[9] the heat-treatment temperatures are low enough that the broadening of the initial profile did not exceed the experimental error. In this case the diffusion term on the right side of expression (6) can be disregarded, and the problem (6)–(9) can be solved in analytic form as

$$N_1(x,t)=N_0(x,t)-2N_2(x,t), \tag{11}$$

$$N_2(x,t)=\frac{z_1(x)B(x)-z_2(x)A(x)\exp\{-\omega(x)t\}}{B(x)-A(x)\exp\{-\omega(x)t\}}, \tag{12}$$

where

$$A(x)=z_1(x)-N_2^0(x),\qquad B(x)=z_2(x)-N_2^0(x),$$

$$z_1(x)=\frac{N_0}{2}+N^*-\frac{\omega(x)}{8\alpha},\qquad z_2(x)=\frac{N_0}{2}+N^*+\frac{\omega(x)}{8\alpha},$$

$$\omega(x)=\beta\left[1+\frac{N_0(x)}{N^*}\right]^{1/2},\qquad N^*=\frac{\beta}{8\alpha}.$$

Therefore, for any fixed selenium atom density $N_0(x)$ corresponding to a certain point of the spatial distribution (Fig. 4) the form of the kinetic curves $N_1(x,t)$ and $N_2(x,t)$ should be determined uniquely by only two parameters — the values of the rate constants α and β for the forward and reverse reactions, respectively. The same values of these parameters correspond to the computed curves, presented in Fig. 5, of the accumulation of C_2 centers (solid lines) for different values of the selenium atom density $N_0(x)$: $\alpha=9\times10^{-21}$ cm^3/s and $\beta=3.5\times10^{-5}$ s^{-1}.

However, if it is assumed that the C_2 centers form via a reaction of the type

$$\mathrm{Se}+Y\underset{\beta_y}{\overset{\alpha_y}{\Leftrightarrow}}\mathrm{Se}Y, \tag{13}$$

where the component Y is not a selenium atom (for example, Y is a dopant atom,[9] an oxygen or carbon atom), then the values obtained in this case for the rate constants for the formation and decomposition of the C_2 centers can satisfactorily describe the kinetics of accumulation of C_2 centers (dashed curves in Fig. 5) only for one point of the spatial distribution. For example, for the top curve in Fig. 5 we have an agreement with $\alpha_y=4\times10^{-22}$ cm^3/s and $\beta_y=5.5\times10^{-4}$ s^{-1}. However, for these values of α_y and β_y a substantial discrepancy is observed between the experimental and computed values of $N_2(t)$ for other sections of the profile and correspondingly for other values of N_0. Therefore, the kinetics of accumulation of C_2 centers in different sections of a profile cannot be described in a self-consistent manner by means of the reactions (13) — the corresponding values of α_y and β_y become coordinate-dependent.

The above-noted features of the kinetics of accumulation and decomposition of centers, specifically, the absence of macroscopic diffusion broadening of the initial doping profile and the reversibility and existence of the relations expressing the conservation of matter in the presence of reactions, in our view, suggest that the stationary state established in time at each point of the spatial distribution

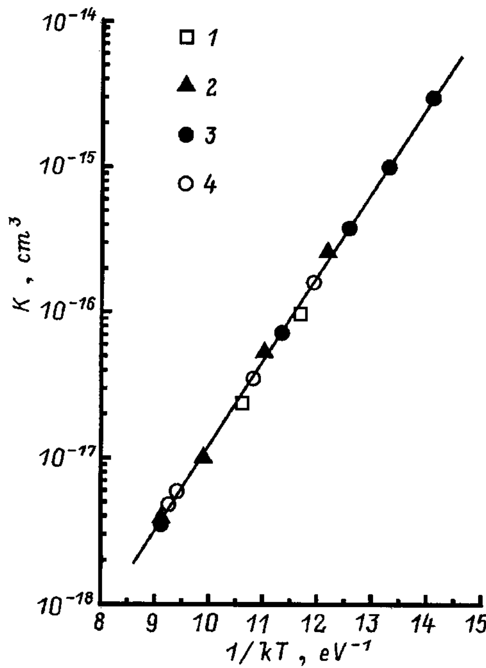

FIG. 6. Equilibrium reaction constants for the reaction $Se+Se \rightleftarrows Se_2$ versus the reciprocal of the temperature for samples from different series: *1* — Implantation dose 100 $\mu C/cm^2$. Diffusion spreading regime — 1200 °C, 6 h; *2* — implantation dose 400 $\mu C/cm^2$, diffusion spreading regime — 1200 °C, 6 h; *3* — implantation dose 200 $\mu C/cm^2$, diffusion spreading regime — 1200 °C, 24 h; *4* — implantation dose 400 $\mu C/cm^2$, diffusion spreading regime — 1200 °C, 76 h.

can be described as locally equilibrium state. In this case the relative densities of the investigated centers correspond to a functional relation between the thermodynamically equilibrium values.

Then the functional relation for stationary densities N_1^∞ and N_2^∞ of single and double, respectively, complexes must correspond to the law of mass action for the reaction (4)

$$\frac{N_2^\infty}{(N_1^\infty)^2}=K(T), \tag{14}$$

where $K(T)$ is the equilibrium constant of the reaction (4), which does not depend on the concentration of the reagents. Figure 6 shows (points) the values of the equilibrium constant of the reaction (4) as a function of the reciprocal of the temperature that correspond to the relation (14) for the stationary densities of C_1 and C_2 centers obtained in samples from different series.

The explicit form of the equilibrium constant in our model of the formation of selenium complexes can be obtained by analyzing the Gibbs thermodynamic potential of the system in the ideal, strongly dilute solution approximation.

For constant temperature T and constant pressure P, disregarding the change in volume in the complex-formation reactions, the condition that the change in the Gibbs potential be minimal is equivalent to the condition that the change in the free energy of the system be minimal:

$$\Delta G_d(N_1,N_2)=\Delta U(N_1,N_2)-T\Delta S(N_1,N_2), \tag{15}$$

where ΔU and ΔS are, respectively, the change in the internal energy and entropy, respectively, per unit volume, and N_1 and N_2 are the densities of isolated and double selenium atoms, respectively.

We have for the change in the internal energy of the system

$$\Delta U(N_1,N_2)=W_1N_1+W_2N_2+\Delta E, \tag{16}$$

where W_1 and W_2 are the changes in the internal energy of the system which are due to the replacement of one Si atom by one Se atom and two neighboring Si atoms by two Se atoms, respectively, and ΔE accounts for the change in the energy of the electronic subsystem.

For a strongly dilute solution (N_1, $N_2 \ll M_L$), ignoring the vibrational contribution, the entropy change is determined by the configurational contribution ΔS_{conf} due to atomic rearrangements and rearrangements in the electronic subsystem ΔS_{el}:

$$\Delta S_{\text{conf}}=k\ \ln\left[\frac{N_L!}{(N_L-N_1)!}\,\frac{(2N_L)!}{(2N_L-N_2)!N_2!}\right]+\Delta S_{el}, \tag{17}$$

where N_L is the total number of lattice sites, and k is Boltzmann's constant.

Minimizing the Gibbs potential with respect to independent variables, with allowance for the charge states (see, for example, Ref. 19) of the initial and final products of the reaction (4), we obtain

$$K(T)=\frac{2}{N_L}e^{\Delta U/kT}\cdot m(T), \tag{18}$$

where ΔU is the change in the energy of the crystal due to the formation of a Se_2 molecule,

$$m(T)=\frac{g_2^0}{(g_1^0)^2}\,\frac{n^2(n^2+nQ_2^++Q_2^+Q_2^{++})}{(n^2+nQ_1^++Q_1^+Q_1^{++})^2}, \tag{19}$$

Q_i^+ and Q_i^{++} are the Shockley–Read factors which are known from the statistics of the multiply charged centers, g_i^0 are degeneracy factors, and n is the electron density in the conduction band.

In the coordinates $\log(K)-1/kT$ (Fig. 6) the experimental values of $K(T)$ are fit well by a straight line with slope $\Delta U=1.35$ eV. In the approach considered here, the slope of this straight line corresponds to the binding energy of the ''quasimolecule'' Se_2. The point of intersection of this straight line with the ordinate also agrees well with the value of the preexponential factor in the expression (18).

In summary, the quasichemical approach makes it possible to describe satisfactorily the main laws of the intertransformations of electrically active complexes associated with selenium in silicon.

It should be noted that comparing the computed curves of the kinetics of accumulation of Se_2 quasimolecules with the experimental values of $N_2(t)$ shows the following systematic discrepancies:

1. For all points of the profile shown in Fig. 4, at the initial stage of heat-treatment ($t \leq 15$ min) the C_2 density is less than the computed value (Fig. 5).

2. For the section of the profile with the density of selenium atoms less than 1×10^{16} cm^{-3}, the density of C_2 centers which is obtained by annealing at 670 °C for 1 h is systematically lower than the computed value (dashed curve in Fig. 4).

3. The quantity $Ns_1+2\times Ns_2=Ns_0$ during annealing at 670 °C is still not conserved (Fig. 3, top curve), but rather it decreases, though very little, by not more than 10%.

The first two circumstances could be due to the fact that the change in the spatial distribution of the reagents in the course of the reaction is neglected in the scheme of quasichemical reactions.

In the first place, as is well known (see, for example, Ref. 20), the computed complex-formation rates are too high because of instantaneous random distribution of the reagents, which is implicitly incorporated in the quasichemical scheme.

In the second place, at low atomic selenium density only the quasimolecules Se_2, whose components were located at distances comparable to the diffusion length, have enough time to form during annealing.

The observed very small decrease in the total number of selenium atoms during annealings could be due to the existence of channels parallel to the reactions (4)–(5), for example, reactions leading to the interaction of selenium with oxygen or carbon, whose products are electrically neutral centers. This circumstance can be easily taken into account in the phenomenological scheme examined above by introducing an additional reaction of the type (13) leading to the absorption of atomic selenium, which, of course, will change the absolute values of the obtained rates α and β of formation and decomposition, respectively, of Se_2 quasimolecules but does not influence their ratio. In this sense, the values obtained for the equilibrium constants of the reaction (4) were determined more reliably.

CONCLUSIONS

In the process of intertransformations of electrically active complexes formed in selenium-doped silicon, at all heat-treatment temperatures in the range 670–1000 °C the total number of impurity atoms participating in complex-formation reactions remains unchanged at any point of the spatial distribution.

Repeated annealing of samples which have undergone low-temperature treatment, at the initial temperature of diffusion spreading (not more than 5 min at 1200 °C) restores the initial relative densities of the observed donor centers.

The kinetics of accumulation of the center with ionization energy 0.2 eV is described satisfactorily by the scheme of quasichemical reactions of formation and decomposition of Se_2 quasimolecules with the same values of the rate constants α and β of the forward and reverse reactions, respectively, throughout the entire extent of the spatial distribution of the impurity.

The observed stationary states of the impurity system can be described well on the basis of the ideal, strongly dilute solution approximation. The relative stationary densities of the components of the quasichemical reactions give 1.35 eV for the binding energy of the Se_2 quasimolecule.

We wish to thank Professor L. S. Smirnov for showing interest in this work and for a number of valuable remarks. We are also grateful to S. S. Shaĭmeev for reading the manuscript and for a helpful discussion of the results.

This work was supported by Grant No. 96-15-97272 from the Russian Fund for Fundamental Research.

[1] F. A. Trumbor, Bell Syst. Tech. J. **39**, 205 (1960).
[2] V. E. Borisenko and S. G. Yudin, Phys. Status Solidi **101**, 123 (1987).
[3] A. M. Myasnikov, V. I. Obodnikov, V. G. Seryapin, E. G. Tishkovskiĭ, B. I. Fomin, and E. I. Cherepov, JETP Lett. **60**, 102 (1994).
[4] A. M. Myasnikov, V. I. Obodnikov, V. G. Seryapin, E. G. Tishkovskiĭ, B. I. Fomin, and E. I. Cherepov, Fiz. Tekh. Poluprovodn. **31**, 338 (1997) [Semiconductors **31**, 279 (1997)].
[5] A. M. Myasnikov, V. I. Obodnikov, V. G. Seryapin, E. G. Tishkovskiĭ, B. I. Fomin, and E. I. Cherepov, Fiz. Tekh. Poluprovodn. **31**, 703 (1997) [Semiconductors **31**, 600 (1997)].
[6] P. A. Stolk, H.-J. Gossmann, D. J. Eagleham, D. C. Jacolson, J. M. Poat, and H. S. Luftman, Appl. Phys. Lett. **66**, 568 (1995).
[7] P. A. Stolk, D. J. Eagleham, H.-J. Gossmann, and J. M. Poat, Appl. Phys. Lett. **66**, 1370 (1995).
[8] V. L. Bonch-Bruevich, I. P. Zvyagin, R. Kaĭner, A. G. Mironov, R. Énderlaĭn, and B. Ésser, *Electronic Theory of Disordered Semiconductors* [in Russian], Nauka, Moscow, 1987.
[9] H. R. Vydyanath, J. S. Lorenzo, and F. A. Kröger, J. Appl. Phys. **49**, 5928 (1978).
[10] V. A. Singh, U. Lindefelt, and A. Zunger, Phys. Rev. B **27**, 4909 (1983).
[11] H. Overhof, M. Scheffler, and C. M. Weinert, Phys. Rev. B **43**, 12 494 (1991).
[12] G. Pensl, G. Roos, C. Holm, and P. Wagner, Mater. Sci. Forum **10–11**, 911 (1986).
[13] H. G. Grimmeiss and E. Janzen, MRS Symp. Proc. **14**, 33 (1983).
[14] N. N. Gerasimenko, B. A. Zaĭtsev, A. A. Taskin, E. G. Tishkovskiĭ, Fiz. Tekh. Poluprovodn. **24**, 4901/88 (1990) [Sov. Phys. Semicond. **24**, 244 (1990)].
[15] E. Janzen, R. Stedman, G. Grossmann, and H. G. Grimmeiss, Phys. Rev. B **29**, 1907 (1983).
[16] J. C. Swartz, D. H. Lemmon, and R. N. Thomas, Solid State Commun. **36**, 331 (1980).
[17] B. A. Zaĭtsev, A. A. Taskin, and E. G. Tishkovskiĭ, Preprint 2, Institute of Semiconductor Physics, Siberian Branch of the USSR Academy of Sciences, Novosibirsk, 1990.
[18] C. W. Gardiner, *Handbook of Stochastic Methods for Physics, Chemistry, and the Natural Sciences* (Springer-Verlag, N. Y., 1985; Mir, Moscow, 1986).
[19] V. L. Vilestkiĭ and G. A. Golodar', *Static Interaction of Electrons and Defects in Semiconductors* [in Russian], Naukova Dumka, Kiev, 1969.
[20] M. Koiwa, Cryst. Lattice Defects **4**, 65 (1973).

Translated by M. E. Alferieff

ELECTRONIC AND OPTICAL PROPERTIES OF SEMICONDUCTORS

Experimental study of the transverse Ettingshausen–Nernst effect and thermoelectric power in the presence of a large temperature gradient

M. M. Gadzhialiev and V. A. Elizarov

Institute of Physics, Dagestan Science Center of the Russian Academy of Sciences, 367003 Makhachkala, Russia

(Submitted March 19, 1998; accepted for publication April 20, 1998)
Fiz. Tekh. Poluprovodn. **32**, 1313–1314 (November 1998)

The transverse Ettingshausen–Nernst effect and the thermoelectric power of compensated germanium with electron density $n=2\times10^{11}$ cm^{-3} are investigated as a function of the temperature gradient in the range $2-1.5\times10^{3}$ K·cm^{-1} at average temperature 350 K. It is shown that the mechanism of charge-carrier scattering does not depend on the temperature gradient, while the Benedick thermoelectric power is due to heating of the current carriers by the heat field. © *1998 American Institute of Physics.* [S1063-7826(98)00411-6]

In Ref. 1 it is shown that investigation of transport phenomena in the presence of a large temperature gradient (LTG) makes it possible to take into account the contribution of the nonequilibrium minority current carriers that arise in the process. Here a large temperature gradient means a temperature gradient such that $L_D>L_T$, where L_D is the diffusion length of minority current carriers, and $L_T=T/\nabla T$ is the reduced length. If the length Δx of the minimal section of the sample whose ends have different temperatures ($T_1\neq T_2$) is comparable to L_D, then the condition $L_D>L_T$ becomes $\Delta T>T$. This latter inequality is the condition under which the system of electrons is far from being in thermodynamic equilibrium with the lattice.[2] The condition $L_D>L_T$ implies that the LTG depends on the material in which a temperature gradient is produced.

It is well-known that the presence of a LTG is indicated by the appearance of Benedick's thermoelectric power due to nonequilibrium minority current carriers.[3,4] In Ref. 4 it is shown that the inequality $L_D>L_T$ holds in germanium and therefore the Benedick thermoelectric power appears in the presence of a temperature gradient of the order of 10^3 K·cm^{-1}.

In the present work we investigate the mechanism of scattering of nonequilibrium current carriers and the behavior of the thermoelectric power and transverse Ettingshausen–Nernst (E–N) effect under conditions far from thermodynamic equilibrium.

We have accordingly measured the transverse E–N effect and the thermoelectric power of compensated electronic germanium ($n=2\times10^{11}$ cm^{-3}) as a function of the temperature gradient (TG). The latter was varied in the range $2-1.5\times10^{3}$ K·cm^{-1} with a constant average sample temperature $\bar{T}=350$ K.

Slow variation of the TG in the above-indicated interval with constant average sample temperature

$$\bar{T}=(T_h+T_c)/2$$

was effectuated by the method described in Ref. 4 . Here T_h and T_c are the temperature of the heater and cooler, respectively. At first, holding the cooler (soldered to one end of the sample) in liquid-nitrogen vapor, we switched on the heater (soldered to the opposite end of the sample) at very low power. This is the starting point of the experimental curves with $\nabla T=2$ K·cm^{-1} and $\bar{T}=350$ K (see Fig. 1). Next, gradually immersing the cooler in liquid-nitrogen vapor (and then in liquid nitrogen) and increasing at the same time the power of the heater, we produced experimental conditions corresponding to $\nabla T>10$ K·cm^{-1} and $\bar{T}=350$ K. When a temperature gradient $\nabla T>10^2$ K·cm^{-1} was produced, liquid helium was used to cool the refrigerator and the power released in the heater reached 2 kW.

Figure 1 shows curves of the transverse E–N coefficient Q_1 and the differential thermoelectric power α as functions of the temperature gradient ∇T, which were measured in *n*-Ge at $\bar{T}=350$ K. The coefficient Q_1 was measured in a 10-kOe magnetic field, corresponding to the condition that the field for measuring the E–N effect in electronic germanium at the indicated average sample temperature is weak.

The measurements of Q_1, performed by the standard method[5] under conditions such that the positive TG is directed along the positive *X* axis, while the magnetic field is directed along the positive *Z* axis, showed that under these conditions a field directed along the negative *Y* axis appears as a result of the transverse E–N effect (right-hand coordinate system); i.e., the coefficient Q_1 is negative. As one can see from the figure (curve *2*), the sign $Q_1<0$ remains in the entire interval of TGs. The coefficient Q_1 decreases sharply in absolute magnitude as the LTG region is approached, i.e., when the temperature gradient is of the order of 10^3 K·cm^{-1}.

We can say the following about the function $Q_1(\nabla T)$ in the presence of a LTG. Since the sign of Q_1 remains negative in the entire interval of TGs, the minority nonequilib-

 © 1998 American Institute of Physics

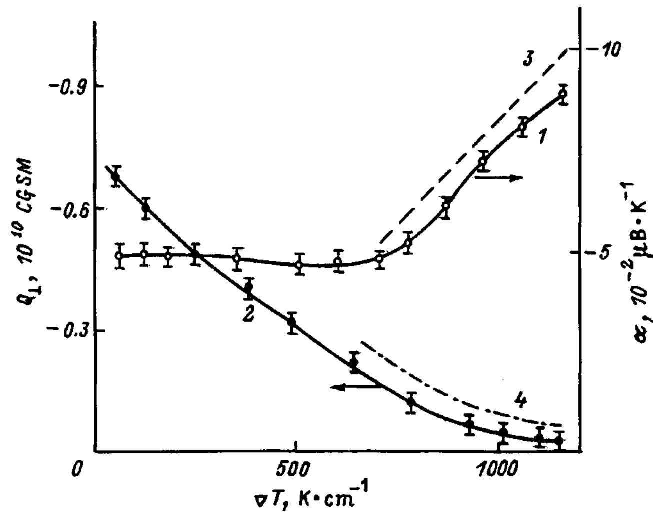

FIG. 1. Thermoelectric power α (*1*) and Ettingshausen–Nernst coefficient Q_1 (*2*) versus the temperature gradient ∇T for electronic germanium ($n=2\times10^{11}$ cm^{-3}) with average temperature $\bar{T}=350$ K. Dashed line *3* — theory of thermoelectric power, dot-dashed line 4 shows the proportionality $|Q_1|\sim(\nabla T)^{-3}$ in the region with a large temperature gradient.

rium current carriers (holes), just as the majority carriers, in the region of intrinsic conductivity of *n*-Ge are scattered by acoustic phonons.[5] The sharp decrease in Q_1 in the presence of a LTG as $Q_1\sim(\nabla T)^{-3}$ (curve *4*) can be qualitatively explained by a decrease in the effective mobility accompanying the appearance of nonequilibrium current carriers.[1]

It is evident from Fig. 1 that the thermoelectric power is constant for small TGs and increases for TGs close to 10^3 K·cm^{-1}. The variation of thermoelectric power in the presence of a LTG (curve *1*) is compared with the theoretical curve (curve *3*) obtained using the formula from Ref. 3 for the case that the current carriers lose energy on acoustic phonons and momentum on ionized impurities:

$$\alpha_B=\frac{57k_B^3(\Delta T)^2\tau_i^3(T_0+T_1)}{|e|(m^*)^2v_3^2(\Delta x)^2T_0^2T_1^2}, \quad (1)$$

where T_1 and T_0 are the temperatures of the hot and cold ends of the sample, respectively; $\Delta T=T_1-T_0$; τ_i is the momentum relaxation time on impurity ions; Δx is the sample length; v_3 is the speed of sound; k_B is Boltzmann's constant; m^* is the effective mass; and e is the electron charge. We see that the observed increase in the thermoelectric power in the LTG region (curve *1*) agrees qualitatively with the theoretical curve *3*.

Two mechanisms leading to the appearance of the Benedick thermoelectric power are known. The first one, called the Tauc mechanism,[1] operates when $L_D>L_T$. If $L_T^2>l_\varepsilon^2$ holds in addition to $L_D>L_T$ ($l_\varepsilon=\sqrt{D\tau_\varepsilon}$ — cooling length, τ_ε — energy relaxation time), then the Benedick thermoelectric power appears as a result of the heating of the current carriers by the heat field — the so-called heating mechanism.[3]

In germanium with electron density $n=2\times10^{11}$ cm^{-3} the conditions $L_D>L_T$ and $L_T^2>l_\varepsilon^2$ for $\bar{T}=350$ K hold with $\nabla T\simeq8\times10^2$ K·cm^{-1}. Therefore, the observed change in the thermoelectric power is explained by the heating mechanism of Benedick's thermoelectric power. We note that the formula used to obtain curve *3* is derived in Ref. 3 for the case of the heating mechanism of the Benedick thermoelectric power.

[1] J. Tauc, *Photo and Thermoelectric Effects in Semiconductors* (Pergamon Press, N. Y., 1962; Inostr. Lit., Moscow, 1962).

[2] V. L. Bonch-Bruevich and S. G. Kalashnikov, *Semiconductor Physis* [in Russian], Nauka, Moscow, 1977.

[3] L. P. Bulat and R. B. Ladyka, Fiz. Tverd. Tela (Leningrad) **24**, 1221 (1982) [Sov. Phys. Solid State **24**, 691 (1982)].

[4] M. M. Gadzhialiev in *Plasma in Semiconductors* [in Russian], Makhachkala, 1984, p. 21.

[5] I. M. Tsidil'kovskiĭ, *Thermomagnetic Effects in Semiconductors* (Academic Press, N. Y., 1962; Fizmatgiz, Moscow, 1960), p. 290.

Translated by M. E. Alferieff

Nonlinear waves of interacting charge carriers in semiconductors

V. E. Stepanov

Siberian Physicotechnical Institute, 634050 Tomsk, Russia

(Submitted February 2, 1998; accepted for publication April 29, 1998)
Fiz. Tekh. Poluprovodn. **32**, 1315–1317 (November 1998)

Nonideality effects of charge carriers in semiconductors have been theoretically demonstrated, being derived from the equation of state in the hydrodynamics approximation. The nonlinear terms in the density in the equation of state are conditioned by the Coulomb interaction and lead to the existence of solitary and periodic waves for perturbations of the charge-carrier density. © *1998 American Institute of Physics.* [S1063-7826(98)00511-0]

The ideal gas model for charge carriers in semiconductors is the dominant model for equilibrium and nonequilibrium phenomena. This representation is naturally based on the small magnitude of the mean potential energy $\langle V\rangle = e^2 n^{1/3}/\varepsilon$ (n is the density, and ε is the dielectric constant) in comparison with the mean kinetic energy $\langle T\rangle$. For a classical gas $\langle T\rangle = kT$ and for a quantum (degenerate) gas $\langle T\rangle = (3/5)[(3\pi)^2\hbar^2 n^{2/3}/2m^*]$ (m^* is the effective mass). Therefore, the criterion of ideality holds only in the region of low densities of the charge carriers for a classical gas and only in the region of high densities for a quantum gas. For all other values of the density it is important to take into account the interaction between the charge carriers (the case of tight binding). There has been no progress in the analysis of the tight-binding case for quite some time now, and the state of the problem, as identified in Ref. 1, remains as true today as when first enunciated. Realization of the traditional program, in which the excitation spectrum is found on the basis of the Hamiltonian and the theory of equilibrium and nonequilibrium phenomena is constructed on this basis, has proven to be fraught with difficulty.

Let us consider a macroscopic manifestation of nonideality, for definiteness in the classical electron gas of a semiconductor. In the macroscopic case, deviations from ideality can be taken into account via the the equation of state. In a microscopic treatment it follows that in addition to the kinetic pressure, there exists a pressure due to the interaction between the electrons, defined by the expression[2]

$$P_{\text{int}} = \int (\mathbf{s}\nabla_s)\frac{e^2}{\varepsilon s} g_2(\mathbf{r},\mathbf{s},t)\,d\mathbf{s},$$

where g_2 is the momentum-averaged two-particle correlation function. Since calculation of the correlation function for a Coulomb system is difficult, we will make use of the concept of a local equilibrium state, which is a necessary attribute of the hydrodynamic description. At equilibrium the interaction pressure is given by $P_{\text{int}} = -\partial F_{\text{int}}/\partial V$, where F_{int} is the free energy of the interaction. In this expression the hydrodynamic variables (for the case under investigation these reduce to the density n) are functions of the spatial coordinates and of time. In what follows, we will make use of the expansion of the free energy of the interaction in the density obtained in Ref. 3 using the Matsubara technique. This expansion includes the self-consistent Debye–Hückel correction and the following correlation correction. For the sum P of the kinetic pressure and the interaction pressure we have

$$(kTn_0)^{-1}P \equiv p = n(1-\sqrt{\pi}\alpha n^{1/2}/3) - \frac{\pi}{6}\alpha^2 n^2(\ln 4\pi\alpha^2 n + 1), \tag{1}$$

where $\alpha = (e^2 n_0^{1/3}/\varepsilon kT)^{3/2}$ is the nonideality parameter, n_0 is the mean equilibrium electron density, which follows from global electrical neutrality, and we use the dimensionless density $n \to n/n_0$. For a nonideal classical electron gas in a semiconductor we solve the system of equations of the hydrodynamic approximation

$$\begin{cases} \dfrac{dp}{dn}\nabla n = -n\mathbf{E} + \dfrac{\mathbf{J}}{en_0 D}, \\ \operatorname{div}\mathbf{E} = \mathrm{k}^2(1-n), \qquad \mathrm{k}^2 = 4\pi e^2 n_0/\varepsilon kT, \\ \dfrac{\partial n}{\partial t} - \dfrac{1}{en_0}\operatorname{div}\mathbf{J} = 0, \end{cases} \tag{2}$$

where D is the diffusion coefficient and we use the dimensionless potential $\varphi \to e\varphi/kT$. We consider the equilibrium state after setting the current density J in Eqs. (2) equal to zero. In this case the dependence $n(\varphi)$, which for an ideal gas is the standard Boltzmann distribution, is found from the equation

$$\frac{dp}{dn}\frac{dn}{d\varphi} = n \tag{3}$$

with the additional condition $n(0)=1$. The solution of Eq. (3) has the form

$$\varphi = \ln n + \alpha\sqrt{\pi}(1-\sqrt{n}) - \frac{\pi}{3}\alpha^2(n\ln nA - \ln A), \tag{4}$$

where $A = (\mathrm{e}^{1/3}4\pi\alpha^2)^{3/2}$, and e is the base of the natural logarithms. At the point $n = n_{\mathrm{e}}$, defined by the equation

$$\frac{dp}{dn} = 0, \tag{5}$$

 © 1998 American Institute of Physics

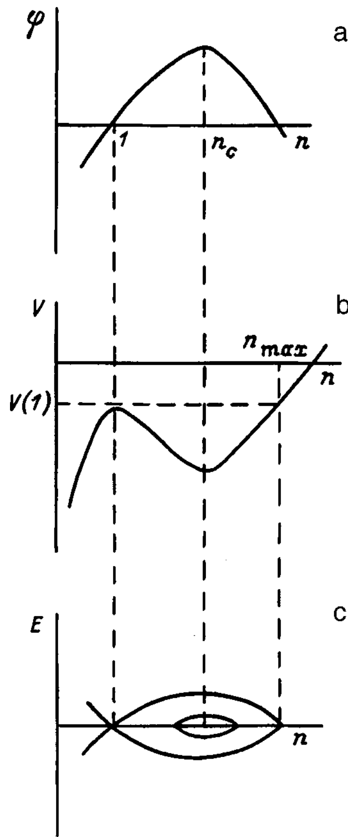

FIG. 1. Dependence of the potential φ (a) and ''potential energy'' V (b) on the normalized electron density; phase diagram of the system (c).

$\varphi(n)$ reaches its maximum. The solution of Eq. (5) defines the boundary of stability of the homogeneous state.[4] The analysis that follows is made for the one-dimensional case. System (2) is integrated once; the arising integral H is

$$H=\frac{E^2}{2}+V(n). \tag{6}$$

It is natural to call this integral the Hamiltonian. Equations (1) and (2) yield the following expression for the ''potential energy'' $V(n)$:

$$V(n)=\mathrm{k}^2[\varphi(n)-p(n)]. \tag{7}$$

The first two equations of system (2) are Hamilton's equations of motion arising from the Hamiltonian defined by Eqs. (6) and (7) if the variable

$$\tau=-\int n\left(\frac{dp}{dn}\right)^{-1}dx \tag{8}$$

is assumed to be analogous to time. Analysis in the phase plane (E,n) shows that there are two singular points: the hyperbolic point $n=1$ and the elliptical point $n=n_c$. Figure 1 plots the dependences $\varphi(n)$ and $V(n)$, and the phase diagram of the system. The value $H=V(1)$ defines the separatrix. The solution on the separatrix is a static solitary wave—a soliton; for $H<V(1)$ nonperiodic solutions exist—these are general results of the nonlinear dynamics of Hamiltonian systems.[5] In light of the complexity of expression (7) we use the extrapolation

$$V(n)=V(1)+6[V(1)-V(n_c)]\times\left[-\frac{1}{2}\left(\frac{n-1}{n_c-1}\right)^2+\frac{1}{3}\left(\frac{n-1}{n_c-1}\right)^3\right]. \tag{9}$$

This expression approximates expression (7) well in the interesting region of electron densities and also coincides with the analogous quantity in the stationary KdV theory.[5] We can at once write out solutions for the nonlinear waves. For the static soliton we have

$$n=1+\frac{3}{2}\,\frac{n_c-1}{\cosh^2\gamma(\tau-c)}, \tag{10}$$

where the position of the soliton c is determined by the boundary conditions and the variable $\tau(x)$ is given by an expression following from Eq. (8) using the extrapolation (9),

$$\frac{2}{3}\gamma\tau-\tanh\gamma\tau=\frac{\mathrm{k}^2}{6\gamma}x. \tag{11}$$

The width of the soliton γ^{-1} is given by

$$\gamma=\frac{1}{n_c-1}\sqrt{\frac{3}{2}[V(1)-V(n_c)]}.$$

In the case $H<V(1)$ a periodic solution exists

$$n=n_3+(n_1-n_3)dn^2\left(\tau\sqrt{\frac{n_1-n_2}{n_c-1}[V(1)-V(n_c)]},s\right), \tag{12}$$

where $n_1>n_2>n_3$ are the roots of the equation $H=V(n)$, and dn is the Jacobi elliptical function with modulus $s^2=(n_1-n_2)/(n_1-n_3)$. The period of the nonlinear periodic wave is equal to $4K(s)\sqrt{(n_c-1)/[V(1)-V(n_c)](n_1-n_3)}$, where $K(s)$ is the complete elliptic integral of the first kind.

Let us turn now to the nonequilibrium case, in which there is a current density J. To search for stationary solutions in system (2) we introduce the wave argument $\xi=x+ut$. Then, it follows from the equation of continuity that $J=J_0+eun_0(n-1)$, where J_0 is the external current. Transforming to the variable τ defined implicitly by Eq. (11) with x replaced by ξ, we obtain the following equations from the remaining equations of system (2):

$$\frac{d^2n}{d\tau^2}+\frac{1}{n^2D}\left(\frac{J_0}{n_0}-eu\right)\frac{dn}{d\tau}=-\frac{dV}{dn}. \tag{13}$$

This equation is analogous to the equation for a nonlinear oscillator with friction. The friction is due to the interaction of the electrons with phonons and defects. For the work of the friction force to equal zero it is necessary to choose the speed of the nonlinear wave $u=J_0/eu_0$. Then attenuation is absent and we return to the results of the analysis for the equilibrium case. The solitons and nonlinear periodic waves obtained in this analysis remain invariant, but propagate with velocity u. A new mechanism of charge-carrier transport in semiconductors via nonlinear waves arises. Since the phase volume (the Hamiltonicity of the system) is conserved as the

nonlinear waves propagate, it is necessary to prescribe the corresponding phase volume at the boundary in any experimental realization.

This work was carried out with the support of the Russian Fund for Fundamental Research (Grant No. 97-02-16241) and INTAS (Grant No. 93-3430-Ext).

[1] N. H. March, W. H. Young, and S. Sampanthar, *The Many-Body Problem in Quantum Mechanics* (Cambridge University Press, Cambridge, 1967; Mir, Moscow, 1969).

[2] S. R. de Groot and L. G. Suttorp, *Foundations of Electrodynamics* (North-Holland, Amsterdam, 1972; Nauka, Moscow, 1982).

[3] A. A. Vedenov and A. I. Larkin, Zh. Éksp. Teor. Fiz. **36**, 1133 (1959) [Sov. Phys. JETP **9**, 806 (1959)].

[4] L. D. Landau and E. M. Lifshitz, *Statistical Physics*, 2nd ed. (Pergamon Press, Oxford, 1969; Nauka, Moscow, 1964).

[5] R. Z. Sagdeev, D. A. Usikov, and G. M. Zaslavsky, *Nonlinear Physics: From the Pendulum to Turbulence and Chaos* (Harwood, Chur, 1988; Nauka, Moscow, 1988).

Translated by Paul F. Schippnick

The magnetoplasma effect in single crystals of antimony at $T \geqslant 80$ K

A. A. Zaĭtsev

Elets State Pedagogical Institute, 399740 Elets, Lipetskaya Oblast', Russia

K. G. Ivanov

St. Petersburg State University of Technology and Design, 191186 St. Petersburg, Russia

V. M. Grabov

Russian State Pedagogical University, 191186 St. Petersburg, Russia
(Submitted February 5, 1998; accepted for publication May 14, 1998)
Fiz. Tekh. Poluprovodn. **32** 1318–1319 (November 1998)

Transmission spectra of infrared laser radiation ($\lambda = 10.6$ μm) passed through samples consisting of two symmetric halves of an antimony single crystal separated by a small gap are investigated in pulsed magnetic fields $B \leqslant 20$ T at temperatures $T \geqslant 80$ K. The magnetoplasma effect was observed for the magnetic induction $B \approx 15$ T, with change in the transmission close to 100%. The magnetoplasma relaxation time has been determined. The possibility of using such objects as IR optical valves with response time not worse than 10^{-4} s is demonstrated.
© *1998 American Institute of Physics.* [S1063-7826(98)00611-5]

A study of the transmission of infrared laser radiation ($\lambda = 10.6$ μm) by a symmetric streak line (SSL) consisting of two symmetric halves of an antimony single crystal separated by a gap on the order of the radiation wavelength has been carried out. The measurements were performed in pulsed magnetic field with induction as high as 25 T, in the temperature interval 80 − 140 K. The experimental technique is described in Ref. 1.

The abrupt growth of the transmission coefficient of the SSL as a function of the magnetic field is interpreted as the magnetoplasma effect corresponding to the edge of the magnetoplasma reflection of antimony crystals.[2,3] The field position of the edge and the shape of the spectrum agree with the results of Refs. 2 and 3 on magnetoplasma reflection obtained at liquid-helium temperature.

Figure 1 plots the experimental dependence of the transmitted signal as a function of the magnetic induction along the binary axis (curve *1*) and bisectrix (curve *2*) for polarization $E \perp C_3$ (C_3 is the trigonal axis). The abrupt growth of the signal in fields on the order of 15 T is the magnetoplasma effect.

The complex dielectric constant, which governs the interaction of the radiation with the charge-carrier plasma in a magnetic field, has the form

$$\varepsilon_{\pm} = \varepsilon_{\infty}\left[1 - \frac{\omega_p^2}{\omega(\omega \pm \omega_c - i\tau^{-1})}\right]$$

$$\omega_p = \sqrt{Ne^2/(m^* \varepsilon_{\infty})} \tag{1}$$

under the conditions $S \| B$, $E \perp B$ (S is the wave vector) in the case of isotropic effective mass. The $\pm$ sign corresponds respectively to left and right circular polarization of the radiation, ω is the frequency of the radiation, ε_{∞} is the dielectric constant at frequencies $\omega \gg \omega_p$, $\omega_c = (eB/m^*)$ is the cyclotron frequency, N, m^*, and τ are the concentration, the effective mass, and the relaxation time of the charge carriers, and ω_p is the plasma frequency.

Taking into account the electron and hole contributions in antimony in its semimetallic state in the additive approximation allows one to reduce expression (1) to the form

$$\varepsilon_{\pm} = \varepsilon_{\infty}\left[1 - \sum_j \frac{\omega_{pj}^2}{\omega(\omega \pm \omega_{cj} - i\tau_j^{-1})}\right]. \tag{2}$$

The sum in expression (2) must be carried out over three electron and six hole ellipsoids, with allowance for isotropy and localization in the Brillouin zone.[4] In the calculations we used the data $N_c = N_h = 5.54 \times 10^{19}$ cm^{-3} (Ref. 5) and $\varepsilon_{\infty} = 85$ (Ref. 6).

Figure 2 plots the experimental (curve *1*) and model (curve *2*) SSL transmission spectrum in the geometry $B \| C_1$, $E \perp C_3$ at $T = 80$ K. Agreement between the model and ex-

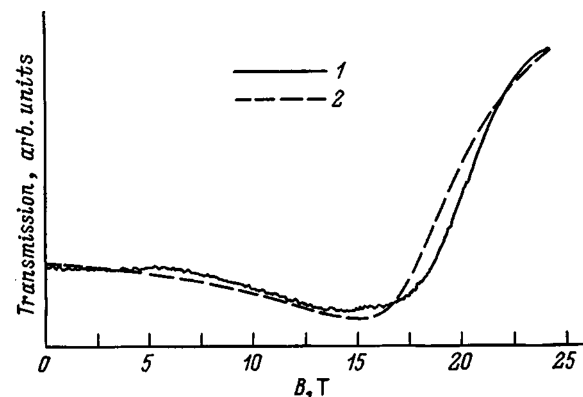

FIG. 1. Dependence of the signal passing through a symmetric streak line of antimony for $E \perp C_3$ and $B \| C_1$ (*1*), $B \| C_2$ (*2*). $T = 80$ K.

 © 1998 American Institute of Physics

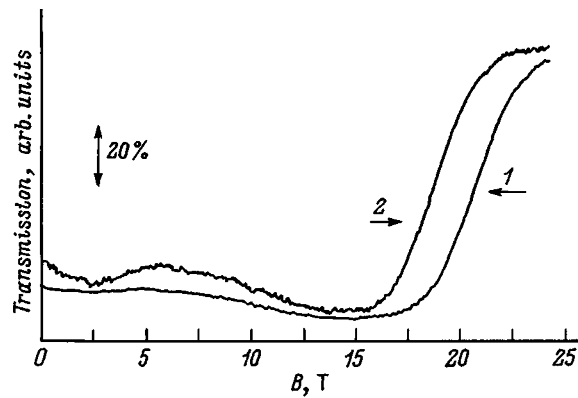

FIG. 2. Experimental (1) and model (2) magnetotransmission spectra of an antimony symmetric streak line for $E \perp C_3$ and $B \| C_1$. $T=80$ K.

perimental spectra over the entire investigated temperature interval was reached for the electron and hole effective masses coinciding with their values at $T=4.2$ K (Ref. 4), which is due to the strong degeneracy of the charge carriers. The best agreement in the shape of the transmission spectra was achieved for $\tau=1.9\times10^{-13}$ s at $T=80$ K (Fig. 2) and for $\tau=1.3\times10^{-13}$ s at $T=140$ K. Agreement between the model magnetoreflection spectrum based on Eq. (2) with the experimental spectrum[2] at $T=4.2$ K is achieved for $\tau=4\times10^{-13}$ s. The values obtained of the magnetoplasma relaxation time in antimony crystals indicates that it has a temperature dependence similar to that observed for the plasma reflection relaxation time in bismuth.[7]

The plasma frequency for antimony almost coincides with the fundamental mode of the CO_2 laser, $\lambda=10.6$ μm. As a result, the possibility arises of using an SSL of single-crystal antimony as a magnetic-field tunable optical valve at this wavelength. The modulation depth approaches 100% (Fig. 1), and the response time, determined by the duration of the magnetic field pulse, is estimated as 10^{-4} s.

[1] K. G. Ivanov, S. V. Kondakov, S. V. Brovko, and A. A. Zaĭtsev, Fiz. Tekh. Poluprovodn. **30**, 1585 (1996) [Semiconductors **30**, 831 (1996)].
[2] M. S. Dresselhaus and J. G. Mavroides, Solid State Commun. **2**, 297 (1964).
[3] M. J. Apps, J. Phys. F: Metal Phys. **4**, 46 (1974).
[4] W. R. Datars and J. Venderkooy, IBM J. Res. Dev. **8**, 247 (1964).
[5] Z. Altounian and W. R. Datars, Can. J. Phys. **53**, 459 (1975).
[6] C. Manney, Phys. Rev. **129**, 109 (1963).
[7] M. I. Belovolov, A. D. Belaya, V. S. Vavilov, V. D. Egorov, V. S. Zemskov, and S. A. Roslov, Fiz. Tekh. Poluprovodn. **10**, 1382 (1976) [Sov. Phys. Semicond. **10**, 819 (1976)].

Translated by Paul F. Schippnick

Influence of crystal orientation of the growth surface due to molecular beam epitaxy on the optical properties of Si-doped GaAs layers

V. G. Mokerov, G. B. Galiev, Yu. V. Slepnev, and Yu. V. Khabarov

Institute of Radio Engineering and Electronics, Russian Academy of Sciences, 103907 Moscow, Russia
(Submitted December 1, 1997; accepted for publication May 20, 1998)
Fiz. Tekh. Poluprovodn. **32**, 1320–1324 (November 1998)

Photoluminescence (PL) spectra of GaAs (100), (111)A and (111)B layers grown by molecular-beam epitaxy at different ratios of the partial pressures $P_{As_4}/P_{Ga}=\gamma$ are investigated. Depending on the crystal orientation and γ values, either two PL bands (B-Si bands) or a single PL B-band are observed. The B-band corresponds to band-to-band radiative recombination $(e\rightarrow h)$ and the Si band is attributed to optical transitions between the conduction band and the Si acceptor states $(e\rightarrow A)$. The observed variations of the PL spectra and of the type and magnitude of the electrical conductivity as functions of the orientation and γ value are interpreted in terms of changes in the Si-acceptor concentration and their energy spectrum as well as a change in the ratio of the concentrations of the Si donor and acceptor states. These results are explained in the framework of the kinetic approach based on the multiplicity (energy) of the dangling chemical bonds on the different surfaces, with the influence of the molecular flux densities taken into account. © *1998 American Institute of Physics.* [S1063-7826(98)00711-X]

1. INTRODUCTION

Studies of silicon doped GaAs layers grown by molecular-beam epitaxy (MBE) on differently oriented growth surfaces have demonstrated the importance of kinetic phenomena in the formation and doping of these layers.[1–4] This is manifested in the extraordinary variety of their electrical and optical properties, depending on the orientation of the growth surface and the conditions of growth, namely, the ratio of the molecular fluxes and the growth temperature (T_g).[1–3] However, the results of various authors on the photoluminescence (PL) spectra and their interpretation are, in our view, too widely divergent.[2] In particular, this pertains to the PL bands arising in silicon-doped GaAs layers at photon energies $h\nu$ somewhat lower than the width of the band gap E_g^0, which are often attributed to stoichiometry defects, but can be connected with the acceptor behavior of a certain fraction of the Si atoms. The latter is of interest in connection with the problem of the amphoteric behavior of silicon as a group-IV element in III–V compounds, for example, in connection with the possibility of the formation of layers of both n and p type, or even $p-n$ junctions by using only a silicon impurity.

The present study investigates the PL spectra and electrical properties of silicon-doped GaAs layers with (100), (111)A, and (111)B orientations grown by MBE at various ratios of the arsenic and gallium partial pressures $P_{As_4}/P_{Ga}=\gamma$. It is shown that the optical properties of these layers at energies somewhat lower (<100 meV) than E_g^0 are conditioned by the Si acceptor states, whose concentration and energy spectrum depend on the orientation of the growth surface and the value of γ. The results are analyzed in the framework of a kinetic approach based on differences in the multiplicity of the dangling bonds at surfaces with different orientation with the value of γ taken into account.

2. EXPERIMENTAL PART

Silicon-doped GaAs layers were grown by MBE on semi-insulating GaAs substrates with orientations (100), (111)A, and (111)B for different ratios γ (from 10 to 77) at a growth temperature $T_g=600\,^\circ$C. The value of γ was varied by varying the As_4 pressure, while the Ga pressure was held constant. Layers of all three orientations were grown side-by-side in each production run. The grown structures included: an undoped buffer layer of GaAs of thickness 0.5 μm, and an upper silicon-doped ''active'' layer of thickness 0.2 μm. The temperature of the silicon source was set such as to provide a conduction electron concentration $n=1\times10^{18}\,\text{cm}^{-3}$ for $\gamma=16-20$ in the GaAs (100) layers. The carrier concentration and type of conductivity were determined by measuring the Hall coefficient and the capacitance–voltage $(C-V)$ characteristics. The PL spectra were measured at $T=77$ K in the photon energy range $h\nu=1.3-1.7$ eV. To excite photoluminescence we used an Ar^+ laser with wavelength $\lambda=514.5$ nm and radiation intensity 20 W/cm^2.

3. RESULTS OF MEASUREMENTS

Figures 1–3 plot the PL spectra of GaAs layers with different orientations. It follows from the figures that the shape of the spectra is different and depends differently on γ for different orientations. We will consider separately the results for small γ, i.e., $\gamma<15-16$, ''normal'' values of γ [implying standard conditions for the (100) layers], and large γ, i.e., $\gamma>16$.

3.1. ''Normal'' and enhanced values of γ: $16<\gamma<77$

GaAs layers grown with orientations (100) and (111)B always have n-type conductivity. We found that the shape of their PL spectra for ''normal'' and enhanced arsenic pres-

 © 1998 American Institute of Physics

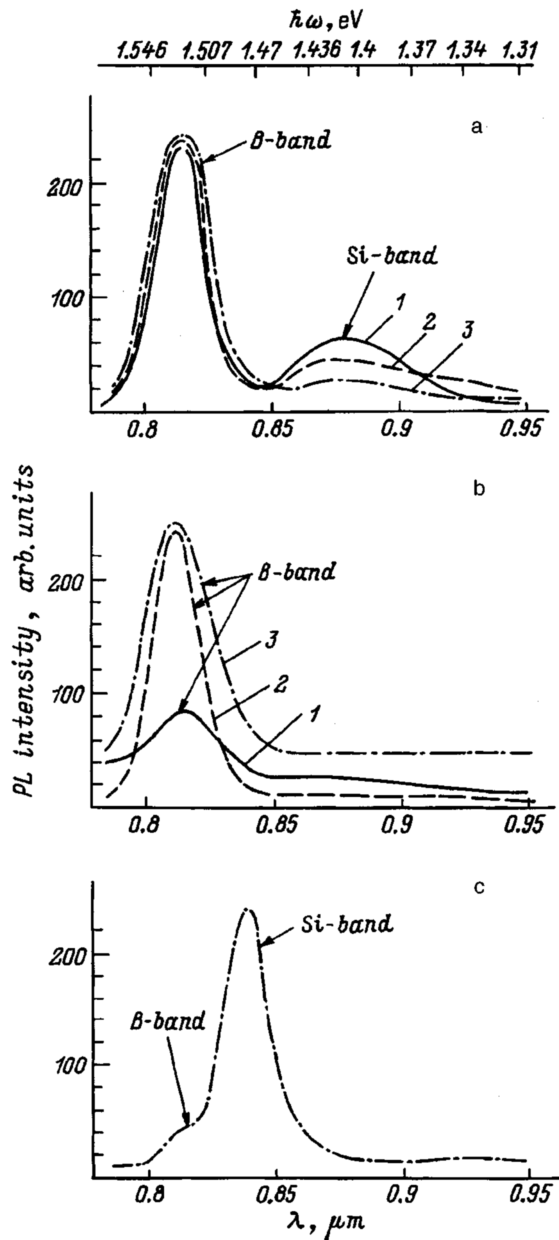

FIG. 1. Photoluminescence spectra at $T=77$ K of GaAs epitaxial layers grown at different flux ratios $As_4/Ga=\gamma$ on substrates with orientations (100) (a), (111)B (b), (111)A (c). γ: *1* — 16, *2* — 36, *3* — 77, *4* — 12.

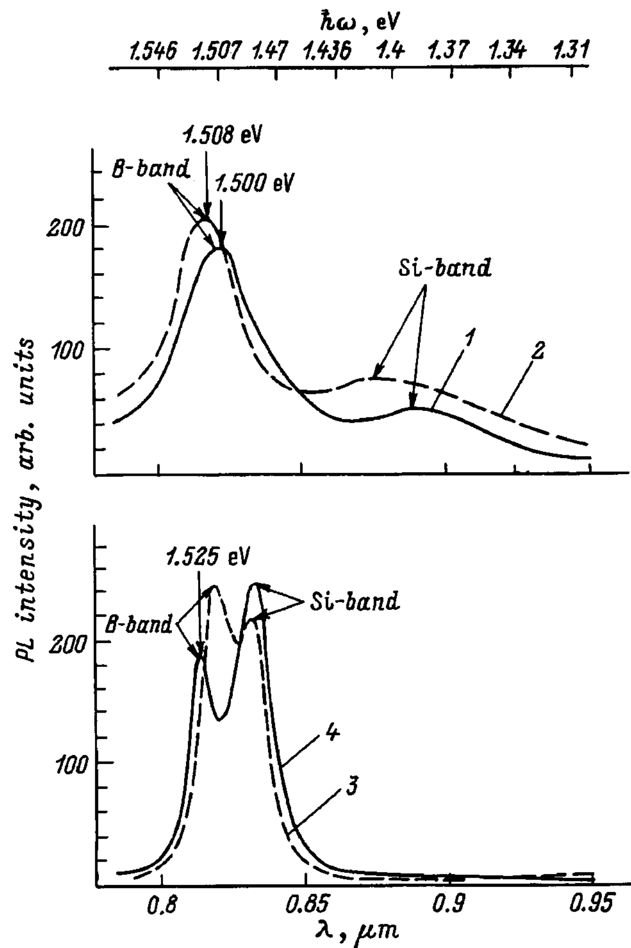

FIG. 2. Photoluminescence spectra at $T=77$ K for GaAs epitaxial layers grown on substrates with (111)A orientation for different γ; curves *1–4* are for $\gamma=16$, 25, 50, 70.

sures remains almost invariant (see Figs. 1a and 1b). In the case of (100) layers two PL bands are observed. One of them, located at higher photon energies $h\nu$ and denoted here as the B band, corresponds to band-to-band radiative recombination ($e\rightarrow h$), and the second, located at lower $h\nu$ and present only in the silicon-doped samples, we denote as the Si band. In accordance with the amphoteric properties of silicon, we attribute the impurity band to the optical transitions between the conduction band and the acceptor level ($e\rightarrow A$) corresponding to the Si atoms at arsenic sites. On the other hand, in the layers with (111)B orientation in this γ range only the B band is present. The parameters and behavior of the B band (as a function of γ) in the samples of both orientations are very similar. The low-energy edge (or "tail") of the B band is always located lower than the width of the band gap E_g^0 in undoped GaAs ($E_g^0=1.508$ eV at $T=77$ K), whereas its peak is shifted in comparison with E_g^0 toward higher photon energies $h\nu$: by 20–22 meV for the (111)B and by 12–16 meV for the (100) orientation.

Such a situation is typical for degenerate n-type GaAs, for which the Fermi level E_F is located above the bottom of the conduction band. This leads to a shift of the band-to-band optical transitions to higher energies (the Burstein–Moss effect).[5] It is also well known that at high concentrations the silicon donor states form an impurity band which overlaps the conduction band. This leads to a decrease in the effective width of the band gap E_g^{eff} and correspondingly to a shift of the low-energy edge of the photoluminescence B band to lower $h\nu$ (Ref. 5).

The presence of the Si band in the (100) layers for $h\nu=1.400-1.405$ eV indicates that the Si atoms at the arsenic sites form an acceptor level located 100 meV above the top of the valence band. Increasing the arsenic pressure results in a small decrease in the intensity of the Si band (see Fig. 1a).

In layers with (111)A orientation according to Refs. 1 and 2, p-type conductivity is observed at small and intermediate values of γ (in our case this means $\gamma<20$). As γ is increased from 20 to 30, the conduction of the (111)A layers drops almost to zero, and for $\gamma>30$ n-type conduction arises,

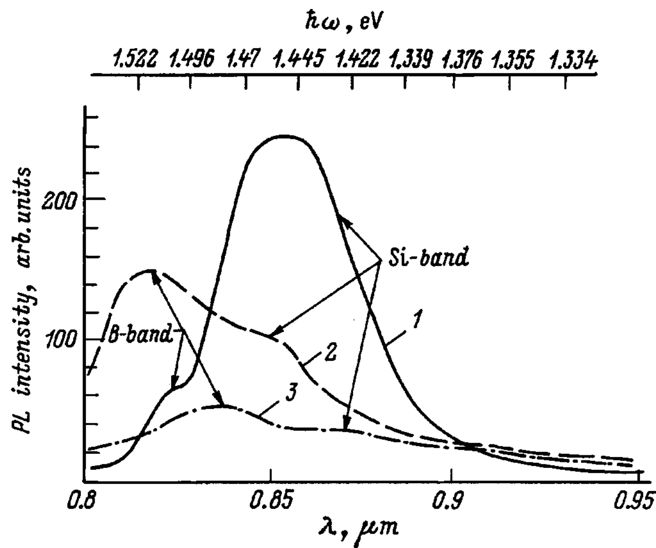

FIG. 3. Photoluminescence spectra at $T=77$ K for GaAs epitaxial layers grown at $\gamma=10$ on substrates with orientations: *1* — (100), *2* — (111)B, *3* — (111)A.

growing with further increase of γ. In the PL spectra of the (111)A layers (see Figs. 1c, 2, and 3) both the B band and the Si band are always present. For $\gamma<20$ the maximum of the B band is located at $h\nu<E_g^0$, thus: $h\nu_B=1.500$ eV for $\gamma=16$. Such a situation is typical for p-GaAs with a high acceptor concentration,[6] where the latter form an impurity band overlapping the valence band. As a result, the effective width of the band gap E_g^{eff} is lowered and correspondingly the band-to-band optical transitions are shifted to lower energies. In p-type samples this effect predominates over the Burstein–Moss effect (which is proportional to the Fermi energy $E_F\sim h^2p/2m_h$) by virtue of the smallness of the latter since the effective hole mass m_h in GaAs is almost an order of magnitude greater than the effective electron mass m_e. As γ is increased, the maximum of the B band shifts toward higher energies such that for $\gamma\simeq 25$ it is located near 1.508 eV (i.e., for $h\nu\simeq E_g^0$), and for $\gamma=70$ it is located at 1.525 eV. This shift is associated with a smooth transition from p-type conductivity to n-type conductivity and subsequent growth of the occupancy of the conduction band by electrons.

It also follows from Figs. 1 and 2 that the spectral position and shape of the Si band in the (111)A layers varies substantially as γ is varied. Thus, for $\gamma<20$ the Si band is very wide, its half-width is around 150 meV, and its maximum is located near 1.42 eV. These parameters do not vary greatly in the region of transitional γ values, i.e., in the range from 20 to 30. However, the situation changes radically for $\gamma>30-40$, where n-type conductivity arises and grows. Here an abrupt narrowing of the Si band is observed, its shape acquires the form of a sharp, intense resonance, and the peak shifts toward larger $h\nu$, resulting in a spectral convergence of the B and Si bands. For $\gamma=70$ the half-width of the Si band no longer exceeds 30 meV (i.e., it becomes five times narrower than for $\gamma<20$) with its peak at 1.48 eV. The peak intensity becomes greater than for the B band. These results demonstrate that the concentration of silicon acceptor states is highest in the (111)A layers (in comparison with the other orientations). For $\gamma<20$ it obviously exceeds the concentration of silicon donors, and, as has already been mentioned, the silicon acceptors form an impurity band that merges with the valence band. This is the reason for the p-type conductivity and the observed shape of the PL spectrum. Further, it follows from the PL spectra (the spectra position of the maximum of the B band) that in the range of γ values from 20 to 30 the silicon acceptor and donor concentrations equalize, but for $\gamma>30-40$ the concentration of the latter becomes larger. As for the Si band, the above-described transformation of its shape as γ increases to 40–50 and higher can be explained by the fact that with decrease of the concentration of the silicon acceptors, corresponding to an increase of the mean distance between them, the acceptor band narrows and separates from the valence band and then, as a result of a Mott transition,[7] is transformed into a narrow local level. As follows from the PL spectra, this level is located roughly 28 meV above the top of the valence band.

3.2. Small values of γ ($10<\gamma<15$)

As γ is decreased in this range for layers with (111)A orientation, a further increase in the p-type conductivity occurs. The Si band becomes still wider, and the maximum of the B band is shifted toward still smaller $h\nu$ (Fig. 3).

In the case of the (111)B and (100) orientations n-type conduction is preserved, but its magnitude falls as γ is decreased. It is important to note that in the PL spectra of (111)B layers, for $\gamma<14$ a PL band analogous to the Si band arises in the (100) and (111)A samples. In this case, in the (100) layers the intensity of the Si band becomes so great that it dominates over the B band. For all of the layers, as γ is decreased in this range, there takes place a noticeable shift of the maximum of the B band toward lower $h\nu$ (see Fig. 3).

The above results are interpreted on the basis of the substantial growth of the silicon acceptor concentration and corresponding decrease of the silicon donor concentration with decrease of γ.

4. DISCUSSION

Let us analyze the above results on the basis of the difference in energy of the dangling bonds on GaAs surfaces with different orientations,[1–3] with allowance for the influence of the corresponding molecular (or atomic) flux densities, and competition of Si adatoms with As and Ga adatoms for incorporation into surface sites.

The probability $R_{ij}^{A_i}$ of incorporation of an A_i adatom from the molecular (atomic) flux Φ_{A_i} into a j-type site on the growth surface during MBE can be represented as

$$R_{ij}^{A_i}\sim W_{ij}\cdot\rho_j(W_{kj},\Phi_{A_k})\Phi_{A_i}. \quad (1)$$

Here W_{ij} is the probability for the formation of a chemical bond between the A_i adatom (in our case a silicon atom) and the substrate at a j-type site on its surface, where this probability depends on the energy (multiplicity) of the corresponding dangling bond; Φ_{A_i} is the density of the flux containing the A_i atoms; $\rho_j(W_{kj},\Phi_{A_k})$ is the density of va-

cant j-type surface sites for A_i adatoms, which depends on the occupancy of these sites by competing A_k adatoms. In our case these are As atoms for the arsenic sites and Ga atoms for the gallium sites. Accordingly, $\rho_j(W_{kj}, \Phi_{A_k})$ depends on whether an A_k adatom already formed a chemical bond with the substrate surface at a j-type site. Therefore, ρ_j also depends on the density of the flux Φ_{A_k} that contains the A_k atoms.

Let us begin the discussion with the (100) orientation. In this case the dangling double bonds appear on the surface both for the Ga adatoms and the As adatoms. Formation of double bonds ensures not only the incorporation into the lattice of Ga adatoms, but also the effective dissociation of As molecules and subsequent incorporation into the lattice of As adatoms.[2] The presence of n-type conductivity in silicon-doped GaAs(100) layers is a direct indication that a large fraction of the Si atoms occupy gallium sites and are shallow donors. However, the presence of a saturation effect and subsequent lowering of the electron concentration with increase of the doping level N_{Si} above $(4-6)\times 10^{18}\,\mathrm{cm}^{-3}$ indicates that for large N_{Si} the fraction of silicon acceptors grows. However, it is still unclear from the literature, in our opinion, what the story is regarding the parameters of the silicon acceptor states; for example, it is not clear whether they are the same for different orientations or not. We have shown (see Fig. 1a) that in (100) layers Si acceptors also show up at moderate concentrations ($N_{Si}<10^{17}\,\mathrm{cm}^{-3}$), but, as follows from Fig. 1a, their number falls as the arsenic flux Φ_{As_4} is increased. This circumstance, according to Eq. (1), can be explained by the decrease in the density of arsenic sites for Si adatoms due to a growth in their occupancy by As atoms. The data presented demonstrate that on a (100) surface a Si = As bond is somewhat more favored than a Si = Ga bond, although their energies probably do not differ by all that much, as is indicated by the tendency toward equalization of the silicon donor and acceptor concentrations with increase of the flux Φ_{Si} (Ref. 5).

In the case of the (111)B orientation on the GaAs surface dangling triple bonds appear on the surface for the As adatoms and dangling single bonds for the Ga adatoms.[3] The presence of triple bonds ensures the largest energy and the most favorable conditions for dissociation of the As_4 molecules and subsequent incorporation of the As adatoms into the surface sites. In this regard, Si adatoms can here turn out to be the least competitive in comparison with As adatoms in the filling of arsenic sites, and the probability for the formation of silicon acceptor states should be the lowest. This is consistent with the absence of a Si band (for $\gamma>16$) and with the highest values of $h\nu$ for the maximum of the B band in the (111)B layers, and also with the presence of n-type conductivity for all γ.

The arguments presented above in favor of the highest concentrations of silicon acceptors in GaAs (111)A layers are also naturally substantiated on the basis of a consideration of the surface bonds. Indeed, the presence for this orientation of only single dangling bonds for the As adatoms diminishes, in comparison with other orientations, the efficiency of dissociation of As_4 molecules and makes the Si adatoms more competitive in comparison with the As adatoms in populating the arsenic sites.

For small $\gamma<15$, by virtue of the lowering of the arsenic flux density Φ_{As_4}, the density of vacant arsenic sites ρ_{As} should increase for all orientations as should also the probability of their being filled by silicon adatoms. At low arsenic pressures the formation of arsenic vacancies is also possible, i.e., arsenic sites not occupied by Si atoms or As atoms. Such conditions can give rise to the formation of complexes of Si atoms at arsenic sites with arsenic vacancies, which will alter the shape and spectral position of the Si band. All this makes it possible to explain the effects observed at small γ: the growth of p-type conductivity in the (111)A layers and the decrease of n-type conductivity in the (100) and (111)B layers, the low-energy shifts of the B band for all orientations, the increase in the intensity of the Si band in the (100) and (111)A layers, the appearance of the Si band in the (111)B layers, and the modification of the shape and spectral position of the Si band in all the layers.

It should also be noted that according to the above results, the silicon acceptor states formed on surfaces of different orientations during MBE are not identical. Thus, for example, for $\gamma=70$ the silicon acceptor level in layers with (100) orientation is deeper ($E_a\simeq 100$ meV) than in layers with (111)A orientation, where it is located roughly 28 meV above the top of the valence band.

[1] W. I. Wang, E. E. Mendez, T. S. Kuan, and L. Esaki, Appl. Phys. Lett. **47**, 826 (1985).
[2] F. Piazza, L. Pavesi, M. Henin, and D. Johnston, Semicond. Sci. Technol. **7**, 1504 (1992).
[3] A. Chin, P. Martin, P. Ho, J. Ballingall, T. Yu, and J. Mazurowski, Appl. Phys. Lett. **59**, 1899 (1991).
[4] Y. Okano, H. Seto, H. Katahama, S. Nishine, I. Fujimoto, and T. Suzuki, Jpn. J. Appl. Phys. **28**, L151 (1989).
[5] G. Borghs, K. Bhattacharyya, K. Deneffe, P. Van Mieghem, and R. Mertens, J. Appl. Phys. **66**, 4381 (1989).
[6] J. Maguire, R. Murray, R. C. Newman, R. B. Beall, and J. J. Harris, Appl. Phys. Lett. **50**, 516 (1987).
[7] N. F. Mott, Adv. Phys. **16**, 49 (1967).

Translated by Paul F. Schippnick

Effect of electron-phonon energy exchange on thermal wave propagation in semiconductors

Yu. G. Gurevich and G. González de la Cruz

Instituto Politecnico Nacional, Apartado Postal 14-740, 0700 Mexico, Distrito Federal, Mexico

G. N. Logvinov and M. N. Kasyanchuk

Ternopol State Pedagogical University, 282009 Ternopol, Ukraine
(Submitted December 30, 1997; accepted for publication February 25, 1998)
Fiz. Tekh. Poluprovodn. **32**, 1325–1330 (November 1998)

Nonequilibrium, periodic (in both space and time) temperature distributions in the electron and phonon subsystems of a geometrically bounded semiconductor (thermal waves) are calculated self-consistently with the electron–phonon interaction taken into account. Modulated laser radiation, which is converted into heat on the surface of the sample, serves as the external source of energetic nonequilibrium. The dependence of the amplitude and phase of the electron and phonon temperatures on the modulation frequency is analyzed for different sample thicknesses and a number of characteristic parameters of the problem. It is shown that by varying the modulation frequency over a wide range (up to frequencies of the electron–phonon energy exchange) it is possible to generate thermal waves in the electron and phonon subsystems separately. © *1998 American Institute of Physics.*
[S1063-7826(98)00811-4]

1. INTRODUCTION

The physics of thermal waves is continuing to develop vigorously because of the successful development of its applications and, more importantly, because of the development of photothermal methods of studying various materials, in particular, semiconductors.[1–3] The constantly growing interest in these methods is due to their relative simplicity and their universality, which allows one to study the most diverse characteristics of matter—thermal, optical, mechanical, relaxational, etc.

All photothermal methods are based on the detection by one means or another of a transient temperature characterizing the thermal waves that arise in the sample as a result of absorption of the energy of a periodically modulated electromagnetic radiation (as a rule, laser radiation), which is converted into heat in the bulk and on the surface of the sample. The corresponding experimentally measured response (acoustic, piezoelectric, etc.) enables one to obtain information about the heat sources generating the thermal waves and about characteristics of the medium in which they propagate (thermal parameters, structural formations, inhomogeneities, etc.).

Theoretical studies of photothermal processes in semiconductors are similar in their goals: to find the transient temperature distributions and responses to them, and to decide on how best to model the thermal sources. Thus, for example, in Ref. 4 it was assumed that liberation of heat takes place instantly and at the same point of the sample where the light is absorbed. A series of studies[5–7] considers intrinsic absorption of light in a bipolar semiconductor with allowance for the formation of nonequilibrium electrons and holes, and for their diffusion and recombination.

In the present work we focus our attention on the role of energy exchange in the electron–phonon interaction in periodic heat transfer processes. It is well known that at temperatures above 1 K scattering of electrons by acoustic phonons is of a quasi-elastic character. Regarding radiative phenomena this means that there is a characteristic diffusion length l_ε (the cooling length), at which the excited electrons and phonons equalize their energy.[8] In steady-state thermal processes in monopolar semiconductors this leads to the appearance of two nonequilibrium temperatures—the electron temperature $T_e(x)$ and the phonon temperature $T_p(x)$ (Ref. 8), where x is the spatial coordinate. In bulk semiconductors ($a \gg l_\varepsilon$, where a is the length of the sample) this difference is manifested at distances of the order of l_ε from the surfaces, which are the source of energetic nonequilibrium; in submicron films, in which usually $a \leqslant l_\varepsilon$, mismatch of these temperatures occurs over the entire bulk of the sample.[9] It is completely obvious that photothermal processes in semiconductors must, in general, be considered from the viewpoint of the presence of two thermal-wave processes—an electron thermal-wave process and a phonon thermal-wave process, each of which is characterized by its own temperature distribution: $T_e(x,t)$ and $T_p(x,t)$, where t is the time. These temperatures are established self-consistently in accordance with the nature of the electron–phonon heat transfer (internal heat source) and the thermal boundary conditions (BC) (surface heat sources). This question was first discussed for semi-infinite samples in Ref. 10. To find the temperature distributions and analyze them in geometrically bounded semiconductor media is the aim of the present work.

 © 1998 American Institute of Physics

2. ELECTRON AND PHONON THERMAL WAVES

For simplicity, we consider an isotropic, monopolar semiconductor and we assume that it has the shape of a parallelepiped, one of whose sides ($x=0$) is illuminated by modulated high-frequency electromagnetic radiation with frequency ω. The surface $x=a$ is kept at the constant temperature T_0, and the lateral faces are adiabatically insulated. In general, the absorption of light in a semiconductor is an extraordinarily complex process, which is accompanied by the generation of electron and hole excitations, heating of the charge-carrier gas with subsequent energy relaxation to the crystalline lattice, recombination and thermal-diffusion processes, etc. With the aim of simplifying the problem, we restrict it to just surface absorption. Such a model can be realized, in particular, if we cover the face $x=0$ with a good radiation-absorbing film, e.g., a metallic film. In this case the semiconductor acquires energy from outside in the form of heat. In addition, we assume that all of the conditions necessary for a correct determination of the nonequilibrium electron and phonon temperatures are met (see Ref. 8).

If the electron–phonon coupling is taken into account, the unknown electron and phonon temperatures can be determined self-consistently from the following system of equations of energy balance:[10]

$$\begin{cases} \dfrac{\partial^2 T_e(x,t)}{\partial x^2} - k_e^2[T_e(x,t)-T_p(x,t)] = \dfrac{1}{\alpha_e}\dfrac{\partial T_e(x,t)}{\partial t}, \\ \dfrac{\partial^2 T_p(x,t)}{\partial x^2} - k_p^2[T_e(x,t)-T_p(x,t)] = \dfrac{1}{\alpha_p}\dfrac{\partial T_p(x,t)}{\partial t}. \end{cases} \tag{1}$$

Here $k_{e,p}^2 = P/\chi_{e,p}$; $P=k_B n \nu_\varepsilon^0$ (Ref. 8) is a coefficient defining the intensity of electron–phonon energy exchange, n is the electron concentration, ν_ε^0 is the energy relaxation frequency of the electron–phonon interaction; k_B is the Boltzmann constant; $\alpha_{e,p}=\chi_{e,p}/(\rho c)_{e,p}$ are the electron and phonon thermal diffusivities; $\chi_{e,p}$, $\rho_{e,p}$, and $c_{e,p}$ are the thermal conductivity, density, and specific heat of the electron and phonon gases, respectively. In all of the calculations we ignore the temperature dependence of all the coefficients, assuming that the intensity of the absorbed radiation is small enough for that purpose. As a result, system of equations (1) is linear.

To assign the boundary conditions at the surface $x=0$ we note that the carrier frequency of the incident radiation is *a priori* much greater than all the characteristic energy frequencies (the largest of these, ν_ε^0, in semiconductors amounts to 10^8-10^{10} s^{-1}, for example, a He–Ne laser used in the experimental study (Ref. 11), lasing at 633 nm), so that neither the electron temperature nor the phonon temperature can track this rapidly varying perturbation. By self-averaging, it forms the static part of the thermal flux in the sample while the dynamic part, which is time-dependent, is entirely determined by the modulated component of the incident radiation.

In addition, it is necessary to bear in mind the fact that the electron and phonon surface thermal conductivities of the semiconductor, which govern heat transfer to the external medium, are different. The boundary conditions for each of these subsystems of quasiparticles should therefore be assigned separately.[8]

It follows from what has been said so far that the boundary conditions on Eqs. (1) can be represented by the system of equations

$$\begin{cases} Q_{e,p}(x,t)|_{x=0} = Q_{e,p}^0 + \Delta Q_{e,p}\, e^{i\omega t}, \\ T_{e,p}(x,t)|_{x=a} = T_0. \end{cases} \tag{2}$$

In Eqs. (2) $Q_{e,p}$ are the electron and phonon heat flux densities, and $Q_{e,p}^0$ and $\Delta Q_{e,p}\, e^{i\omega t}$ are their static and dynamic components. In the theory we are about to develop here, they enter as phenomenological, independent parameters.

Without dwelling on the formalities of the solution of system of equations (1), we write out the final form of the desired dependences:

$$T_e(x,t) = T_0 + A(a-x) + \frac{k_e^2}{k^2} B \frac{\sinh k(a-x)}{\cosh ka} + e^{i\omega t}\left(C_1 \frac{\sinh \sigma_1 (a-x)}{\cosh \sigma_1 a} + C_2 \frac{\sinh \sigma_2 (a-x)}{\cosh \sigma_2 a} \right); \tag{3}$$

$$T_p(x,t) = T_0 + A(a-x) + \frac{k_p^2}{k^2} B \frac{\sinh k(a-x)}{\cosh ka} + e^{i\omega t}\left(D_1 \frac{\sinh \sigma_1 (a-x)}{\cosh \sigma_1 a} + D_2 \frac{\sinh \sigma_2 (a-x)}{\cosh \sigma_2 a} \right). \tag{4}$$

Here

$$A = \frac{Q_e + Q_p}{\chi_e + \chi_p}; \quad B = \frac{1}{4}\left(\frac{Q_e}{\chi_e} - \frac{Q_p}{\chi_p} \right);$$

$$C_1 = \frac{1}{\sigma_1(\sigma_2^2 - \sigma_1^2)} \left[\frac{\Delta Q_p}{\chi_p} k_e^2 + \frac{\Delta Q_e}{\chi_e} (\sigma_2^2 - \sigma_e^2) \right];$$

$$C_2 = \frac{1}{\sigma_2(\sigma_2^2 - \sigma_1^2)} \left[\frac{\Delta Q_p}{\chi_p} k_e^2 + \frac{\Delta Q_e}{\chi_e} (\sigma_1^2 - \sigma_e^2) \right];$$

$$D_{1,2} = -\frac{\sigma_{1,2}^2 - \sigma_e^2}{k_e^2} C_{1,2}; \quad k_{e,p}^2 = P/\chi_{e,p}; \quad k^2 = k_e^2 + k_p^2;$$

$$\sigma_{1,2}^2 = \frac{1}{2}(\sigma_e^2 + \sigma_p^2) \pm \frac{1}{2}[(\sigma_e^2 - \sigma_p^2)^2 + 4k_e^2 k_p^2]^{1/2};$$

$$\sigma_{e,p}^2 = k_{e,p}^2 + \frac{i\omega}{\alpha_{e,p}}.$$

It follows from expressions (3) and (4) that the finite energy exchange between the electron and phonon subsystems has a substantial influence on the nature of the

thermal-wave distribution. Indeed, in the case of an infinitesimally weak interaction[1)] ($P\to 0$) there are two independent temperature profiles in the sample:

$$T_{e,p}(x,t)=T_0+\frac{Q^0_{e,p}}{\chi_{e,p}}(a-x)+\frac{\Delta Q_{e,p}}{\sigma_{e,p}\chi_{e,p}}\frac{\sinh\sigma_{e,p}(a-x)}{\cosh\sigma_{e,p}a}e^{i\omega t}, \quad (5)$$

where $\sigma^2_{e,p}=i\omega/\alpha_{e,p}$.

In the other limiting case – an unbounded strong electron-phonon interaction ($P\to\infty$) – both temperature distributions collapse into one:

$$T_e(x,t)=T_p(x,t)=T_0+\frac{Q^0_e+Q^0_p}{\chi_e+\chi_p}(a-x)+\frac{\Delta Q_e+Q_p}{(\chi_e+\chi_p)\sigma}\frac{\sinh\sigma(a-x)}{\cosh\sigma a}e^{i\omega t}, \quad (6)$$

where

$$\sigma^2=\frac{i\omega}{\chi_e+\chi_p}\left(\frac{\chi_p}{\alpha_p}+\frac{\chi_e}{\alpha_e}\right).$$

Comparing expressions (3) and (4) with expressions (5) and (6), we see that allowance for the finite electron–phonon energy exchange leads to a doubling of the number of thermal waves in each of the quasiparticle subsystems. This is because in the given case mutually interrelated periodic inflows and outflows of heat from the one subsystem to the other and vice versa arise in the semiconductor, i.e., each of these two subsystems is an internal periodic heat source relative to the other.

3. ELECTRON AND PHONON THERMAL WAVES FOR $\chi_p\gg\chi_e$

To further simplify the problem, let us consider semiconductors in which the phonon thermal conductivity greatly exceeds the electron thermal conductivity ($\chi_p\gg\chi_e$). Such a relationship between thermal conductivities is characteristic of many nondegenerate semiconductors.[12] In this case, expressions (3) and (4) simplify substantially and take on the following form:

$$T_{e,p}(x,t)=T^s_{e,p}(x)+T^d_{e,p}(x,t),$$

where

$$T^s_{e,p}(x)=T_0+\frac{Q_e+Q_p}{\chi_p}(a-x)+\frac{\beta_{e,p}}{k_e}\left(\frac{Q_e}{\chi_e}-\frac{Q_p}{\chi_p}\right)\times\frac{\sinh k_e(a-x)}{\cosh k_e a}$$

are the electron and phonon static parts of the temperature profiles, $\beta_e=1$, $\beta_p=(k_p/k_e)^2$;

$$T^d_e(x,t)=e^{i\omega t}\left[F_1\frac{\sinh\sigma_1(a-x)}{\cosh\sigma_1 a}+F_2\frac{\sinh\sigma_2(a-x)}{\cosh\sigma_2 a}\right] \quad (7)$$

is the dynamic component of the electron temperature;

$$T^d_p(x,t)=e^{i\omega t}G\frac{\sinh\sigma_2(a-x)}{\cosh\sigma_2 a} \quad (8)$$

is the dynamic component of the phonon temperature. Here $\sigma^2_1=\sigma^2_e=k^2_e+i\omega/\alpha_e$; $\sigma^2_2=i\omega/\alpha_p$;

$$F_1=\frac{1}{\sigma_e}\left(\frac{k^2_e}{\sigma^2_2-\sigma^2_e}\frac{\Delta Q_p}{\chi_p}+\frac{\Delta Q_e}{\chi_e}\right);$$

$$F_2=-\frac{k^2_e}{\sigma_2(\sigma^2_2-\sigma^2_e)}\frac{\Delta Q_p}{\chi_p};$$

$$G=\frac{1}{\sigma_2}\frac{\Delta Q_p}{\chi_p}.$$

It is important to note that now four thermal waves are propagating in the electron subsystem, and two in the phonon subsystem. The reason for this is that for $\chi_p\gg\chi_e$ the energy in the ''phonon thermal waveguide'' varies only slightly due to the inflow of heat from the electron subsystem. On the other hand, the electron gas is subjected to an intense periodic thermal perturbation coming from the phonon gas. In other words, the electron gas is heated by surface and volume heat sources, while the phonon gas is heated only by surface sources. As a result, the dynamic part of the electron temperature depends on the parameters of the electron and phonon subsystems; the dynamic part of the phonon temperature depends only on the characteristic features of the phonon gas.

We define the thermal wavelengths $\lambda_{1,2}$ and attenuation lengths $L_{1,2}$ by the following obvious formal relations:

$$\lambda_1=2\pi/\mathrm{Im}\ \sigma_1=2\sqrt{2}\pi l_\varepsilon\left(\sqrt{1+(\omega\tau_\varepsilon)^2}-1\right)^{-1/2};$$
$$\lambda_2=2\pi/\mathrm{Im}\ \sigma_2=2\pi a(\omega\tau_r)^{-1/2}; \quad (9)$$
$$L_1=1/\mathrm{Re}\ \sigma_1=\sqrt{2}l_\varepsilon\left(\sqrt{1+(\omega\tau_\varepsilon)^2}+1\right)^{-1/2};$$
$$L_2=1/\mathrm{Re}\ \sigma_2=a(\omega\tau_r)^{-1/2}.$$

Here $l_\varepsilon=k_e^{-1}$ is the electron cooling length[8]; $\tau_r=a^2/2\alpha_p$ is the relaxation time of heat conduction in the phonon subsystem; and $\tau_\varepsilon=1/\alpha_e k^2_e$.

It is noteworthy first that the thermal wavelengths are shorter than the attenuation lengths, and second, that they are defined, respectively, in terms of the imaginary and real parts of the wave numbers $\sigma_{1,2}$. In real wave processes (e.g., in the propagation of electromagnetic waves) everything is just the opposite. This is explained by the fact that in actual fact expressions (3) and (4) are not wavelike. They were obtained not from a wave equation, but from a diffusion equation. Relations (3) and (4) acquired their outer resemblance to wave motion because of the specific boundary conditions (2). From the physical point of view, the process under consideration must be treated as periodic (in space and time) heat transfer in the electron and phonon subsystems.

It is easy to show that $\tau_\varepsilon=(3/2)\tau^0_\varepsilon$, where $\tau^0_\varepsilon=1/\nu^0_\varepsilon$ is the energy relaxation time of the electron–phonon interaction.

Thus, the characteristic frequencies of a semiconductor for propagation of thermal waves are the frequencies

$\nu_r=\tau_r^{-1}$ and $\nu_\varepsilon=\tau_\varepsilon^{-1}$, whose ratio is equal to $\nu_r/\nu_\varepsilon=2\alpha_p l_\varepsilon^2/\alpha_e a^2$. Given the dimensions of the sample and the cooling length, it depends on the ratio of the thermal diffusivities and, conversely, given α_e and α_p, it is determined by the ratio of the indicated characteristic lengths. Numerical estimates give, for example, for GaAs at $T=300$ K: $\nu_\varepsilon\simeq 1.5\times 10^7\ \mathrm{s}^{-1}$, $l_\varepsilon\simeq 22\times 10^{-4}$ cm (Ref. 13), $\alpha_e\simeq 70$ cm^2/s, $\alpha_p\simeq 0.4$ cm^2/s (in what follows all numerical calculations are for GaAs for the indicated parameters). This means that the frequencies ν_r and ν_ε can be commensurate in samples having a length on the order of 2.35×10^{-4} cm, i.e., much less than the cooling length. Therefore, in bulk semiconductors it is always the case that $\nu_\varepsilon \gg \nu_r$, and in submicron samples cases are possible for which $\nu_\varepsilon\gg\nu_r$ and also $\nu_\varepsilon\ll\nu_r$.

The presence of the three independent parameters ω, τ_ε, and τ_r gives rise to a number of limiting cases, of which the most interesting from the point of view of the problem at hand are the following:

1. $\omega\tau_r\simeq 1$, $a\gg l_\varepsilon$ (*bulk samples*).

The dynamic parts of the temperatures T_e^d and T_p^d, defined by Eqs. (7) and (8), turn out to be equal and are given by the expression

$$T_e^d=T_p^d=\frac{\Delta Q_p}{\chi_p}\frac{a}{\sqrt{2i\omega\tau_r}}\frac{\sinh\sqrt{2i\omega\tau_r}(1-x/a)}{\cosh\sqrt{2i\omega\tau_r}}e^{i\omega t}. \quad (10)$$

Note that temperatures (10) are determined solely by the parameters of the phonon subsystem.

2. $\omega\tau_r\simeq 1$, $\omega\tau_\varepsilon\ll 1$, $a\ll l_\varepsilon$ (*thin samples*).

Here these distributions are different:

$$T_e^d=\frac{\Delta Q_e}{\chi_e}a\left(1-\frac{x}{a}\right)e^{i\omega t}, \quad (11)$$

$$T_p^d=\frac{\Delta Q_p}{\chi_p}\frac{d}{\sqrt{2i\omega\tau_r}}\frac{\sinh\sqrt{2i\omega\tau_r}(1-x/a)}{\cosh\sqrt{2i\omega\tau_r}}e^{i\omega t}. \quad (12)$$

The dynamic part of the phonon temperature is unchanged, while the temperature T_e^d acquires a quasi-steady-state character.

3. $\omega\tau_\varepsilon\simeq 1$.

In this limiting case both in bulk samples and in submicron (for $\omega\tau_r\gg 1$) samples, thermal waves propagate preferably by way of the electron gas and are governed exclusively by its parameters.

For $a\gg l_\varepsilon$ the dynamic part of the temperature is phase-shifted:

$$T_e^d=\frac{\Delta Q_e}{\chi_e}\frac{l_\varepsilon}{\sqrt{1+i\omega\tau_\varepsilon}}e^{ik_e x\sqrt{1+i\omega\tau_\varepsilon}}e^{i\omega\tau}, \quad (13)$$

and for $a\ll l_\varepsilon$ and $\omega\tau_r\gg 1$ it is quasi-steady-state:

$$T_e^d=\frac{\Delta Q_e}{\chi_e}a\left(1-\frac{x}{a}\right)e^{i\omega t}. \quad (14)$$

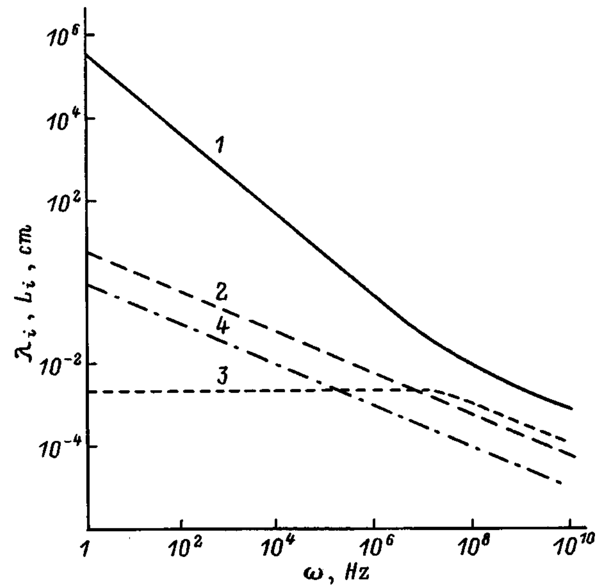

FIG. 1. Frequency dependence of wavelengths and attenuation lengths: *1*— λ_1, *2*—λ_2, *3*—L_1, *4*—L_2.

4. FREQUENCY DEPENDENCE OF THE THERMAL-WAVE PARAMETERS

The frequency dependence of the wavelengths $\lambda_{1,2}$ and the attenuation lengths $L_{1,2}$ is plotted in Fig. 1. It can be clearly seen that for all modulation frequencies $\lambda_1\gg\lambda_2$. The relation between the corresponding attenuation lengths is different for different frequency intervals. In the "low-frequency" interval $[\omega<\omega_1$, where $\omega_1\simeq(2\alpha_p/\alpha_e)\nu_\varepsilon$ is the modulation frequency at which $L_1=L_2$ and $\omega_1\simeq 1.6\times 10^5\mathrm{s}^{-1}]$ $L_2\gg L_1$ and conversely, for $\omega>\omega_1$ $L_2\ll L_1$. It is characteristic that the attenuation length L_1 depends weakly on the frequency up to the highest values of ω. Thus, the recording of various forms of thermal waves over the entire bulk of the sample depends on its length and on the frequency ω. In bulk superconductors, only the low-frequency thermal wave with wavelength λ_2 can propagate. In thin films at low frequencies the wave with wavelength λ_2 dominates; at high frequencies it attenuates rapidly in contrast to the wave with wavelength λ_1, which becomes predominant.

Under experimental conditions the temperature response is recorded, as a rule, on the surface of the sample by direct measurement of the thermal radiation by the gas-microphone method or by using the mirage effect.[7] Figures 2 and 3 plot the phase shifts and corresponding amplitudes of the electron and phonon thermal waves as functions of the modulation frequency ω on the surface $x=0$. It is important to note that these functional dependences are different for different lengths of the sample and (with the exception of the amplitudes $|F_2|$ and G and corresponding phase shifts φ_2 and φ_3) and different values of the parameter

$$K=\frac{\Delta Q_e}{\chi_e}\frac{\chi_p}{\Delta Q_p}.$$

This latter parameter determines the ratio of the magnitudes of the electron and phonon temperature gradients in the skin layer. In the present study we assign it phenomenologically

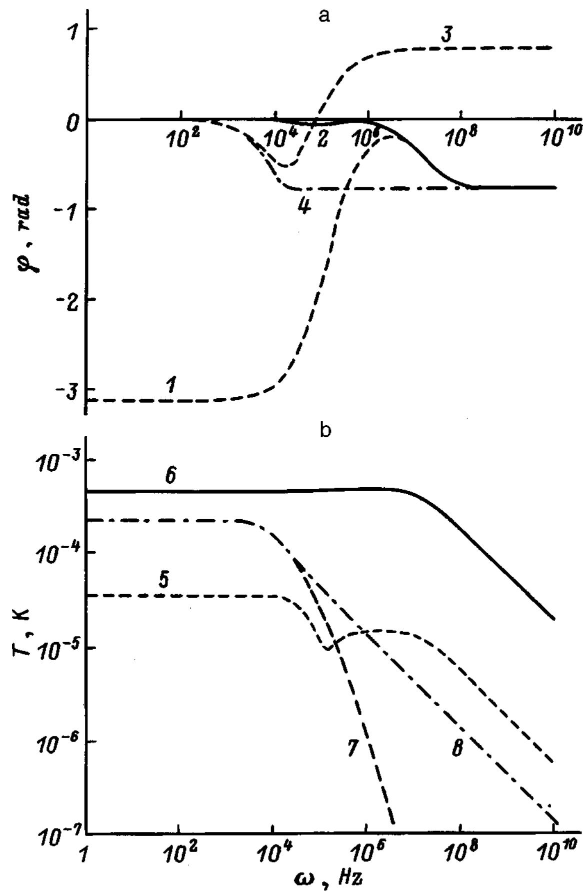

FIG. 2. Frequency dependence of phase shifts (a) and the corresponding amplitudes of the temperature waves (b) on the surface $x=0$ for $a=10^{-2}$ cm: *1*—φ_1 ($K=0.3$), *2*—φ_1 ($K=10$), *3*—φ_2, *4*—φ_3, *5*—F_1 ($K=0.3$), *6*—F_1 ($K=10$), *7*—F_2, *8*—G.

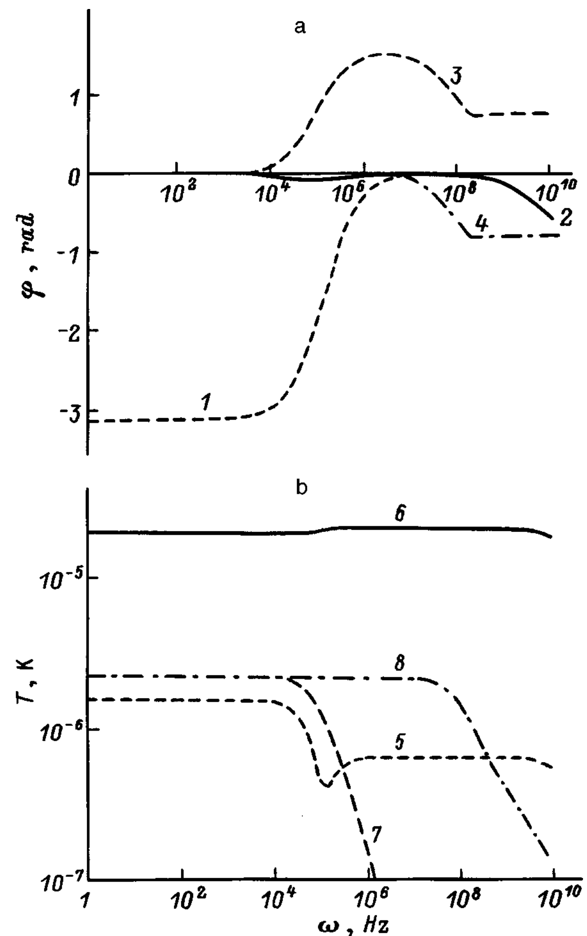

FIG. 3. Frequency dependence of phase shifts (a) and the corresponding amplitudes of the temperature waves (b) on the surface $x=0$ for $a=10^{-4}$ cm: *1*—φ_1 ($K=0.3$), *2*—φ_1 ($K=10$), *3*—φ_2, *4*—φ_3, *5*—F_1 ($K=0.3$), *6*—F_1 ($K=10$), *7*—F_2, *8*—G.

with the aim of establishing systematic features of the investigated phenomena that show up upon variation of this parameter.

In the bulk sample ($a=10^{-2}$ cm), for example, at $K=0.3$ (Fig. 2) in the frequency region $\omega<10^5$ s^{-1} we have $|F_1|\ll|F_2|\simeq|G|$. Thermal waves are generated in the electron and phonon subsystems, but depend only on the parameters of the phonon subsystem. The phases of the oscillations φ_2 and φ_3 in this case are equal to 0. At frequencies $\omega\geqslant\nu_r$ the amplitudes $|F_2|$ and $|G|$ undergo a rapid monotonic decrease, while $|F_1|$, after reaching a minimum grows and at $\omega>10^5$ s^{-1} predominates after passing through a maximum. At $\omega>10^5$ s^{-1} the phase φ_1, which corresponds to the amplitude $|F_1|$, also increases, tending toward a maximum, and the maxima of the phase and amplitude are observed at the same frequency $\omega\simeq2\times10^6$ s^{-1}. With further increase of the frequency the phase φ_1 tends to $-\pi/4$. At $K=10$ for all frequencies $|F_1|>|F_2|$, $|G|$ and for $\omega>10^4$ s^{-1} it becomes dominant. At $\omega\geqslant\nu_\varepsilon$ the amplitude $|F_1|$ decreases and the phase tends to $-\pi/4$.

As the length of the sample is decreased to 10^{-4} cm at $K=0.3$ (Fig. 3), at low frequencies ($\omega<10^4$ s^{-1}) the behavior of the amplitudes is analogous to the corresponding case for bulk samples. At $\omega\simeq10^4$ s^{-1} the amplitude $|F_2|$ decreases rapidly, and the amplitude $|G|$ dominates and maintains its constant value up to a frequency of the order of 10^7 s^{-1}. With further increase of the frequency the amplitude $|G|$ decreases and its phase tends to $-\pi/4$. At a frequency on the order of 10^8 s^{-1} the values of the amplitudes $|F_1|$ and $|G|$ equalize and with further increase of the frequency, the amplitude $|F_1|$ predominates. At $K=10$ the amplitude $|F_1|$ predominates in the entire frequency interval under consideration. Its phase is of the order of 0 and has a small minimum at $\omega\simeq10^5$ s^{-1}.

Note that as the length of the sample is increased, the given amplitudes increase almost linearly. It is also characteristic that the extrema of the amplitudes and phases become sharper as the length of the sample is increased.

In summary, we may conclude that

1) Allowance for the finite electron–phonon exchange leads to the necessity of considering two thermal waves—an electron thermal wave and a phonon thermal wave.

2) The character of these thermal waves depends substantially on the relative values of the modulation frequency of the incident radiation, the relaxation frequency of heat conduction in the phonon subsystem, and the energy relaxation frequency of the electron–phonon interaction, and also on the relative values (ratio) of the length of the sample and the electron cooling length.

3) By varying the modulation frequency over wide limits (up to the frequency of the electron–phonon interaction) it is possible to obtain separate information about the thermal parameters of the electron and phonon subsystems in one combined photothermal experiment.

This work was supported in part by the Consejo Nacional de Ciencia y Tecnologia (CONACYT) of Mexico.

1) This case can be realized in a semiconductor whose length a is less than the cooling length.

[1] A. Mandelis, *Photoacoustic and Thermal-Wave Phenomena in Semiconductors* (North-Holland, Amsterdam, 1978).
[2] H. Vargas and L. C. Miranda, Phys. Rev. **161**, 43 (1988).
[3] *Progress in Photothermal and Photoacoustic Science and Technology*, edited by A. Mandelis (Prentice-Hall, New Jersey, 1994).
[4] A. Rosencwaig and A. Gersho, J. Appl. Phys. **47**, 64 (1976).
[5] V. A. Sablikov and V. B. Sandomirskiĭ, Fiz. Tekh. Poluprovodn. **17**, 81 (1983) [Sov. Phys. Semicond. **17**, 50 (1983)].
[6] V. A. Sablikov and V. B. Sandomirski, Phys. Status Solidi B **120**, 471 (1983).
[7] A. N. Vasil'ev, V. A. Sablikov, and V. B. Sandomirskiĭ, Izv. Vuzov MV i SSO SSSR. Fizika, No. 6, 119 (1987).
[8] F. G. Bass, V. S. Bochkov, and Yu. G. Gurevich, *Electrons and Phonons in Bounded Semiconductors* [in Russian] (Nauka, Moscow, 1984).
[9] G. N. Logvinov, Fiz. Tekh. Poluprovodn. **25**, 1815 (1991) [Sov. Phys. Semicond. **25**, 1092 (1991)].
[10] G. González de la Cruz and Yu. G. Gurevich, J. Appl. Phys. **80**, 1726 (1996).
[11] G. I. Bulakh, O. V. Volchans'kiĭ, and I. Ya. Kucherov, Ukr. Fiz. Zh. **40**, 1228 (1995).
[12] R. A. Smith, *Semiconductors* (Cambridge Univ. Press, Cambridge, 1978; Mir, Moscow, 1982).
[13] T. N. Sitenko, V. T. Layashenko, and I. P. Tyagulski, Phys. Status Solidi A **9**, 51 (1972).

Translated by Paul F. Schippnick

Nature of the donor action of Gd impurity in crystals of lead and tin telluride

D. M. Zayachuk and O. A. Dobryanskiĭ

L'vov State Polytechnical University, 290646 L'vov, Ukraine
(Submitted January 27, 1998; accepted for publication March 4, 1998)
Fiz. Tekh. Poluprovodn. **32**, 1331–1333 (November 1998)

Electron spin resonance and the Hall effect are investigated in n-$Pb_{1-x}Sn_xTe$:Gd crystals grown from melt. It is found that there is no direct correlation between the free electron density and the density of the Gd^{3+} impurity in these crystals. The conclusion is drawn that the the electron conductivity of $Pb_{1-x}Sn_xTe$:Gd crystals is not caused by the Gd impurity but by intrinsic defects of the crystal lattice which have zero activation energy due to the Gd impurities. © *1998 American Institute of Physics.* [S1063-7826(98)00911-9]

1. Gadolinium, as an impurity in IV–VI crystals, has attracted a great deal of attention in recent years.[1–8] This has been due mainly to the efficiency of its influence on the system of intrinsic defects of the crystals, in particular, the possibility of varying over wide limits the free-charge-carrier concentrations, which is important from the point of view of the practical utilization of the given semiconductors. Doping with gadolinium lowers the hole concentration and leads to an inversion of the conductivity type of IV–VI crystals from hole to electron conductivity; i.e., in the investigated materials Gd behaves as a donor.[2–8] There is still no agreed-upon viewpoint regarding the reasons for the donor activity of Gd. Some authors link this effect with a direct donor activity of the impurity, assuming that Gd enters into the lattice of IV–VI crystals in the relatively ionized state Gd^{3+} (Refs. 4, 5, and 8). Others suggest that Gd in IV–VI crystals is an electrically neutral impurity, but the electronic conductivity of gadolinium-doped and undoped crystals is due to chalcogen vacancies.[2,3]

2. To elucidate this question of the mechanism of donor activity of Gd impurity in IV–VI crystals, we have undertaken a study of the Hall effect and also of electron spin resonance (ESR), and we have also carried out an electron-probe microanalysis of n-$Pb_{1-x}Sn_xTe$ crystals with composition $0 \leqslant x \leqslant 0.25$, Bridgman-grown and doped with Gd during growth. The actual impurity concentration in the investigated samples did not exceed 6×10^{20} cm^{-3}. The conditions of growth and the procedure of the microanalysis and the electrical measurements were similar to those described in Refs. 3 and 6. The electron spin resonance was recorded on a spectrometer with a sensitivity of 10^{12} spins at 9.4 GHz. The problem is solved by searching for correlations between the actual Gd impurity concentration N_{Gd}, the concentration of Gd^{3+} ions, and the concentration of free electrons n in the doped crystals.

3. From the point of view of the stated question the main results of our studies reduce to the following.

– There is no direct correlation between the concentration of the Gd impurity and the free-electron concentration in $Pb_{1-x}Sn_xTe$: Gd crystals. For a fixed composition of the crystal matrix the ratio between these concentrations is different in different segments of the bar (Fig. 1), and the electrical activity of the Gd impurity is lowest at the starting point of the bar, where the ratio N_{Gd}/n is maximum, and can reach values exceeding an order of magnitude. In the end region of the bar, where the Gd concentration falls off abruptly, the free-electron concentration begins to exceed it.

– In Gd-doped samples the free-electron concentration in the region of impurity conductivity does not depend on the temperature.

– The less tin there is in the matrix of the doped crystal, the higher will the electron concentration be, all else being equal.

– In the investigated samples ESR spectra of gadolinium, which are characteristic of Gd^{3+} ions ($S=7/2$) in a crystal field of cubic symmetry, are observed (Fig. 2).

– The concentration of Gd^{3+} ions forming the ESR spectrum of the $Pb_{1-x}Sn_xTe$:Gd crystals is an order of mag-

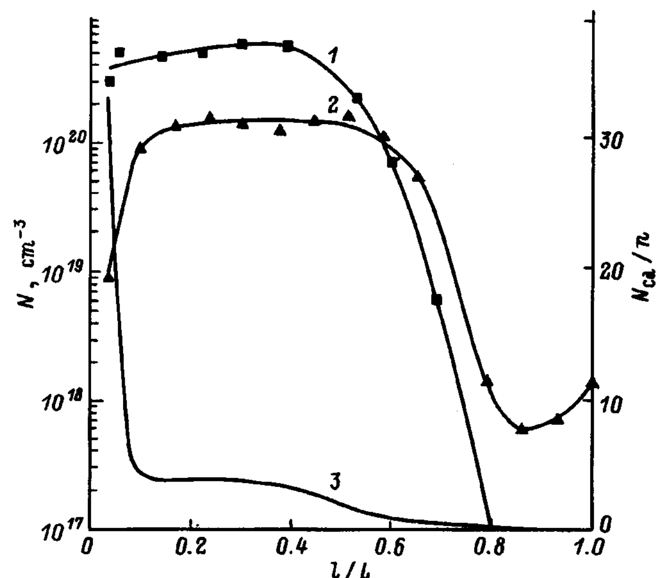

FIG. 1. Distribution along a bar (l is distance from the starting point of growth of the bar, L is the overall length of the bar) of the Gd concentration (*1*), the free-electron concentration (*2*), and the ratio of their mean values n/N_{Gd} (*3*) for a PbTe : Gd crystal grown from a starting mixture with Gd content $N_{Gd}=1.7\times10^{20}$ cm^{-3}.

 © 1998 American Institute of Physics

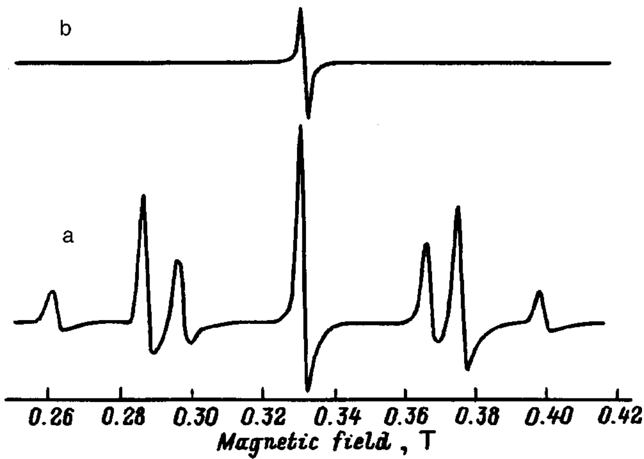

FIG. 2. Room-temperature ESR spectra (gain V equal to: a — 4×10^3, b — 0.5×10^2). a) n-PbTe : Gd. Total Gd concentration from the microanalysis data 2.3×10^{19} cm^{-3}. Concentration of Gd^{3+} ions from the ESR data 2.3×10^{17} cm^{-3}. Free-electron concentration 3.9×10^{18} cm^{-3}. b) Sample of ultramarine with calibrated spin content 1.5×10^{17}, used as a reference for determining the concentration of Gd^{3+} ions in the investigated $Pb_{1-x}Sn_xTe$: Gd samples.

nitude or two orders of magnitude lower than the concentration of free electrons in the samples.

4. It follows from the above data that in Gd-doped crystals of $Pb_{1-x}Sn_xTe$:Gd there does not exist a direct correlation between the total impurity concentration and the free-electron concentration or between the concentration of the impurity in the ionized state relative to the crystalline lattice, Gd^{3+}, and n. Thus, we can unambiguously state that the change in the electrical parameters of IV–VI crystals when doped with Gd is not due to ionization of the impurity. Otherwise, the concentration of Gd^{3+} ions in the investigated crystals would be equal to n or greater, considering the possibility for the existence in the crystals of compensating acceptor centers. Consequently, the presence of free electrons in $Pb_{1-x}Sn_xTe$:Gd crystals is due to intrinsic defects of the crystalline lattice. Since n does not depend on T in the doped crystals, these donor centers should possess zero activation energy. Such centers in IV–VI crystals, as is well known, are chalcogen vacancies.[9,10] The role of Gd thus reduces to a change in the ratio of electrically active, intrinsic point defects in equilibrium at the crystallization point in favor of the indicated vacancies. In undoped $Pb_{1-x}Sn_xTe$ crystals, as is well known, the situation is the opposite.[11]

5. Within the framework of the expounded model of the electrical activity of Gd impurity in IV–VI crystals, the reason for the absence of a correlation between the Gd concentration and the free-electron concentration in doped crystals is obvious. Logically, this also explains the dependence of the concentration of the free electrons due to gadolinium doping on the composition of the matrix of the bar, and within its limits, on the spatial coordinate. In $Pb_{1-x}Sn_xTe$ solid solutions the position of the maximum on the liquidus curve depends on the percent Sn content. It is that much more strongly shifted into the tellurium-enriched region relative to stoichiometry the larger is x (Ref. 11). Therefore, as x is increased, it is necessary to have a larger amount of Gd in order to shift this maximum into the region of compositions enriched by metallic components, which is equivalent to decreasing n while keeping N_{Gd} fixed. The minimal donor activity of Gd in the initial segments of doped bars grown from melt is explained by the action of tellurium, which in the absence of doping separates out in such bars in the form of precipitates. As is well known, tellurium always precipitates out in $Pb_{1-x}Sn_xTe$ crystals grown from melt, but the concentration of such precipitates is maximum at the starting point of the bars.[12–14] To a significant extent, this tellurium neutralizes the donor activity of Gd. It should be noted that this is a typical phenomenon in the interaction of Te precipitates and donor impurities in the investigated materials.[15,16]

We wish to thank Prof. S. Waplak and Mr. W. Bednarski (Institute of Molecular Physics, Polish Academy of Sciences) for assistance with carrying out the ESR studies and for useful discussions.

[1] M. Bartkowski, D. J. Northcott, J. M. Park, and A. H. Reddoch, Solid State Commun. **56**, 659 (1985).
[2] D. M. Zayachuk, D. D. Ivanchuk, R. D. Ivanchuk, V. I. Mikityuk, and P. M. Starik, Fiz. Tekh. Poluprovodn. **23**, 1654 (1989) [Sov. Phys. Semicond. **23**, 1023 (1989)].
[3] D. M. Zayachuk, D. D. Ivanchuk, R. D. Ivanchuk, S. S. Maslyanchuk, and V. I. Mikityuk, Phys. Status Solidi A **119**, 215 (1990).
[4] M. Gorska, J. R. Anderson, G. Kido, S. M. Green, and Z. Gołacki, Phys. Rev. B **45**, 11 702 (1992).
[5] T. Story, M. Gorska, M. Arciszewska, E. Grodzicka, Z. Gołacki, and R. R. Gałązka, J. Magn. Magn. Mater. **140–144**, 2041 (1995).
[6] D. M. Zayachuk, E. L. Matulenis, and V. I. Mikityuk, J. Cryst. Growth **121**, 235 (1992).
[7] D. M. Zayachuk, R. D. Ivanchuk, V. I. Kempnik, and V. I. Mikityuk, Fiz. Tverd. Tela **38**, 2502 (1996) [Phys. Solid State **38**, 1373 (1996)].
[8] T. Story, M. Gorska, A. Łusakowski, M. Arcizewska, W. Dobrowolski, E. Grodzicka, Z. Gołacki, and R. R. Gałązka, Phys. Rev. Lett. **77**, 3447 (1996).
[9] N. J. Parada and G. W. Pratt, Phys. Rev. Lett. **22**, 180 (1969).
[10] B. A. Volkov and O. A. Pankratov, Zh. Éksp. Teor. Fiz. **88**, 280 (1985) [Sov. Phys. JETP **61**, 164 (1985)].
[11] G. Nimtz and B. Schlicht, in *Narrow-Gap Semiconductors*, Springer Tracts in Modern Physics Series, Vol. 98 (Springer-Verlag, Berlin, 1985), p. 1.
[12] R. Breschi, A. Camanzi, and V. Fano, J. Cryst. Growth **58**, 399 (1982).
[13] M. Muchlberg and D. Hesse, Phys. Status Solidi A **76**, 513 (1983).
[14] T. Watanabe and K. Kinoshita, J. Cryst. Growth **80**, 391 (1987).
[15] P. M. Starik and D. M. Zayachuk, Ukr. Fiz. Zh. **31**, 1377 (1986).
[16] D. M. Zayachuk, P. M. Starik, and V. A. Shenderovskii, Phys. Status Solidi A **107**, 95 (1988).

Translated by Paul F. Schippnick

Effect of laser-induced defects on luminescence in InP crystals

F. B. Baimbetov and N. G. Dzhumamukhambetov

Atyrau University, 465000 Atyrau, Kazakhstan
(Submitted January 29, 1998; accepted for publication April 18, 1998)
Fiz. Tekh. Poluprovodn. **32**, 1334–1336 (November 1998)

Experimental data on luminescence in laser-modified InP crystals are compared with the theory of radiative recombination of heavily doped, compensated semiconductors. It is established that the band with maximum at 1.35 eV observed at 77 K is due to radiative transitions through the tails of the density of states which are formed as a result of the random distribution of defects and impurities showing up after laser treatment. The effective depth of the tails of the density of states is estimated to be equal to 67 meV. © *1998 American Institute of Physics.* [S1063-7826(98)01011-4]

The authors of Ref. 1 have reported observation of a new bright band with energy position of the maximum $h\nu_m = 1.35$ eV in the photoluminescence spectra of laser-modified InP crystals at 77 K. This band is due to radiative transitions through the tails of the density of states which are formed as a result of the random distribution of defects and impurities after laser treatment. Radiative transitions through the tails of the density of states are possible in heavily doped, compensated semiconductors (HDCS). This provides a basis for comparing experimental results with the theory of luminescence of heavily doped, compensated semiconductors.[2]

Since inversion of the type of conductivity from n to p takes place in the modified near-surface layer and since the carrier concentration is $\sim 10^{19}$ cm^{-3} (Ref. 3), the most probable recombination channels, as in HDCS with p-type conductivity, are ''tail–to–tail'' transitions (TT transitions). We have therefore performed a detailed comparison of the temperature dependences of the parameters of the new emission band at 1.35 eV with the theory of luminescence of heavily doped, compensated semiconductors[2] for the case of radiative TT transitions.

According to the theory, in TT transitions the energy position of the maximum varies nonmonotonically as the temperature T is increased and at some temperature T^* reaches a minimum, as was also observed experimentally.[1]

The temperature dependence of the energy position of the maximum of the photoluminescence band for $T<T^*$ is due to destruction of deep states of the ''tail'' of the minority-carrier band and should be linear, while the temperature coefficient of the energy position of the maximum should be greater than the temperature coefficient of the width of the band gap E_g.

The experimental results give a linear temperature dependence of the energy position of the maximum[1] with temperature coefficient $\alpha_1 = 3.7\times 10^{-4}$ eV/K, which is greater than the temperature coefficient for E_g ($\alpha_g = 3.6\times 10^{-4}$ eV/K), also indicating an agreement between theory and experiment.

In the temperature region $T^*<T<220$ K radiative recombination is governed by states in the tails near the edges of the allowed bands, and there are many more of these states than deep states. The temperature dependence of the energy position of the maximum here should be given by the formula

$$h\nu_m = E_g - \lambda I_a (2T_0/3)^2 T^{-2}, \tag{1}$$

or

$$h\nu_m = E_g - \alpha_2 T^{-2}, \tag{2}$$

where $T_0 = 850$ K is the ''freezing'' temperature of the impurities in the InP lattice, λ is a quantity of the order of unity, and $\alpha_2 = \lambda I_a (2T_0/3)^2$ is the temperature coefficient of

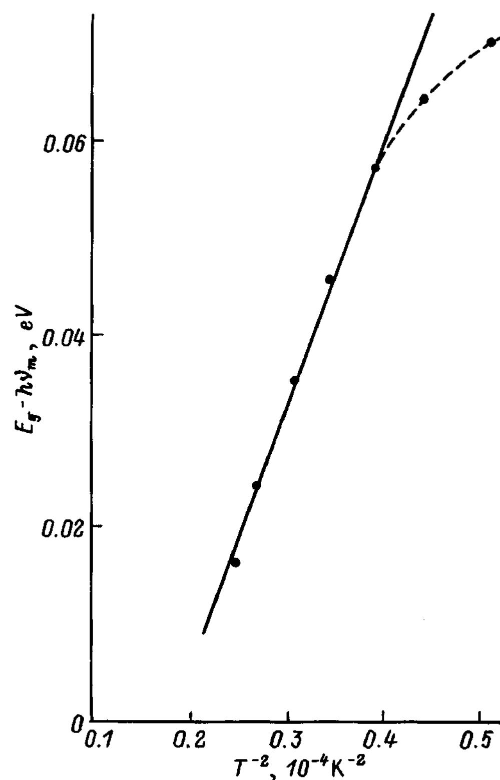

FIG. 1. Temperature dependence of the energy position of the maximum of the photoluminescence spectra of laser-modified crystals of InP in the temperature interval $150<T<220$ K.

 © 1998 American Institute of Physics

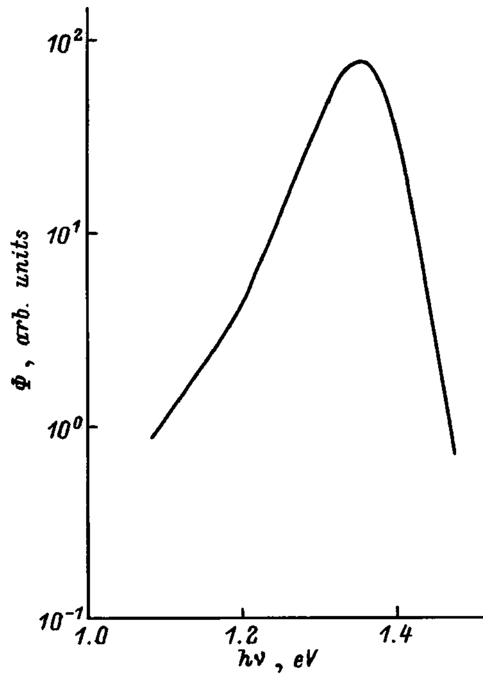

FIG. 2. Photoluminescence spectrum of laser-modified crystals of InP at 77 K.

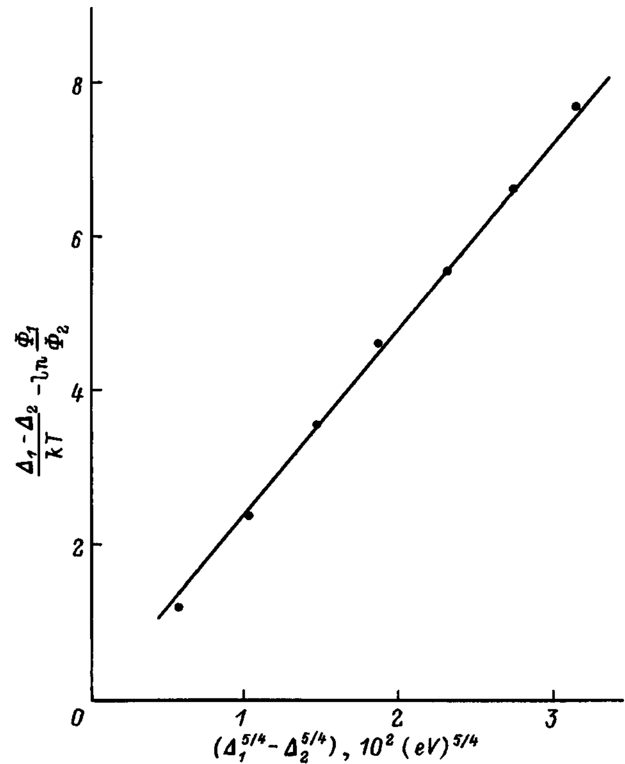

FIG. 3. Short-wavelength falloff ($h\nu > h\nu_m$) of the photoluminescence band.

the energy position of the maximum. Thus the dependence of $E_g - h\nu_m$ on T^{-2} should be a straight line, as was observed experimentally (Fig. 1), and the temperature coefficient is $\alpha_2 = 2.6\times 10^3\ \mathrm{eV\cdot K^2}$. Comparing the temperature coefficient α_2 in the region $T^* < T < 220$ K with its theoretical expression, we estimated the ionization energy of a single acceptor (I_a), which turns out to be equal to 8 meV for $\lambda = 1$. At $T > 220$ K the energy position of the maximum falls linearly as E_g.

The total intensity of the 1.35-eV band decreases exponentially with increasing temperature, and its half-width varies nonmonotonically.[1] In the temperature region $77 < T < 220$ K it increases linearly, and it decreases at $T > 220$ K. This confirms the presence of various radiative mechanisms.

Consequently, luminescence of modified InP crystals in the temperature region $T < 220$ K is due to transitions through the tails of the density of states (TT transitions). In the high-temperature region $T > 220$ K the main recombination channels are band-to-band transitions.

Thus, the temperature dependence of the main parameters of the new emission band in the temperature region $77 < T < 220$ K functionally coincides with that predicted by theory for the radiative TT transitions. This provides a basis for comparing the shape of the spectrum of the new band at 1.35 eV (Fig. 2) with its theoretically expected shape.

In the short-wavelength region ($h\nu > h\nu_m$), according to the theory,[2] the falloff of the intensity $\Phi(h\nu)$ depends on the temperature and should have the form

$$\Phi(h\nu) = \Phi_0 \exp[(E_g - h\nu)/kT - 2\pi^{1/2} \times (E_g - h\nu)^{5/4}/5I_d^{5/4}(Na_e^3)^{1/2}]. \quad (3)$$

Setting $\Delta = E_g - h\nu$ and $A = 2\pi^{1/2}/5I_d^{5/4}(Na_e^3)^{1/2}$, we write expression (3) in the form

$$\Phi(h\nu) = \Phi_0 \exp(\Delta/kT - A\Delta^{5/4}). \quad (4)$$

Thus, in the coordinates $[(\Delta_1 - \Delta_2)/kT - \ln(\Phi_1/\Phi_2)]$ and $[\Delta_1^{5/4} - \Delta_2^{5/4}]$, where Φ_1, Φ_2 and Δ_1, Δ_2 correspond to two arbitrary photon energies, $h\nu_1$ and $h\nu_2$, the dependence $\Phi(h\nu)$ should be a straight line.

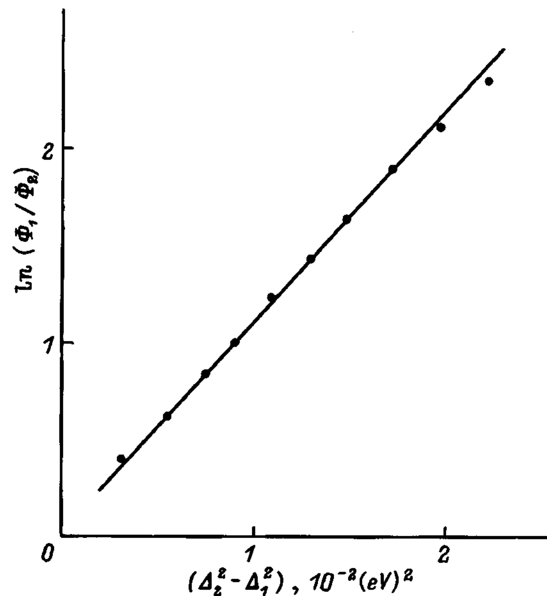

FIG. 4. Long-wavelength falloff ($h\nu < h\nu_m$) of the photoluminescence band.

At 77 K, when the 1.35-eV band predominates, the falloff of $\Phi(h\nu)$ in the short-wavelength region is satisfactorily approximated by expression (4) (Fig. 3). In the construction of the dependence in Fig. 3, $h\nu_1$ was fixed and $h\nu_2$ was varied. The coefficient A, found from the slope of the line, turned out to be equal to 238 $eV^{-5/4}$, which corresponds to an ionization energy of a single donor $I_d = 4.8$ meV and is close to the energy of a shallow donor in InP.

In the long-wavelength region ($h\nu < h\nu_m$), according to the theory, the nature of the emission spectrum is determined by the falloff of the density of states with penetration into the band gap (from above) and can be written as

$$\Phi(h\nu) = \Phi_0 \exp(-\Delta^2/2\gamma^2). \quad (5)$$

In the coordinates $\ln(\Phi_1/\Phi_2)$ and $(\Delta_2^2 - \Delta_1^2)$ the dependence $\Phi(h\nu)$ should be a straight line. The experimental dependence confirms the theoretically predicted dependence and is described by expression (5) (Fig. 4). The effective depth of the tails of the density of states (γ), found from the slope of the line at 77 K, is 67 meV, which is almost twice the theoretically calculated value of the mean-square fluctuation of the potential in InP (Ref. 4) and is explained by the formation of a large number of dislocations in the surface region of the crystal.[5]

In summary, all of the experimental results are in satisfactory agreement with the Levanyuk–Osipov theory of luminescence of heavily doped, compensated semiconductors. These results give us reason to conclude that radiative recombination in laser-modified InP crystals is due to transitions through the tails of the density of states.

[1] N. G. Dzhumamukhambetov and A. G. Dmitriev, Fiz. Tekh. Poluprovodn. **27**, 641 (1993) [Semiconductors **27**, 356 (1993)].
[2] A. P. Levanyuk and V. V. Osipov, Usp. Fiz. Nauk **133**, 427 (1981) [Sov. Phys. Usp. **24**, 187 (1981)].
[3] N. G. Dzhumamukhambetov, in *Abstracts of the Seventh International Conference on Solid-State Radiation Physics* [in Russian] (MGIÉM, 1996), p. 118.
[4] A. L. Efros, Usp. Fiz. Nauk **111**, 451 (1973) [Sov. Phys. Usp. **16**, 789 (1973).
[5] N. G. Dzhumamukhambetov, Fiz. Khim. Obrab. Mater. [Physics and Chemistry of Processing of Materials], No. 2, 121 (1997).

Translated by Paul F. Schippnick

SEMICONDUCTOR STRUCTURES, INTERFACES, AND SURFACES

Study of the dynamical characteristics of an insulator–semiconductor interface

Y. G. Fedorenko and A. M. Sverdlova

Saratov State University, 470071 Saratov, Russia

A. Malinin

Electron Physics Laboratory, Helsinki University of Technology, Otakaary 7A, FIN-02150 Espoo, Finland
(Submitted April 7, 1998; accepted for publication April 27, 1998)
Fiz. Tekh. Poluprovodn. **32**, 1337–1342 (November 1998)

A study of charge relaxation processes in metal–insulator–semiconductor structures containing the rare-earth oxides Gd_2O_3 and Lu_2O_3 as the insulator has been performed using the deep-level transient spectroscopy (DLTS) method in combination with a study of nonlinear oscillations in the metal–insulator–semiconductor structure connected to an external inductive circuit. On the basis of the DLTS results and the variation with temperature of the configuration of the period multiplicity regions of the controlling parameters (the amplitude and frequency of the applied voltage) it is shown that the generation of nonlinear oscillations in a metal–insulator–semiconductor structure is governed by the properties of the insulator–semiconductor interface, in particular, the density of surface states and the capture cross sections. © *1998 American Institute of Physics.* [S1063-7826(98)01111-9]

One of the main directions of development of present-day solid-state electronics is the search for dynamic charge instabilities for use as information carriers. In metal–insulator–semiconductor (MIS) structures the particular features of the dynamic processes are attributable to the formation and resorption of a packet of charge carriers bound to holes and in the free state on the surface of the semiconductor. To utilize MIS structures in functional electronic devices it is necessary to establish the influence of processes of generation, accumulation, and recombination of charge carriers with participation of the surface states on the formation of current instabilities which are the reason for the appearance of dynamical regimes in MIS systems.

To understand the electronic processes at the insulator–semiconductor (IS) interface, which complicate the current dynamics in an MIS structure under nonequilibrium conditions, e.g., upon application of a variable voltage, it is necessary that we combine a classical approach to the study of electronic processes at the IS interface and an approach based on the ideas and methods of nonlinear dynamics. The mechanism for the appearance of nonlinear oscillations in an MIS structure is closely linked with phenomena and regularities of the occurrence of electronic processes on the surface of the semiconductor, which have been examined using classical methods of study.

In our study the goal was to establish an interrelationship between charge relaxation processes in an MIS structure and the appearance of complex dynamical regimes in a simple electronic system—a nonautonomous series circuit with an MIS structure connected in series. We have carried out an experimental study of the peculiarities of the relaxation of electronic processes at the interface of rare-earth oxides and silicon using deep-level transient spectroscopy (DLTS), which has allowed us to obtain a quantitative estimate of the parameters of the surface states (e.g., the capture cross section) and to perform a qualitative analysis of charge-carrier relaxation processes in the MIS structure in conjunction with the results of a study of nonlinear oscillations.

1. EXPERIMENTAL PROCEDURE

We investigated samples containing rare-earth oxides (Lu_2O_3 and Gd_2O_3). The oxide films were fabricated by thermal oxidation of metallic films of these elements in vacuum. Oxidation took place in a flux of dried oxygen or in air at a temperature of 500 °C for 15–20 min. Aluminum electrodes were prepared by thermal evaporation in vacuum. The area of the electrodes ranged from 3.3×10^{-3} to 5.0×10^{-3} cm^2. An aluminum contact was deposited on the back side of the wafer (the reverse side from the polished side) by thermal evaporation. The main electrical parameters of the films—the dielectric constant, effective surface charge, the dependence of the surface potential on the voltage across the field electrode, etc. were estimated from rf capacitance–voltage characteristics (CVC) measured at a frequency of 1 MHz.

DLTS spectra were obtained on a DLS-82 measurement complex having the following specifications. The sensitivity of determination of the capacitance was $\Delta C=2\times10^{-5}$ pF for the signal-to-noise ratio SNR = 1. The frequency of the filling pulse ranged from 2.5 to 2500 Hz, and its amplitude was $\Delta U=0.1$ V. The available software enabled us to carry out measurements in real time, identify errors, and analyze the data. The measurement technique and the technique used

 © 1998 American Institute of Physics

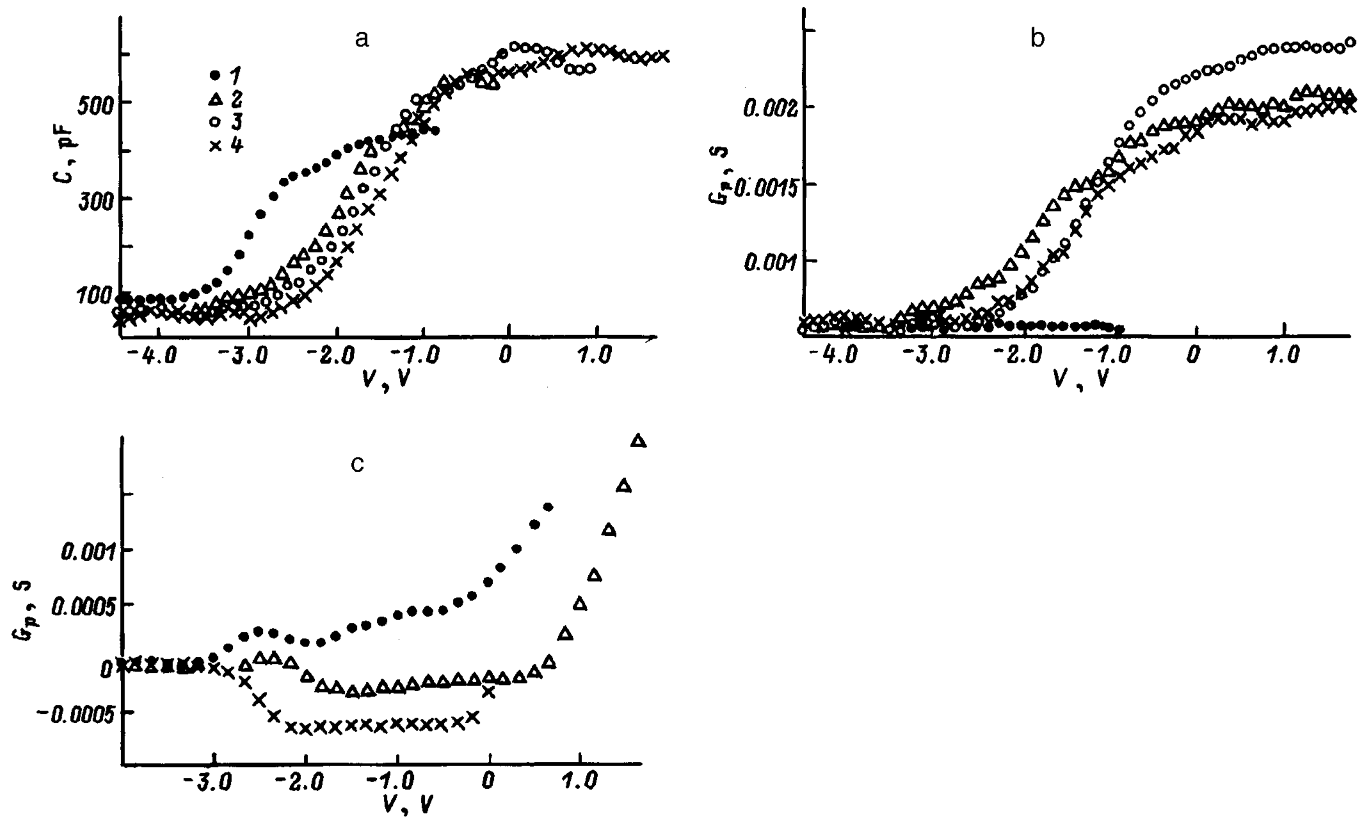

FIG. 1. Capacitance–voltage (a) and conductance–voltage (b, c) characteristics of Gd_2O_3 MIS-structures at different temperatures, K: *1* — 300, *2* — 212, *3* — 166, *4* — 77.

to process the spectra were chosen on the basis of an analysis of Refs. 1–3. To avoid difficulties associated with the presence of mobile charge in the oxide and recharging of electron capture centers in the insulator during tunneling, which can contribute to the total signal for values of the surface potential close to its enriching values, we subjected the samples to a preliminary field treatment at a negative bias voltage $U = -4-6$ V for one hour, which allowed us to achieve an outflow of positive charge from the oxide to the metal.

2. RESULTS AND DISCUSSION

The capacitance–voltage characteristics of the samples had the form typical of MIS structures (Figs. 1a and 2a). For the samples with Gd_2O_3 films (Fig. 1a) the presence of a positive built-in charge is characteristic, the voltage of the flat bands V_{fb} varies from -2.6 to -1.8 V, the fixed charge in the insulator $Q_f = (3.2-3.8)\times 10^{-8}$ C/cm^2, the slope of CVC $(1/C)\cdot dC/dV$ is equal to $0.5-0.6\,\mathrm{V}^{-1}$, and the ca-

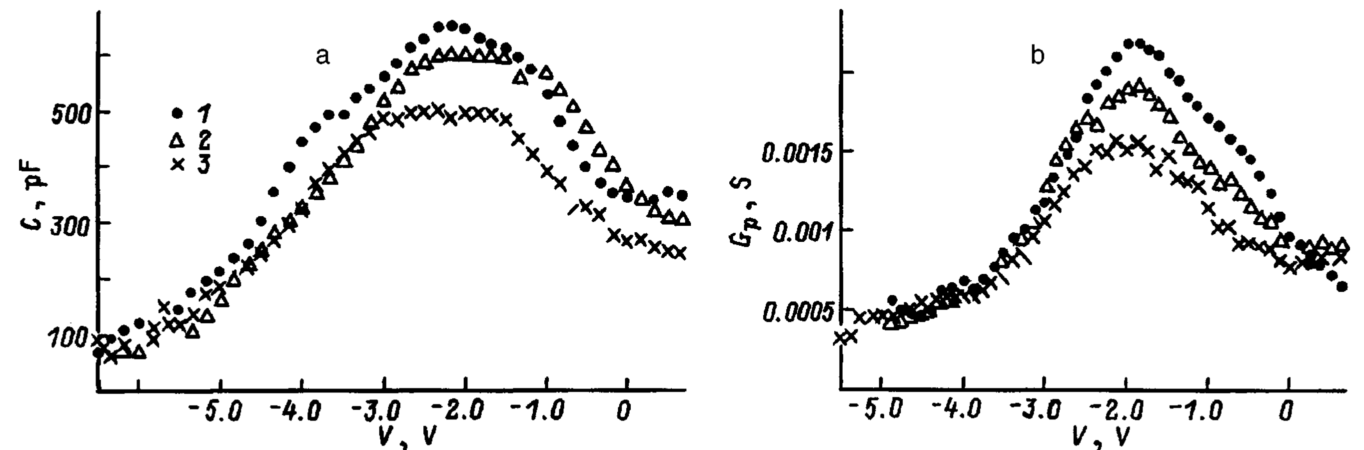

FIG. 2. Capacitance–voltage (a) and conductance–voltage (b, c) characteristics of Lu_2O_3 MIS-structures at different temperatures, K: *1* — 300, *2* — 140, *3* — 77.

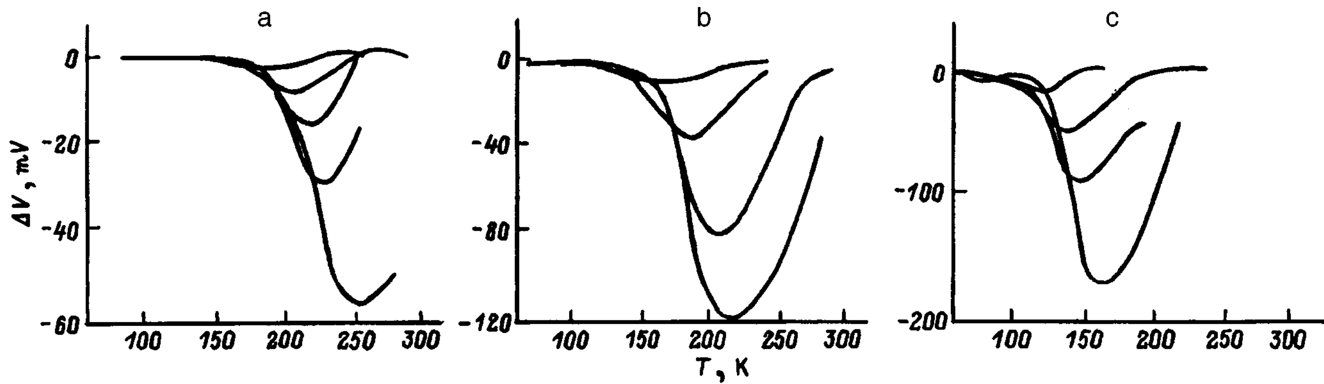

FIG. 3. DLTS spectra of Gd_2O_3 MIS-structures for different values of the surface potential φ_s, eV: a — 0.42, b — 0.28, c — 0.2.

pacitance overlap coefficient was 10–12. The dielectric constant ε, determined from the rf CVC at 1 MHz was 10–12. In the voltage dependence of the active component of the conductivity G_p-V we observed a smooth growth of the conductivity in the transition from depletion to enrichment, with saturation in the inversion region (Fig. 1b). For a number of samples, lowering the temperature led to a change of sign of the active component of the conductivity (Fig. 1c) in the region of values of the surface potential corresponding to the transition from inversion to surface depletion, and a segment of weak dependence of G_p on V on the depleting bends of the bands, changing over to growth of the conductivity upon enrichment. Such a change in the G_p-V dependence upon lowering the temperature is possible in the case of variation of the charge of the surface states upon intersection of the Fermi level and the the surface state level up to voltages corresponding to surface inversion. The observed recharging effect is characteristic of surface states with small capture cross sections. The shift of the CVC toward positive voltages upon lowering of the temperature, the increase in the capacitance of the structure, and the change in the slope of the characteristics on the depletion segment all confirm the assumption that the negative charge of the surface states increases.

MIS structures with Lu_2O_3 are distinguished by flat-band voltages V_{fb} equal to -1.4 to -1.0 V (see Fig. 2a), and consequently by smaller values of the fixed charge in the insulator $Q_f=(8.2-9.5)\times 10^{-9}$ C/cm^2. The conductance–voltage curves (Fig. 2b) are characterized by the presence of a maximum at the flat-band voltage and a tendency toward saturation in the region of voltages corresponding to inversion. An estimate of the density of surface states from the magnitude of the peak in the G_p-V curves gives the value $\sim(1.8-2.8)\times 10^{11}\,\mathrm{cm}^{-2}\cdot\mathrm{eV}^{-1}$. As the temperature is lowered, some decrease of the capacitance and conductivity takes place at voltages greater than the flat-band voltage. The capacitance–voltage characteristics are shifted in a parallel manner along the voltage axis, without significant change in slope, and the shift of the flat-band voltage ΔV_{fb} is equal to -0.2 to -0.25 V, which suggests a continuous distribution of surface states or their constant contribution to the capacitance at relatively low densities. Increasing the positive voltage causes a falloff of the active and the reactive components of the conductivity, which is evidence of nonequilibrium filling of the surface states and an increase in the leakage of electrons through the insulator. It also leads to a decrease in enrichment on the silicon surface and consequently to a lowering of the capacitance and the conductivity.

In the DLTS spectra, features associated with the individuality of the interface formed by different insulators were also observed . Let us consider features of the spectra of MIS structures with Gd_2O_3. Figure 3 shows a family of curves measured at different values of the surface potential. As the depleting voltage is lowered, the spectra shift smoothly toward lower temperatures, which is characteristic of a continuous energy distribution of the surface states. A characteristic feature of the spectra is the strong dependence of the signal amplitude on the temperature. As was shown in Ref. 4, such a dependence of the signal amplitude in the structures considered there—a $p-n$ junction and a Schottky barrier—can be due to interaction of the charge carriers with the two allowed bands. In this case, a temperature-dependent amplitude factor appears in the analytical expression for the DLTS spectra:

$$\begin{aligned} A_1 &= e_n/(e_n+e_p) \\ &= 1/[1+(c_pN_v/c_nN_c)\cdot\exp(-(E_p-E_m)/kT)] \\ &\equiv 1/[1+\lambda\cdot b\cdot\exp(\Delta E/kT)], \end{aligned}$$

where $\Delta E=E_p-E_n$, $b=N_v/N_c$, and $\lambda=c_p/c_n$. It can be seen that if the amplitude grows as the temperature is lowered, then the level is located above the middle of the band gap ($E_n<E_p$). An estimate of the capture cross section from the Arrhenius plots gives $\sigma_n=2.8\times 10^{-20}-1.2\times 10^{-21}\,\mathrm{cm}^{-2}$ in the energy interval $E_n=0.268-0.157$ eV from the bottom of the conduction band, confirming the above-stated assumption.

MIS structures with Lu_2O_3 (Fig. 4) exhibited higher-temperature peaks, which demonstrates the presence of deep surface states with energy $E_n=0.45-0.4$ eV. The amplitudes of the peaks decrease somewhat as the temperature is lowered, and at values of the surface potential corresponding to weak surface depletion remain essentially unchanged. The width of the peaks grows substantially as the surface potential is decreased, which suggests that electrons fill the levels

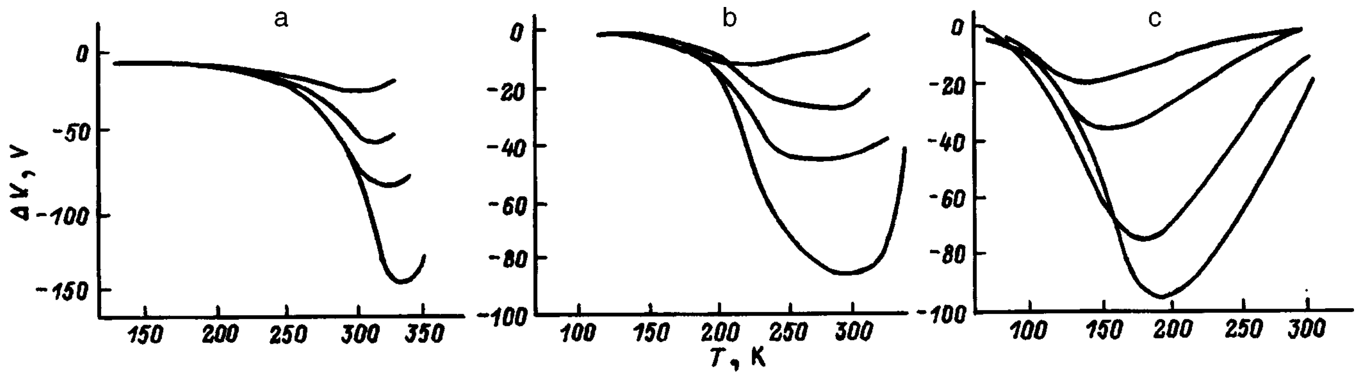

FIG. 4. DLTS spectra of Lu_2O_3 MIS-structures for different values of the surface potential φ_s, eV: a — 0.42, b — 0.28, c — 0.2.

which are found above the Fermi level. As a result of the absence of techniques for processing spectra of such complicated makeup, we did not attempt a quantitative estimate of the capture cross sections. Efforts to separate the contribution of the surface states above and below the Fermi level by using a smaller amplitude of the filling pulse $\Delta V = 0.05$ V did not yield a positive result.

A general feature of the spectra is the decrease of the amplitude of the peaks as the frequency of the filling pulses is lowered from 2500 to 2.5 Hz, which reveals the contribution of the slow surface states.

An analysis of such characteristics of the spectra as the amplitude and peak width as functions of the temperature and surface potential reveals aspects of the interaction of the carriers with both bands and allows us to make an assumption about the depth of the level and its position relative to the middle of the band gap. Thus, the monotonic decrease of the signal amplitude with growth of the temperature for MIS structures with Gd_2O_3 (Fig. 4) is evidence of the presence of a continuous distribution of the surface states with a distribution minimum near the middle of the silicon band gap.

For MIS structures with Lu_2O_3 the dependence of the signal amplitude on the temperature has a nonmonotonic character and the amplitude was found to increase at temperatures near room temperature, which suggests that deep surface centers contribute to the total signal. On the basis of the above data we may conclude that relaxation processes at the rare-earth-oxide–silicon interface take place as a result of the interaction of surface states with both allowed bands, and that the Si–Gd_2O_3 interface is characterized by the presence of surface states in the upper half of the band gap with small capture cross sections resulting in an increase in the negative charge of the surface states as the temperature is lowered and in the appearance of inversion at depleting values of the surface potential. For structures with Lu_2O_3 deep surface centers near the middle of the band gap are detected at the interface. These centers contribute substantially to the signal at high temperatures $T = 310 - 340$ K.

A study of the temperature dependence of excitation of oscillations in a series circuit with an MIS structure connected in series has shown that the topology of the regime diagrams is configured chiefly by processes of recharging of the surface states. Figure 5 shows diagrams of oscillational regimes for structures with Gd_2O_3. It can be seen that as the temperature is lowered, the current dynamics in the system is characterized by a transition to oscillations with a smaller period nT_0, $n = 2$. Random oscillations do not arise below

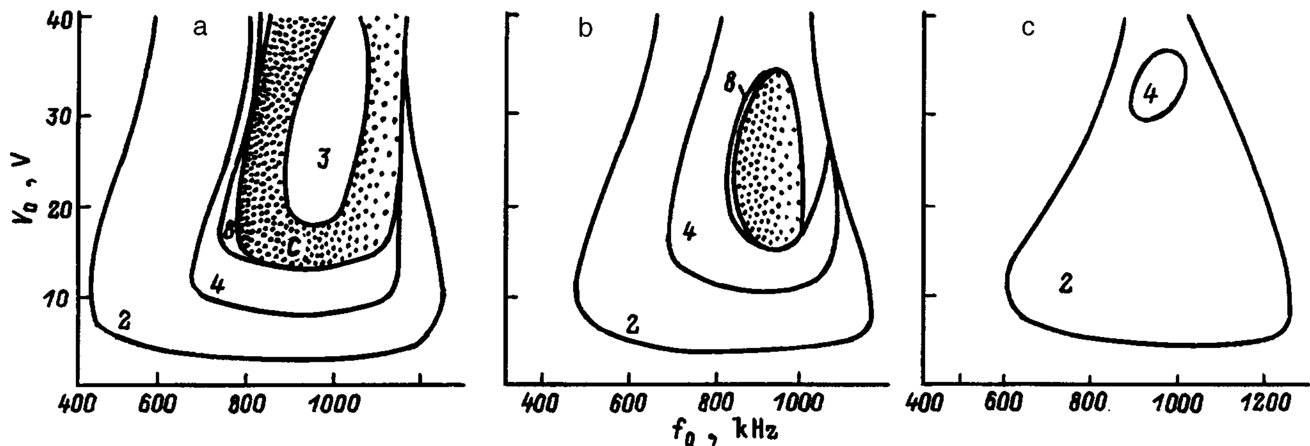

FIG. 5. Diagrams of oscillatory regimes in a series circuit with a Gd_2O_3 MIS-structure connected in series at different temperatures, K: a — 300, b — 220, c — 180. The figures *1, 2, 3, 4, 6, 8* indicate the duration of the period of the oscillations as a multiple of the period of the external voltage T_0. C is the region of generation of random oscillations.

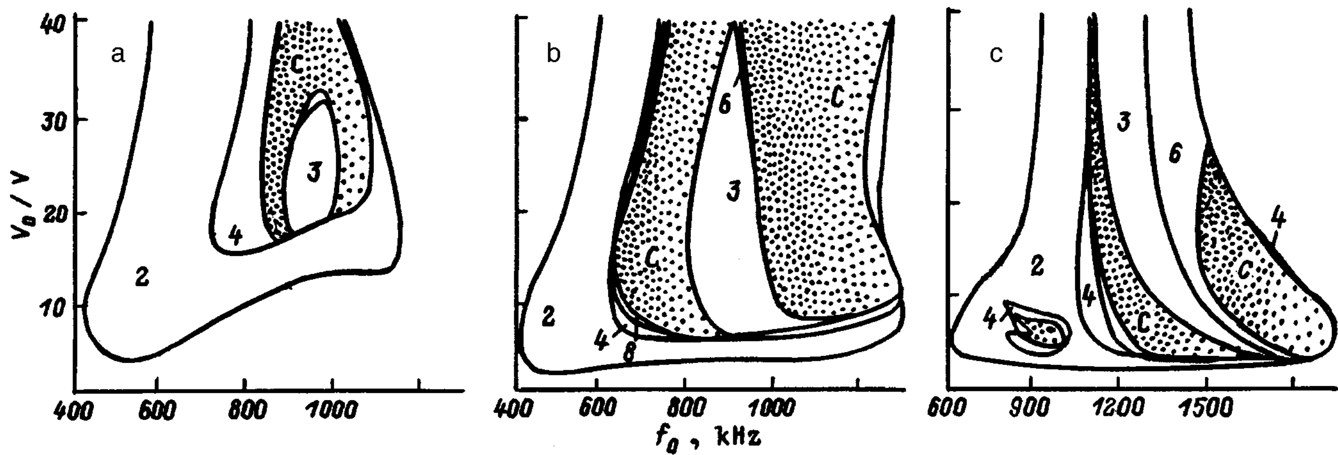

FIG. 6. Diagrams of oscillatory regimes in a circuit including a Lu_2O_3 MIS-structure at different temperatures, K: a — 300, b — 180, c — 77. The notation is the same as in Fig. 5.

$T=190-170$ K anywhere in the entire range of frequencies and amplitudes of the applied voltage. This characteristic feature of the temperature variations of the regime diagrams can be attributed to the appearance of negatively charged surface states at these temperatures, which causes the electrons to recombine with the minority carriers under inversion conditions over the course of one period of the applied voltage.

Figure 6 shows regime diagrams in the coordinates ''amplitude and frequency of the applied voltage'' for an MIS structure with Lu_2O_3. As can be seen, at all temperatures the region of chaotization divides into two ''sleeves,'' between which the periodic regimes $3T_0$ and $6T_0$ are observed. As the temperature of the sample is lowered from 300 to 180 K, the range of frequencies and amplitudes at which excitation of nonlinear oscillations is possible broadens, but with further lowering of the temperature the existence region of random oscillations is bounded from above by values of the amplitude of the applied voltage $V_0=25$ V, and with growth of the amplitude, the frequency range of existence of oscillations with periods $2T_0$, $3T_0$, $4T_0$, and $6T_0$ narrows.

The change in the topology of the regime diagrams in the ''amplitude–frequency'' plane can be explained as follows. As the temperature is lowered, surface states with lower energy are included into the relaxation process and the amplitudes of the applied voltage needed to fill the level decrease. The shift of the frequency range from 400–1100 to 600–1600 kHz confirms their inclusion in the surface-state relaxation process even with shorter relaxation times. However, the substantial differences in the topology of the regime diagrams for different insulators cannot be explained in the framework of a change in the equilibrium filling of the surface states with lowering of the temperature. It is possible to explain the preservation of the variety of types of oscillations at liquid-nitrogen temperatures in MIS structures with Lu_2O_3 by taking into account deeper surface levels. The ejection of carriers into the conduction band at low temperatures is insignificant by virtue of its thermal-activation character.

The absence of equilibrium filling of the surface states may be assumed as the reason for the continued generation of complex oscillations at low temperatures in samples with Lu_2O_3: if it were present, it would lead to the possibility of dynamic redistribution of the carriers between the surface states and the bands upon application of a variable external voltage. Thus, in the case of nonequilibrium filling of the surface states, surface states from a wider interval of energies, characterized by a wider interval of relaxation times, are included in the exchange of carriers between bands. This makes it possible to observe oscillatory regimes at low temperatures. Nonequilibrium filling of surface states is the reason for the substantial broadening of the peak of the DLTS signal as the temperature is lowered, consistent with the measured capacitance–voltage and conductivity–voltage characteristics. Note the close match between the temperature interval $T=160-220$ K, in which broadening of the DLTS peaks is observed, and the temperature interval $T=150-220$ K, where an increase in the range of frequencies and amplitudes of the applied voltage is observed, at which nonlinear oscillations, including random oscillations, are excited.

In summary, the results of measurements of the electrical properties of a silicon–rare-earth-oxide interface, of its DLTS spectra, and of the current oscillations in a series circuit, with an MIS structure connected in series, have revealed previously unknown connections between such parameters as the density of the surface states and their capture cross sections, on the one hand, and the DLTS data and conditions of generation of nonlinear oscillations, on the other. Such an approach opens up the totally new possibility of determining nonequilibrium properties of an interface by studying electronic processes at the surface of the semiconductor.

This work was carried out with the financial support of a grant for young scientists in the Goskomvuz system of the Russian Federation; the organization carrying out the competition St. Petersburg State University.

[1] K. Yamasaki, M. Yoshida, and T. Sugano, Jpn. J. Appl. Phys. **18**, 113 (1979).
[2] D. S. Gusta, M. M. Chandra, and V. Kumar, Phys. Status Solidi A **80**, K209 (1983).
[3] T. Katsube and K. Kakimoto, J. Appl. Phys. **52**, 3504 (1983).
[4] A. A. Lebedev, Fiz. Tekh. Poluprovodn. **31**, 437 (1997) [Semiconductors **31**, 371 (1997)].

Translated by Paul F. Schippnick

Effect of hydrogenation on the properties of metal–GaAs Schottky barrier contacts

V. G. Bozhkov, V. A. Kagadeĭ, and N. A. Torkhov

Scientific-Research Institute of Semiconductor Devices, 634000 Tomsk, Russia
(Submitted August 29, 1997; accepted for publication May 26, 1998)
Fiz. Tekh. Poluprovodn. **32**, 1343–1348 (November 1998)

The effect of hydrogenation (incorporation of atomic hydrogen) on the properties of n-GaAs and the characteristics of Au–GaAs Schottky barrier contacts (the ideality factor of the current–voltage characteristic n, the barrier height φ_b, and the reverse voltage V_r at a current of 10 μA) has been investigated. The n-GaAs surface was bare (A-type samples) or was protected by an ultrathin (~50 Å) layer of SiO_2 (B-type samples) during hydrogenation. It was shown that there was an optimal hydrogenation regime for the A-type samples (temperature range 150−250 °C and duration 5 min), for which n and V_r reached their minimum and maximum values, respectively. For the B-type samples, n and V_r improve starting from minimal durations and temperatures of hydrogenation and remain constant or even improve over the entire investigated range of temperatures (100−400 °C) and durations (1–50 min). The donor impurity passivation processes are roughly the same for the A- and B-type samples.
© *1998 American Institute of Physics.* [S1063-7826(98)01211-3]

INTRODUCTION

The effect of treatment in hydrogen plasma on the properties of semiconductor materials has been studied extensively since the beginning of the 1980s. As a result, it has been established that it is mainly due to the interaction of atomic hydrogen with structural defects, deep and shallow impurity centers located on the surface and in the volume, into which atomic hydrogen penetrates as a result of diffusion. A consequence of this interaction is passivation (suppression of activity) of the indicated defects and centers, accompanied by a substantial change in the electrical characteristics and properties of the material: the concentration of the majority charge carriers, their mobility, the lifetime of the minority charge carriers, the photoluminescence intensity, homogeneity, etc.[1–3] It should also be noted that the interaction of atomic hydrogen with the surface of a semiconductor leads to reduction of the surface oxides (i.e., efficient surface cleaning) and etching of the material.[4–7]

Such strong action as hydrogenation has on the properties of semiconductor materials is of great practical interest. Studies that have been carried out so far have shown that passivation by atomic hydrogen can be used to protect the surface of silicon[1,8,9] and gallium-arsenide[10] diodes, enhance the efficiency of silicon solar cells,[11,12] improve the forward and reverse current–voltage characteristics (CVC) of Schottky-barrier diodes,[13,14] and substantially improve (in combination with other production processes) the characteristics of silicon field devices.[15] At the same time, it must be acknowledged that the number of such studies has been quite limited and it cannot be said that hydrogenation is used extensively in the fabrication of semiconductor devices.

In our study the goal was to investigate the effect of treatment with atomic hydrogen (hydrogenation) on the characteristics of Schottky barrier metal–GaAs contacts. The fact that hydrogen has a beneficial effect on both the bulk and surface properties of semiconductor materials makes this treatment especially attractive for devices using surface-barrier structures.

EXPERIMENTAL PROCEDURE

Hydrogen plasma was created with the help of a reflection arc discharge by a hollow cathode and an incandescent element. We were the first to employ such a technique for creating atomic hydrogen for treatment of semiconductors.[16] The discharge heating voltage was 180–200 V at a current of 2 A.

The samples were treated in a chamber with an initial vacuum of 4.2×10^{-6} Torr. The flow rate of the hydrogen fed into it was maintained at 700 atm·cm^3/h. The hydrogen pressure in the chamber was 1.3×10^{-4} Torr. Such a low pressure substantially differentiates the conditions of hydrogenation in this setup from those used earlier. Another important feature of this setup is that the design of the atomic-hydrogen generator (small emission opening in the cathode and significant distance from it of the target holding the samples to be treated) shielded the samples from bombardment by the high-energy particles of the plasma.

The rate of cooling of the sample holder after termination of treatment was greater than 15 °C/s in the temperature interval 400−250 °C. The treatment parameters which we were able to vary were the sample temperature ($T_{\rm treat}$) and treatment time ($t_{\rm treat}$).

Epitaxial layers of GaAs:Sn of thickness 0.5 μm, grown on an n^+-GaAs:Te substrate with [100] orientation were subjected to hydrogen-plasma treatment (AB treatment). The charge-carrier concentration in the epitaxial layer was $(3-4.2)\times10^{16}\,\mathrm{cm}^{-3}$, and in the substrate, $2\times10^{18}\,\mathrm{cm}^{-3}$. Before commencement of treatment, an ohmic contact was created on the substrate by electrochemical deposition of GaNi + Au with subsequent annealing in a

nitrogen atmosphere at a temperature of 450 °C for 5 min. After chemical cleaning, the epitaxial layers were treated with a solution of $NH_4OH:H_2O = 1:5$ to remove native oxide, whose thickness was monitored with an ellipsometer and amounted to 7–10 Å after cleaning. Next, the epitaxial layers were protected with a thin (~50 Å) plasma-chemically deposited insulating layer (SiO_2). This was done in order to avoid possible surface damage during AB treatment, as reported in Refs. 17 and 18. Some of the semiconductor wafers were subjected to treatment without the protective layer (it was removed with a buffered etchant immediately before treatment). This made it possible to visually assess the role of the protective layer.

The investigated Schottky-barrier structures were formed by electrochemical deposition of a gold film of thickness 0.8 μm onto the windows of a photoresist (on the wafers with unprotected surfaces) with subsequent removal of the photoresist, or onto windows in the insulating layer (for the protected wafers). The diameter of the windows was 325 μm. In what follows, we will call the samples (Schottky-barrier structures) prepared on unprotected wafers *A*-type samples, and those prepared on protected wafers, *B*-type samples. Control samples were prepared together with the test samples. The control samples were not subjected to treatment in an atmosphere of atomic hydrogen. Results for them are referred to in the figures as ''untreated.''

The distribution of the ionized donor impurity concentration N_d with thickness of the epitaxial layer (concentration profiles) was deduced from measurements of the capacitance–voltage characteristics (CVC) at 1 MHz. Values of the barrier height φ_b were determined from the current–voltage characteristics and the magnitude of the saturation current. The ideality factor of the current–voltage characteristics was determined from the slope of a semi-log plot of the current–voltage characteristic.[19]

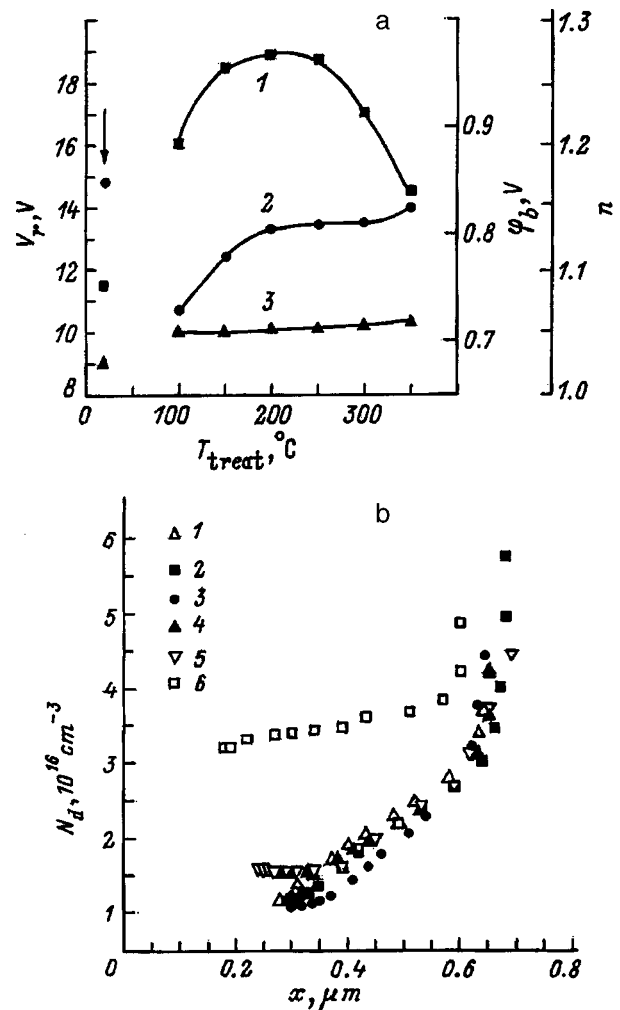

FIG. 1. Variation of the parameters of Au/$n-n^+$-GaAs contacts (*A*-type samples) as functions of the treatment temperature of $n-n^+$-GaAs structures treated with atomic hydrogen (T_{treat}); treatment time 5 min. a—dependence of the reverse bias voltage V_r (*1*), barrier height φ_b (*2*), and ideality index of the current–voltage characteristic n (*3*) on the treatment temperature T_{treat}; the arrow indicates the parameter values of the untreated samples. b—profiles of the distribution of ionized impurity $N_d(x)$ for various values of T_{treat}, °C: *1* — 100, *2* — 200, *3* — 250, *4* — 300, *5* — 350. The empty squares (*6*) plot the distribution $N_d(x)$ in the untreated sample.

RESULTS AND DISCUSSION

We were guided in our choice of the treatment temperatures and times by the results of existing studies[13,14] and by our preliminary results.

Figure 1a plots the dependence of the barrier height, ideality factor of the current–voltage characteristic, and reverse voltage V_r (at a current of 10 μA) on the treatment temperature for *A*-type samples. The samples were prepared from one wafer and were subjected to AB treatment individually. Treatment time was 5 min. It can be seen that the ideality factor varied only weakly over the entire interval of treatment temperatures. The reverse voltage passes through a maximum in the temperature interval 150–250 °C and stays above its values for the untreated (control) samples over the entire temperature interval. The barrier height undergoes substantial changes at low temperatures.

Figure 1b plots concentration profiles corresponding to the above-indicated treatment regimes (Fig. 1a). Note that passivation of the dopant impurity is pronounced already at the minimum treatment temperature 100 °C. Further changes in the profile (at higher temperatures) are insignificant. An increase in the impurity concentration (weaker passivation) is usually observed at treatment temperatures T_{treat} >250 °C. In some experiments this effect was more pronounced. Its manifestation was strongly influenced, as we were able to determine, by the cooling rate of the samples after treatment. The slower the cooling, the more pronounced the effect. The reason for this is obvious: partial reactivation of the impurity takes place during slow cooling. From our estimates, at the cooling rate we were able to achieve (better than 15 °C/s) the role of this effect was not large.

Additional information about the nature and reasons for changes in the CVC parameters of the current–voltage characteristics brought about by AB treatment of GaAs wafers can be obtained from the dependence on the treatment time (Figs. 2a and 2b). Measurements of this dependence were made at a treatment temperature of 150 °C, which is nearly optimal (judging from the foregoing results). As it turned out, a treatment time of 5 min is optimal from the point of

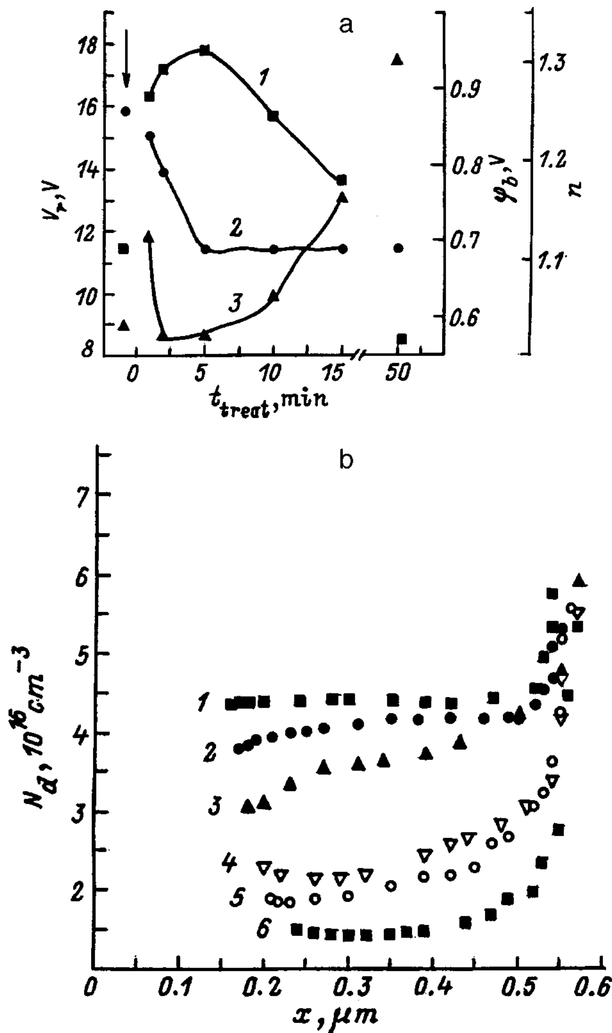

FIG. 2. Variation of the parameters of Au/$n-n^+$-GaAs contacts as functions of the treatment time of $n-n^+$-GaAs structures treated with atomic hydrogen (t_{treat}) for $T_{treat}=150$°C (*A*-type samples). a—dependence of the reverse bias voltage V_r (*1*), barrier height φ_b (*2*), and ideality index of the current–voltage characteristic n (*3*) on the treatment time t_{treat}; b—profiles of the distribution of ionized impurity $N_d(x)$: *1* — untreated sample, *2–7* — treatment time t_{treat}, min: *2* — 1/3, *3* — 1, *4* — 5, *5* — 15, *6* — 50.

view of obtaining the best CVC parameters: maximum value of the reverse voltage, minimum value of the ideality factor, and stable value of the barrier height. Comparison of Figs. 1a and 1b, and also Figs. 2a and 2b, indicates that variation of the reverse voltages V_r for Schottky-barrier structures cannot be explained just by passivation of the impurity. This is indicated by the absence of a strict correlation between variations of the values of V_r and N_d. This conclusion is also confirmed by other results, which are presented below.

The above-described behavior of the Schottky-barrier characteristics for the *A*-type samples can be explained as follows. At low treatment temperatures and short treatment times surface damage is possible (and with it a deterioration of the values of n). This damage is attributable to selective etching (reduction) of the surface oxides of GaAs in a stream of atomic hydrogen. As is well known (see, for example, Refs. 5 and 6), arsenic oxide is reduced by atomic hydrogen more effectively than gallium oxide, and this process already goes forward at room temperature. Surface damage as a result of bombardment of the sample by high-energy ions from the plasma is improbable, taking into account the design of the generator. With increase of the treatment temperature and time, oxides and organic contaminants are removed, ''healing'' of intrinsic defects occurs, and the surface structure approaches ideal.[5,6] Values of the ideality factor in this case reach their minimum, and values of the reverse voltage reach their maximum.

Deterioration of the values of n at high temperatures (greater than 200 °C) observed for short treatment times (1 min) and for long times (>5 min), taking into account the parallel falloff of the reverse voltages, can be linked with growth of the density of defects on the surface and/or in the skin layer. It can be assumed that under these conditions, a chemical reaction between the atomic hydrogen and the GaAs surface is possible, first of all with arsenic, accompanied by a breakdown of the surface stoichiometry since compounds of hydrogen with group-V elements are usually volatile. Such behavior is highly pronounced, for example, in InP (Ref. 18). It cannot be ruled out for GaAs, although it occurs in a significantly weaker form.[4,5]

Although reasons for the behavior of the ideality factor of the current–voltage characteristics can in some measure also explain the variations of the reverse voltages, the decrease of V_r can be linked with damage (defects) of another kind. It is noteworthy that V_r decreases under conditions of growth (albeit weak) of the passivation level with increasing treatment time (Fig. 2b), but remains above its untreated value. Only for 50-min treatment does the reverse voltage drop below its untreated value (Fig. 2a).

Still more complicated is the explanation of the variations of the barrier height, which can be influenced by the surface structure, the presence of oxides and contaminants, and structural and impurity defects. In any event, the barrier height falls to some degree as a result of AB processing, and at temperatures above 200 °C and times greater than 5 min it varies insignificantly.

The explanation suggested above finds qualitative support in the results of analogous studies on the *B*-type samples [i.e., in the presence of a protective insulating layer (SiO_2) on the surface of the GaAs wafers during AB processing]. The thickness of the insulating layer was chosen on the basis of an experiment, whose results are shown in Fig. 3. The samples were treated at 200 °C for 20 min. As can be seen, for thicknesses greater than 100 Å the insulating layer becomes opaque to diffusion of atomic hydrogen. We chose a thickness of about 50 Å. Note that the observed changes in the passivation level do not always correspond to the change in the thickness of the insulating layer. In particular, the passivation level for the unprotected surface is usually somewhat lower than for insulating layer thicknesses of 50–100 Å. This behavior can be explained by the fact that on a bare GaAs surface, adsorption and diffusion of atomic hydrogen are accompanied by its removal in the form of volatile hydrides (during etching of the surface). At the same time, for a protected surface the latter effect is excluded.

Results of a study of the characteristic features of *B*-type samples are plotted in Figs. 4 and 5. As can be seen from

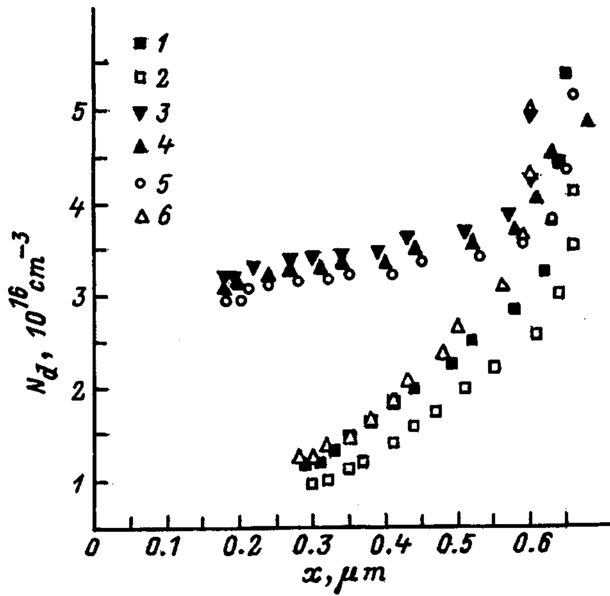

FIG. 3. Effect of thickness of the protective insulating SiO_2 layer during treatment of $n-n^+$-GaAs structures with atomic hydrogen (T_{treat} $=200\,°C$, $t_{treat}=20$ min) on the distribution profile of ionized donor impurity $N_d(x)$. SiO_2 thickness, Å: *1* — 45, *2* — 110, *3* — 215, *4* — 1000, *5* — 1470, *6* — 0.

these figures, in contrast to the *A*-type samples (Figs. 1 and 2) in the given case abrupt changes in the values of the CVC ideality factor and the barrier height as functions of the treatment temperature and time are absent. The reverse voltage of the Schottky barrier behaves quite characteristically and differently from the case of the *A*-type samples. It varies hardly at all as a function of the treatment time after an initial jump (see the arrow in Fig. 5), while passivation proceeds almost the same. As the treatment temperature is raised , the values of V_r remain the same and then even increase slightly (see Fig. 4a). This happens despite the fact that the passivation level of the dopant impurity decreases at 350 and 400 °C (see Fig. 4b). These results, in our view, point to the very important role of the surface in the changes of the characteristics of the Schottky-barrier contacts taking place as a result of hydrogenation. At the same time, it is possible to agree with the authors of Ref. 14, who suggest that passivation of electrically active, bulk defects can play a definite role in such behavior of V_r. It has been suggested[20] that their reactivation requires a higher-temperature treatment (or anneal). The diametrically opposite situation, in which the increase in the reverse voltages is a result of the generation of new defects that affect the mobility and hence the breakdown voltage, cannot be ruled out.

The complex nature of the processes, which take place during hydrogenation and which exert an influence on the characteristics of the Schottky-barrier contacts, is indicated by the following results. Removal of the protective insulating layer from the *B*-samples using a buffered etchant leads to a significant decrease (by 3–5 V) in the reverse voltages. Subsequent etching of the sample in the form of a mesa to a depth of 0.1 μm slightly alters the value of V_r, and only etching to a depth greater than 1 μm regains the initial values of V_r (before removal of the protective insulating layer).

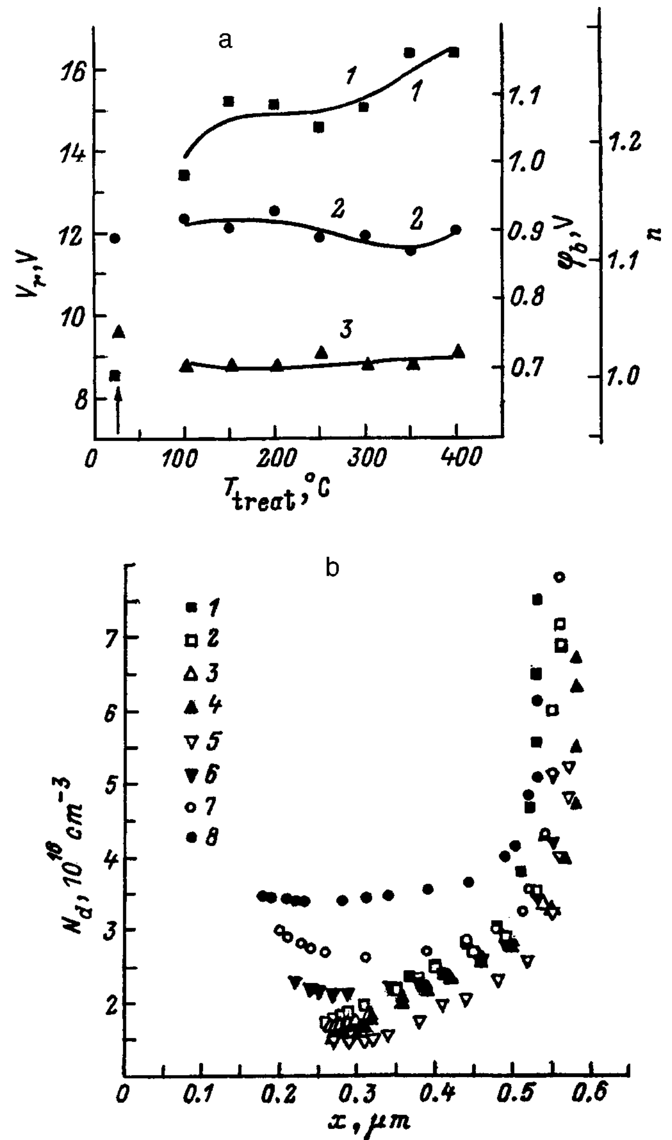

FIG. 4. The same as in Fig. 1, but for *B*-type samples. The numerals in the legend in *b* correspond to the following values of T_{treat}, °C: *1* — 100, *2* — 150, *3* — 200, *4* — 250, *5* — 300, *6* — 350, *7* — 400. The filled circles (*8*) plot the distribution $N_d(x)$ for the untreated sample.

As for the control samples, for them removal of the insulating layer and weak etching (to a depth of 0.1 μm) of the mesa-sample results in an insignificant decrease (by 0.2–0.3 V) followed by an insignificant increase (by the same amount) in V_r. Deep etching (to a depth greater than 1 μm) increases the values of V_r by 4 or 5 V.

Judging from the above results, changes in the SiO_2–GaAs interface have a greater effect on the changes in V_r taking place during AB treatment than do changes in the epitaxial layer. It can be assumed that passivation of defects at the interface leads simultaneously to a substantial decrease in the fringing fields in Schottky-barrier structures, which is the reason for the growth of V_r against a background of partial reactivation of the impurity (Fig. 4a; $T_{treat}>300°C$) and its decrease after removal of the SiO_2 layer. It is also conceivable that the effect is associated with changes in the insulating layer itself during treatment.

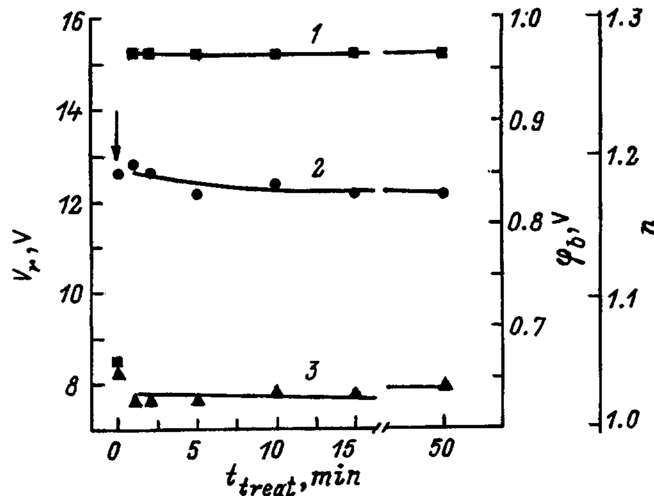

FIG. 5. Dependence of the reverse bias voltage V_r (*1*), barrier height φ_b (*2*), and ideality index of the current–voltage characteristic n (*3*) on the treatment time t_{treat} for *B*-type samples. The arrow indicates parameter values of the untreated samples.

We also performed experiments in which Schottky-barrier structures with unprotected and protected periphery (thickness of the insulating layer 50 Å) were subjected to AB treatment. Treatment temperature and time were 150 °C and 5 min. It was expected that passivation of the dopant impurity along the periphery can lead to growth of the reverse voltages. However, no noticeable effect was detected, and removal of the insulating layer, as in the case described above, led to a decrease of V_r. A return to its initial values was observed upon etching the mesa-sample to a depth greater than 0.3 μm. The reason for such behavior of the characteristics of Schottky barriers is still unclear.

CONCLUSION

Our studies have demonstrated the efficiency of the implemented atomic-hydrogen generator and the optimal conditions of treatment of structures for improving the most important parameters of surface-barrier devices (SBD): the ideality factor of the current–voltage characteristics and the reverse voltage. Especially interesting and promising for practical purposes are the results, obtained here for the first time, on samples in which the semiconductor surface is protected (during treatment) by a thin insulating layer which is transparent for atomic hydrogen. In this case, the improvement of the characteristics (decrease of the CVC ideality factor and increase of the reverse voltages of the Schottky barrier) is of a more reproducible and stable character. Processes taking place right at the SiO_2–GaAs interface, as the results have shown, play a large role in this improvement.

The first-of-its-kind comparative study of protected structures subjected to hydrogen-plasma treatment reported here is of great importance for understanding the nature of the changes in the properties of semiconductors. It allows one, to a significant degree, to differentiate the contribution of surface and bulk effects to the observed changes and thereby to eliminate unfounded assumptions from the discussion of their relative role.[7,13,14,21]

[1] S. J. Pearton, J. Electron. Mater. **14a**, 737 (1985).
[2] É. M. Omel'yanovskiĭ and A. Ya. Polyakov, Vysokochist. Veshchestva, No. 5, 5 (1988).
[3] J. Chevallier and M. Aucouturier, Annu. Rev. Mater. Sci. **18**, 219 (1988).
[4] R. P. H. Chang and S. Darack, Appl. Phys. Lett. **38**, 989 (1981).
[5] J. A. Schaefer, V. Persch, S. Stock, Th. Allinger, and A. Goldman, Europhys. Lett. **12**, 563 (1990).
[6] Z. Lu, M. T. Schmidt, D. Chen, R. M. Osgood, Jr., W. M. Holber, D. V. Podlesnik, and J. Forster, Appl. Phys. Lett. **58**, 143 (1991).
[7] N. Watanabe, T. Nittono, H. Ito, N. Kondo, and Y. Nanishi, J. Appl. Phys. **73**, 8146 (1993).
[8] J. I. Pankove, M. A. Lampert, and M. L. Tarng, Appl. Phys. Lett. **32**, 439 (1978).
[9] J. I. Pankove and M. L. Tarng, Appl. Phys. Lett. **34**, 156 (1979).
[10] S. J. Pearton, E. E. Haller, and A. G. Elliot, Appl. Phys. Lett. **44**, 684 (1984).
[11] C. H. Seager, D. S. Ginley, and J. D. Zook, Appl. Phys. Lett. **36**, 831 (1980).
[12] J. I. Hanoka, C. H. Seager, D. J. Sharp, and J. K. G. Panitz, Appl. Phys. Lett. **42**, 618 (1983).
[13] A. Paccagnella, A. Callegari, E. Latta, and M. Gasser, Appl. Phys. Lett. **55**, 259 (1989).
[14] U. K. Chakrabarti, S. J. Pearton, W. S. Hobson, J. Lopata, and V. Swaminathan, Appl. Phys. Lett. **57**, 887 (1990).
[15] V. V. Aristov, S. V. Koveshnikov, S. V. Nosenko, E. B. Yakimov, and A. M. Surma, Mikroelektronika **24**, No. 3, 198 (1995).
[16] V. A. Kagadeĭ, O. E. Troyan, and D. I. Proskurovskiĭ, Patent Application No. 93026207/07 (025856) dated 07.05.93.
[17] L. M. Weegels, T. Saitoh, and H. Kanbe, Appl. Phys. Lett. **66**, 2870 (1995).
[18] S. Balasubramanian, V. Kumar, and N. Balasubramanian, Appl. Phys. Lett. **64**, 1696 (1994).
[19] S.M. Sze, *Physics of Semiconductor Devices* (Wiley, New York, 1969; Mir, Moscow, 1984).
[20] W. C. Dautremont Smith, J. Chevallier, C. W. Tu, J. C. Nabity, V. Swaminathan, N. Stavola, and S. J. Pearton, Appl. Phys. Lett. **49**, 1098 (1986).
[21] Y. G. Wang and S. Ashok, J. Appl. Phys. **75**, 2447 (1994).

Translated by Paul F. Schippnick

Electrical characteristics of silicon–rare-earth fluoride layered switching structures

V. A. Rozhkov and M. B. Shalimova

Samara State University, 443011 Samara, Russia
(Submitted February 2, 1998; accepted for publication April 8, 1998)
Fiz. Tekh. Poluprovodn. **32**, 1349–1353 (November 1998)

Switching and memory effects in the electrical conductance of layered structures based on rare–earth fluorides are investigated. These investigations reveal the existence of high- and low-resistance states in structures of metal–insulator–semiconductor type. It is shown that the characteristics of the low-resistance state of such structures are described by a metal–tunneling insulator–semiconductor model. © *1998 American Institute of Physics.*
[S1063-7826(98)01311-8]

The recent observation of electrical switching and memory effects in the conductance of structures with thin-film insulators[1–3] suggests new ways of fabricating various kinds of switches, dc reprogrammable memory elements, control elements, and other functional units. These structures exhibit a number of attractive characteristics, among them a large difference in the resistances of the low-resistance and high-resistance states, a nearly unlimited number of nondestructive switching cycles for an optimal choice of the switching regime, and small switching times and energies. Although the phenomenon of conductance switching exhibits some overall regularities in the majority of thin-film materials and structures, at present these transitions from a high-resistance state to a low-resistance state and conversely have yet to be explained unambiguously.

An analogous type of electrical conductance switching with memory effects is exhibited by thin-film structures based on rare-earth fluoride elements.[4–6] However, the switching parameters of these structures, e.g., the high-to-low ratio of switching resistances (10^6-10^7), the switching time (fractions of microseconds), the energy required for switching ($\sim 10^{-8}$ J), and the device radiation hardness, exceed any other analogous structures by several orders of magnitude. This makes it imperative to study the fundamental regularities of conductance switching with memory in these structures, their dependences on internal and external factors, and the properties of the high-resistance and low-resistance states. Hence, we have chosen as the goal of this paper the study of these properties in structures made with thin-film cerium, dysprosium, and erbium fluorides.

For these experimental studies, we prepared samples with metal-insulator-semiconductor (MIS) and metal-insulator-metal (MIM) structures. The insulating rare-earth fluoride films were made by thermal sputtering of powdered CeF_3, DyF_3, and ErF_3 in vacuum. The substrates for the MIS structures were films of single-crystal in silicon with *n*- and *p*-type conductivity, industrial brands KEF-5 (111) or KDB-4.5 (100), respectively. The insulating films of rare-earth fluorides were made by thermal sputtering of the powered fluorides in a vacuum of $\sim 5\times10^{-4}$ Pa from a molybdenum boat at a substrate temperature of ~ 300 °C on a VUB-5 setup. The thickness of the rare-earth fluoride films was 0.2–0.5 μm. In making MIM structures, we first deposited a thick layer of aluminum on a silicon or glass-ceramic substrate, then the insulating layer of rare-earth fluoride, and finally contacts made of aluminum.

Electron-diffraction studies showed that the rare-earth fluoride films grow in a textured way, with the texture axis pointing perpendicular to the substrate plane. In this case the structure of the films varied as a function of the thickness of the deposited layer. We first vacuum-sputtered an amorphous layer of rare-earth fluoride on the heated substrate, and then polycrystalline layers with arbitrarily oriented crystallites. Although the final layers were textured, the presence of a preferred orientation did not affect the structure of the lower layers, which indicates that the texturing occurs during the growth of the films obtained.

Figure 1 shows typical switching current-voltage (I–V) characteristics of MIS structures grown on silicon substrates with *n*-type conductivity. Our studies showed that these structures can exist in two states with very different values of the resistance and current-voltage characteristics. The samples were in a state with a high resistance $(2-4)\times10^{11}$ Ω (Fig. 1, branch AB) when first prepared, and remained in that state as long as an applied voltage, whose polarity corresponds to depletion of the semiconductor surface of majority carriers did not exceed a certain threshold value $V_t=5-200$ V. When this threshold voltage was exceeded, the resistance of the sample decreased abruptly as the sample switched into a low-resistance state with resistance 10^4-10^5 Ω (Fig. 1, branch CD). A structure in the initially high-resistance state was switched by a voltage with opposite polarity when the value of the current through the sample reaches 100–600 μA. In this case the voltage for switching back was in the range $V_0=3-20$ V for variouas samples.

We were able to repeatedly (more than 10^4 times) and reproducibly switch these structures from one state to another and back using both dc and pulsed voltages. Both states could be maintained for long periods (more than 30 days) at room temperature when held at the switch-off voltage.

The MIM structures also possessed switching properties with a high resistance of $\sim 10^7$ Ω in their initial state. In the

 © 1998 American Institute of Physics

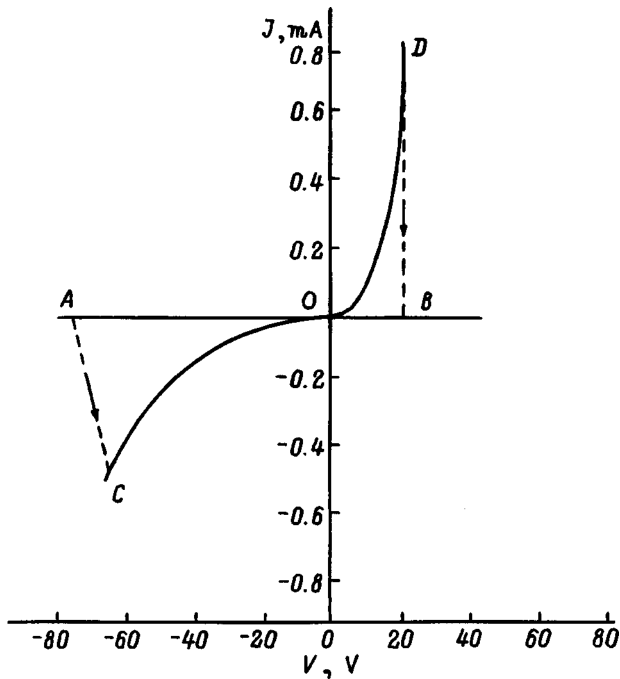

FIG. 1. The I–V characteristics of silicon MIS structures with rare-earth fluorides. *AB*—high-resistance state; *CD*— low-resistance state.

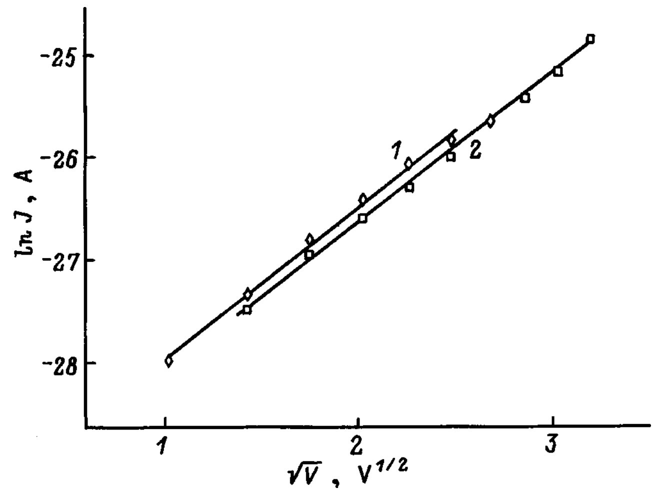

FIG. 2. The I–V characteristics of an Al–ErF_3–Si MIS structure in the high-resistance state. *1* — $V>0$; *2* — $V<0$.

low-resistance state, the resistances of the structures were a few ohms. MIM structures could be switched from a high-resistance state to a low-resistance state and back by applied voltages of either polarity; the only difference between the forward and backward switching was in the magnitudes of the current and voltage required.

Our studies showed that the magnitude of the current flowing through a MIS structure in the insulating state was $\sim 10^{-11}-10^{-12}$ A at a voltage of 1 V. In this case the current-voltage characteristics, which were nearly independent of the polarity of the applied voltage, were well rectified in $\ln J-\sqrt{V}$ coordinates, which are characteristic of the Poole-Frenkel effect. Typical current-voltage characteristics for a MIS structure with a film of erbium fluoride in the high-resistance state are shown in Fig. 2. For both polarities a satisfactory description of these characteristics is given by

$$J=\exp(\alpha\sqrt{V}), \tag{1}$$

where $\alpha=2.5-3.5$.

We found that the current through the structure in the insulating state increased exponentially with increasing temperature. The temperature dependence of the current in this case was characterized by an activation energy of $\sim 0.5-0.8$ eV for the various fluorides in the temperature range 300–480 K. Curve *1* in Fig. 3 shows this dependence for MIS structures with cerium fluoride.

In the low-resistance state the I–V characteristics of MIS structures are unipolar in form, with a rectification factor of $10-10^4$. Curve *1* in Fig. 4 shows the I–V characteristics with small rectification factors and large reverse currents. In the opposite case, represented by Fig. 4 (curve *2*), the I–V characteristics are analogous to those of a Schottky diode with a rectification factor $\sim 10^4$. In the latter case, the reverse current tends toward saturation with increasing voltage (region *a*), but for a sufficiently large voltage the current through the structure increases abruptly (region *b*). This region of abrupt increase of the reverse current arises from avalanche multiplication of free carriers in the silicon, for which the temperature coefficient of voltage breakdown is positive. For both structures with this I–V characteristic the forward current in the low-resistance state was only weakly dependent on temperature, and the temperature activation energy for the conductivity was 0.03– 0.1 eV at a forward bias of ~ 1 V (Fig. 3, curve *2*).

Our studies of the electrical properties of MIM structures with rare-earth fluorides in the low-resistance state established that a conductivity channel forms in the rare-earth fluoride films in the low-resistance state with a positive temperature coefficient of the resistance, along with a low resistivity characteristic of the metal. This gives us grounds to assume that the conducting channel is essentially in a metallic phase. Estimates of the radius of the conductivity channel based on the value of the spreading resistance of the silicon substrates yield typical values in the range of $1-5$ μm.

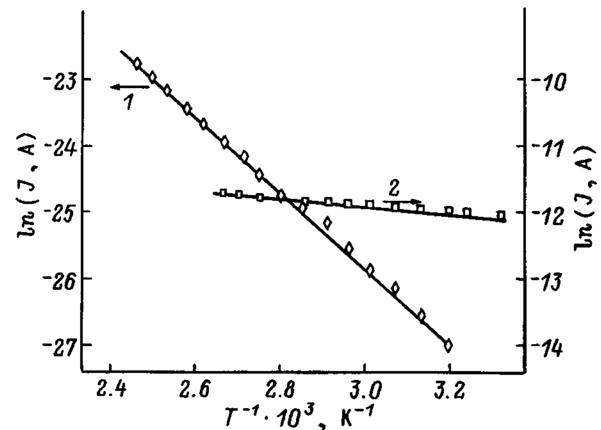

FIG. 3. Temperature dependence of the current through an Al–CeF_3–Si structure in the high-resistance (*1*) and low-resistance (*2*) states.

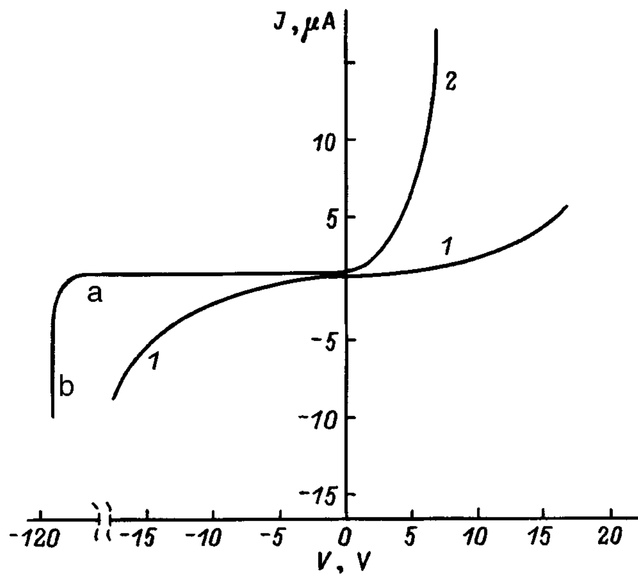

FIG. 4. The I–V characteristics of an Al–CeF_3–nSi structure in the low-resistance state.

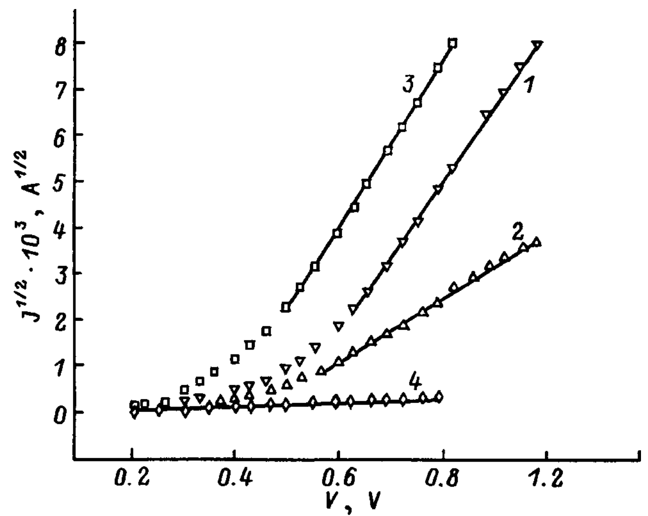

FIG. 5. Square-law approximation of the I–V characteristics of a Al–CeF_3–Si structure in the low-resistance state, for forward biases $V>\varphi_S^0$. φ_S^0, eV: *1* — 0.5, *2* — 0.43, *3* — 0.38, *4* — 0.17.

We found that the primary factor that influenced the electrical characteristics of MIS structures in the low-resistance state was the presence of a layer of ultrathin insulator at the boundary between the semiconductor and the metal conductivity channel. Our analysis of the experimental current-voltage characteristics of the MIS structures with rare-earth fluorides showed that the magnitude of the current flowing through the structure in the low-resistance state was determined by the thickness d of the layer of ultra-thin insulator and the value of the surface potential φ_S^0 at the silicon substrate. For estimated thicknesses of the layer of ultrathin insulator of order 10 Å after switching into the conducting state, the experimental reverse branch of the current-voltage characteristic is described by an exponential function with a region of current saturation.

Our studies showed that the forward branches of the I–V characteristic exhibited three characteristic regions for an initial band bending φ_S^0 corresponding to majority-carrier depletion of the semiconductor surface.

The first region corresponds to limiting of the current through the structure by the semiconductor, when the voltage applied to the structure $V<\varphi_S^0$. In this case the current through the structure is determined by above-barrier emission of majority carriers from the semiconductor into the metal, with an exponential dependence of the current on applied voltage

$$J \sim \exp\left(\frac{qV}{nkT}\right), \tag{2}$$

where q is the electron charge, k is the Boltzmann constant, T is the absolute temperature, and n is the nonideality factor.

The second region comes from limiting of the current by tunneling conductivity of the insulator in the voltage range $\varphi_S^0<V<1.2$ V. In this case the bands are flattened and a voltage of $V-\varphi_S^0$ is dropped across the insulator. In this region the I–V characteristics are determined by the dominant direct tunneling of majority carriers from the semiconductor to the metal, and are described by the relation

$$J \approx B(V-\varphi_S^0)^2, \tag{3}$$

where B is a constant (Fig. 5).

In the third region for $V \geqslant 2$ V the forward current is primarily limited by the spreading resistance of the silicon substrate.

Our investigations showed that the capacitance-voltage characteristics of these structures in the high-resistance state correspond to typical rf capacitance-voltage dependences of MIS structures, with a characteristic saturation of the capacitance in the regions of accumulation and inversion at the semiconductor surface, and exhibit hysteresis phenomena (Fig. 6). For structures with a p-type silicon substrate this hysteresis is caused by the drift of ions in the insulator, while

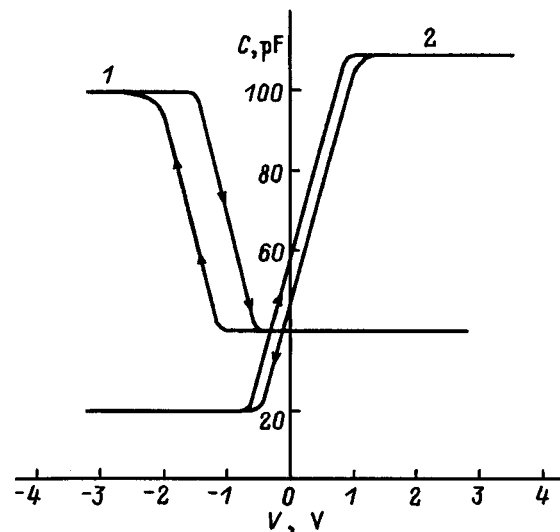

FIG. 6. Capacitance-voltage characteristics of an Al–DyF_3–Si structure. *1*—p-type Si substrate, *2*—n-type Si substrate. The measurement frequency $f=1$ MHz.

for samples with an n-type silicon substrate it is due to trapping of carriers at surface states at the semiconductor-insulator boundary. MIS structures based on p-type silicon store positive charge in the insulator, while for n-type material this charge is negative. The effective density of surface states calculated from capacitance-voltage characteristics at flat-band voltages come to $2.8\times 10^{10}\ \mathrm{cm}^{-2}$ and $2.6\times 10^{11}\ \mathrm{cm}^{-2}$ for structures based on DyF_3 and n- and p-type silicon, respectively.

Switching the MIS structures into the low-resistance state changes their capacitance-voltage characteristics. The values of the insulator capacitance, which are defined as the capacitance of the structure in the range of positive voltages and which correspond to accumulation of charge at the semiconductor surface, turn out to be smaller in the high-resistance state than in the low-resistance state; however, the value of the difference does not exceed 15 pF.

The capacitance in the accumulation regime for a MIS structure in the high-resistance state has the form

$$C_{BC}=\frac{\varepsilon_0\varepsilon_i S}{d_0}, \tag{4}$$

where ε_i is the dielectric constant of the rare-earth fluoride, ε_0 is the dielectric constant of vacuum, S is the contact area, and d_0 is the thickness of the insulator between the contacts.

In the low-resistance state, we should include an additional capacitance parallel to C_{BC}: the capacitance C_i of the thin tunneling insulator layer in a region of the conductivity channel of area A_f. Since $(S-A_f)\cong S$, the capacitance of the structure in the low-resistance state can then be written in the form

$$C_{HC}=\frac{\varepsilon_0\varepsilon_i(S-A_f)}{d_0}+\frac{\varepsilon_0\varepsilon_i^* A_f}{d}\approx C_{BC}+C_i, \tag{5}$$

where ε_i^* is the dielectric constant of the ultrathin insulator layer. Using the value $C_i=1-15$ pF, we can estimate the thickness of the thin tunneling insulator layer d:

$$C_i=C_{HC}-C_{BC}=\frac{\varepsilon_0\varepsilon_i^* A_f}{d}. \tag{6}$$

Setting $\varepsilon_i^*=4$, $r=3\ \mu$m, and $A_f=\pi\cdot r^2=2.83\times 10^{-11}\ \mathrm{m}^2$, we obtain $d=7\times 10^{-11}-10^{-9}\ \mathrm{m}=0.7-10$ Å, while for $r=5\ \mu$m, $A_f=\pi\cdot r^2=7.85\times 10^{-11}\ \mathrm{m}^2$ we obtain $d=2\times 10^{-10}-2.8\times 10^{-9}\ \mathrm{m}=2-28$ Å. These values of d are comparable to those of MIS structures with thin tunneling insulators, in which the dielectric constant ε_i^* of the thin tunneling layer is set equal to the dielectric constant of SiO_2. Since the dielectric constant of rare-earth fluorides is $\sim 8-15$, substitution of this value into Eq. (6) indicates a thicker insulator.

Figure 7 shows experimental plots of the inverse square of the breakdown capacitance per unit area versus voltage for MIS structures based on rare-earth fluorides in the low-resistance state for the example of a Al–Si–CeF_3 structure. From this figure it is clear that at sufficiently large reverse biases there is a direct proportionality between $1/C^2$ and V,

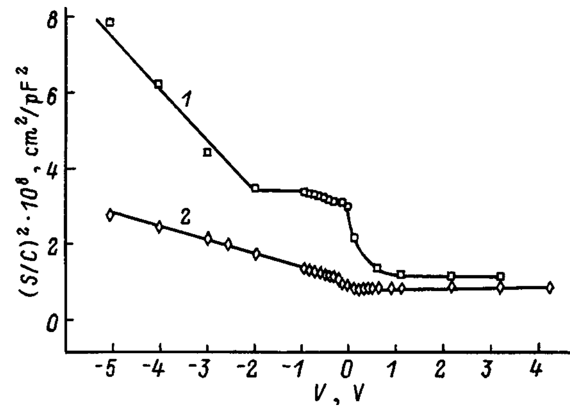

FIG. 7. Experimental dependences of $(S/C)^2$ on voltage for a Al–CeF_3–Si structure. *1*—n-Si–CeF_3, *2*—p-Si–CeF_3; S is the contact area, $f=1$ MHz.

which is characteristic of $p-n$ junctions or Schottky barriers, and that when $V>-2$ V, the C^2-V characteristic deviates from a straight line.

In order to explain these curves we must above all take into account the degree of electrical connection between the metal and semiconductor, which is determined by the insulator thickness. Literature data[7] indicates that for narrow Schottky barriers the high-frequency dependence of C^{-2} on V is well approximated by a straight line for all depletion values of voltages, because in this case the dependence of the capacitance on bias in the region of nonequilibrium depletion is determined by the increase in the thickness of the space-charge region with voltage across the gate. In this case the surface states are in equilibrium with the metal, and so the occupation of surface traps does not change with bias voltage. However, for structures with thin tunneling insulators the approximation of nonequilibrium depletion is not valid if a layer of partial inversion is created at the semiconductor surface.[7] In this case the surface states are in equilibrium with the semiconductor, and the slope of the function C^{-2} versus V is determined by the expression[7]

$$\frac{dC^{-2}}{dV}=\frac{2}{q\varepsilon_S N}\left(1\pm\frac{q^2N_T}{C_i}\frac{dF_T}{d\varphi_S}\right)^{-1}, \tag{7}$$

where N is the concentration of donors or acceptors, N_T is the concentration of hole or electron traps at the semiconductor insulator surface, F_T is their relative occupation at a voltage V, C_i is the capacitance of the insulator, and φ_S is the surface band bending.

For Schottky diodes, when the occupation of interface states is determined completely by the Fermi level in the metal, the condition $dF_T/d\varphi_S=0$ holds, and in this case we can find the concentration of impurities N from Eq. (7). Conversely, given a known N, we can determine the value of the diffusion potential V_{D0}. For metal-thin tunneling insulator-semiconductor structures, when the occupation of interface states is determined by the Fermi level in the semiconductor, the slope is proportional to $(N^*)^{-1}$, where

$$N^*=N\left(1\pm\frac{q^2N_T}{C_i}\frac{dF_T}{d\varphi_S}\right). \tag{8}$$

In this case the point of intersection of the $C^{-2}-V$ characteristics with the voltage axis does not give the value of the diffusion potential V_{D0}.

Thus, the unipolar behavior of the I–V characteristics of MIS structures with rare-earth fluorides in the low-resistance state must be related not to the properties of the channel itself but rather to the contacts between the conducting channel and the semiconductor. Our investigations show that the conducting channel in the rare-earth fluoride film is separated from the substrate by a thin tunneling insulator layer which determines the electrical characteristics of the MIS structures in the low-resistance state. Analysis of our experimental results shows that the thickness of this tunneling insulating layer is 10–40 Å in MIS structures made with rare-earth fluorides in the low-resistance state. Structures with thinner insulator layers ~10–20 Å have characteristics analogous to those of narrow Schottky barriers or $p-n$ junctions.

[1] S. R. Ovshinsky, Phys. Rev. Lett. **21**, 1450 (1968).
[2] J. R. Bosnell and C. B. Thomas, Solid-State Electron. **15**, 665 (1972).
[3] G. S. Nadkarni and V. S. Shirodrar, Thin Solid Films **105**, 115 (1983).
[4] V. A. Rozhkov and M. B. Shalimova, Pis'ma Zh. Tekh. Fiz. **18**, 74 (1992) [Sov. Tech. Phys. Lett. **18**, 53 (1992)].
[5] V. A. Rozhkov and M. B. Shalimova, Fiz. Tekh. Poluprovodn. **27**, 438 (1993) [Semiconductors **27**, 245 (1993)].
[6] V. A. Rozhkov and N. N. Romanenko, Pis'ma Zh. Tekh. Fiz. **19**, 6 (1993) [Tech. Phys. Lett. **19**, 135 (1993)].
[7] Vassilliki Bredimas, J. Appl. Phys. **75**, 7922 (1994).

Translated by Frank J. Crowne

LOW-DIMENSIONAL SYSTEMS

The spectrum of real-space indirect magnetoexcitons

N. E. Kaputkina

Moscow Institute of Steel and Alloys, 117936 Moscow, Russia

Yu. E. Lozovik

Institute of Spectroscopy, Russian Academy of Sciences, 142092 Troitsk, Russia
(Submitted January 12, 1998; accepted for publication February 5, 1998)
Fiz. Tekh. Poluprovodn. **32**, 1354-1362 (November 1998)

This paper discusses two-dimensional excitons with spatially separated electrons and holes in coupled quantum wells and vertically coupled quantum dots in a transverse magnetic field for a wide range of two characteristic quantities of the problem—the distance between wells or dots d and the magnetic field H. Dispersion relations $E_{nm}(P)$ are calculated for coupled quantum wells at various values of d and H (where P, the magnetic momentum along the well, is a conserved quantity in the magnetic field). The spectrum is calculated by numerically diagonalizing the Hamiltonian in various bases—either a Coulomb or a Landau basis (the choice of basis is determined by the value of effective magnetic field). Asymptotic energy dependences (with respect to d, H, P) are determined analytically. As the momentum P increases, the exciton spectrum in a weak fixed H crosses over from Coulombic to magnetic, and for large P consists of bands adjacent to the Landau levels. Also discussed is the problem of an electron spatially separated from a charged impurity in coupled quantum wells. © *1998 American Institute of Physics.* [S1063-7826(98)01411-2]

1. INTRODUCTION

Recently, systems of real-space indirect excitons (i.e., excitons with spatially separated electrons and holes) in coupled quantum wells, and also in double and coupled quantum dots, have been studied experimentally, notably in external transverse magnetic fields (see Refs. 1–13).

Analysis of the physical properties of electron-hole systems in coupled quantum wells,[14,15] especially in a transverse magnetic field,[16–21] reveals very interesting collective properties and a number of different phases. Possible phenomena such as the superfluidity of real-space indirect excitons predicted in Ref. 14, which would manifest itself as a nonattenuating electric current in each of the quantum wells (see also Refs. 15, 21, and 22, and the interesting quasi-Josephson effects predicted in Refs. 23–25, would be particularly interesting, especially if observed directly. The possibility of observing these phases is determined by the ratio of the exciton lifetime to the time needed to establish equilibrium (the lifetime should be considerably longer than the relaxation time). For an electron and hole localized in different quantum wells, the overlap of the wave function is small, which decreases the probability of mutual annihilation. The application of an electric field perpendicular to the electron and hole layers also decreases the rate of recombination by decreasing the overlap of the wave function. A magnetic field influences the lifetime, the diffusion coefficient,[4–6] and the photoluminescence spectrum of the excitons (see Refs. 1–13). The observed effects are attributed to superfluidity of the real-space indirect excitons.

These facts make a detailed investigation of an isolated exciton with spatially separated electrons and holes (a ''real-space indirect'' exciton) in a transverse magnetic field interesting. The problem of two-dimensional ($2D$) excitons in strong magnetic fields was discussed in Ref. 16 for direct excitons and in Refs. 14 and 15 for real-space indirect excitons. However, in these papers the investigators usually study only the asymptotic case of extremely high magnetic fields, when the Coulomb interaction can be treated as a small perturbation.

In this paper we will discuss the general problem of spatially separated $2D$ excitons in an external transverse magnetic field for a wide range of values of the magnetic field H and interwell distance d. We will find the dispersion relation $E_{nm}(P)$ in coupled quantum wells for various d and H (where P is the magnetic momentum along the quantum well, which is conserved in a magnetic field). As the value of the effective magnetic field increases (see below) the energy spectrum changes from a hydrogenic spectrum at $H = 0$ to equidistant Landau levels. Note that the effective magnetic field is increased not only by increasing the external field H but also by increasing d and P (for $H \neq 0$).

We will also discuss the problem of spatially separated excitons in vertically coupled quantum dots with parabolic confining potentials.

For these calculations we will use diagonalization of the exact Hamiltonian in various bases.

 © 1998 American Institute of Physics

2. SPATIALLY SEPARATED 2D EXCITONS IN A TRANSVERSE MAGNETIC FIELD

Consider a spatially separated electron e and hole h in different planes in an external transverse magnetic field. This model is valid for narrow quantum wells such that $D \ll a^*$, where $a^* = \hbar\varepsilon/2m^* e^2$ is the radius of the two-dimensional exciton in one plane in the absence of a field, ε is the dielectric constant,[1)] $m^* = m_e^* m_h^*/m_e^* + m_h^*$ is the reduced mass, and $m_{e,h}^*$ are effective masses of the electron and hole. In light of the axial symmetry of the problem, we will use $\mathbf{A} = \mathbf{H}\mathbf{r}/2$, i.e., a symmetric gauge for the vector potential.

The Schrödinger equation has the form

$$\left[\frac{1}{2m_e^*}\left(-i\hbar\nabla_e + \frac{e}{c}A_e\right)^2 + \frac{1}{2m_h^*}\left(-i\hbar\nabla_h - \frac{e}{c}A_h\right)^2 - \frac{e^2}{\varepsilon((\mathbf{r}_e - \mathbf{r}_h)^2 + d^2)^{1/2}}\right]\psi = E\psi, \tag{1}$$

where d is the distance between electron and hole layers (the width of the barrier layer in the coupled quantum wells), and $\mathbf{r}_{e,h}$ are the coordinates of the electron and hole along the quantum well. The role of two-dimensional momentum of the exciton in a magnetic field is played by a conserved quantity—the magnetic momentum, whose operator is

$$\hat{P} = -i\hbar\nabla_e + \frac{e}{c}(\mathbf{A}_e - \mathbf{A}_h) - \frac{e}{c}[\mathbf{H}, \mathbf{r}_e - \mathbf{r}_h] \tag{2}$$

and $\hat{P}$ commutes with the Hamiltonian (see Refs. 16, 26, and 27). The conservation law for P is related to invariance of the system with respect to simultaneous translation of e and h and a gauge transformation.

Let us impose the change of coordinates that separates the center of mass coordinate of the exciton $\mathbf{R} = m_e/m_e + m_h \mathbf{r}_e + m_h/m_e + m_h \mathbf{r}_h$ from the coordinate of relative motion of the electron and hole $\mathbf{r} = \mathbf{r}_e - \mathbf{r}_h$.

Then $\hat{P} = -i\hbar\nabla_p - e/2c\,[\mathbf{H},\mathbf{r}]$. The eigenfunctions of the operator $\hat{P}$ are

$$\psi_p(\mathbf{r}_e\mathbf{r}_h) = \psi_p(\mathbf{r},\mathbf{R}) = \exp\left\{\left(iP + \frac{e}{2c}[\mathbf{H},\mathbf{r}]\frac{R}{\hbar}\right)\right\}\psi_p(\mathbf{r}),$$

$$\hat{P}\psi_p = P\psi_p. \tag{3}$$

Introducing $M = m_e^* + m_h^*$ and $\gamma = m_h^* - m_e^*/m_h^* + m_e^*$, we can rewrite the equation for the relative motion of the electron and hole in the form

$$\left\{-\frac{\hbar^2}{2m^*}\nabla\mathbf{r} + \frac{ie\hbar}{2m^*c}\gamma H[\mathbf{r},\nabla\mathbf{r}] + \frac{e^2}{8m^*c^2}[\mathbf{H},\mathbf{r}]^2 + \frac{e^2}{m^*c}[\mathbf{P},\mathbf{H}]r - \frac{e^2}{\varepsilon(r^2+d^2)^{1/2}} + \frac{P^2}{2M}\right\}\psi_p(\mathbf{r}) = E\psi_p. \tag{4}$$

Using the transformation (see Refs. 16 and 27)

$$\psi(\mathbf{r}) = \Phi(\mathbf{r} - \boldsymbol{\rho}_0)\exp\left(\frac{i\gamma\mathbf{r}\mathbf{P}}{2\hbar}\right),$$

$$\boldsymbol{\rho}_0 = \frac{c}{eH^2}[\mathbf{H},\mathbf{P}], \quad \boldsymbol{\rho} = \mathbf{r} - \boldsymbol{\rho}_0 \tag{5}$$

the equation for relative motion of the electron and the hole takes the form

$$\left\{-\frac{\hbar^2}{2m^*}\nabla\rho + \frac{ie\hbar}{2m^*c}\gamma H[\rho\nabla] + \frac{e^2}{8m^*c^2}H^2\rho^2 - \frac{e^2}{8m^*c^2}H^2\rho^2 - \frac{e^2}{\varepsilon((\boldsymbol{\rho}+\boldsymbol{\rho}_0)+d^2)^{1/2}}\right\}\Phi(\boldsymbol{\rho}) = E\Phi(\boldsymbol{\rho}). \tag{6}$$

Let us introduce the following units of energy, length, cyclotron frequency, and magnetic field:

$$E_0 = \frac{2m^*e^4}{\varepsilon^2\hbar^2}, \quad r_0 = \frac{\hbar^2\varepsilon}{2m^*e^2},$$

$$\omega_{c_0} = \frac{2m^*e^4}{\varepsilon^2\hbar^3}, \quad H_0 = \frac{2(m^*)^2e^3}{\varepsilon^2\hbar^3}c \tag{7}$$

(the units of measurement for energy and length correspond to binding energy and radius of a two-dimensional exciton). Making these equations dimensionless reduces them to the form

$$\left[\Delta\rho - i\gamma\omega_L\frac{\partial}{\partial\Theta} - \frac{\omega_L^2}{4}\rho^2 + \left(\left(\frac{1}{\boldsymbol{\rho}+\boldsymbol{\rho}_0}\right)^2 + d^2\right)^{1/2} + E\right]\Phi(\boldsymbol{\rho}) = 0, \tag{8}$$

where $\omega_L = \omega_c/2$ is the Larmor frequency. In our units the magnetic length is $r_H = \sqrt{1/\omega_L}$.

This equation can be solved numerically by expanding in a suitable basis of functions that gives rapid convergence for a given ratio of parameters of the problem. In an ''effectively weak'' magnetic field, all the parameters—H (or ω_L), d, and P (or ρ_0)—are all small at the same time, i.e., the quantity $\omega_L(d^2 + \rho_0^2 + 1)$ is small. In this case, a suitable basis will be a basis of hydrogenic functions (for the 2D case, a basis for two-dimensional hydrogen). In an effectively strong magnetic field [for large values of $H(\omega_L)$, or d, or ρ_0] a suitable basis will be a basis of functions that coincide formally with wave functions for a charged particle in a magnetic field. In reality this basis will be suitable for intermediate magnetic fields as well, and is especially good for efficient coupling. In the limit of ultra-strong magnetic fields and for $d = 0$, our results coincide with the results of Ref. 16.

For weak magnetic fields a suitable basis will be a basis of functions close to the eigenfunctions of the equation

$$\left[\Delta\rho + E_{0_{nm}} + \frac{1}{((\boldsymbol{\rho}+\boldsymbol{\rho}_0)^2 + d^2)^{1/2}}\right]f_{nm}(\boldsymbol{\rho}) = 0. \tag{9}$$

Let us make the replacement

$$f_{nm}(\boldsymbol{\rho})=\chi_{nm}(\boldsymbol{\rho}+\boldsymbol{\rho}_0)=\chi_{nm}(\mathbf{r}). \quad (10)$$

Starting from the symmetry of the problem, we set $\chi_{nm}(\mathbf{r}) = e^{im\Theta}\Phi_{nm}(r)A_{nm}$, where

$$\frac{\partial^2\Phi_{nm}}{\partial r^2}+\frac{1}{r}\frac{\partial\Phi_{nm}}{\partial r}+\left(E_{0_{nm}}-\frac{m^2}{r^2}+\frac{1}{(r^2+d^2)^{1/2}}\right)\Phi_{nm}=0. \quad (11)$$

For large interlayer distances $d\gg 1$ the problem reduces to an oscillator problem. The eigenfunctions have the same form as the magnetic functions:

$$\Phi_{nm}(r)=A_{nm}L_n^{|m|}\left(\frac{\omega_d}{2}r^2\right)e^{-\frac{\omega_d}{2}\frac{r^2}{2}}r^{|m|};$$

$$A_{nm}=\left(\frac{1}{\pi}\frac{n!}{(n+|m|)!}\left(\frac{\omega_d}{2}\right)^{\frac{|m|+1}{2}}\right)^{1/2}, \quad (12)$$

where $\omega_d=\sqrt{\omega_L^2+2/d^3}$.

The energy eigenvalues are

$$E_{nm_0}=2\omega_d\left(n+\frac{|m|+1}{2}\right)-\gamma m\omega_L-1/d. \quad (13)$$

These results are correct not only for effectively weak magnetic fields (when $\omega_L^2\ll 1/d^3$ and $\omega_d\sim\sqrt{1/2d^3}$), but also for arbitrary magnetic fields (in the approximation $d\gg 1$; see below).

For small d the field is no longer effectively weak. In our computations we used an expansion in a basis of hydrogenic functions.

The system of eigenfunctions is

$$\Phi_{mn}(r)=C_{nm}e^{-\sqrt{|E_{0_n}|}r}(\sqrt{|E_n|})^{|m|+1/2}\,r^{|m|}\times\sum_{s=0}^{n-|m|}A_s\sqrt{|E_{0_n}|^s}r^s, \quad (14)$$

where $A_0=1$, $A_s=A_{s-1}\,2(S+|m|-n-1)/S(S+2|m|)$ $(S>0)$, and C_{nm} is a normalizing coefficient.

The energy eigenvalues are:

$$E_{0_n}=-\frac{1}{4(S+|m|+1/2)^2}=-\frac{1}{4(n+1/2)^2}, \quad (15)$$

where $n=S+|m|=0,1,2\ldots$.

The energy depends on a single quantum number $n=S+|m|$.

Let us discuss the effects of a weak magnetic field, i.e., the Zeeman effect for a $2D$ exciton. To first order in perturbation theory, when $V_{00}=\omega_c^2/4(r^2+\rho_0^2-2r\rho_0\cos\Theta)$ we have $\langle 00|V_{00}|00\rangle=(\omega_c/2)^2 2\rho_0$. For $\rho_0=0$ $(P=0)$ the correction reduces to zero.

The first correction to a level with quantum numbers $m=0$, $n=0$ $(n_1=1)$ has a minimum with respect to ρ_0, i.e., with respect to the magnetic momentum P, at $\rho_0=0$ (a minimum at $\rho_0=0$ will occur for the ground state in strong fields as well). In weak magnetic fields the correction to the hydrogenic energy levels is $\langle nm|V_{00}|nm\rangle\sim a_1\omega_c^2+a_2\boldsymbol{P}\omega_c$, i.e., for small momenta the energy is quadratic in the magnetic field ω_c, while for large momenta it is linear.

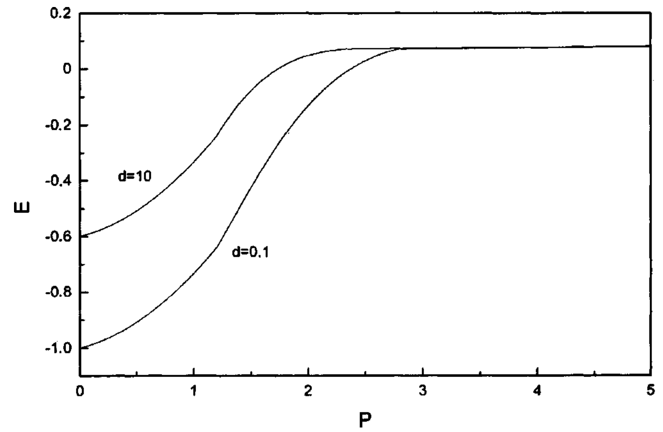

FIG. 1. Dispersion relation $E(P)$ for the ground state of a magnetoexciton for interlayer distances $d=0.1$, 10; the Larmor frequency for the magnetic field $\omega_L=0.1$, $\gamma=0$.

Numerical diagonalization of the Hamiltonian in a basis of two-dimensional hydrogenic functions, which correspond to the Coulomb interaction of an electron and hole, determines the excitonic energy spectrum to high accuracy in a weak magnetic field H. The calculated results appear on the left side (Fig. 1), which corresponds to values of P that are moderately large.

With increasing d and fixed H the magnetic field becomes effectively stronger (compared to the interaction between e and h) and it is more convenient to use a basis for particles in a magnetic field. The magnetic field becomes effectively stronger at large magnetic momenta $P(\rho_0)$ as well, due to the increase in average distance of e and h along the layer $\rho_{eh}\sim P$.

For effectively strong magnetic fields (and also, as numerical calculations show, in the case of intermediate magnetic fields) a basis of eigenfunctions determined by the following equation is a suitable basis:

$$\left[\Delta_\rho+E_{0_{nm}}-i\gamma\omega_L\frac{\partial}{\partial\Theta}-\frac{\omega_L^2}{4}\rho^2\right]f_{nm}(\boldsymbol{\rho})=0, \quad (16)$$

where ω_L is the Larmor frequency.

The system of eigenfunctions has the form

$$f_{nm}(\boldsymbol{\rho})=e^{im\Theta}L_n^{|m|}\left(\frac{\omega_L}{2}\rho^2\right)e^{-\frac{\omega_L}{2}\frac{\rho^2}{2}}\rho^{|m|}\times\left(\frac{1}{\pi}\frac{n!}{(n+|m|)!}\left(\frac{\omega_L}{2}\right)^{|m|+1}\right)^{1/2}. \quad (17)$$

The corresponding energy eigenvalues are

$$E_{0_{nm}}=2\omega_L\left(n+\frac{|m|-\gamma m+1}{2}\right), \quad (18)$$

where $n=0,1,2\ldots$ $m=0,\pm1,\pm2\ldots$ (for $\gamma=1$ they coincide with the Landau spectra).

The eigenfunctions of the problem coincide formally with the wave functions of a single charged particle in the magnetic field. As for the energy levels, in contrast to the problem of a single particle these are split (if $\gamma\neq 1$) with

respect to quantum number m. The unperturbed spectrum of the system f_{nm} is completely discrete, but the energy levels are degenerate with respect to **P** (or ρ_0).

For very strong effective magnetic fields, we can estimate the energy spectrum (and wave functions) by including only transitions between levels with the same symmetry. Then the energy levels are determined by the condition $\Sigma_n[(E_0)_{nm}-E]\delta_{nn'}+V^m_{nn'}=0$, where

$$V^m_{nn'}=-\frac{2}{\pi}\sqrt{\frac{n!n'!}{(n+|m|)!(n'+|m|)!}}\sum_{i=0}^{n}\sum_{j=0}^{n'}\frac{(-1)^{i+j}}{i!j!}\times\binom{n+|m|}{n-i}\binom{n'+|m|}{n'-j}\int\frac{e^{-t}t^{i+j+|m|}}{(d^2+(\sqrt{t}\sqrt{2/\omega_L}+\rho_0)^2)^{1/2}}\times K\left(\left(\frac{4\rho_0\sqrt{2/\omega_L}\sqrt{t}}{d^2+(\rho_0+\sqrt{2\omega_L}\sqrt{t})^2}\right)^{1/2}\right)dt, \tag{19}$$

and $K(x)$ is a complete elliptic integral of the first kind.

$V^m_{nn'}$ corresponds to excitations with transitions to levels with the same symmetry, i.e., with the same quantum number m. Note that we do not limit the analysis to the first correction in perturbation theory for the Coulomb interaction, although in the limit of superstrong fields the results of calculations to first order in perturbation theory already give good accuracy for the results and the correct asymptotic dependences (for $d\rightarrow 0$; see the results of Refs. 16 and 17). However, by not ignoring the transitions between levels we extend the region of applicabilities of our method to intermediate magnetic fields as well.

In general, transitions to levels with different symmetries $m\neq m'$ will correspond to the matrix element

$$V^{mm'}_{nn'}=-\sqrt{\frac{n!n'!}{(n+|m|)!(n'+|m'|)!}}\frac{1}{\pi}\times\sum_{i=0}^{n}\sum_{j=0}^{n'}\frac{(-1)^{i+j}}{i!j!}\binom{n+|m|}{n-i}\binom{n'+|m'|}{n'-j}\times\int_0^\infty\int_0^{2\pi}\frac{e^{-t}t^{i+j+\frac{|m|+|m'|}{2}}dt\,e^{i(m-m')\Theta}d\Theta}{\left(d^2+\rho_0^2+\left(\frac{2}{\omega_L}\right)t+2\rho_0\left(\sqrt{\frac{2}{\omega_L}}\right)\sqrt{t}\cos\Theta\right)}. \tag{20}$$

Thus, numerical diagonalization of the Hamiltonian in a basis of the corresponding magnetic functions f_{nm} can give us energy spectra of spatially separated excitons over a wide range of magnetic fields **H** and distances d between the e and h layers.

Figure 1 shows the dependence of the energy of the ground state on momentum P (the dispersion relation) for a weak magnetic field $H=0.1$ and various d. As P increases, the energy levels reduce to levels of Landau type in a magnetic field [see Eq. (18)]. The same thing happens with increasing separation d. Thus, increasing H, d, or P causes a reconstruction of the spectrum from hydrogenic to magnetic.

Figure 2 shows the dispersion relations $E(P)$ for low-energy levels of the spectrum of spatially separated excitons in a magnetic field obtained by numerical diagonalization of the Hamiltonian in a strong magnetic field H for the corresponding basis. The spectrum consists of bands adjacent to the corresponding Landau levels (n,m) that evolve as the magnetic momentum P (the quantity ρ_0) changes continuously. With increasing H, the energy increases, and with increasing d, it converts to Landau levels. With increasing effective magnetic field [i.e., increasing H and (or) d], these energy bands contract and are still more strongly separated from one another, and the spectrum approaches the unperturbed spectrum f_{nm}, i.e., a system of Landau levels (for the degenerate levels see below).

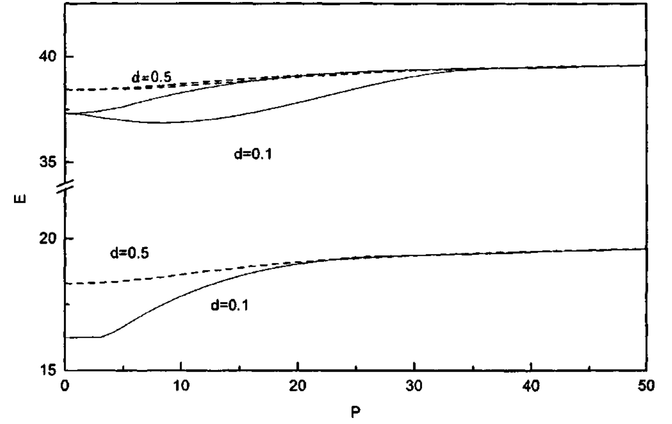

FIG. 2. Dispersion relation $E(P)$ for the lowest levels of the energy spectrum of a magnetoexciton for interlayer distances $d=0.1$, 0.5; the Larmor frequency of the magnetic field $\omega_L=10$, $\gamma=0$.

For the ground state with the corresponding quantum numbers $(n=0,\ m=0)$ there is a single extremum (a minimum) at $\rho_0=0$. For energy levels that correspond to excited states other (lateral) extrema can also exist, in particular, more minima. For nonzero d, as the effective magnetic field increases, i.e., as the ratio $d/r_H=d\sqrt{\omega_L}$ increases, the lateral minima and maxima become progressively shallower, and finally disappear. For the level with quantum numbers $n=0$, $m=1$ the smoothing-out and disappearance of lateral

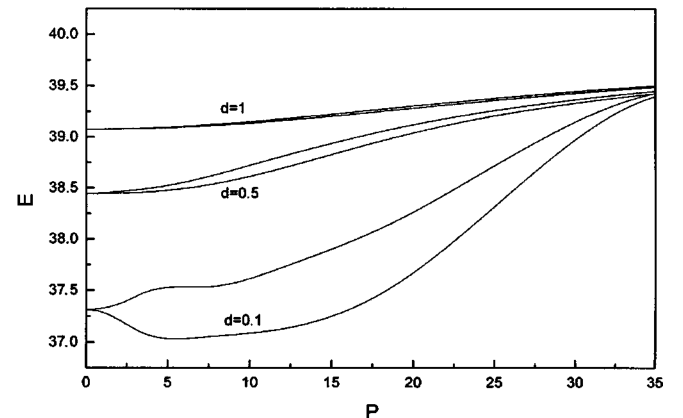

FIG. 3. Dispersion relation $E(P)$ for the energy of the first degenerate state of a magnetoexciton for interlayer distances $d=0.1$, 0.5, 1; the Larmor frequency of the magnetic field $\omega_L=10$, $\gamma=0$. The disappearance of the "roton" minimum with increasing d is apparent.

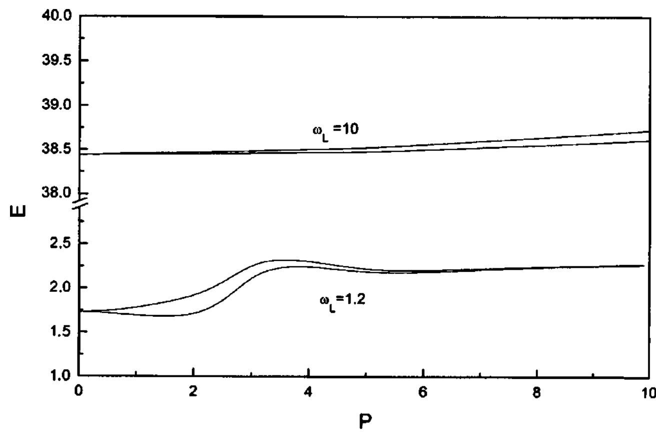

FIG. 4. Dispersion relation $E(P)$ for the energy of the first degenerate state of a magnetoexciton for interlayer distance $d=0.5$; the Larmor frequencies of the magnetic field $\omega_L=1.2$, 10, $\gamma=0$. The disappearance of the ''roton'' minimum with increasing ω_L is apparent.

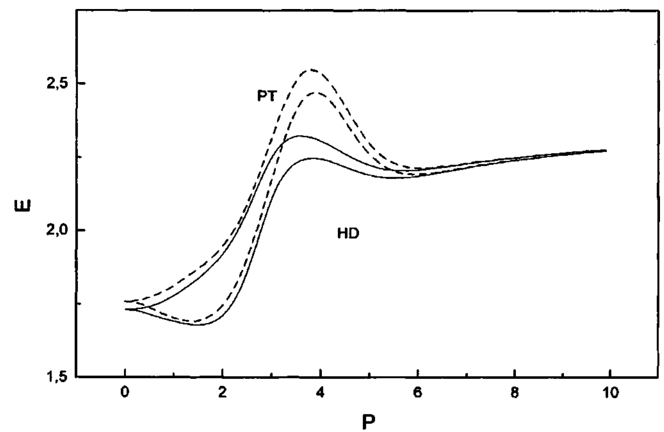

FIG. 5. Comparison of the dispersion relations $E(P)$ for the energy of the first degenerate state of a magnetoexciton for interlayer distances $d=0.5$ and the Larmor frequency of the magnetic field $\omega_L=1.2$, $\gamma=0$, obtained by perturbation theory with respect to the Coulomb interaction (curve PT) and numerical diagonalization of the Hamiltonian (curves HD).

minima with increasing d and H (and consequently with increasing ratio d/r_H) is shown in Figs. 3 and 4.

The matrix elements corresponding to transitions with the same symmetry give the main contribution for small ρ_0 and have extrema for $\rho_0=0$ $(P=0)$. Therefore, the dispersion curves have extrema for $\rho_0=0$ $(P=0)$.

For large momenta $P\gg 1$ $(\rho_0\gg 1)$ the correction to the energy is

$$E^{(1)}_{nm}=V^{nm}_{nm}(P,d)$$
$$=-\sqrt{\omega_L}\left[\frac{\sqrt{\omega_L}}{P}+\frac{(\langle\rho^2\rangle_{nm}-2d^2)\omega_L}{4}\left(\frac{\omega_L}{P}\right)^3\right],$$

where the characteristic size of the wave function of a charged particle in a magnetic field is $\langle\rho^2\rangle_{nm}\sim r_H^2=1/\omega_L$ for n and m that are moderately large.

In strong magnetic fields the primary contribution to the energy eigenvalues comes from levels with the same symmetry, since $V^{mm'}_{nn'}\ll V^{mm}_{nn'}$, $m\neq m'$. The corresponding matrix elements are

$$V^m_{nn'}\rightarrow-\frac{\delta_{nn'}}{\sqrt{\rho_0^2+d^2}}\quad\text{for}\quad\rho_0\neq 0\quad\text{or}\quad d\neq 0.$$

Here the role of a small parameter is played by the magnetic length $1/\sqrt{\omega_L}=r_H$.

For the ground state $n=0$, $m=0$ if ρ_0 or the interlayer distance d greatly exceed the magnetic length r_H, then the correction to the Landau level energy is $E^1_{00}\approx V^{00}_{00}\approx-1/\sqrt{\rho_0^2+d^2}\,(1-1/\rho_0^2+d^2\,r_H^2)$. If, however, both d and $\rho_0\ll r_H$, then the correction to the energy is $E^1_{00}\approx V^{00}_{00}\approx-\sqrt{\pi/2}\,1/r_H$. When $\rho_0=0$, $d=0$, the energy is $E_{00}=E_{0_{00}}+V^{00}_{00}=\omega_L-\sqrt{\pi/2}\sqrt{\omega_L}$.

Although the absolute value of the correction increases with increasing field as $\sqrt{\omega_L}(1/r_H)$, its relative value $|V^{00}_{00}|/E_{0_{00}}$ does not fall off like $1/\sqrt{\omega_L}\,(r_H)$.

For $d\neq 0$ and $\rho_0\neq 0$, starting with certain values of the Larmor frequency for the magnetic field ω_L such that $r_H\ll\max(d,\rho_0)$, the matrix element $V^{00}_{00}\approx-1/\sqrt{\rho_0^2+d^2}\,(1-1/\rho_0^2+d^2\,r_H^2)$. The correction increases with increasing magnetic field, but its relative value $V^{00}_{00}/E_{0_{00}}=1/\sqrt{\rho_0^2+d^2}\,r_H^2(1-1/\rho_0^2+d^2)$ decreases as r_H^2 (i.e., as $1/\omega_L$).

With increasing H, as with increasing P or d, the relative contribution of the Coulomb interaction falls off and, accordingly, the levels become closer and closer to the Landau levels.

However, when the ''magnetic'' terms in $\hat{H}$ are small compared to the Coulomb interaction, the picture is close to the Coulomb problem, i.e., the spectrum is close to that of the two-dimensional hydrogen atom.

For $\gamma=0$, i.e., $m_e=m_h$,

$$E_{0_{nm}}=\frac{\omega_c}{2}(2n+|m|+1)=\omega_L\cdot k,$$

where $k=2n+|m|+1$ $k=1,2\ldots$. The energy $E_{0_{nm}}$ depends only on the quantum number k and the kth unperturbed level is k-fold degenerate. The Coulomb interaction lifts this degeneracy for nonzero momentum $P\neq 0$ $(\rho_0\neq 0)$. This results in the dispersion relation $E(P)$.

The ground-state level $n=0$, $|m|=0$ $(k=1)$ is nondegenerate, and higher levels are degenerate. The dispersion relations for $\rho_0\neq 0$, taking into account the wave interactions, are shown in Figs. 5 and 6. In the unperturbed problem (neglecting the Coulomb interaction) the level with $k=2$ $(n=0,\ |m|=1)$ is doubly degenerate with respect to the quantum number m $(m=\pm 1)$. For ultrastrong magnetic fields we can estimate the splitting by solving a secular equation. We find $E_{k=2}=E_{0_{k=2}}\pm E_{1_{k=2}}$, where

$$E_{0_{k=2}}=2\omega_L+V^{01}_{01}(\rho_0,d);$$
$$E_{1_{k=2}}=-1/(1/2)_2\int_0^\infty e^{-t}t1/\sqrt{b}((a/b)^2-1)^{1/4}$$
$$\times P^2_{-1/2}(a/b/\sqrt{a/b-1})dt;$$

here $P^2_{-1/2}(x)$ is the associated Legendre function.

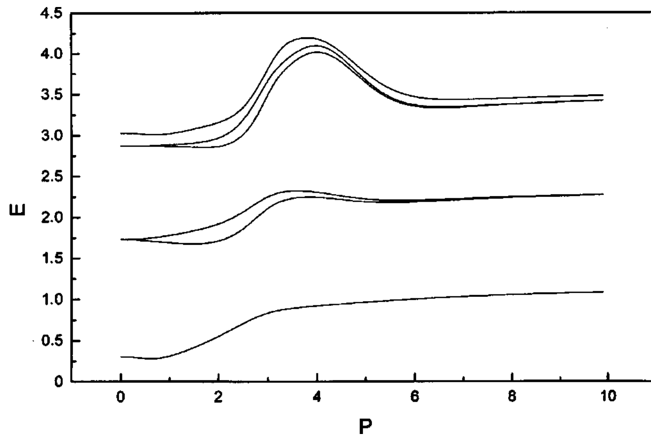

FIG. 6. Dispersion relations $E(P)$ for the lowest energy levels of a magnetoexciton for interlayer distances $d=0.5$; the Larmor frequency of the magnetic field $\omega_L=1.2$, $\gamma=0$.

As the effective magnetic field increases, the splitting decreases. When $P\to\infty$ ($\rho_0\to\infty$) or $d\to\infty$, the splitting $E_{1_{k=2}}\to 0$. For $\rho_0\ll 1$ we have

$$E_{1_{k=2}}\approx-\sqrt{\frac{\pi}{2}\omega_L}\cdot\frac{\omega_L}{16}\left[(3+6d^2\omega_L+d^4\omega_L^2)e^{\frac{d^2\omega_L}{2}}\times\operatorname{erfc}\left(d\sqrt{\frac{\omega_L}{2}}\right)-\frac{2}{\sqrt{\pi}}(5+d^2\omega_L)d\sqrt{\frac{\omega_L}{2}}\right]\rho_0^2.$$

For higher levels the dispersion relation is shown in Fig. 6.

Consider the case of an infinitely heavy hole $\gamma=1(m_h\gg m_e)$. For $P=0$ the energy levels of the impurity and exciton states coincide (for the spatially separated case $d\neq 0$, with impurity charge $+e$):

$$E_{0_{nm}}=2\omega_L\left(n+\frac{|m|-\gamma m+1}{2}\right)=\omega_c\left(n+\frac{1}{2}+\frac{|m|-m}{2}\right).$$

The energy levels $E_{0_{nm}}$ are infinitely degenerate. The Coulomb interaction lifts the degeneracy $P=0\to\rho_0=0$ $V_{nm}^{mm'}=0$ for $m\neq m'$, and the system of equations splits into subsystems. Transitions between levels with different symmetry do not contribute to the energy. For $P=0$ it is necessary to take into account only the interaction of levels with the same symmetry. The matrix elements are $V_{00}^m=(\omega_L/2)^{1+|m|}d^{2|m|}\psi(|m|,|m|+3/2,d^2\omega_L/2)$. The level with $n=n'=0$ acquires a fine structure due to splitting with respect to $|m|$.

For effectively large distances d such that $d^2\omega_L/2\gg 1$ ($d\gg r_H$), the matrix element $V_{00}^m\approx-1/d[1-|m|+1/d^2\omega_L]$. The level with $n=0$, i.e., the ground state, shifts downward by an amount $1/d$, and the fine structure of the level increases upward with increasing $|m|$ equidistantly: $(\approx|m|/d^3\omega_c)$.

For effectively small distances d such that $d^2\omega_L/2\ll 1$ ($d\ll r_H$), we obtain $V_{00}^m\approx-\sqrt{\omega_L/2}\,|m|-1/2/|m|![|m|-1/2-d^2\omega_L/4]$. The fine structure is bunched together from above and below onto the unperturbed level.

As the quantum number m increases, we can estimate the corresponding energy levels via the matrix elements $V_{00}^m\to-\sqrt{\omega_L/2}(1/\sqrt{|m|}-\omega_L d^2/4|m|^{3/2})\to-1/\sqrt{|m|}$ as $|m|\to\infty$.

For an impurity with charge $Z\neq 1$ we include a factor of Z in all the expressions listed above: $V_{nn'}^m|_{Z\neq 1}=V_{nn'}^m|_{Z=1}\cdot Z$.

For rational $\gamma=P/q$, energy levels $E_{0_{nm}}$ and $E_{0_{n'm'}}$ will coincide without including the Coulomb interaction if

$$\frac{2(n-n')-|m'|+|m|}{m-m'}=\gamma=\frac{P}{q},$$

$$P=2(n-n')+|m|-|m'|,\quad q=m-m'.$$

These quasidegeneracies are accidental crossings of energy levels and do not reflect any internal symmetry of the problem. Since our method allows us to include mixing of levels with different quantum numbers, they likewise do not limit its applicability (in contrast to the construction of first-order perturbation theory in the Coulomb interaction, as was done for example in Ref. 16).

Inclusion of the film thickness for sufficiently thin layers in the case of strong magnetic fields changes the dispersion relation somewhat quantitatively, but not qualitatively; with increasing momentum, this change decreases (see also Refs. 26 and 28).

There is reasonable agreement between results calculated by numerical diagonalization of the Hamiltonian in the corresponding basis and experimental results (see Refs. 4–6, 8, and 9).

3. REAL-SPACE INDIRECT EXCITONS IN COUPLED QUANTUM WELLS

Situations in which an exciton is localized in a quantum well[8,29] due to surface roughness of the boundary can be experimentally realized; this roughness generates ''natural'' quantum dots. Also possible is localization of an exciton in an artificial quantum dot or in vertically coupled quantum dots. For this reason, we now discuss the energy spectrum of a real-space indirect $2D$ exciton within the following model which describes the experimental situations mentioned above: an electron e and a hole h with effective masses m_e^* and m_h^* are located in two vertically coupled two-dimensional quantum dots separated by a barrier of width d and described respectively by parabolic potentials $U=\alpha_e r_e^2$ and $U=\alpha_h r_h^2$ (where $\mathbf{r}_e$ and $\mathbf{r}_h$ are the two-dimensional radius vectors of e and h along the plane of the quantum dots) (we will use units of the curvature parameter α_0 for the confining potential: $\alpha_0=E_0/r_0^2$).

Making the coordinate substitutions that separate out the motion of the center of mass $\mathbf{R}=\mu_e\mathbf{r}_e+\mu_h\mathbf{r}_h$ and $\mathbf{r}=\mathbf{r}_e-\mathbf{r}_h$, we transform the Schrödinger equation to the form

$$\left[\mu_e\mu_h\Delta_{\mathbf{R}}+\Delta_{\mathbf{r}}+E+\frac{i\gamma\omega_c m}{2}\frac{\partial}{\partial\theta_r}-\left(\alpha_e+\alpha_h+\frac{\omega_c^2}{4}\right)R^2 -\left(\mu_h^2\left(\alpha_e+\frac{\omega_c^2}{4}\right)+\mu_e^2\left(\alpha_h+\frac{\omega_c^2}{4}\right)\right)r^2+\frac{1}{(r^2+d^2)^{1/2}} -2\left(\frac{\omega_c^2}{4}(\mu_h-\mu_e)+\mu_h\alpha_e-\mu_e\alpha_h\right)\mathbf{rR}\right]\psi=0. \quad (21)$$

For simplicity we consider the case $\omega_c^2/4(\mu_h-\mu_e)+\mu_h\alpha_e-\mu_e\alpha_h=0$. This equation will hold, for example, when the quantum dots are identical and $\mu_e=\mu_h$. Then it is possible to separate the motion of the center of mass of the exciton from the relative motion of the electron and hole. Setting $\psi(\mathbf{R,r})=\psi_R(\mathbf{R})\psi_r(\mathbf{r})$, we obtain the system of equations:

$$\left(\Delta_{\mathbf{R}}+\frac{E_R}{\mu_e\mu_h}-\alpha_1R^2\right)\psi_R=0, \quad (22)$$

$$\left(\Delta_{\mathbf{r}}+E_r-\alpha_2r^2+\frac{1}{(r^2+d^2)^{1/2}}\right)\psi_r=0, \quad (23)$$

$$E=E_R+E_r+\frac{i\gamma\omega_c m}{2}, \quad (24)$$

where $\alpha_1=\alpha_e+\alpha_h/\mu_e\mu_h+\omega_c^2/4$ and $\alpha_2=\mu_h^2\alpha_e+\mu_e^2\alpha_h+\omega_c^2/16$.

Thus, Eq. (22) for the center of mass has the form of a harmonic oscillator equation. Its solution gives for the center of mass energy E_R and eigenfunctions ψ_R:

$$E_{R_{nm}}=4\alpha_1^{1/2}\left(n+\frac{|m|+1}{2}\right), \quad (25)$$

$$\psi_{R_{nm}}=\left(\frac{n!}{\pi(|m|+n)!}(\alpha_r)^{|m|+1}\right)^{1/2}\times R^{|m|}e^{-\sqrt{\alpha_1}R^2/2}L_n^{|m|}(\sqrt{\alpha_1}R^2)e^{im\theta}. \quad (26)$$

The equation of relative motion Eq. (23) differs from the equation for the center of mass Eq. (22) by the inclusion of the electron-electron interaction. In accordance with symmetry of the problem, the wave function of relative motion can be written in the form $\psi_r(\mathbf{r})=f_m(r)\exp(im\theta)$, where $m=0, \pm1\ldots$; the radial function $f_m(r)$ satisfies the equation

$$\frac{\partial^2 f}{\partial r^2}+\frac{1}{r}\frac{\partial f}{\partial r}+\left(E_r-\alpha_2r^2+\frac{1}{(r^2+d^2)^{1/2}}-\frac{m^2}{r^2}\right)f=0. \quad (27)$$

Let us expand $f_m(r)$ in a basis of eigenfunctions of the problem without the Coulomb interaction between the electrons: $f_m=\Sigma_n C_{nm}f_{nm}$, where $f_{nm}=(n!/(|m|+n)!\,\alpha_2^{|m|+1})^{1/2}r^{|m|}e^{-\sqrt{\alpha_2}r^2/2}L_n^{|m|}(\sqrt{\alpha_2}r^2)$. By numerically diagonalizing the Hamiltonian in the basis of these functions we find the solution to Eq. (27). The energy eigenvalues are determined from the equation

$$\det\{V_{nn'}^m+\delta_{nn'}(\varepsilon_{nm}-E_r)\}=0, \quad (28)$$

where

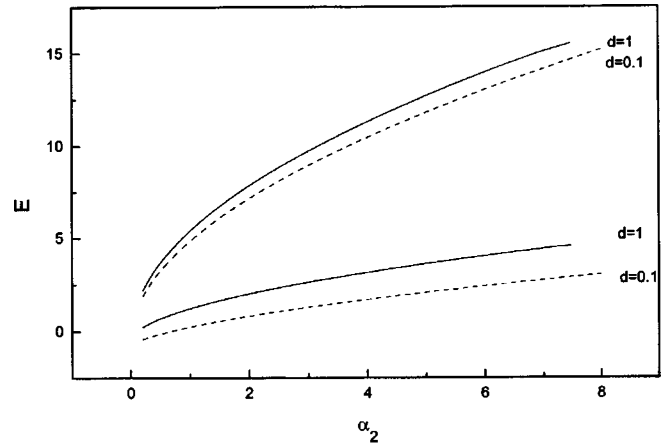

FIG. 7. Dependence of the lowest energy levels E_r for a spatially separated exciton in coupled quantum dots on the confinement potential parameter α_2.

$$\varepsilon_{nm}=4\sqrt{\alpha_2}\left(n+\frac{|m|+1}{2}\right); \quad (29)$$

$$V_{nn'}^m=\left(\frac{n!n'!}{(n+|m|)!(n'+|m|)!}\right)^{1/2}\times\sum_{i=0}^{n}\sum_{j=0}^{n'}\frac{(-1)^{i+j}}{i!j!}\binom{n+|m|}{n-i}\binom{n'+|m|}{n-j}\times\alpha_2^{(|m|+i+j+1)/2}\Gamma(i+j+|m|+1)d^{2(i+j+|m|+1/2)}\times\Psi(i+j+|m|+1,i+j+|m|+3/2;\sqrt{\alpha_2}d^2). \quad (30)$$

The dependences of the lowest energy levels E_r on the parameter α_2 are shown in Fig. 7. The values of energy levels increase monotonically with increasing α_2.

When α_2 is sufficiently large (the case of a strong confining potential or a large interlayer separation), the electron-electron interaction is small compared to other parameters and the energies of relative motion E_r asymptotically reduce

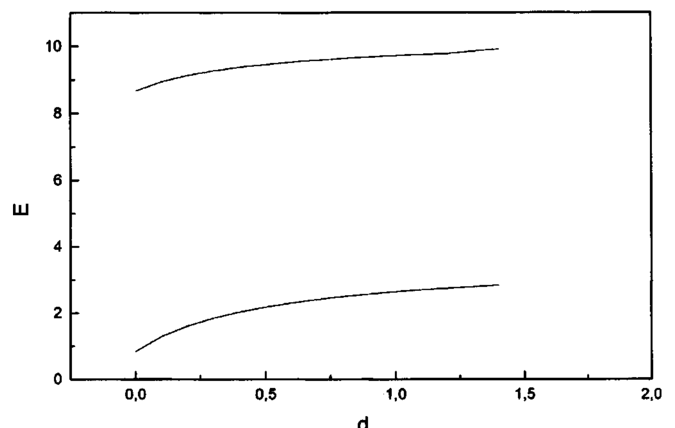

FIG. 8. Dependence of the lowest energy levels on the interlayer distance d.

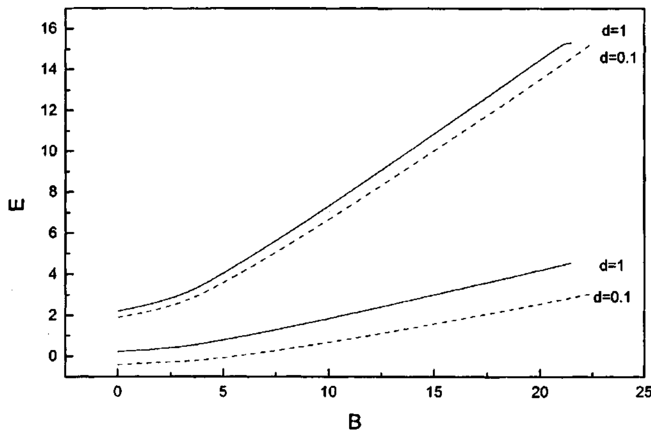

FIG. 9. Dependence of the lowest energy levels for relative motion of a spatially separated exciton in coupled quantum dots on the magnetic field B for $\alpha_2=0.2$.

to the energy levels Eq. (29) of a two-dimensional harmonic oscillator, i.e., they are linear in $\sqrt{\alpha_2}$. This is clear from Fig. 7.

The dependence of low-lying energy levels on the interlayer distance d is shown in Fig. 8. The contribution of the Coulomb interaction to the energy decreases with increasing d, and the energy levels asymptotically reduce to ε_{nm} Eq. (29).

The dependences of the lowest energy levels for relative motion on magnetic field are shown in Fig. 9. The values of the energy increase with increasing field and asymptotically reduce to $2\sqrt{\alpha_2'}(2n+|m|+1)+\gamma\omega_c m$. In the limit of ultra strong magnetic fields the energy levels asymptotically reduce to Landau levels, as in the case where there is no parabolic dependence for the confining potential (for example, the ''hard wall'' model; see Refs. 16, 17, and 28).

For large interlayer distances d the asymptotic dependence of the energy is as follows: $d\rightarrow\infty$, $E\sim 2\sqrt{\alpha_2'}(2n+|m|+1)+\gamma\omega_c m-1/d+1/(\sqrt{\alpha_2'})$.

For small d, as $d\rightarrow 0$, the matrix element becomes

$$V_{nn'}^{m}\rightarrow -\left(\frac{n!n'!}{(n+|m|)!(n'+|m|)!}\sqrt{\alpha_2'}\right)^{1/2}\sum_{i=0}^{n}\sum_{j=0}^{n'}\frac{(-1)^{i+j}}{i!j!}\times\binom{n+|m|}{n-i}\binom{n'+|m|}{n'-j}\Gamma\left(i+j+|m|+\frac{1}{2}\right).$$

The value $d=0$ corresponds to the case of a single quantum well with two carriers (see Ref. 30).

This work was supported by the Russian Fund for Fundamental Research, INTAS, and the program ''Physics of Solid-State Nanostructures.''

The work of N. E. Kaputkina was supported by the ISSEP program for aspirants.

[1)]We will assume identical dielectric constants for the layers with carriers (e and h) and the barrier layer. In reality, the materials used to make real semiconductor heterostructures have dielectric constants that are similar but do not coincide.

[1] T. Fukuzawa, E. E. Mendez, and J. M. Hong, Phys. Rev. Lett. **64**, 3066 (1990); J. A. Kash, M. Zachav, E. E. Mendez, J. M. Hong, and T. Fukuzawa, Phys. Rev. Lett. **66**, 2247 (1991).
[2] U. Sivan, P. M. Solomon, and H. Strikman, Phys. Rev. Lett. **68**, 1196 (1992).
[3] K. Brunner, G. Abstreiter, G. Böhm, G. Tränkle, and G. Weiymann, Phys. Rev. Lett. **73**, 1138 (1994).
[4] A. Zrenner, L. B. Butov, M. Hang, G. Abstreiter, G. Böhm, and G. Weiymann, Phys. Rev. Lett. **72**, 3382 (1994).
[5] L. V. Butov, A. Zrenner, G. Abstreiter, G. Böhm, and G. Weiymann, Phys. Rev. Lett. **73**, 304 (1994).
[6] L. V. Butov, A. Zrenner, G. Abstreiter, A. V. Petinova, and K. Eberl, Phys. Rev. B **52**, 12 153 (1995).
[7] S. P. Cheng, S. Kono, B. D. McCombe, I. Lo. W. C. Mitcel, and G. E. Stuts, Phys. Rev. Lett. **74**, 450 (1995).
[8] V. D. Kulakovskiĭ and L. V. Butov, Usp. Fiz. Nauk **165**, 229 (1995) [Phys. Usp. **28**, 125 (1995)].
[9] M. Bayer, V. B. Timofeev, T. Gutbrod, A. Forchel, R. Steffen, and S. Oshinno, Phys. Rev. B **52**, R11 623 (1995).
[10] M. Bayer, A. Schmidt, A. Forchel, F. Faller, T. L. Reineeke, P. A. Knipp, A. A. Dremin, and V. D. Kulakovskii, Phys. Rev. Lett. **74**, 3439 (1995).
[11] M. Bayer, V. B. Timofeev, F. Faller, T. Gutbrod, and A. Forchel, Phys. Rev. B **54**, 8799 (1996).
[12] A. I. Filin, V. B. Timofeev, S. I. Gubarev, D. Birkedal, and J. M. Huan, JETP Lett. **65**, 656 (1997).
[13] E. S. Moskalenko, A. L. Zhmodikov, V. V. Krivolapchuk, D. A. Mazurenko, I. K. Poletaev, S. T. Fokson, and T. S. Chung, in *Semiconductors-97* [in Russian] (FIAN, Moscow, 1997), p. 246.
[14] Yu. E. Lozovik and V. I. Yudson, JETP Lett. **22**, 274 (1975).
[15] Yu. E. Lozovik and V. I. Yudson, Zh. Éksp. Teor. Fiz. **71**, 1167 (1976) [Sov. Phys. JETP **44**, 889 (1976)].
[16] I. V. Lerner and Yu. E. Lozovik, Zh. Éksp. Teor. Fiz. **80**, 1488 (1981) [Sov. Phys. JETP **54**, 783 (1981)]; Zh. Éksp. Teor. Fiz. **82**, 1188 (1982) [Sov. Phys. JETP **55**, 691 (1982)].
[17] I. V. Lerner and Yu. E. Lozovik, Zh. Éksp. Teor. Fiz. **78**, 1167 (1980) [Sov. Phys. JETP **51**, 588 (1980)].
[18] D. S. Chemla, J. B. Stark, and W. H. Knox, in *Ultrafast Phenomena* VIII, edited by J.-L. Martin *et al.* (Springer 1993), p. 21.
[19] A. B. Dzuybenko and Yu. E. Lozovik, Fiz. Tverd. Tela (Leningrad) **25**, 1519 (1983) [Sov. Phys. Solid State **25**, 874 (1983)]; Fiz. Tverd. Tela (Leningrad) **26**, 1540 (1983) [Sov. Phys. Solid State **26**, 1420 (1983)].
[20] A. B. Dzuybenko and Yu. E. Lozovik, J. Phys. **24**, 415 (1991).
[21] Yu. E. Lozovik, O. L. Berman, and V. G. Tsvetus, JETP Lett. **66**, 332 (1997).
[22] Yu. E. Lozovik and O. L. Berman, Zh. Éksp. Teor. Fiz. **111**, 1879 (1997) [JETP **84**, 1027 (1997)].
[23] A. V. Klyuchnik and Yu. E. Lozovik, Zh. Éksp. Teor. Fiz. **76**, 670 (1979) [Sov. Phys. JETP **49**, 335 (1979)].
[24] Yu. E. Lozovik and A. V. Klyuchnik, J. Phys. C **11**, L483 (1978).
[25] Yu. E. Lozovik and A. V. Poushnov, Phys. Lett. A **194**, 105 (1994).
[26] Yu. E. Lozovik and A. M. Ruvinsky, Zh. Éksp. Teor. Fiz. **112**, 1791 (1997) [JETP **85**, 1651 (1997)].
[27] L. D. Gor'kov and I. E. Dzyaloshinskiĭ, Zh. Éksp. Teor. Fiz. **53**, 717 (1967) [Sov. Phys. JETP **26**, 449 (1968)].
[28] Yu. E. Lozovik and A. M. Ruvinsky, Phys. Lett. A **227**, 271 (1997).
[29] G. S. Gevorkyan and Yu. E. Lozovik, Fiz. Tverd. Tela (Leningrad) **27**, 1800 (1985) [Sov. Phys. Solid State **27**, 1079 (1985)].
[30] N. E. Kaputkina and Yu. E. Lozovik (to be published).

Translated by Frank J. Crowne

Resonant tunneling dynamics of heterostructures based on semiconductors with two-valley spectra

G. F. Karavaev and A. A. Voronkov

Siberian Physicotechnical Institute, 634050 Tomsk, Russia
(Submitted March 4, 1998; accepted for publication April 16, 1998)
Fiz. Tekh. Poluprovodn. **32**, 1363–1370 (November 1998)

Time-dependent characteristics of electron resonant tunneling in quantum heterostructures based on GaAs and AlAs are investigated using the two-valley model. Analysis of the phases of the transmitted and reflected waves yields analytic expressions for tunneling and reflection times. The solution to the problem incorporates the decay of Γ- and *X*- valley resonant states in these heterostructures. Numerical solution of the nonstationary Schrödinger equation is used to demonstrate the tunneling of wave packets through double- barrier heterostructures.
© *1998 American Institute of Physics.* [S1063-7826(98)01511-7]

INTRODUCTION

Resonant tunneling, which is observed in quantum-well semiconductor structures, provides a physical basis for the development of high-speed devices. For this reason, it is important to investigate its time-dependent characteristics.[1–9] The overwhelming majority of theoretical treatments of this problem have used envelope-function approximations based on a single-valley model of the semiconductor band structure, or have treated the case of a free particle incident on a barrier. However, it is known that in the most widely used structures based on semiconducting III-V compounds the single-valley description is often inadequate. Hence, a more exact approach, which takes into account the multivalley character of the energy spectrum, is required.

For structures based on GaAs/AlAs (001) it has been established experimentally and theoretically that $\Gamma-X$ intervalley scattering of electrons at the heterojunction is a very important feature of the quantum dynamics. Calculations described in a number of papers[10–13] based on tight-binding and pseudopotential methods have established that the so-called three-valley $\Gamma_1-X_1-X_3$ model gives a very good description of the spectra of electrons passing through GaAs/AlAs (001) heterostructures.

In Refs. 14 and 15, Ting and McGill used the method of Wannier functions and empirical tight binding to analyze time-dependent characteristics of the resonant tunneling of electrons in structures based on GaAs/AlAs. This type of investigation is very laborious, and therefore many questions regarding the tunneling dynamics have still not been clarified. For this reason a simpler approach, which can incorporate multivalley structure into the band spectra of the heterojunction components while retaining the advantages of the envelope function method, is required. Such an approach would allow us to discuss a larger number of different structures, including structures in external fields.

Although the three-valley model meets these requirements, in this paper we prefer to start by investigating the simpler two-valley model, within which analytic techniques can be employed practically to the end of a calculation. Analytic results, in turn, are simpler to analyze and lend themselves more readily to qualitative conclusions. Our calculations show that the two-valley model gives a qualitatively correct description of the transmission spectrum of electrons passing through GaAs/AlAs heterostructures and that quantitative discrepancies are not fundamental. In Ref. 16 Yumin and Hazhi used the envelope function method to numerically investigate the residence time of a wave packet within a GaAs quantum well, along with a simplified picture of the $\Gamma-X$ interaction. However, their study did not systematically treat all the time-dependent characteristics of resonant tunneling in the presence of $\Gamma-X$ scattering.

MODEL

Assume that the electronic states and energy spectra of the heterojunction components are well described by the two-valley model. With semiconductor materials like GaAs and AlAs in mind, we will consider conduction-band Γ- and *X*- valleys. Figure 1 shows the conduction band energy profiles of the Γ- and *X*- valleys in the absence of an external field for a two-barrier heterostructure.

Our studies of the characteristics of heterostructures will focus on the most interesting energy interval for an incident electron wave: $E^X_{\mathrm{AlAs}} \leqslant E \leqslant E^X_{\mathrm{GaAs}}$.

In this energy range the *X*-electronic states see the AlAs layers as quantum wells and the GaAs layers as barriers, while the Γ-electronic states see the opposite. In the discussion that follows, the concepts "barriers" and "wells" will have their usual meanings for the Γ- electronic states (AlAs and GaAs, respectively), while for *X*-electronic states we will speak of an *X*-barrier (GaAs) and an *X*-well (AlAs). When an electron is within a layer, it can occupy either a Γ- or an *X*- valley; however, when it crosses the heterojunction, it can undergo $\Gamma-X$ scattering. Therefore, in order to describe the electronic processes we will derive equations for Γ- and *X*-valley envelopes F^Γ, F^X within the framework of effective mass theory, and conditions for matching these envelopes at the heterojunction boundaries.

 © 1998 American Institute of Physics

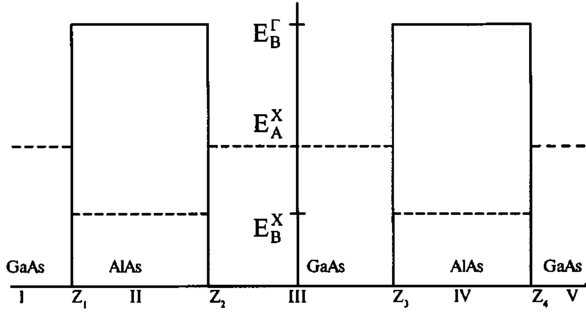

FIG. 1. Energy profile of the Γ- and *X*- valleys in the conduction band of a two-barrier heterostructure based on GaAs and AlAs.

We will use the matching conditions discussed previously in Refs. 17–20; specifically,

$$F_A^\Gamma = F_B^\Gamma, \quad a_0 \frac{m_0}{m_A^\Gamma} \frac{\partial}{\partial z} F_A^\Gamma = a_0 \frac{m_0}{m_B^\Gamma} \frac{\partial}{\partial z} F_B^\Gamma + (-1)^n t F_X^B,$$

$$F_A^X = F_B^X, \quad a_0 \frac{m_0}{m_A^X} \frac{\partial}{\partial z} F_A^X = a_0 \frac{m_0}{m_B^X} \frac{\partial}{\partial z} F_B^X + (-1)^n t F_\Gamma^B, \tag{1}$$

where labels *A* and *B* denote the different components of the heterojunction, m_A^Γ, m_B^Γ, m_A^X, and m_B^X are effective masses, t is a dimensionless $\Gamma - X$- mixing parameter, m_0 is the mass of the free electron, and a_0 is the lattice constant. The integers n at the heterojunction boundaries differ by one if the region between them includes an odd number of molecular layers, but if the distance between heterojunction layers includes an even number of molecular layers they are the same for both boundaries. This difference arises from the fact that the $|\Gamma\rangle$ and $|X\rangle$ Bloch functions have different periods along the [001] direction.

TRANSMISSION AND REFLECTION TIME, DECAY TIME FOR A RESONANT STATE

In each of the heterojunction layers solutions to the Schrödinger equation for the envelopes of each valley can be written in the form of superpositions of a wave moving (or attenuating) from left to right and a wave moving (or attenuating) from right to left. Using the matching conditions Eq. (1) at each boundary, we can construct a transfer matrix Q_i through the boundary between the ith and $i+1$th layers.

By multiplying the transfer matrices through two successive boundaries $z=z_1$, $z=z_2$ we can obtain a transfer matrix $M_1 = Q_1 Q_2$ through a single barrier. This matrix connects the envelope coefficients in the first layer with the envelope coefficients in the third layer. The equations that connect the incident, transmitted, and reflected waves have the form

$$\begin{pmatrix} A_1 \\ B_1 \\ C_1 \\ D_1 \end{pmatrix} = M_1 \begin{pmatrix} A_3 \\ B_3 \\ C_3 \\ D_3 \end{pmatrix}, \tag{2}$$

where A_i, B_i and C_i, D_i are coefficients belonging to the Γ-wave and to the *X*-wave respectively; A_i and C_i are amplitudes of waves moving (attenuating) from left to right, and B_i and D_i are amplitudes of waves moving (attenuating) from right to left.

If only a Γ-wave is incident on the barrier from the left, and there is no wave incident on the barrier from the right, we can set $C_1 = B_3 = D_3 = 0$. In this case it follows from Eq. (2) that

$$A_3 = \frac{\beta_{11}^1}{\alpha_{11}^1 \beta_{11}^1 - \gamma_{11}^1 \delta_{11}^1} A_1. \tag{3}$$

The definition of the quantities entering into Eq. (3) is explained in *Appendix* I. For a two-barrier heterostructure with identical barriers whose left-hand edges are separated by an even number of molecular layers, the transfer matrix through the second barrier M_2 is analogous to the transfer matrix through the first barrier M_1, and we need only replace the coordinates z_1 and z_2 by z_3 and z_4, respectively. The transfer matrix through the two-barrier structure can be written in block form:

$$M = M_1 M_2 = \begin{pmatrix} \alpha_{ij} & \gamma_{ij} \\ \delta_{ij} & \beta_{ij} \end{pmatrix}, \quad i, j = 1,2. \tag{4}$$

The matrix M connects the coefficients of the Γ- and *X*-waves on different sides of the two-barrier heterostructure. By analogy with the previous case, setting $C_1 = D_5 = B_5 = 0$, we find

$$A_5 = \frac{\beta_{11}}{\alpha_{11}\beta_{11} - \gamma_{11}\delta_{11}} A_1. \tag{5}$$

Expressions for α_{ij}, β_{ij}, γ_{ij}, and δ_{ij} are given in *Appendix* II.

The squared moduli of the right sides of Eqs. (3) and (5) without A_1 are transmission coefficients, and their phases determine the transmission time.

Let us discuss the time-dependent characteristics. The problem of defining a tunneling time for an electron through a potential barrier has caused more than a few arguments, because time in quantum mechanics does not have the status of a dynamic variable. In this paper we use the standard wave packet analysis.

We can identify three characteristic processes associated with the tunneling of an electron wave through a heterostructure: transmission, reflection, and trapping of the wave within the heterostructure. Corresponding to these processes we can identify times for transmission, reflection, and lifetime of a resonant state (if the energy of the incident electron is close to a resonance level). The transmission and reflection times are referenced to the motion of the wave packet crest.[21,22]

Then the transmission (tunneling) time of an electron wave is

$$\tau_T = \hbar \frac{\partial \Phi_T}{\partial E} + \frac{z' - z_1}{v_G}, \quad v_G = \frac{1}{\hbar} \frac{\partial E}{\partial k}, \tag{6}$$

where $\Phi_T(k)$ is the phase accumulated by a wave with wave number k as it tunnels through the heterostructure [$z' = z_2$ for a single-barrier heterostructure, where $\Phi_T(k)$ is derived from Eq. (3), while $z' = z_4$ for a two-barrier heterostructure,

where $\Phi_T(k)$ is derived from Eq. (5)]. The reflection time τ_R of a wave packet from the heterostructure is defined as the difference between the time at which the maximum of the reflected wave packet appears at point $z=z_1$ and the arrival time of the incident wave packet maximum. Thus,

$$\tau_R=\hbar \frac{\partial \Phi_R}{\partial E}, \tag{7}$$

where $\Phi_R(k)$ is the phase accumulated by the wave as it is reflected from the heterostructure.

In order to find the lifetime of a resonant state in the heterostructure we must solve the problem of resonant state decay, which we will consider below.

The phase accumulated by the wave as it passes through the structure is

$$\Phi_T=\Phi_1-k_A a, \tag{8}$$

where $\tan \Phi_1=-f_3/f_2$ for a single-barrier structure, and

$$\Phi_T=\Phi_2-k_A(2a+d), \tag{9}$$

where $\tan \Phi_2=-P_3/P_2$ for a two-barrier structure. The form of the functions f_2, f_3 and P_2, P_3 is given in *Appendices* I and II.

The tunneling time of a Γ-wave, e.g., through a two-barrier heterostructure, has the form

$$\tau_T=\hbar \frac{\partial \Phi_2}{\partial E}=\frac{\hbar}{P_2^2+P_3^2}\left[P_2 \frac{\partial P_3}{\partial E}-P_3 \frac{\partial P_2}{\partial E}\right]. \tag{10}$$

Let us consider the time for reflection of an electron wave from the heterostructure. The coefficient B_1 of the reflected wave can be written in terms of elements of the transfer matrix M as follows:

$$B_1=\frac{\alpha_{21}\beta_{11}-\gamma_{21}\delta_{11}}{\alpha_{11}\beta_{11}-\gamma_{11}\delta_{11}} A_1 . \tag{11}$$

Note that the coefficients A_5, B_1 have the same denominator, and differ only in the form of their numerators. Analysis of the numerator of B_1 shows that it is an imaginary function; consequently, the times for transmission τ_T and reflection τ_R coincide. All the features exhibited by the tunneling time are also exhibited by the reflection time.

Let us consider the lifetime of the resonant state. In a two-barrier heterostructure, $\Gamma-X$ mixing will cause any Γ-resonant states to be accompanied by *X*- electronic resonant states. The lifetimes of these and other states can be found by solving the system of equations (2) for a single-barrier heterostructure. For a two-barrier heterostructure, the system to solve differs from Eq. (2) by the replacements $M_1\rightarrow M$, $A_3 \rightarrow A_5$, and $C_3\rightarrow C_5$. Now, however, we must set $A_1=C_1=B_{3(5)}=D_{3(5)}=0$ in these equations. The conditions for solvability of these equations give a complex equation that determines the poles of the corresponding scattering matrix:

$$f_2(E)+i f_3(E)=0 \quad \text{for a single-barrier structure,} \tag{12}$$

$$P_2(E)+i P_3(E)=0 \quad \text{for a double-barrier structure.} \tag{13}$$

These equations can be solved numerically by Newton's method. The resulting energies are complex: $E=E_R+iE_i$ ($E_i<0$), and the decay time of a resonant state is estimated from the expression $\tau_D=-\hbar/2E_i$.

In this paper, in addition to calculating the characteristics of the tunneling process based on analysis of solutions to the time-independent Schrödinger equation, we also simulated the tunneling of an electron through a two-barrier heterostructure by solving the time-dependent Schrödinger equation, taking into account $\Gamma-X$-scattering at the heterojunction. In simulating the transmission of a wave packet, we used a forward grid method and a three-layer implicit and absolutely stable Dufour-Frankel algorithm[23]; $\Gamma-X$-scattering at the heterojunctions of the structure was taken into account in accordance with the matching conditions (1). We simulated a region of length $L\approx 28000$ Å, including a two-barrier heterostructure consisting of AlAs barriers 10 molecular layers thick and GaAs wells 24 molecular layers thick. We chose a time step $\Delta t=$ 0.001 fs and a spatial coordinate step $\Delta x=$ 2.825 Å. The half-width of the wave packet was chosen to be $\delta z=$ 1000 Å. In the energy range we considered ($E=$ 0.2–0.4 eV), the energy uncertainty of the wave packet for a given δx was $\delta E\approx 10^{-3}$ eV; this allows us to speak of a tunneling time accuracy of $\delta t \geqslant \hbar/2\delta E\approx$ 300 fs. The time for spreading of the wave packet was $\approx m_A^\Gamma(\delta x)^2/\hbar\approx$ 5800 fs for GaAs, i.e., much longer than the simulation time.

RESULTS AND DISCUSSION

Numerical calculations based on analyzing the solution of the steady-state Schrödinger equation were carried out for a number of single-barrier and two-barrier heterostructures, along with solution of the time-dependent Schrödinger equation for several structures. In these calculations we used the following parameters: $m_A^\Gamma=0.067m_0$, $m_B^\Gamma=0.13m_0$, $m_A^X=m_B^X=1.2m_0$, $E_B^\Gamma=1.0$ eV, $E_B^X=0.2$ eV, $E_A^X=0.4$ eV, $a_0=5.65$ Å.

Our computed transmission spectra corresponded to well- known results.[13,20,21] Let us discuss the time-dependent characteristics. The tunneling time calculated according to Eq. (10) for one- and two-barrier heterostructures as a function of peak energy corresponded to peaks in the transmission coefficient. The presence of *X*- and Γ-resonant peaks in the tunneling time was clearly apparent, along with a fine structure in the *X*-peak (see Figs. 2 and 3). From these figures it is clear that $\Gamma-X$-scattering has a very strong effect on the transmission time of an electron wave through the heterostructure. If the energy of an incident wave coincides with an allowed *X*-energy level in AlAs, then $\Gamma-X$-mixing at the heterojunction will cause the electron to be trapped in the *X*-state and localized in the barrier. Because of this circumstance, the time for transmission is markedly increased. Calculations show that the transmission times for peaks near the *X*-level differ by three orders of magnitude from results in which the effect of $\Gamma-X$-mixing is disregarded.

Note that despite the complicated form of the electronic spectrum for transmission through the heterostructure (peaks and zeros), the tunneling time exhibits no peculiarities in the

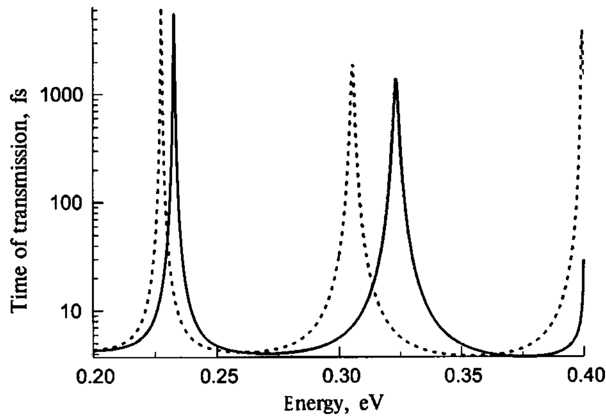

FIG. 2. Transmission time of an electron through a single-barrier structure; solid curve—AlAs (eight molecular layers), dotted curve—AlAs (nine molecular layers).

neighborhood of these zeros. Features in the spectrum of the transmission coefficient and tunneling time when the energy of an incident electron is close to the X-level are the same for both the two-barrier and one-barrier heterostructures. The presence of two X-levels in a two-barrier heterostructure is not manifested in any way at all. For a two-barrier heterostructure, the situation changes when the X-level is close in energy to a Γ-resonant level of the well. In this case the degeneracy of the X-level is lifted and it is split into two levels, and this is observed both in the transmission spectrum and in the spectrum of the transmission lifetime (for example, in Fig. 3 we observe a group of two X- levels and one Γ-level for energies in the range $\approx$ 0.3 eV, while for the two-barrier heterostructure with a well made up of 16 monolayers and the same barriers only one X-peak is observed, because the Γ- levels are located at other energies).

Equations (6) and (7) allow us to study the dependence of the tunneling time on the $\Gamma-X$-mixing parameter t. With increasing t, the transmission peaks become wider and the tunneling time decreases, which obviously must happen. The larger the $\Gamma-X$-mixing, the easier it is for an electron to tunnel along the $\Gamma-X-\Gamma-X-\Gamma$ channel and propagate almost freely through each of the structure layers.

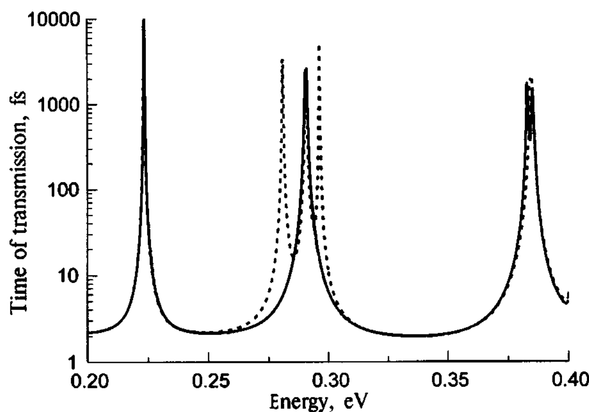

FIG. 3. Transmission time of an electron through a two-barrier structure: solid line—AlAs (10) / GaAs (16) / AlAs (10), dashed line—AlAs (10) / GaAs (24) / AlAs (10).

TABLE I. Decay and transmission times τ_D and τ_T of an electron wave for a single-barrier heterostructure with N (AlAs)= 10 and 11 molecular layers.

Peak	τ_T, fs	τ_D, fs
	N (AlAs) = 10	
$X1$	4500	2240
$X2$	900	540
$X3$	700	390
	N (AlAs) = 11	
$X1$	5000	2680
$X2$	1500	700
$X3$	700	370

Let us discuss the decay times of the resonant states. For this we must solve Eqs. (12) and (13) for complex energy E. These calculations indicate that the values of the real part of E for the resonant states are to good accuracy the same as the energies where the Γ- and X-peaks in the transmission coefficient occur, while the imaginary components turn out quite small. Comparing these times, we see that the transmission time turns out to be rather close to twice the decay time of the resonant states (see Tables I and II).

Varying the $\Gamma-X$ mixing parameter t reveals that the decay time for the resonant state increases as the parameter t decreases. The smaller the parameter t, the larger the localization of the X- and Γ-levels is and the longer the lifetime.

We simulated the tunneling process for GaAs / AlAs(10) / GaAs(24) / AlAs(10) / GaAs heterostructures near the X- and Γ-peaks of the transmission coefficient.

Figure 4 shows the scattering of a wave packet with average energy $E=$ 0.2910 eV, which approximately corresponds to the position of the Γ- resonance. The left column of plots illustrates the motion of a wave packet as a whole, while the right side depicts the processes that occur in a two-barrier heterostructure in detail. Figure 4 shows clearly how the wave packet fits itself to the heterostructure, how the transmission and reflection waves from the wave packet interfere, and how reflection and transmission take place. In the more detailed scheme it is apparent how the electron wave penetrates the structure, and that Γ-states appear in the well whose presence is due to tunneling and $\Gamma-X$-mixing, and that X- electronic states also appear in the barriers due to

TABLE II. Decay and transmission times τ_D and τ_T of an electron wave for a double-barrier heterostructure with N (AlAs) = 8 and N (GaAs) = 8, N (AlAs) = 10 and N (GaAs) = 24 molecular layers.

Peak	τ_T, fs	τ_D, fs
	N (AlAs) = 8, N (GaAs) = 8	
$1X$	7500	3930
1Γ	900	490
$2X$	1300	700
$3X$	4500	2300
	N (AlAs) = 10, N (GaAs) = 24	
$1X$	9100	19200
$2X$	3400	1630
2Γ	2200	1280
$3X$	5100	2530
$4X$	1900	750

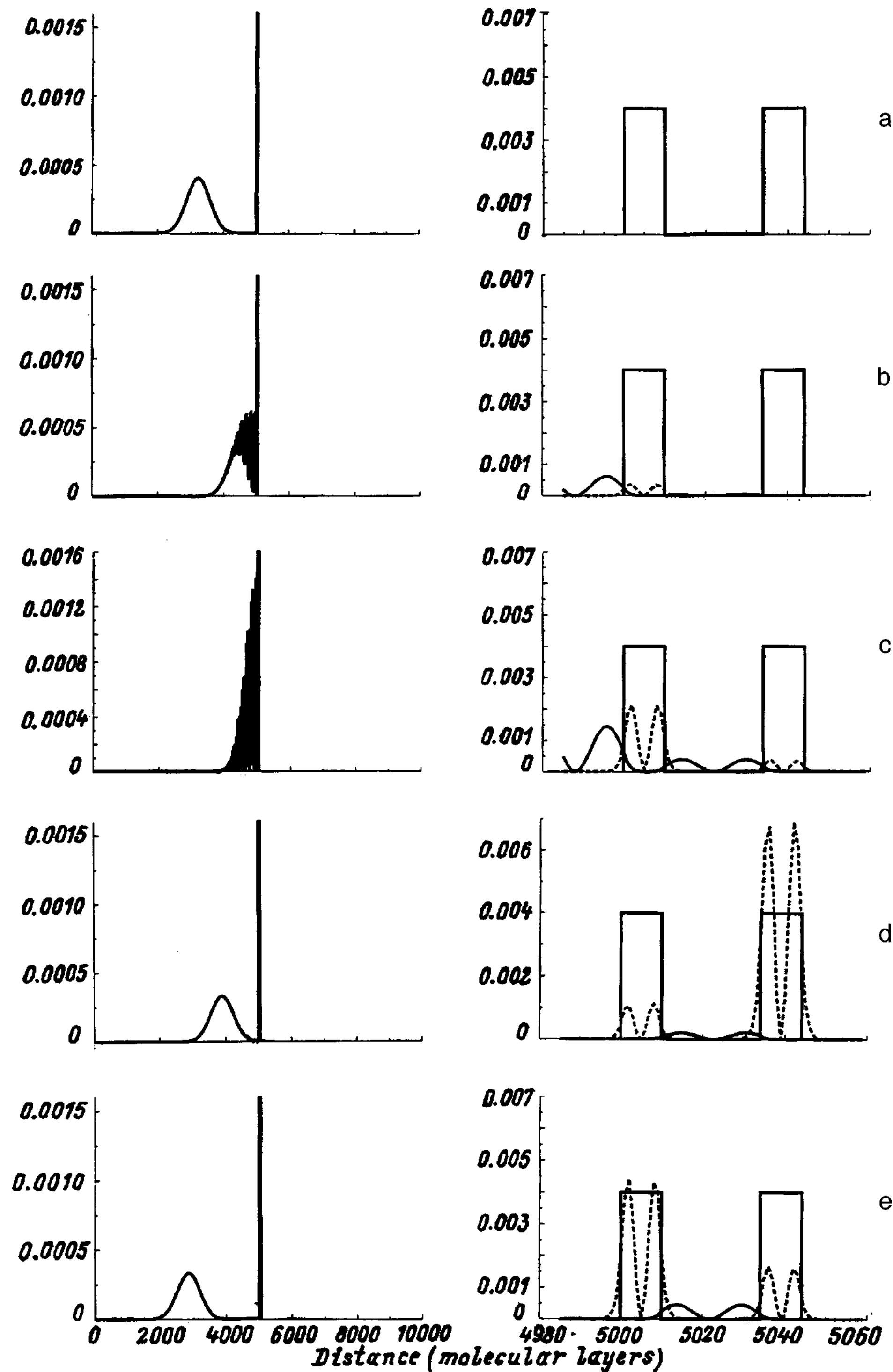

FIG. 4. Dynamics of tunneling and reflection of a wave packet outside and inside a two-barrier heterostructure for the Γ-energy level. Time, fs: a — 0, b — 300, c — 410, d — 660, e — 900.

the same mixing. Γ-electronic states are concentrated in the quantum well, while X-electronic states are concentrated in the X-wells. At the time the wave packet is reflected and moves to the left, the electron densities of the Γ- and X-states of the two-barrier heterostructure are maximal. As time passes, the wave packet leaves the limits of the simulation region, and the electron densities in the Γ- and X-states of the heterostructure slowly decay. It is clear from Figs. 4c–4e that oscillations take place in the electron density between the barriers (see also Ref. 14).

The narrowness of the peaks in the transmission coefficients of the heterostructure makes it very difficult to access the maximum of a peak, and therefore the packet transmission through the heterostructure is small.

An actual time-dependent characteristics is illustrated in Fig. 5, where we show the time dependence of the total elec-

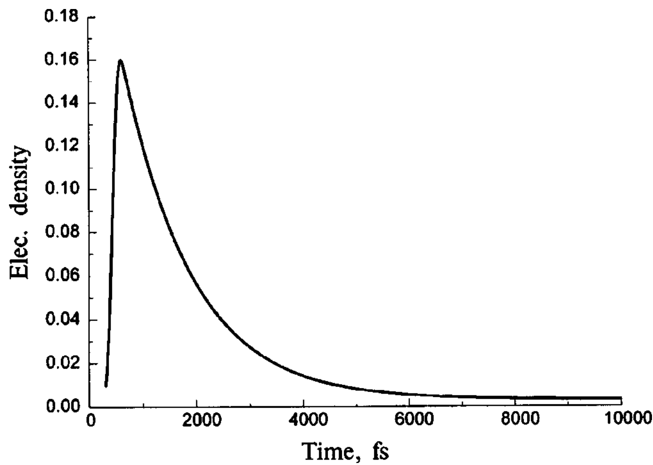

FIG. 5. Time dependence of the electron density near a two-barrier structure.

tron density of the Γ- and X-states within the heterostructure. Note that there is a certain time at which strong accumulation of the probability density occurs within the heterostructure, while later the probability density decays according to an exponential law.

We have defined the tunneling time for a wave packet as the difference between times for escape of the maximum in the wave packet that passes through the heterostructure and the arrival of the maximum of the wave packet incident on the heterostructure. From this simulation it follows that this time is $\tau_{\text{mod}} = 300$ fs. Note that at the instant of escape of the transmitted wave, the electron density in the heterostructure differs only slightly from its maximum value. Thus, the structure discharges slowly, which will decrease the speed of the heterostructure under discussion.

Simulation of resonant tunneling of a wave packet at energies that correspond to the X-energy levels of the system reveals strong accumulation of the electron density in the two- barrier structure, while the X-electron density is extremely large. Because of this circumstance, charging of the heterostructure is slower.

In conclusion, we note two favorable aspects from a device standpoint. When a wave packet is scattered with an energy corresponding to a Γ-resonant state close to a X- resonant state, the electron density in the X-states turns out to be comparable to the electron density in the Γ- states. This probably hapens because for AlAs(10) / GaAs(24) / AlAs(10) structures the Γ-resonant level is surrounded by levels $2X$ and $3X$; therefore, the role of $\Gamma-X$ mixing is large. A second advantageous fact, revealed by simulating the scattering of a wave packet with energies corresponding to the $4X$ energy level, is that no wave packet passes through the heterostructure—the electron density simply leaks away from the structure over time.

Thus, our simulations of tunneling processes (which allow us to include the discharging of the heterostructure) indicate that the effect of $\Gamma-X$ mixing greatly decreases the speed of this type of heterostructure. The heterostructure is found to discharge more rapidly at energies corresponding to Γ than at energies corresponding to X levels.

COMPARISON OF ANALYTIC AND MODEL RESULTS

The simulation of tunneling processes of a wave packet through a two-barrier heterostructure gives much useful information about the interaction of a wave packet with the structure, and about the effect of $\Gamma-X$ mixing of electronic states at the heterojunction boundaries. Unfortunately, implementation of the simulation algorithm takes up a great deal of computer time; therefore, we are strongly motivated to determine how well the characteristics obtained from the simulation agree with the same characteristics obtained by analysis of the phase of the transmitted wave. It turns out that for the example of a AlAs(10) / GaAs(24) / AlAs(10) heterostructure the data suggest that the characteristics are in good agreement with one another. This good agreement shows that the analytically derived times yield adequate qualitative and reasonable quantitative description of the process of tunneling of an electron through a quantum heterostructure. Both analytic and model calculations show the importance of including the phenomenon of $\Gamma-X$ mixing, which increases the transparency of the heterostructure and also the (overall) tunneling time of a wave through the latter.

CONCLUSIONS

In this paper we have discussed the problem of resonant tunneling of electrons in quantum heterostructures based on GaAs and AlAs within the framework of a two-band effective-mass model. We discussed the influence of $\Gamma-X$ mixing, which increases the transparency of the heterostructure and leads to the appearance of new peaks and zeros in the transmission coefficient related to X- resonant states in the heterostructure.

From analysis of the phases of the transmitted and reflected waves we obtained analytic expressions for the tunneling and reflection times. We have shown that for the symmetric heterostructures we have investigated these two times coincide. We have solved the problem of decay of resonant states which are present at quasilocalized levels of the heterostructure. We have found that the peaks in the tunneling time correspond to resonances of the system, and that a consequence of including $\Gamma-X$ mixing is the appearance of time peaks that correspond to X- peaks in the transmission coefficient. The narrower the peak in the transmission coefficient, the longer the tunneling time through the heterostructure.

By numerically solving the time-dependent Schrödinger equation we simulated the process of tunneling of a wave packet through a double-barrier heterostructure, taking into account $\Gamma-X$ mixing. The simulation revealed that $\Gamma-X$ mixing increases the time for tunneling through the heterostructure, and also significantly slows the process of discharging.

Comparison of the time-dependent characteristics of tunneling obtained analytically and by simulation clearly indicate that the two methods are in good agreement with one another.

Because we used model representations in this paper, we cannot give precise recommendations for the design of devices based on heterostructures. However, our work reveals

the need to include the influence of $\Gamma-X$ mixing on the time (frequency) characteristics of the heterostructure. Our results lead us to conclude that in order to improve the temporal (frequency) properties of resonant tunneling it is necessary to choose the dimensions of the quantum well and barrier so as to avoid the appearance of X-resonances close to the Γ-resonance which provides the primary contribution to the current through the heterostructure.

APPENDIX I

One-barrier structure

The transfer matrix M_1 has the form

$$M_1=\begin{bmatrix}\alpha^1_{ij} & \gamma^1_{ij}\\ \delta^1_{ij} & \beta^1_{ij}\end{bmatrix},$$

where α^1_{ij}, β^1_{ij}, γ^1_{ij}, δ^1_{ij} are 2×2 matrices.

$$\alpha^1_{11}=(\alpha^2_{22})^*=\exp(ik_A a)\left\{\frac{GcGt}{Gc-Gt}-(-1)^n\frac{g_\Gamma g_X}{Xc-Xt}\right\},$$

$$\alpha^1_{12}=(\alpha^2_{21})^*=\exp(-ik_A(z_1+z_2))\times\left\{\frac{\gamma_\Gamma^{-2}-1}{Gc-Gt}-(-1)^n\frac{g_\Gamma g_X}{Xc-Xt}\right\},$$

$$\beta^1_{11}=\exp(-\sigma a)\left\{\frac{XcXt}{Xc-Xt}-(-1)^n\frac{g_\Gamma g_X}{Gc-Gt}\right\},$$

$$\beta^1_{22}(a)=\beta^1_{11}(-a),$$

$$\beta^1_{12}=\beta^1_{21}\exp(2\sigma(z_1+z_2))=\frac{1}{2}\exp(\sigma(z_1+z_2))\left\{-\frac{1-\gamma_X^{-2}}{Xc-Xt}-(-1)^n\frac{g_\Gamma g_X}{Gc-Gt}\right\},$$

$$\gamma^1_{11}=(\gamma^1_{21})^*=-\exp(-\sigma z_2)\exp(-ik_A z_1)\frac{g_\Gamma}{2}\times\left\{(-1)^n\frac{Gc+Gt}{Gc-Gt}-\frac{Xc+Xt}{Xc-Xt}\right\},$$

$$\gamma^1_{12}=(\gamma^1_{22})^*=-\exp(\sigma z_2)\exp(-ik_A z_1)\frac{g_\Gamma}{2}\times\left\{(-1)^n\frac{Gc+Gt}{Gc-Gt}-\frac{\bar{X}c+\bar{X}t}{Xc-Xt}\right\},$$

$$\delta^1_{11}=(\delta^1_{12})^*=\exp(-\sigma z_1)\exp(ik_A z_2)\frac{g_X}{2}\times\left\{\frac{Gc+Gt}{Gc-Gt}-(-1)^n\frac{Xc+Xt}{Xc-Xt}\right\},$$

$$\delta^1_{21}=(\delta^1_{22})^*=-\exp(-\sigma z_1)\exp(ik_A z_2)\frac{g_X}{2}\times\left\{(-1)^n\frac{Gc+Gt}{Gc-Gt}-\frac{\bar{X}c+\bar{X}t}{Xc-Xt}\right\},$$

where we have made use of the notation $a=z_2-z_1$ for the thickness of the barrier, and

$$\gamma_\Gamma=-\frac{k_A m_B^\Gamma}{k_B m_A^\Gamma},\quad \gamma_X=i\frac{\sigma}{q},$$

$$g_\Gamma=\frac{t}{a_0 m_0}\frac{m_A^\Gamma}{ik_A},\quad g_X=-\frac{t}{a_0 m_0}\frac{m_X}{\sigma},$$

$$Gc=1+i\beta_\Gamma\coth\varphi,\quad Gt=1+i\beta_\Gamma\tanh\varphi,$$

$$Xc=1+\frac{q}{\sigma}\cot\phi,$$

$$Xt=1-\frac{q}{\sigma}\tan\phi,\quad \bar{X}c=2-Xc,\quad \bar{X}t=2-Xt,$$

$$\beta_\Gamma=-i\gamma_\Gamma^{-1}=\frac{k_B m_A^\Gamma}{k_A m_B^\Gamma},\quad \varphi=k_B a/2,\quad \phi=qa/2,$$

where $k_A=\sqrt{2m_A^\Gamma E/\hbar^2}$, $ik_B=\sqrt{2m_B^\Gamma(E-E_B^\Gamma)/\hbar^2}$, $q=\sqrt{2m_B^X(E-E_B^X)/\hbar^2}$, and $i\sigma=\sqrt{2m_A^X(E-E_A^X)/\hbar^2}$ are the wave numbers for the Γ- wave in GaAs, Γ- wave in AlAs, X- wave in AlAs, and X- wave in GaAs, respectively.

The functions f_2 and f_3 can be written in the form

$$f_2=\frac{XcXt}{Xc-Xt}\cosh 2\varphi+\frac{|g_\Gamma|g_X}{2\beta_\Gamma}\frac{Xc+Xt}{Xc-Xt}\sinh 2\varphi,$$

$$f_3=\frac{1-\beta_\Gamma^2}{2\beta_\Gamma}\frac{XcXt}{Xc-Xt}\sinh 2\varphi-\frac{|g_\Gamma|g_X}{2}\times\left[\frac{Xc+Xt}{Xc-Xt}\cosh 2\varphi-(-1)^n+\frac{|g_\Gamma|g_X}{\beta_\Gamma(Xc-Xt)}\sinh 2\varphi\right].$$

APPENDIX II

Double-barrier structure

The transfer matrix through the two-barrier structure is $M=M_1M_2$.

The coefficients of the matrix M required to calculate the transmission coefficient and temporal characteristics are:

$$\alpha_{11}=\alpha^1_{11}\alpha^2_{11}+\alpha^1_{12}\alpha^2_{21}+\gamma^1_{11}\delta^2_{11}+\gamma^1_{12}\delta^2_{21},$$

$$\alpha_{21}=\alpha^1_{21}\alpha^2_{11}+\alpha^1_{22}\alpha^2_{21}+\gamma^1_{21}\delta^2_{11}+\gamma^1_{22}\delta^2_{21},$$

$$\gamma_{11}=\alpha^1_{11}\gamma^2_{11}+\alpha^1_{12}\gamma^2_{21}+\gamma^1_{11}\beta^2_{11}+\gamma^1_{12}\beta^2_{21},$$

$$\gamma_{21}=\alpha^1_{21}\gamma^2_{11}+\alpha^1_{22}\gamma^2_{21}+\gamma^1_{21}\beta^2_{11}+\gamma^1_{22}\beta^2_{21},$$

$$\delta_{11}=\delta^1_{11}\alpha^2_{11}+\delta^1_{12}\alpha^2_{21}+\beta^1_{11}\delta^2_{11}+\beta^1_{12}\delta^2_{21},$$

$$\beta_{11}=\delta^1_{11}\gamma^2_{11}+\delta^1_{12}\gamma^2_{12}+\beta^1_{11}\beta^2_{11}+\beta^1_{12}\beta^2_{21}.$$

The functions P_1, P_2, P_3 were obtained by the following process:

$$P_1=\beta_{11},\quad P_2=\mathrm{Re}\,(\alpha_{11}\beta_{11}-\gamma_{11}\delta_{11}),$$

$$P_3=\mathrm{Im}\,(\alpha_{11}\beta_{11}-\gamma_{11}\delta_{11}).$$

[1] E. H. Hauge and J. A. Stavney, Rev. Mod. Phys. **61**, 917 (1989).
[2] V. S. Olkhovsky and E. Rcoami, Phys. Reports **214**, 339 (1992).
[3] R. Landauer and Th. Martin, Rev. Mod. Phys. **66**, 217 (1994).
[4] T. E. Hartman, J. Appl. Phys. **33**, 3427 (1962).
[5] K. W. H. Stevens, J. Phys. C **16**, 3649 (1983).
[6] D. Collins, D. Lowe, and J. R. Barker, J. Phys. C **20**, 6213 (1987).
[7] N. A. Chuprikov, Fiz. Tekh. Poluprovodn. **27**, 799 (1993) [Semiconductors **27**, 650 (1993)].
[8] J. G. Muga and H. Cruz, Physica B **179**, 326 (1992).
[9] V. D. Dymnikov and O. V. Konstantinov, Fiz. Tekh. Poluprovodn. **28**, 844 (1994) [Semiconductors **28**, 494 (1994)].
[10] T. Ando, S. W. Kahora, and H. Akera, Phys. Rev. B **40**, 11 609 (1989).
[11] T. Ando and H. Akera, Phys. Rev. B **40**, 11 618 (1989).
[12] G. F. Karavaev, S. N. Krinyaev, and V. N. Chernyshev, Izv. Vuzov. Fizika **35**(9), 64 (1992) [in Russian].
[13] S. N. Krinyaev, G. F. Karavaev, and V. N. Chernyshev, Fiz. Tekh. Poluprovodn. **28**, 1393 (1994) [Semiconductors **28**, 784 (1994)].
[14] D. Z-Y. Ting and T. C. McGill, J. Vac. Sci. Technol. B **7**, 1031 (1989).
[15] D. Z-Y. Ting and T. C. McGill, J. Vac. Sci. Technol. B **10**, 1980 (1992).
[16] Z. Yumin and Z. Hazhi, Appl. Phys. Lett. **65**, 1036 (1994).
[17] T. Ando and H. Akera, in *Proceedings 19th International Conference on the Physics of Semiconductor*, W. Zawadzki [Ed.] (Institute of Physics, Polish Academy of Sciences. Warsawa, 1988), p. 603.
[18] J.-B. Xia, Phys. Rev. B **41**, 3117 (1990).
[19] E. L. Ivchenko, A. A. Kiselev, Y. Fu, and M. W. Willander, Phys. Rev. B **50**, 7747 (1994).
[20] G. F. Karavaev, V. N. Chernyshev, and A. A. Voronkov, Izv. Vuzov. Fizika **40**(1), 63 (1997) [in Russian].
[21] E. P. Wigner, Phys. Rev. **98**, 145 (1995).
[22] M. L. Goldberg and K. Watson, *Collision Theory* (J. Wiley, N. Y.–London–Sydney, 1964), ch. 3.
[23] D. E. Potter, *Computational Physics* (Wiley, New York, 1973; Mir, Moscow, 1975).

Translated by Frank J. Crowne

Effect of ion dose and annealing mode on photoluminescence from SiO_2 implanted with Si ions

G. A. Kachurin, A. F. Leĭer, K. S. Zhuravlev, I. E. Tyschenko, A. K. Gutakovskiĭ, and V. A. Volodin

Institute of Semiconductor Physics, 630090 Novosibirsk, Russia

W. Skorupa and R. A. Yankov

Research Center Rossendorf, D-01314 Dresden, Germany

(Submitted November 27, 1997; accepted for publication April 27, 1998)
Fiz. Tekh. Poluprovodn. **32**, 1371–1377 (November 1998)

This paper discusses the photoluminescence spectra of 500-nm-thick layers of SiO_2 implanted with Si ions at doses of 1.6×10^{16}, 4×10^{16}, and 1.6×10^{17} cm^{-2} and then annealed in the steady-state region (30 min) and pulsed regime (1 s and 20 ms). Structural changes were monitored by high-resolution electron microscopy and Raman scattering. It was found that when the ion dose was decreased from 4×10^{16} cm^{-2} to 1.6×10^{16} cm^{-2}, generation of centers that luminesce weakly in the visible ceased. Moreover, subsequent anneals no longer led to the formation of silicon nanocrystallites or centers that luminesce strongly in the infrared. Annealing after heavy ion doses affected the photoluminescence spectrum in the following ways, depending on the anneal temperature: growth (up to $\sim$700 °C), quenching (at 800–900 °C), and the appearance of a very intense photoluminescence band near 820 nm (at $>$900 °C). The last stage corresponds to the appearance of Si nanocrystallites. The dose dependence is explained by a loss of stability brought on by segregation of Si from SiO_2 and interactions between the excess Si atoms, which form percolation clusters. At low heating levels, the distinctive features of the anneals originate predominantly with the percolation Si clusters; above $\sim$700 °C these clusters are converted into amorphous Si-phase nanoprecipitates, which emit no photoluminescence. At temperatures above 900 °C the Si nanocrystallites that form emit in a strong luminescence band because of the quantum-well effect. The difference between the rates of percolation and conversion of the clusters into nanoprecipitates allows the precipitation of Si to be controlled by combinations of these annealings. © *1998 American Institute of Physics.* [S1063-7826(98)01611-1]

INTRODUCTION

Interest in fabricating light-emitting elements based on silicon is motivated by the requirements of integrated microelectronic circuits. For a number of physical reasons, radiative recombination in Si is strongly hindered, which significantly limits its usefulness for making optical elements and circuits. Only in recent years has a real path opened up to solving this problem—the use of quantum-well effects in silicon nanostructures. Starting with porous silicon, and later using layers of SiO_2 with excess Si, researchers have succeeded in producing efficient radiative recombination at room temperature in the visible (or near-infrared) regions. Especially promising is the possibility of creating similar nanostructures by ion implantation (see Refs. 1–9). However, because the reasons for the appearance of intense emission are still not completely understood, the nature of the radiative recombination centers remains a controversial subject.[10,11] Researchers commonly assert that the alternative sources of emission are imperfections in the SiO_2. Such assertions are not without justification, since more than one researcher has observed the appearance of bands of luminescence without additional annealing, decreases in the intensity of light emission upon heating, and an enhancement of light emission upon implantation of ions of inert gases, and its dependence on the anneal conditions.[2,9,12–16] In Refs. 6 and 7 we argued that the variations in intensity and wavelength of the emission as a function of how the implanted layers were processed are associated not with defects but rather with distinctive features of the excess Si liberated from SiO_2. The scheme we proposed for the evolution of the overall emission process explained the available experimental data. However, in order to deepen our understanding, it is necessary to investigate the dependence of the luminescence on the ion dose and annealing regimes. This is the subject of the present paper.

METHOD

Si^+ ions with energies of 200 and 100 keV were embedded in 500-nm-thick, thermally grown layers of SiO_2. Two implantation energies were used to obtain a layer with a relatively uniform distribution of excess Si. Calculations using the program TRIM indicated that such a distribution would result if the ratio of doses at large and small energies was chosen to be 1:0.6. We used three total doses–1.6×10^{17},

 © 1998 American Institute of Physics

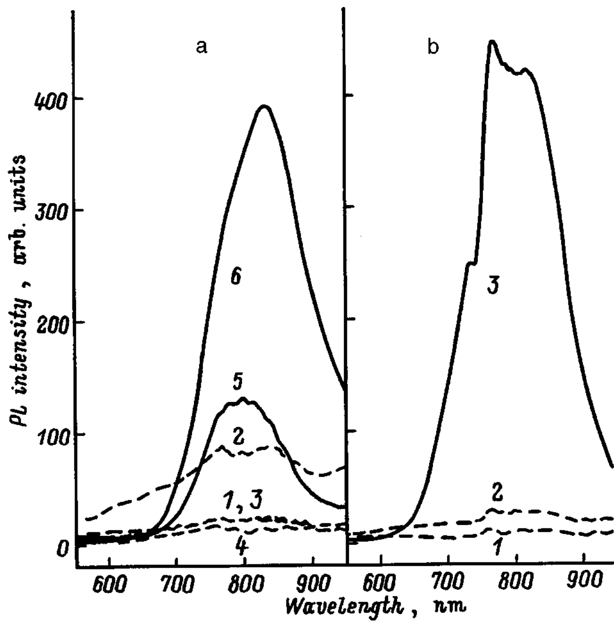

FIG. 1. Change in the PL spectrum with increasing T_a after implantation of large (a) and medium (b) doses of Si ions. The temperatures of 30-min annealing T_a, °C: a) *1* — 600, *2* — 700, *3* — 800, *4* — 900, *5* — 1000, *6* — 1150; b) *1* — 400, *2* — 1000, *3* — 1150. For the dashed curves the ordinates are increased by a factor of 3.

4×10^{16}, and 1.6×10^{16} cm^{-2}— and in what follows we will refer to them as high, medium, and low respectively. Post-implantation anneals were carried out both sequentially in a furnace for 30 min in the temperature range $T_a=400-1150$ °C and under a pulsed lamp with heating durations of 1 s and 20 ms. Photoluminescence (PL) spectra in the wavelength range $\lambda=$ 550–950 nm were taken under the same detection conditions at 20 °C with fixed-power excitation by an argon laser ($\lambda=$ 480 nm). These systems were also studied by high-resolution electron microscopy using a JEM-4000EX microscope.

RESULTS

Decreasing the total dose of Si ions within a single order of magnitude affected the photoluminescence in square-root fashion. The ''high'' dose led to considerable emission even after minimal annealing over the entire spectral range of interest (Fig. 1). For the ''medium'' and ''small'' doses the signal was at background level. Increasing the anneal temperature T_a led to significantly different results. After the high dose, three stages of evolution in the PL were clearly seen with increasing T_a. Up to 700 °C it increased for all the wavelengths while maintaining an overall maximum near $\lambda=$ 800 nm. In the range $T_a=800-900$ °C the emission fell almost to zero. Increasing T_a to 1000 and 1150 °C caused a repeatable and very sharp increase in the PL with the formation of intense and well-defined bands in the infrared region ($\lambda_{max}=$ 820 nm). After the medium dose, the first two stages were practically undetectable, and up to $T_a=1000$ °C the emission was very weak. The spectra after $T_a=600-900$ °C were close to the spectra 1 shown in Fig. 1b. Generation of very intense bands was observed only when T_a was increased to 1150 °C. As is clear from Fig. 1, the compound nature of the spectrum was revealed in much clearer form than after a high dose. In contrast to the latter, the intensity of the short-wavelength edge (for example, at $\lambda=$ 700 nm) increased, while the long-wavelength edge ($\lambda=$ 900 nm) decreased. After the small dose we found that intense emission could not be created by any annealing. The only noticeable change was a certain increase in the yellow-orange emission after a 1000 °C anneal; however, this also disappeared at T_a = 1150 °C (see Fig. 2c).

Previously,[7,8] we observed that nanocrystallites of Si form rapidly during annealing under conditions where the ordinary diffusion length of Si atoms in SiO_2 is insufficient to transport them to growth-center ''sinks.'' Therefore, we were interested in identifying whether or not nanocrystallites could be formed by pulsed heating if the implantation dose was decreased. It turned out that an intense infrared band

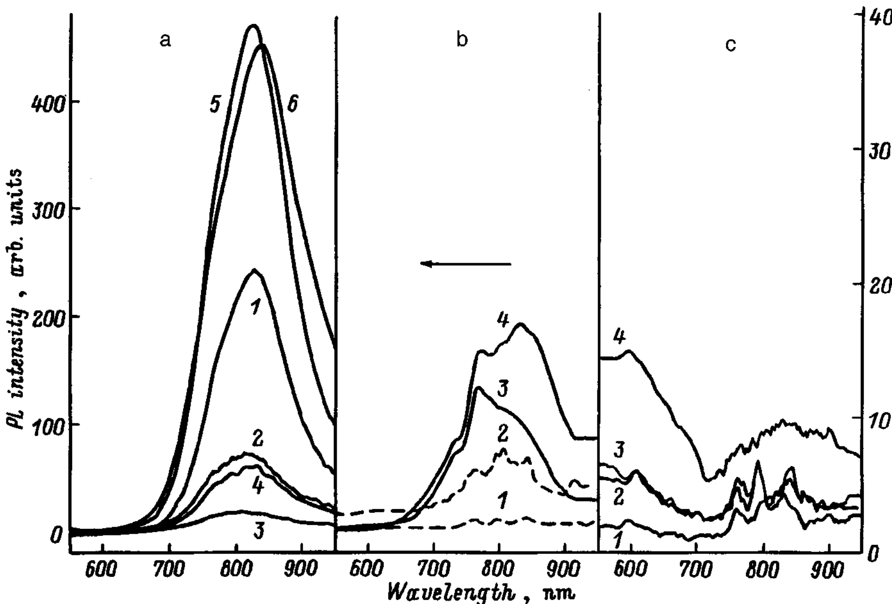

FIG. 2. Change in the PL spectrum with increasing T_a after implantation of large (a), medium (b), and small (c) doses of Si ions and high-temperature pulsed annealings. a) initial heating to 1200 °C, 1 s (*1*), then annealings for the following temperature T_a, °C: *2*—700, *3*—800, *4*—900, *5*—1000, *6*—1150. b) initial heating to 1200 °C, 1 s (*1*), then annealing for T_a, °C: *2*—900, *3*—1000, *4*—1150. The ordinates for the dashed curves are increased by a factor of 3. c) *1*—before annealing, and also after annealing at 1350 °C for 20 ms or after $T_a=1150$ °C, 30 minutes, *2*—after annealing at $T_a=1000$ °C, 30 minutes. *3*—initial heating to 1350 °C, 20 ms, then $T_a=1150$ °C 30 minutes. *4*—initial heating to 1350 °C, 20 ms, then $T_a=1000$ °C, 30 min.

formed under the action of weak thermal pulses only after the high dose (Fig. 2). After the small and medium doses annealing produced no such bands, either for 20 ms or 1 s anneal times. A post-impulse re-annealing of the samples in a furnace gave the following results. In the case of implantation with a small dose, the first thermal pulse, which does not in itself lead to any change in the PL spectrum (Fig. 2c, curve *1*), was capable of generating PL centers, in particular, in the orange region, after a furnace re-annealing at 1000 °C (Fig. 2c, compare curves *2* and *4*). Of course, this emission was weak, and disappeared when the temperature of the re-annealing was increased to 1150 °C (Fig. 2c, curve *3*). After a moderate dose, a 30-min re-annealing led to the appearance of a distinct PL band near 800 nm (Fig. 2b). Its intensity was high but nevertheless lower than the result of a single anneal in the furnace at 1150 °C. On the other hand, preliminary pulsed heating obviously could make it appear earlier. As is clear from a comparison of Figs. 1b and 2b, one furnace anneal at $T_a \leqslant 1000$ °C in fact gave nothing. However, when preliminary pulsed heating was used, the band began to form even after a $T_a = 900$ °C anneal, while after a 1000 °C anneal it was already quite intense.

The results of post-implant re-annealing of samples implanted by a high dose are shown in Figs. 2a and 3. In these samples the centers of intense PL were formed after 1 s at 1200 °C and after 20 ms at 1350 °C. Subsequent annealing in a furnace at comparatively low temperatures resulted in quenching of the PL, and between $T_a = 800$ and 900 °C it practically disappeared. Only for T_a values of 900 °C and above did a sharp growth in intensity take place, which eventually saturated. For comparison, Fig. 3 also shows how the PL intensity of the samples changes with annealing when these samples do not undergo preliminary pulsed heating. As T_a increases to 700 °C, it exhibits some growth, but then the same quenching stage can be seen, followed by a strong increase.

According to the high-resolution electron microscopy data (Fig. 4), nanocrystallites of Si form in SiO_2 only after high-temperature processing, and only after large and medium doses. For small doses nanocrystallites were not observed even after the maximum anneals. These data are in agreement with the conditions for the appearance of an intense band in the near-IR region. For ordinary annealing in a furnace at 1150 °C for 30 min, a high dose gave a high concentration of nanocrystallites with sizes about 3 nm (Fig. 4). For medium doses there were fewer nanocrystallites, which were accompanied by dark noncrystalline regions with nanometer dimensions. Preliminary pulsed heating affected the structural conversion in the layers. Evidence for this was enlargement of the Si crystals after a high dose from 2–3 to 3–5 nm. From Fig. 4c it is clear that a considerable number of these crystals link up with each other, in contrast to the results of moderate implantation doses, for which no increase in the size or number of crystallites was apparent. At small doses nanocrystallites did not form at all.

A comparison of the PL and microscopy data shows an undoubted correlation between the appearance of the intense band in the near-IR region and the formation of Si nanocrystallites. In order to reveal the reasons why the PL is

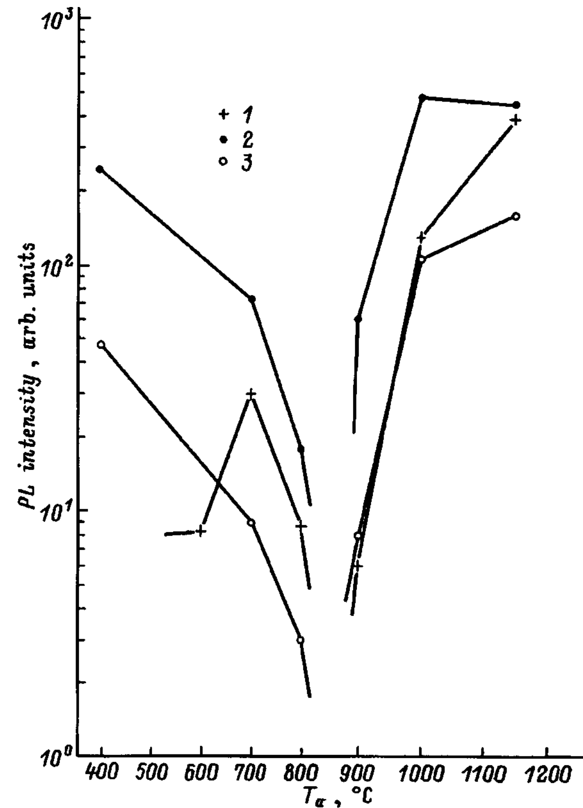

FIG. 3. Change in the maximum PL intensity after 30-min annealings. *1*—annealing in an oven only. *2*—initial heating to 1200 °C, 1 s, then annealing in the oven. *3*—initial heating to 1350 °C, 20 ms, then annealing in the furnace.

quenched at $T_a = 800$ °C (Fig. 3), the same anneal was used on samples implanted with a high dose of Si and subjected to pulsed heating. These samples had previously developed silicon nanocrystallites and achieved intense PL. Raman scattering spectra are shown in Fig. 5. Embedding of Si ions led to additional scattering near 480 cm^{-1}, caused by Si–Si bonds in noncrystalline silicon. This signal was significantly weakened after pulsed heating, and a shoulder appeared on the left side of the 520-cm^{-1} peak, which comes from the silicon crystalline substrate. Such a signal could have come from Si crystals with sizes about 3 nm, as observed in Ref. 6. If, however, the samples were further heated in a furnace at $T_a = 800$ °C after high-temperature pulsed heating, the shoulder on the 520-cm^{-1} peak disappeared and the scattering in the neighborhood of 480 cm^{-1}, which is characteristic of noncrystalline Si, appeared once more. In comparison with the initial situation, it even increased. The disappearance of Si nanocrystallites after annealing at 800 °C for 30 min was directly confirmed by microscopy.

DISCUSSION OF RESULTS

Varying the dose of Si ions over a comparatively narrow interval of $(1.6–16) \times 10^{16}$ cm^{-2} turns out to have an extremely strong influence on the formation of PL centers, and the dose dependences clearly have a threshold character. In this interval of doses, the calculated mean distance between excess Si atoms decreases to $r < 1$ nm. At the same time,

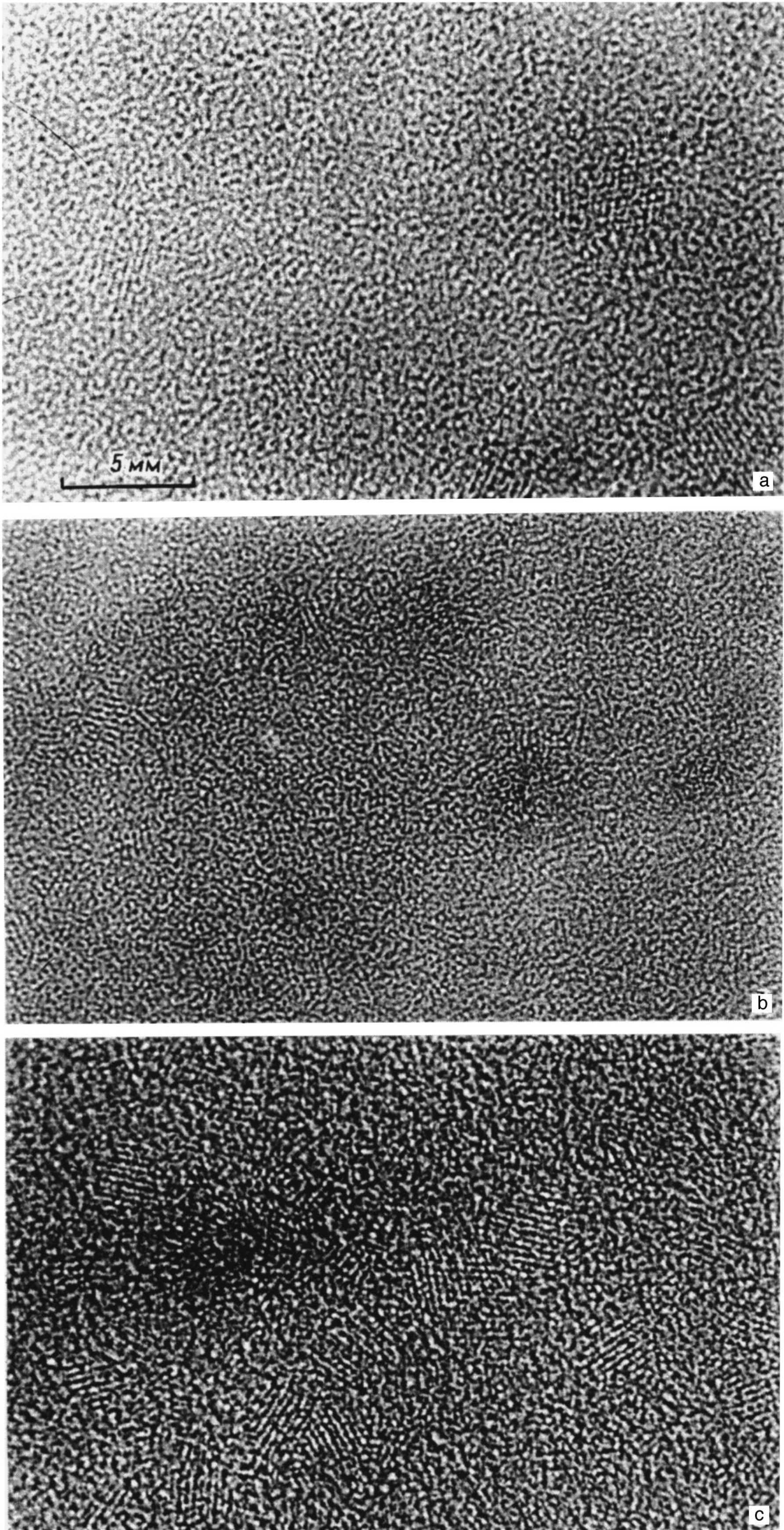

FIG. 4. High-resolution electron microscopy images of samples. Large (a) and medium (b) doses, annealings at 1150 °C, 30 min; c—large dose, annealing at 1200 °C, 1 s, then at 1150 °C, 30 min.

increased PL intensity in the visible and IR regions was observed by us for $T_a < 700$ °C, when (see Ref. 17) the diffusion length of Si in SiO_2 should be less than 0.1 nm. Therefore, at the initial stages of formation of PL centers a decisive role is obviously played not by the diffusion flux of excess Si to centers of precipitation, but rather the possibility of direct interaction of Si atoms among themselves. The transition from $r \sim 1$ nm (medium dose) to $r \sim 1.4$ nm (small dose) turns out to be critical. This rather small increase in r in fact eliminates the possibility of achieving intense PL due to further annealings. Consequently, both the formation at moderate heating levels of centers of weak visible emission, and the formation of nanocrystallites as a result of high-temperature processing with the appearance of distinct IR bands, are consequences of the interaction of closely spaced excess Si atoms. The probability of such interactions depends very strongly on r, and the process itself occurs at sites of random clustering of Si atoms and ceases in the absence of very close nearest-neighbor atoms, i.e., it will have a percolative character. We assume that the appearance at the initial stages of the anneal of a set of centers for PL over the entire spectral range we investigated (Fig. 1) is due to the formation of percolation chains and branching clusters of various sizes and shapes. Such precipitation is not phase segregation since there are no phase boundaries.

Our studies show that the formation of PL centers during annealing takes place in several stages (Figs. 1–3). Our interpretation of the first stage up to $T_a = 700$ °C with no preliminary pulsed heating is obvious. With increasing T_a, the segregation of excess Si from SiO_2 is enhanced with the formation of percolation clusters. At this stage, the diffusion of Si atoms to sinks is very limited; therefore, the number, size, and shapes of the PL centers will be determined by fast-acting percolation. What happens at $T_a = 1000 - 1159$ °C, in light of the PL, microscopy, and Raman scattering data, can also be easily explained. Silicon nanocrystallites form in the SiO_2 layers. These nanocrystallites are capable, because of quantum confinement, of intense luminescence in the near-IR. At $T_a = 1150$ °C, the silicon in SiO_2 already possesses a rather large diffusion coefficient equal to $\sim 2 \times 10^{-16}$ cm^2/s. Despite this fact, after a small dose, when the concentration of Si reaches ~ 1 at. %, no increase in Si nanocrystallites is observed at all. Consequently, in order for these nanocrystallites to form, we need both sufficient mobility of the Si atoms and stable nuclei (sinks). The conditions for formation of nuclei are satisfied when we move to medium doses, where it becomes possible for percolation processes to develop. Thus, percolation causes homogeneous nucleation as the supersaturated solution of Si in SiO_2 decays. An increase in the size of precipitates at $T_a = 1000 - 1150$ °C takes place due to diffusion sinks of individual Si atoms, and is a consequence of coalescence.[18]

During the intermediate stages 700 °C $< T_a <$ 1000 °C, the processes can be understood from considerations of the experiments with re-annealing at $T_a = 800$ °C of samples where the nanocrystallites were already formed by pulsed heating at 1200 or 1350 °C. Here, probably, amorphization (melting) of the nanocrystallites occurs. It is known that the stability of fine crystals is determined by a balance of volume and surface free energies. Due to the destabilizing effect of the surface, the melting temperature of these crystallites is greatly lowered.[19–22] With increasing temperature, the balance shifts in favor of the volume energy and the crystalline state becomes more favorable. In the case of pulsed heating it is also fixed by tempering. Recall that in contrast to crystalline porous Si, amorphous silicon does not give intense red PL,[21,23,24] caused by the presence of dangling bonds and other centers of nonradiative recombination. Incidentally, at $T_a = 800$ °C segregation of Si from SiO_2 takes place, which also explains the increase in the signal in the neighborhood of 480 cm^{-1} (Fig. 5). In light of all this, we naturally connect the observed quenching of PL over the entire spectral range we studied in the course of a simple furnace anneal at temperatures of $T_a \cong 800 - 900$ °C with transformation of the percolating clusters and chains into nanoprecipitates of the amorphous Si phase (Fig. 3). The collapse of formless nonphase inclusions into phase inclusions has a diffusive character, and requires a longer time than percolation. For further increases in T_a, when there are enough diffusive Si sinks, the nanoprecipitates reach sizes at which crystallites are stable, estimated to be $\gtrsim 2$ nm. Particles of smaller size cannot be nanocrystallite. Probably we can associate the observed weak PL after $T_a = 1000$ °C in the orange-yellow

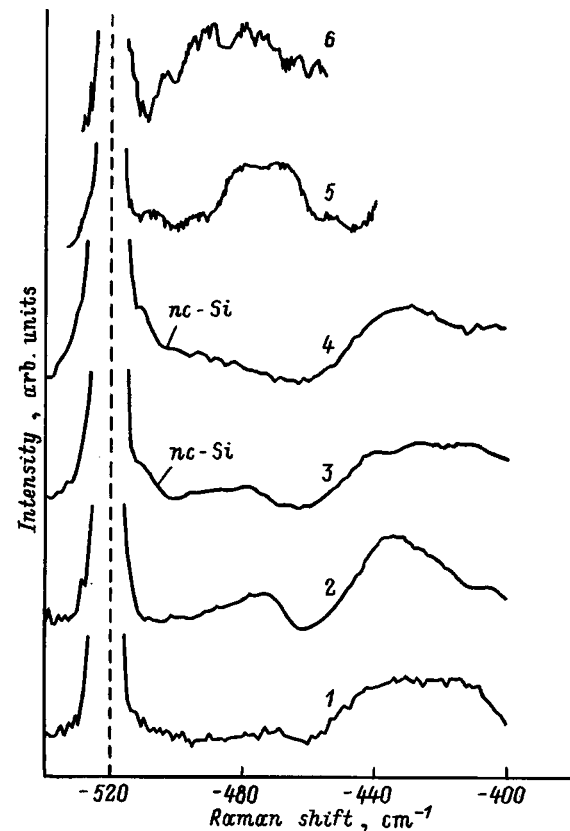

FIG. 5. Raman scattering spectra. *1*—initial SiO_2 layer; *2*—after implantation of a high dose of Si ions; *3* and *4*—after a crystallizing anneals at 1200°C, 1s and 1350 °C, 20 ms, respectively; *5* and *6*– -samples 3 and 4 after an additional anneal at 800 °C, 30 min.

range with them, and also the emission in the range $500<\lambda<700$ nm observed by many authors after high-temperature annealing of SiO_2 with excess silicon.[4,15,25] It is noteworthy that in normal amorphous silicon the concentration of dangling bonds does not exceed 10^{20} cm^{-3} and in principle small volumes could be free of them, especially after annealing.

The approach we have discussed also allows us to explain the effect of high-temperature pulsed heating on subsequent annealing in the furnace. High temperatures ensure displacements on the atomic scale and are capable of increasing the percolating clusters. For higher doses, dense clusters are then able to convert into nanocrystallites. Because percolation does not require long periods of time, after moderate doses the dimensions of the percolating clusters subjected to pulsed heating also increase, but they turn out to be less dense. Transformation of a formless cluster (with small fractal dimensions) into a single nanocrystallite will be hindered. Preliminary simulation on a computer shows that it can even decay into several parts. We assume that the appearance of dark regions (Fig. 4) after moderate doses is a consequence of the formation of large but formless noncrystalline precipitates. Finally, at small doses the large-scale formation of large-scale percolation clusters becomes impossible even under the action of high-temperature pulses. Nevertheless, the formation of a rather small number of fine crystallites is stimulated. Subsequent annealings do not cause them to grow to the size of stable nanocrystallites, but convert them into centers of weak orange-yellow PL. Increasing T_a to 1150 °C causes them to dissolve.

CONCLUSIONS

The dose dependence of PL center formation has a threshold character which is apparent in the dose interval between 1.6×10^{16} and 1.6×10^{17} cm^{-2}, when the average distance r between atoms of implanted Si changes from ~ 1.4 to ~ 0.7 nm. As the dose decreases in this interval (or when r increases from ~ 0.7 to ~ 1.4 nm), the possibility of forming a broad range of centers of weak PL is lost for the entire visible region, along with the possibility of subsequent formation of Si nanocrystallites by high-temperature annealing and the creation of an intense PL band in the near-IR region. If, however, the dose is sufficient, then the annealing proceeds by several stages. Up to $T_a\cong700$ °C, diffusion of Si in SiO_2 can be ignored, so centers form that give weak emission over the entire spectral range we studied. For $T_a=800-900$ °C the PL intensity falls to the background level at all wavelengths. After $T_a=1000-1150$ ° a very strong band appears in the near-IR region, and at the same time Raman scattering and high-resolution electron microscopy indicate the formation of Si nanocrystallites.

These dependences of PL center formation on dose and annealing are interpreted as follows. All the forms of PL we observed are connected with excess Si in SiO_2. For the formation of PL centers it is necessary for r to decrease to 1 nm, in order to provide direct interaction of nearest neighbor silicon atoms. This process will have a percolation character, and will not require heating to temperatures where Si diffusion is significant, although increasing the temperature enables the atomic level displacements and development of percolation clusters. The expulsion of excess Si from SiO_2 dominates up to $T_a\cong700$ °C with the appearance of clusters of various sizes and shapes, giving a broad weak PL spectrum. Subsequent quenching of the PL at $T_a\cong800-900$ °C is a consequence of a slower process—the conversion of non-phase Si inclusions (percolation clusters, chains, etc.) into nanoprecipitates of the amorphous Si phase, containing centers of nonradiative recombination. At $T_a=1000-1150$ °C, because of diffusion sinks of Si atoms and coalescence, the nanoprecipitates of Si reach dimensions where nanocrystallites are stable. Because of the quantum-well effect, the nanocrystallites give a strong emission in the visible and IR regions ($\lambda_{max}\sim820$ nm). The Si inclusions that do not reach the stability size after high-temperature annealing ($\gtrsim2$ nm) are probably responsible for the observed weak and shorter-wavelength emission. By exploiting the competition between rapid percolation processes and relatively slow collapse of clusters into phase nanoprecipitates, we can control the formation of silicon inclusions by using combination annealings.

This work was carried out with the partial support of a grant from the Science Ministry as part of the program ''Physics of Solid-State Nanostructures'' No. 3-011/4.

[1] T. Shimizu-Iwayama, S. Nakao, and K. Saitoh, Appl. Phys. Lett. **65**, 1814 (1994).
[2] H. A. Atwater, K. V. Shcheglov, S. S. Wong, K. J. Vahala, R. S. Rlagan, M. I. Brongersma, and A. Polman, Mater. Res. Soc. Symp. Proc. **321**, 363 (1994).
[3] T. Shimizu-Iwayama, K. Fujita, S. Nakao, K. Saitoh, R. Fujita, and N. Itoh, J. Appl. Phys. **75**, 7779 (1994).
[4] P. Mutti, G. Ghislotti, S. Bertoni, L. Bonoldi, G. F. Cerofolini, L. Meda, E. Grilli, and M. Guzzi, Appl. Phys. Lett. **66**, 851 (1995).
[5] W. Skorupa, R. A. Yankov, I. E. Tyschenko, H. Frob, T. Bohme, and K. Leo, Appl. Phys. Lett. **68**, 2410 (1996).
[6] G. A. Kachurin, I. E. Tyschenko, K. S. Zhuravlev, N. A. Pazdnikov, V. A. Volodin, A. K. Gutakovsky, A. F. Leier, W. Skorupa, and R. A. Yankov, Nucl. Instrum. Methods Phys. Res. B **122**, 571 (1997).
[7] G. A. Kachurin, K. S. Zhuravlev, N. A. Pazdnikov, A. F. Leier, I. E. Tyschenko, V. A. Volodin, W. Skorupa, and R. A. Yankov, Nucl. Instrum. Methods Phys. Res. B **127/128**, 583 (1997).
[8] G. A. Kachurin, I. E. Tyschenko, W. Skorupa, R. A. Yankov, K. S. Zhuravlev, N. A. Pazdnikov, V. A. Volodin, A. K. Gutakovsky, and A. F. Leier, Fiz. Tekh. Poluprovodn. **31**, 730 (1997) [Semiconductors **31**, 626 (1997)].
[9] T. Shimizu-Iwayama, Y. Terao, A. Kamiya, M. Takeda, S. Nakao, and K. Saitoh, Nucl. Instrum. Methods Phys. Res. B **112**, 214 (1996).
[10] F. Koch, V. Petrova-Koch, T. Muschik, A. Nikolov, and V. Gavrilenko, Mater. Res. Soc. Symp. Proc. **283**, 197 (1993).
[11] G. G. Qin, Y. M. Huang, J. Lin, L. Z. Zhang, B. Q. Zong, and B. R. Zhang, Solid State Commun. **94**, 607 (1995).
[12] S. Bota, B. Garrido, J. R. Morante, A. Baraban, and P. P. Konorov, Solid-State Electron. **34**, 355 (1996).
[13] L.-S. Liao, X.-M. Bao, N. S. Li, X.-Q. Zheng, and N.-B. Min, J. Lumin. **68**, 199 (1996).
[14] E. Neufeld, S. Wang, R. Apetz, Ch. Bechal, R. Carias, C. W. White, and D. K. Thomas, Proc. E-MRS 1996 Spring Meeting (Strasbourg, 1996).
[15] G. Ghislotti, B. Nielsen, P. Asoka-Kumar, K. G. Lynn, A. Gambhir, L. F. Di Mauro, and C. E. Bottani, J. Appl. Phys. **79**, 8660 (1996).
[16] T. Komoda, J. Weber, K. P. Homewood, P. L. F. Hemment, and B. J. Sealy, Nucl. Instrum. Methods Phys. Res. B **120**, 93 (1996).
[17] L. A. Nesbit, Appl. Phys. Lett. **46**, 38 (1985).
[18] E. Wendler, U. Herrmann, W. Wesh, and H. H. Dunken, Nucl. Instrum. Methods Phys. Res. B **116**, 332 (1996).
[19] S. Veprek, Z. Iqbal, and F.-A. Sarott, Philos. Mag. B **45**, 137 (1982).

[20] Y. Maeda, Phys. Rev. B **51**, 1658 (1995).
[21] R. R. Kunz, P. M. Nitishin, H. R. Clark, M. Rotschild, and B. Ahem, Appl. Phys. Lett. **67**, 1766 (1995).
[22] A. N. Goldstein, Appl. Phys. A, **62**, 33 (1996).
[23] X.-M. Bao and H.-Q. Yang, Appl. Phys. Lett. **63**, 2246 (1993).
[24] J. C. Barbour, D. Dimos, T. R. Guilinger, M. J. Kelly, and S. S. Tsao, Appl. Phys. Lett. **59**, 2088 (1991).
[25] A. J. Kenyon, P. F. Trwoga, C. W. Pitt, and G. Rehm, J. Appl. Phys. **79**, 9291 (1996).

Translated by Frank J. Crowne

Effect of size dispersion on the optical absorption of an ensemble of semiconductor quantum dots

M. I. Vasilevskiĭ and E. I. Akinkina

N. I. Lobachevskiĭ Nizhniĭ Novgorod State University, 603600 Nizhniĭ Novgorod, Russia

A. M. de Paula

UNICAMP, 13083-970 Campinas, São Paulo, Brazil

E. V. Anda

Universidade Federal Fluminense, Niterói, CEP 24210-340, Rio de Janeiro, Brazil

(Submitted November 27, 1997; accepted for publication May 18, 1998)
Fiz. Tekh. Poluprovodn. **32**, 1378–1383 (November 1998)

The linear optical absorption of an ensemble of semiconductor quantum dots randomly positioned in an insulating matrix is studied theoretically and experimentally for the CdTe/glass system. The calculation of the effective dielectric function of the system, whose imaginary part determines the absorption, is based on a modified Maxwell–Garnett formalism using a diagram technique to calculate the average renormalized polarizability of spherical quantum dots. This approach takes into account both the fluctuations of the polarization interaction due to the random positions of the spheres and their size dispersion. A comparison of the theoretical and experimental spectra permits determination of the mean quantum dot size and concentration. The dependence of these parameters on the postgrowth annealing time of the samples is not consistent with the existing theories on the spinodal decomposition of solid solutions. © *1998 American Institute of Physics.* [S1063-7826(98)01711-6]

INTRODUCTION

Semiconductor microcrystals (quantum dots) grown within an insulating matrix are of interest from the standpoint of nonlinear optical effects. The possibility of controlling the energy spectrum by altering the size of quantum dots (QD's) and the large density of states for the corresponding energy values make such systems promising from the standpoint of creating lasers as well.

Composite materials containing semiconductor QD's can be produced by using various technologies,[1–3] but none of them makes it possible to eliminate the size dispersion of the semiconductor microcrystals.

The size dispersion of QD's causes the discrete linear optical absorption peaks at frequencies corresponding to transitions between quantum-well hole and electron states to broaden dramatically. This effect is usually taken into account by performing averaging using the absorption spectrum of a single QD and a certain size distribution function,[4–6] which is suitable only for obtaining an estimate. Such an approach is valid in the limiting case of a very small volume fraction of the semiconductor ($f\rightarrow 0$), since it disregards: 1) the polarization interaction of the QD's with one another and 2) the variation of the refractive index with the optical frequency in the absorption region.

In this paper we propose a scheme based on a modified Maxwell–Garnett formalism for calculating the effective dielectric function of a composite consisting of isolated semiconductor QD's in an insulating matrix. The proposed approach takes into account both the size dispersion and the dielectric fluctuations associated with the random positioning of the QD's. The formulas obtained are used to simulate the experimental linear optical absorption spectra of SiO_2 matrices with CdTe microcrystals grown from a melt of a borosilicate glass with additions of CdO and Te by a series of successive anneals.

THEORY

Effective dielectric function of a composite

Let us consider an isotropic insulating matrix containing randomly positioned spherical inclusions that are isolated from one another. In the effective-medium approximation its dielectric function ϵ^* is related to the (renormalized) polarizability α^* of the spheres by the Maxwell–Garnett equation:

$$\frac{\epsilon^*-\epsilon_h}{\epsilon^*+2\epsilon_h}=\frac{4}{3}\pi n\alpha^*, \tag{1}$$

where ϵ_h is the dielectric function of the matrix, and n is the concentration of the spheres. If α^* is set equal to the ordinary polarizability of an insulating sphere of radius a_0 with the constant dielectric function ϵ_s in a homogeneous medium, i.e., if

$$\alpha(a_0)=\frac{\epsilon_s-\epsilon_h}{\epsilon_s+2\epsilon_h}a_0^3, \tag{2}$$

then (1) gives the familiar Clausius–Mossotti formula.

The general equation for α^* has the form[7]

 © 1998 American Institute of Physics

$$\alpha^* = \left\langle \alpha \sum_j \overleftrightarrow{V}^{-1}_{ij} \right\rangle, \tag{3}$$

where

$$\overleftrightarrow{V}^{-1}_{ik} \overleftrightarrow{V}_{kj} = \overleftrightarrow{1}\delta_{ij},$$

$$\overleftrightarrow{V}_{ij} = \overleftrightarrow{1}\delta_{ij} - \alpha \Delta \overleftrightarrow{T}_{ij},$$

$$\Delta \overleftrightarrow{T}_{ij} = \overleftrightarrow{T}_{ij} - \langle \overleftrightarrow{T}_{ij} \rangle. \tag{4}$$

In Eq. (4)

$$\overleftrightarrow{T}_{ij} = \mathrm{e}^{-i\mathbf{q}(\mathbf{R}_i - \mathbf{R}_j)}(1-\delta_{ij})\nabla_i \nabla_j \frac{1}{R_{ij}}$$

is the dipole-dipole interaction tensor, $\overleftrightarrow{1}$ is a unit tensor, $R_{ij} = |\mathbf{R}_i - \mathbf{R}_j|$, i and j label the spheres, and the angle brackets denote averaging over the ensemble of spheres. The expansion of $\overleftrightarrow{V}^{-1}_{ij}$ in (3) in powers of $\alpha \Delta \overleftrightarrow{V}_{ij}$ leads to an equation resembling the Dyson equation,[7,8] in which the averaging over the realizations of disorder in the positioning of the spheres can be performed using the diagram technique described in Ref. 7.

Apart from the topological disorder, there is also disorder associated with the size dispersion of the spheres. Both averaging operations can be performed in a certain approximation (which is similar to the averaged T matrix approximation in the theory of alloys), and the following result can be obtained:[8]

$$\alpha^* = \int da_0\ \alpha(a_0) \frac{1 - \sqrt{1 - 4\theta}}{2\theta} F(a_0), \tag{5}$$

where

$$\theta = \frac{8}{3}\pi n \alpha(a_0) \int da\ \frac{\alpha(a)}{(a_0 + a)^3} F(a), \tag{6}$$

and $F(a)$ is the distribution function of the sphere radius a.

Equations (1), (5), and (6) thus relate the effective dielectric function of a composite material to the dielectric functions of the matrix and the inclusions. The linear optical absorption coefficient is defined in the usual manner in terms of ϵ^*:

$$\gamma = \frac{2\kappa\omega}{c},$$

$$\kappa = [(|\epsilon^*| - \mathrm{Re}\,\epsilon^*)/2]^{1/2}.$$

It is not difficult to show that in the limit $f \to 0$

$$\alpha^* \approx \bar{\alpha} = \int da\ \alpha(a) F(a);$$

$$\epsilon^* \approx \epsilon_h(1 + 3f\bar{\alpha}); \quad \gamma \sim \epsilon_h^{1/2} f\ \mathrm{Im}\bar{\alpha}.$$

Dielectric function of a microcrystal

The dielectric function of a microcrystal in the region of interband optical transitions has the form (see, for example, Ref. 9)

$$\epsilon_s = \epsilon_\infty \left[1 + \frac{4\pi e^2}{\epsilon_\infty \hbar m^2 \omega^2 V} \sum_\nu \left| \mathbf{p}_\nu \right|^2 \left(\frac{1}{\omega_\nu - \omega} + \frac{1}{\omega_\nu + \omega} \right) \right]. \tag{7}$$

Here V is the volume, m_0 is the free-electron mass, $\mathbf{p}_\nu$ is the matrix element of the momentum operator between quantized states of the conduction band (E_e) and the valence band (E_h), and

$$\omega_\nu = \left(E_e^\nu + E_h^\nu + E_g - 1.8 \frac{e^2}{\epsilon_0 a_{\mathrm{ex}}} \right) / \hbar, \tag{8}$$

where E_g is the gap width of the semiconductor, ϵ_∞ and ϵ_0 are its high-frequency and static dielectric constants, and ν is the set of quantum numbers which label the dipole-active electron-hole pair states. The last term in (8) is a correlation correction,[10] and a_{ex} is the Bohr radius of a bulk exciton.

In the effective-mass approximation and under the assumption of an infinitely high potential barrier between the semiconductor and the insulator, the electron energy levels are specified by the quantum numbers n and l and are given by the formula[11]

$$E_e = \frac{\hbar^2 K_{n,l}^2}{2 m_e a^2}, \tag{9}$$

where $K_{n,l}$ is the nth root of the lth spherical Bessel function, and m_e is the electron effective mass.

The pattern of hole energy levels is more complicated due to the mixing of states corresponding to different subbands of the valence band of semiconductors with a diamond or sphalerite structure; it was examined in Refs. 12–15. The hole states are classified according to the values of the principal quantum number n and the total momentum F. For each value of F there are two different states (an even and an odd), but there is degeneracy with respect to the projection of the total angular momentum M.

In the limiting case of strong spin-orbit splitting ($\Delta \to 0$) the hole ground state is $1S_{3/2}$ in the notation used in Ref. 15. Its energy is given by the formula

$$E_h = \frac{\hbar^2 K_h^2}{2 m_{hh} a^2}, \tag{10}$$

where K_h is specified by the equation[14]

$$j_{F+1/2}(K_h \beta^{1/2}) j_{F-3/2}(K_h) + \frac{6F-3}{2F+3} j_{F-3/2}(K_h \beta^{1/2}) j_{F+1/2}(K_h) = 0 \tag{2}$$

with $F = 3/2$ and $\beta = m_{lh}/m_{hh}$. Here m_{lh} and m_{hh} are the light- and heavy-hole masses.

The same equation specifies the even hole states $2S_{3/2}, 3S_{3/2}, \ldots$ [the second, third, and ensuing roots of (11), respectively, should be taken], to which transitions of an electron from the $1S_e$ state are possible.

Transitions of an electron from the $1P_e$ state to the $1P_{1/2}^l$ [$K_h = \beta^{-1/2}\phi_1^1$, where ϕ_1^1 is the first root of the first spherical Bessel function, should be used in (10)], $1P_{3/2}$ (the equation for odd states was written out in Ref. 14), $1P_{3/2}^l$ [K_h is specified by (11) with $F = 5/2$], and ensuing hole states are possible.

All the electron-hole pair states just enumerated are degenerate with respect to M and the projection of the total electron angular momentum $j_e = s + l$. The ground state $(1S_e, 1S_{3/2})$ is thus eightfold degenerate, but only $g_1 = 4$ combinations of the projections of the electron and hole angular momenta correspond to states that are radiation-active in the dipole approximation.

The square of the matrix element in (7) can be written as

$$P^2 g_1 \left| \int \Psi_h \Psi_e \, d\mathbf{r} \right|^2,$$

where P^2 is determined by the symmetry of the Bloch amplitudes (the Kane angular momentum matrix element),

$$\Psi_e = (2\pi^2)^{1/2} a^{-3/2} j_0(\pi r/a) Y_{00},$$

$$\Psi_h = C_h a^{-3/2} \left[R_0(r) Y_{00} + R_2(r) \sum_M Y_{2M} \right],$$

$$R_0(r) = j_0(K_h r/a) - j_0(K_h),$$

and the spherical harmonics Y_{lm} are orthonormalized. The part of the hole wave function containing $R_2(r)$ does not make a contribution to the matrix element under consideration; therefore, $R_2(r)$ has not been written out. For $\beta \to 0$ we have $C_h = 6.044$ and $K_h = 5.76$ (Ref. 15), and the calculation of the square of the integral gives $I_1 = 0.874$.

If the variation of P^2 for different electron-hole states is ignored, Eq. (7) can be rewritten in the form

$$\epsilon_s = \epsilon_\infty \left[1 + \frac{4e^2 P^2}{\epsilon_\infty \hbar^3 \omega^2 a^3} \sum_\nu \frac{g_\nu \omega_\nu I_\nu}{(\omega_\nu - i\delta_\nu)^2 - \omega^2} \right]. \quad (12)$$

In (12) we have introduced the natural width of the spectral line $\hbar \delta_\nu$, and g_ν and I_ν are analogous in meaning to g_1 and I_1.

Dielectric function of the matrix

Glasses are known to absorb in the ultraviolet region of the spectrum. In order to take into account this circumstance, the dielectric constant ϵ_h should be equated with the imaginary part, whose frequency dependence can be described by a Gaussian function:

$$\mathrm{Im}\epsilon_h = \rho_0 \frac{\omega_0}{\Gamma_0} \exp\left[-\frac{(\omega - \omega_0)^2}{2\Gamma_0^2} \right], \quad (13)$$

where ρ_0, ω_0, and Γ_0 are parameters. The contribution to $\mathrm{Re}\epsilon_h$ corresponding to (13) can be calculated from the Kramers–Kronig relation.

EXPERIMENT

Samples of glasses with CdTe microcrystals were grown by fusing SiO_2, B_2O_3, Na_2O, ZnO, and the dopants (CdO and metallic Te) in a proportion equal to ~1 wt % (Ref. 3). The melt was then rapidly cooled in a stainless-steel vessel. Semiconductor microcrystals were grown within the glass matrix in successive anneals. The annealing regimes were varied.

Figure 1 shows the absorption spectra of two samples of the VCS37 series, which were cut from a single original matrix and subjected to heat treatment at 560 °C. The best results (from the standpoint of the quantum-well effects) were produced by two-stage annealing. The VCS39 samples (Fig. 2) were obtained by annealing first at 460 °C over the course of $t_a = 270$ h and then at 540 °C (the duration of the second anneal is indicated in the caption of Fig. 2). The spectra of these samples exhibit a series of features associated with transitions between quantum-well states, while the VCS37 samples clearly display only a transition associated with the ground state of the electron-hole pairs $(1S_e, 1S_{3/2})$.

Some results of investigations of similar samples by other methods were previously published in Ref. 16.

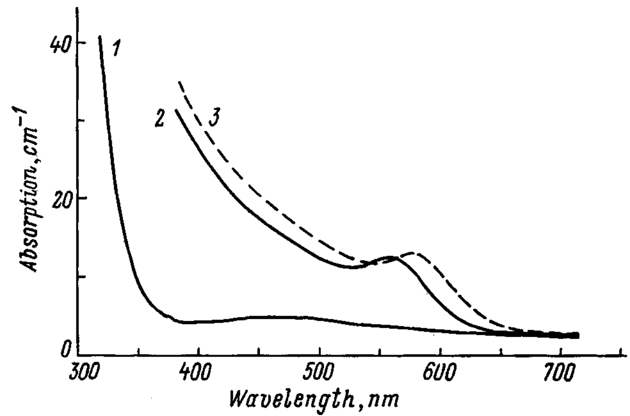

FIG. 1. Experimental absorption spectra of CdTe/glass samples of the VCS37 series immediately after cooling of the melt (*1*) and after annealing at 560 °C for 22 (*2*) and 32 min (*3*).

SIMULATION RESULTS AND DISCUSSION

The first step in calculating the theoretical spectra was to determine the best-fit values of the parameters of the optical absorption band of the glass without QD's using the spectra of samples not subjected to annealing. Thereafter, only the oscillator strength in (13) was varied for the annealed samples.

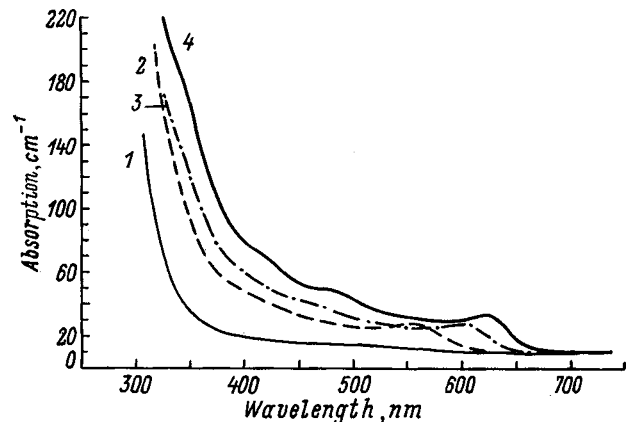

FIG. 2. Experimental absorption spectra of CdTe/glass samples of the VCS39 series obtained by two-stage annealing. The duration t_a of the second (high-temperature) anneal at 540 °C, min: *1* — 60, *2* — 150, *3* — 300, *4* — 420.

TABLE I. Transitions responsible for absorption in the optical region of the spectrum for the VCS39420 sample.

No.	Transition	E, eV	λ, nm	$g_\nu\ I_\nu/g_1 I_1$
1	$1S_{3/2}\rightarrow 1S_e$	2.02	613	1
2	$2S_{3/2}\rightarrow 1S_e$	2.29	541	0.8
3	$1P_{3/2}\rightarrow 1P_e$	2.57	482	2.2
4	$3S_{3/2}\rightarrow 1S_e$	2.70	459	0.5
5	$1P^l_{5/2}\rightarrow 1P_e$	2.85	435	1
6	$1S_{SS}\rightarrow 1S_e$	2.93	423	1.2
7	$1S_{3/2}\rightarrow 1D_e$	3.17	391	3
8	$1P^l_{1/2}\rightarrow 1P_e$	3.36	369	1.2
9	$1D_{7/2}\rightarrow 1D_e$	3.42	362	} 7.8
10	$1P_{SS}\rightarrow 1P_e$	3.42	358	
11	$1S_{3/2}\rightarrow 2S_e$	3.47	357	

Note: The values of the energy E (the wavelength λ) presented were calculated for $\bar{a}=28$ Å using Eqs. (8)–(10). The best-fit values of the relative oscillator strengths of the transitions (the last column) were determined. The value of 7.8 refers to the last three transitions taken together.

The spectra of the samples with QD's were simulated on the basis of the fundamental absorption peak. The mean QD radius $\bar{a}$, which provides the correct position of the peak, was determined, and the energy was calculated from Eqs. (8)–(10). The following values of the parameters of CdTe were used in the process: $P=7\times10^{-8}$ eV·cm, $E_g=1.49$ eV ($T=300$ K), $m_{lh}=m_e=0.09m_0$, and $\Delta_{SS}=0.977$ eV. We note that diverse data have been given in the literature for m_{hh} (from $0.4m_0$ to $0.7m_0$), and that they correspond to different values of K_h for the $1S_{3/2}$ state. The root of Eq. (11) varies almost linearly with β^{-1}, and the value which we adopted, $m_{hh}=0.5m_0$, corresponds to $K_h=3.91$.

In addition to the ground state, the electron-hole pair states listed in Table I were taken into account in ϵ_s. Their energies were calculated as a function of the QD radius, as described above. The best-fit values of the oscillator strengths of the transitions corresponding to their recombination were determined.

We also note that ϵ_∞ in (7) is the value of the dielectric constant for $\hbar\omega \gg E_g$, which naturally differs from the value of 7.8 known from infrared spectroscopy for CdTe. Our calculation of the contribution of the interband transitions for bulk CdTe gave $\epsilon_\infty \simeq 6$, which corresponds to the value for $\hbar\omega \ll E_g$ indicated above.

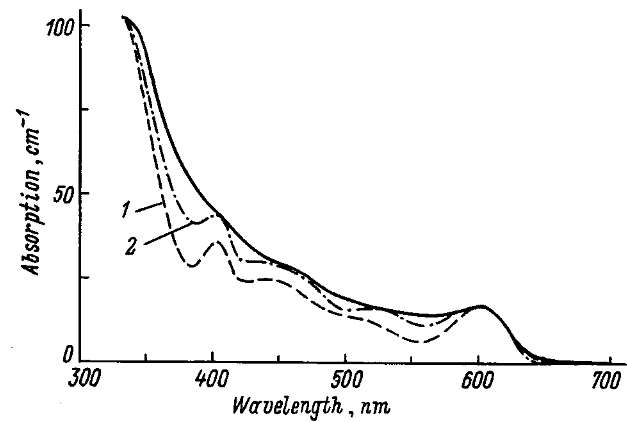

FIG. 4. Same as in Fig. 3, but for a VCS39 sample annealed for 300 min.

The theoretical spectra were fit to the experimental spectra using the Gaussian size distribution function (two parameters, viz., the QD concentration and the variance of the radius, were varied) and the Lifshitz–Slezov size distribution function[17] (only the concentration was varied). The simulation results are shown in Figs. 3–5.

As a whole, the agreement between theory and experiment is good. The transition frequencies ω_ν, calculated with allowance for the mixing of light- and heavy-hole states correspond to the experimentally observed values, as can be seen, for example, from Fig. 3. We used the same value of $\hbar\delta$ for all the transitions. Up to 20 meV, this parameter has scarcely any influence on the form of the spectrum. In principle, the inhomogeneous broadening associated with distortions of the shape of the QD's can also make a contribution to $\hbar\delta$. This contribution should be larger for transitions with larger energies and can lead to further smoothing of the corresponding peaks, in accordance with the experimental spectra.

The first absorption peak for the VCS39 samples is approximated more closely by the Lifshitz–Slezov size distribution function than by the symmetric Gaussian distribution

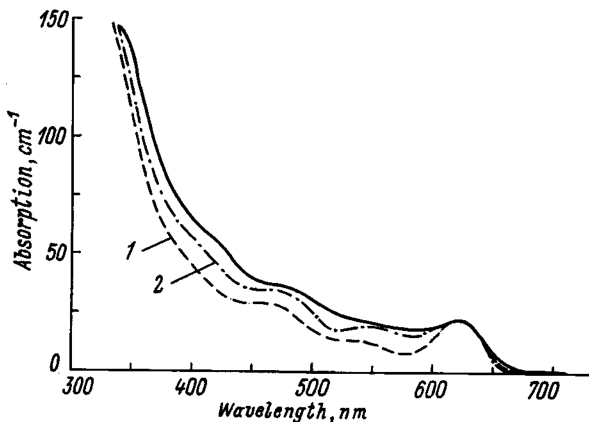

FIG. 3. Experimental absorption spectra of a VCS39 sample annealed for 420 min (solid line) and calculated spectra obtained with consideration of the electron-hole transitions from Table I using the Gaussian (*1*) and Lifshitz–Slezov (*2*) size distribution functions.

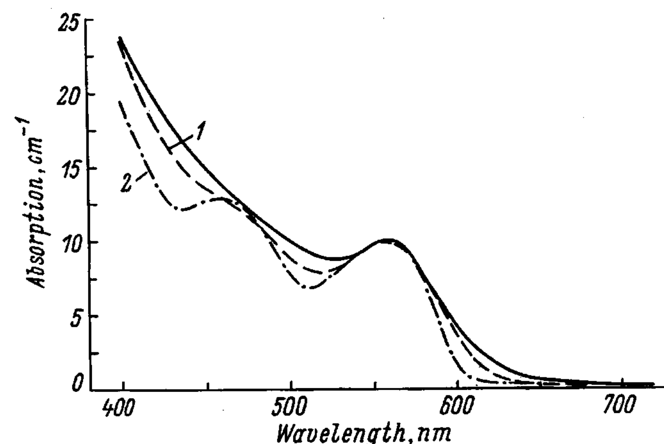

FIG. 5. Same as in Fig. 3, but for a VCS37 sample annealed for 22 min.

TABLE II. Best-fit values of the parameters determined during the simulation of the spectra of the VCS39 samples using the Lifshitz–Slezov size distribution function.

t_a, h	2.5	5	7
n, 10^{16} cm^{-3}	2.683	1.885	2.205
$\bar{a}$, Å	23.6	26.7	28.0

(see Figs. 3 and 4). The Lifshitz–Slezov theory,[17] which, as we know, describes the late stage of phase formation in solid solutions (the growth of large grains as a result of the dissolution of small grains), predicts growth of the mean grain radius according to an $\bar{a} \sim t^{1/3}$ law and a corresponding decline in their number with time. The latter is inconsistent with the values of n determined during the simulation (see Table II). The hypothesis that the decomposition of the solid solution in the samples investigated was interrupted in the early stage of growth of the grains of the semiconductor phase also runs into difficulty. The diffusion-controlled growth of grains from a supersaturated solid solution should be characterized by a dependence of the mean radius on time of the form $\bar{a} \sim t^{0.5}$, which is faster than the one following from Table II. On the other hand, it is not clear how to correctly select the time of onset of this stage of the process with consideration of the prolonged primary anneal. Nevertheless, the form of the spectra of the samples after the primary anneal alone and even after the secondary anneal at 540 °C for 1 h (Fig. 1) does not provide any basis to presume the growth of grains during the low-temperature anneal.

The spectra of the samples obtained by a single anneal at 560 °C are approximated more closely by the Gaussian size distribution function (Fig. 5). This can mean that the technological process was interrupted back in the nucleation stage. The most probable QD radius in the sample annealed for 32 min, however, is only slightly greater than the radius corresponding to the spectrum in Fig. 5 (the dependence on annealing time can be estimated as $\bar{a} \sim t_a^{0.1}$), which is also difficult to explain within the existing theories. Thus, further investigation of the phase-formation processes taking place during the growth of CdTe nanocrystals according to the technology under consideration are needed.

In summary, we have proposed a scheme for taking into account the fluctuation polarization interaction between semiconductor nanocrystals grown within an insulating matrix and the (arbitrary) statistical distribution of their size in the calculation of the linear optical absorption of such systems. The scheme has been tested on CdTe-doped glasses. The mean radius and concentration of the QD's have been determined by comparing the calculated and experimental spectra. It has been shown that the size distribution function is asymmetric for samples obtained by two-stage annealing and falls off in the direction of QD radii exceeding the expectation value. A very weak dependence of the latter on annealing time, which is not consistent with the existing theories on spinodal decomposition, has been discovered.

This work was supported by the Russian Fund for Fundamental Research (Grant 96-02-18852), CNPQ, and JNICT.

[1] A. I. Ekimov and A. A. Onushchenko, Fiz. Tekh. Poluprovodn. **16**, 1215 (1982) [Sov. Phys. Semicond. **16**, 775 (1982)].
[2] B. G. Potter and J. H. Simmons, J. Appl. Phys. **68**, 1219 (1990).
[3] J. A. Medeiros Neto, L. C. Barbosa, C. L. Cesar, O. L. Alves, and F. Galenbeck, Appl. Phys. Lett. **59**, 2715 (1991).
[4] B. G. Potter, J. H. Simmons, P. Kumar, and C. J. Stanton, J. Appl. Phys. **75**, 8039 (1994).
[5] W. Y. Wu, J. N. Shulman, T. Y. Hsu, and U. Efron, Appl. Phys. Lett. **51**, 710 (1987).
[6] H. Matheu, T. Richard, J. Allègre, P. Lefebvre, G. Arnaud, W. Granier, L. Boudes, J. L. Marc, A. Pradel, and M. Ribes, J. Appl. Phys. **77**, 287 (1995).
[7] R. G. Barrera, G. Monsivais, W. L. Mochan, and E. V. Anda, Phys. Rev. B **39**, 9998 (1989).
[8] M. I. Vasilevskiy and E. V. Anda, Phys. Rev. B **54**, 5844 (1996).
[9] W. Hayes and R. Loudon, *Scattering of Light by Crystals*, Wiley, New York (1978).
[10] L. E. Brus, J. Chem. Phys. **80**, 4403 (1984).
[11] Al. L. Éfros and A. L. Éfros, Fiz. Tekh. Poluprovodn. **16**, 1209 (1982) [Sov. Phys. Semicond. **16**, 772 (1982)].
[12] A. I. Ekimov, A. A. Onushchenko, A. G. Plyukhin, and Al. L. Éfros, Zh. Éksp. Teor. Fiz. **88**, 1490 (1985) [Sov. Phys. JETP **61**, 891 (1985)].
[13] Al. L. Efros and A. V. Rodina, Solid State Commun. **72**, 645 (1984).
[14] G. B. Grigoryan, É. M. Kazaryan, Al. L. Éfros, and T. V. Yazeva, Fiz. Tverd. Tela (Leningrad) **32**, 1772 (1990) [Sov. Phys. Solid State **32**, 1031 (1990)].
[15] A. I. Ekimov *et al.*, J. Opt. Soc. Am. B **10**, 101 (1993).
[16] A. M. de Paula, L. C. Barbosa, C. H. B. Cruz, O. L. Alves, J. A. Sanjurjo, and C. L. Cesar, Appl. Phys. Lett. **69**, 357 (1996).
[17] I. M. Lifshitz and V. V. Slyozov, J. Phys. Chem. Solids **19**, 35 (1961).

Translated by P. Shelnitz

AMORPHOUS, GLASSY, AND POROUS SEMICONDUCTORS

Influence of oxygen on the photoluminescence intensity of erbium (at 1.54 μm) in erbium-doped a-Si:H films

V. Kh. Kudoyarova, A. N. Kuznetsov, E. I. Terukov, O. B. Gusev, Yu. A. Kudryavtsev, B. Ya. Ber, and G. M. Gusinskiĭ

A. F. Ioffe Physicotechnical Institute, Russian Academy of Sciences, 194021 St. Petersburg, Russia

W. Fuhs

Hahn-Meitner Institute, D-12489 Berlin, Germany

G. Weiser and H. Kuehne

Fachbereich Physik, Phillips Universität-Marburg, D-35032 Marburg, Germany
(Submitted April 22, 1998; accepted for publication April 27, 1998)
Fiz. Tekh. Poluprovodn. **32**, 1384–1389 (November 1998)

The influence of oxygen on the photoluminescence (PL) of erbium (at 1.54 μm) in erbium-doped hydrogenated amorphous silicon (c-Si⟨Er⟩) is investigated. The a-Si:H⟨Er⟩ films studied are fabricated by cosputtering Si and Er targets using the technology of dc silane decomposition in a magnetic field. The oxygen concentration is varied from 10^{19} to 10^{21} cm^{-3} by increasing the partial pressure of oxygen in the chamber. It is shown that, as in the case of erbium-doped crystalline silicon (c-Si⟨Er⟩), oxygen has an effect on the intensity of the 1.54 μm photoluminescence in a-Si:H⟨Er⟩ films. The values of the erbium and oxygen concentrations at which the maximum Er PL intensity is observed are two orders of magnitude higher than in crystalline silicon. The increase in the Er PL intensity at room temperature and the weaker temperature dependence of the Er PL in comparison to c-Si⟨Er,O⟩ attest to the prospect of using a-Si:H⟨Er⟩films in optoelectronic applications. © *1998 American Institute of Physics.*
[S1063-7826(98)01811-0]

1. INTRODUCTION

The photoluminescence (PL) and electroluminescence (EL) of rare-earth (RE) ions in semiconductor materials have recently been studied extensively. The interest in such research is dictated by the possibility of utilizing the electron pumping of RE ions to create electroluminescent light sources with a wavelength that can be used in photonic communication systems. The largest number of studies has been performed on erbium-doped crystalline silicon (c-Si⟨Er⟩) in connection with the prospect of producing electroluminescent emission at 1.54 μm, which corresponds to the loss minimum in a quartz optical fiber.

The 1.54 μm emission is assigned to the $I_{13/2}-I_{15/2}$ transition in the $4f$ subshell of the Er^{3+} ions. Since the core $4f$ subshell is shielded by the outer $5s$ (two electrons) and $5p$ (six electrons) subshells, the wavelength at which PL is observed does not depend on the matrix in which the Er ion is implanted or on temperature. It has been established during the investigation of the PL of Er in c-Si⟨Er⟩ that 1) the Er^{3+} emission observed in c-Si⟨Er⟩ has a weak intensity at room temperature due to pronounced thermal quenching[1,2] and that 2) oxygen doping increases the erbium photoluminescence intensity at room temperature.[1,3] We recently discovered that efficient PL[4] and EL[5] can be observed at room temperature in Er-doped hydrogenated amorphous silicon (a-Si:H⟨Er⟩). Under identical measurement conditions the Er PL intensity at room temperature in a-Si:H⟨Er⟩ films is more than two orders of magnitude greater than that for samples of c-Si doped with Er and O and annealed to obtain optimal photoluminescence.

In this paper we present the results of experimental studies of the influence of the oxygen concentration on the photoluminescence intensity of Er in a-Si:H⟨Er⟩ films.

2. EXPERIMENT

The a-Si:H⟨Er⟩ films used in our investigations were fabricated by cosputtering Si and Er targets using the technology of dc silane decomposition in a magnetic field. A standard reactor intended for magnetron sputtering was used, but an argon-oxygen-silane mixture was employed instead of an argon-hydrogen mixture (magnetron-assisted silane decomposition or MASD[6]).

In the present work the parameters of the film sputtering process were as follows: gas, 25%SiH_4+75% Ar; magnetic field, 20–100 mT; anode voltage, 200–600 V; discharge power density, W=0.1–1.0 W/cm^2; gas pressure, $P=(2.5-7.0)\times10^{-3}$ Torr. The films were sputtered onto crystalline

 © 1998 American Institute of Physics

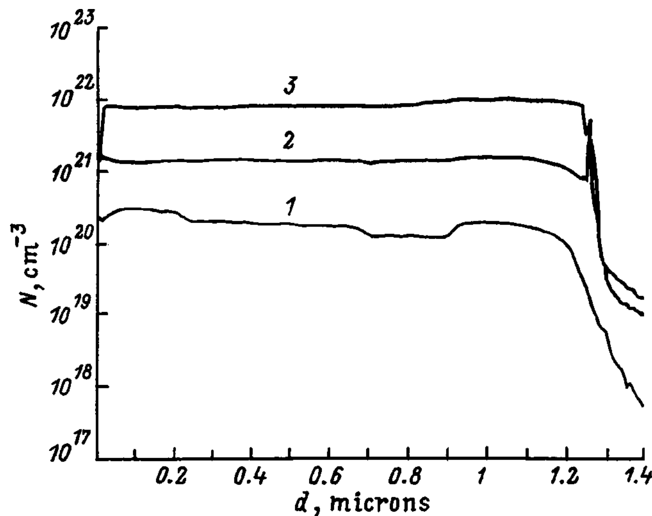

FIG. 1. Typical distributions of Er (*1*), O (*2*), and H (*3*) obtained by SIMS for an a-Si:H⟨Er,O⟩ film with $N_{Er}=2\times10^{20}$ cm^{-3}, $N_O=1.5\times10^{21}$ cm^{-3}, and $N_H=8\times10^{21}$ cm^{-3}.

silicon (c-Si) and fused quartz substrates. The substrate temperature T_s was in the range 250–350 °C.

The concentrations of implanted Er and O, as well as their concentration distribution profiles, were determined by secondary ion mass spectrometry (SIMS) on a Cameca IMS-4*f* spectrometer. The sputtering was effected by a focused beam of $^{32}O_2^+$ ions with an energy of 5.5 keV. The primary current was 0.5 μA, the beam was directed onto a 250×250 raster, and a region with a diameter of 60 μm was analyzed. The intensities were converted into concentrations using standard implanted samples.

The determination of the Er and O concentrations for the high-resistivity samples (with a large oxygen concentration, $N_O>10^{20}$ cm^{-3}) by SIMS was difficult. In such cases the Er and O concentrations were determined using nuclear-physical methods: Rutherford backscattering (RBS) and the $^{16}O(\alpha,\alpha)^{16}O$ nuclear resonance reaction (NRR). RBS and the NRR were observed when a-Si:H⟨Er⟩ films were irradiated by accelerated α particles, whose initial energy was 3.1 MeV. In estimating the oxygen concentration, SiO_2 served as a calibration sample. The hydrogen content in the samples, which was determined by infrared (IR) spectroscopy (by integrating the absorption band at 630 cm^{-1}), was equal to 2–9 at. %.

Photothermal deflection spectroscopy (PDS) was used to determine the concentration N_D of defects (dangling Si bonds).

The photoluminescence was excited by an Ar laser ($\lambda=514$ nm). The emission was recorded by a double monochromator and detected by a nitrogen-cooled Ge detector. The PL excitation power was 50 mW in all cases.

3. RESULTS AND DISCUSSION

In order to observe the 1.54 μm photoluminescence in c-Si⟨Er⟩ at room temperature, Er and O are coimplanted in c-Si samples. In addition, high-temperature anneals are needed to optimize the Er PL. The experimental results show

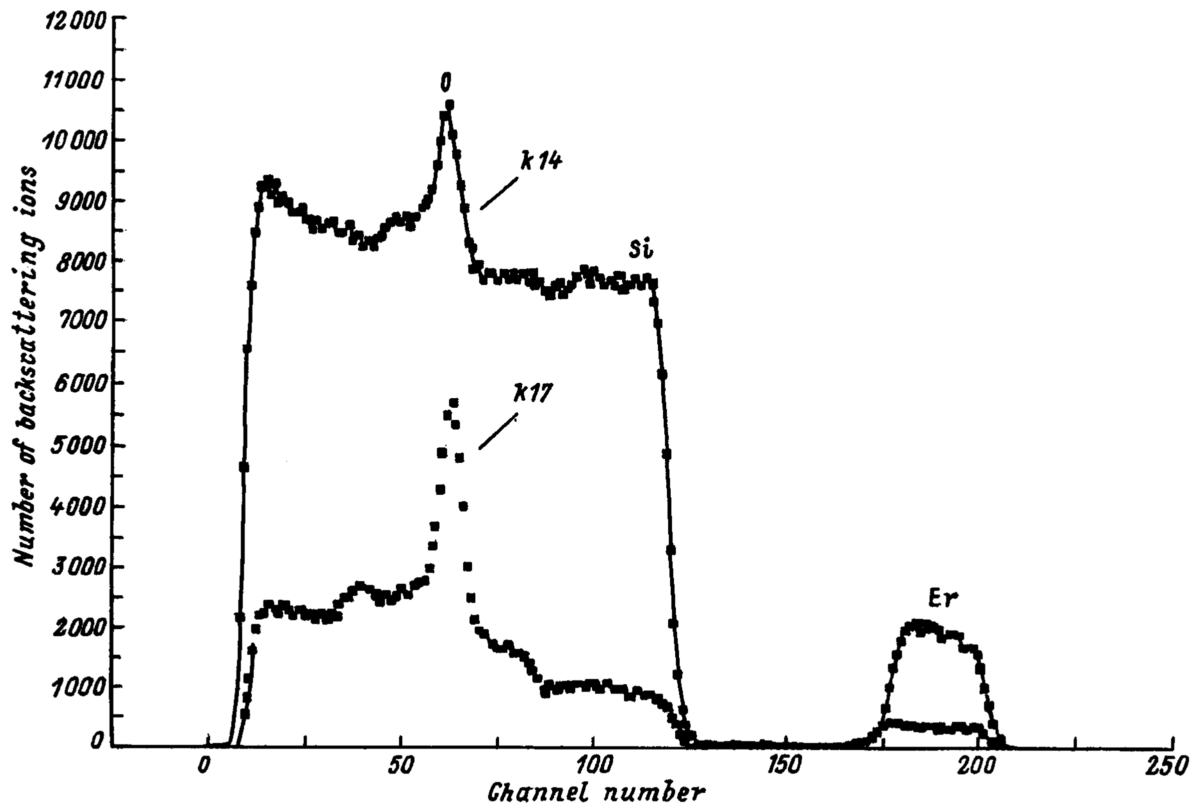

FIG. 2. Spectra of backscattered α particles obtained using RBS and the NRR for two a-Si:H⟨Er,O⟩ films deposited on c-Si substrates: $k14$ — $N_{Er}=7\times10^{20}$ cm^{-3}, $N_O=5.5\times10^{20}$ cm^{-3}; $k17$ — $N_{Er}=5.9\times10^{20}$ cm^{-3}, $N_O=7\times10^{21}$ cm^{-3}.

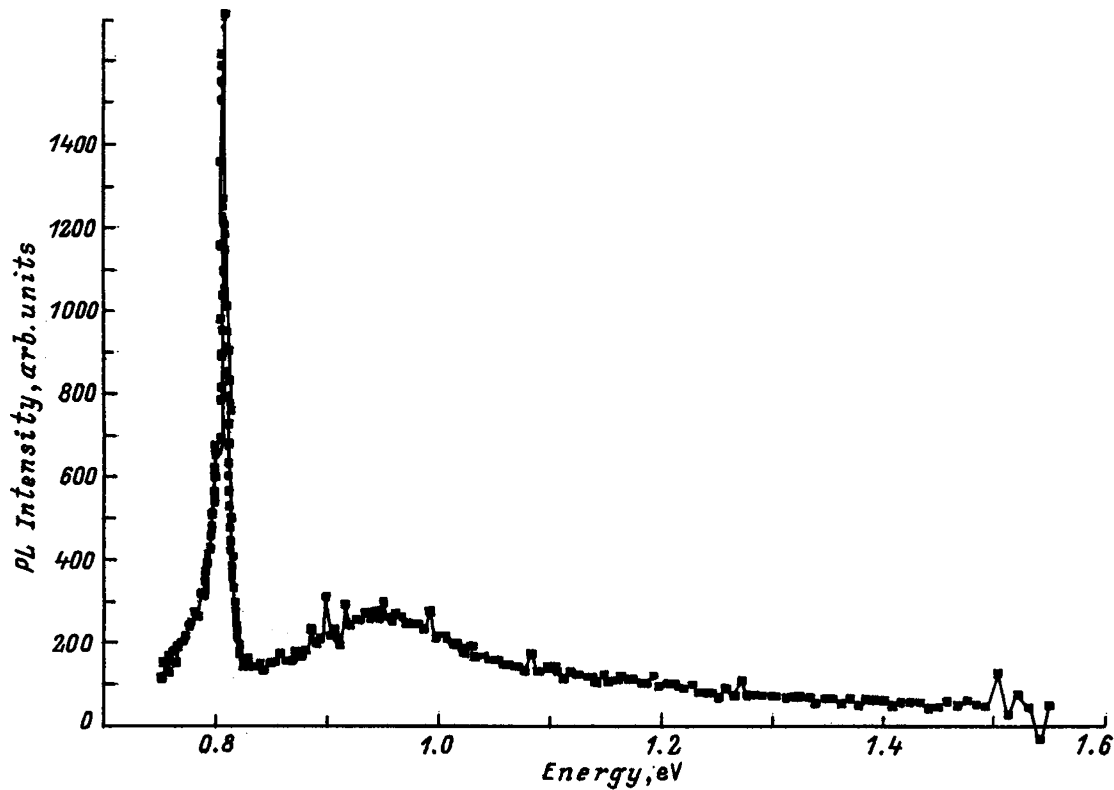

FIG. 3. PL spectrum ($T=77$ K) for an a-Si:H⟨Er,O⟩ film with $N_{\mathrm{Er}}=5\times10^{19}$ cm^{-3} and $N_{\mathrm{O}}\geq10^{21}$ cm^{-3}.

that the maximum value of the 1.54 μm photoluminescence is observed at an oxygen concentration of 10^{18} cm^{-3} (which is equal to the solubility of oxygen in silicon[7]), i.e., at a concentration approximately an order of magnitude higher than the concentration of Er ions.[8]

In the case of hydrogenated amorphous silicon (a-Si:H) the fabrication of samples doped with Er and O is simpler: High concentrations of Er and O can be introduced during cosputtering, and additional high-temperature anneals are not needed to obtain high values of the Er PL intensity. We achieved a homogeneous distribution of Er up to concentrations of 10^{21} cm^{-1} in a-Si:H films, whose thicknesses were equal to 0.8–1.2 μm. Typical distribution profiles of Er and O obtained using SIMS and RBS are presented in Figs. 1 and 2.

The PL spectra were investigated over a broad spectral range from 0.7 to 1.6 eV (Fig. 3). Both the PL peak of Er (0.804 eV) and PL peaks of hydrogenated amorphous silicon, viz., defect (0.9 eV) and intrinsic (1.35 eV) PL peaks, can be observed in this spectral range. Figure 3 shows a typical PL spectrum ($T=77$ K) for a-Si:H⟨Er,O⟩.

As follows from Fig. 3, the PL spectra contain the PL peak of Er (0.804 eV) and the defect PL peak (0.9 eV) in the spectral range just indicated, but do not contain the intrinsic PL peak of a-Si:H (1.35 eV). This is because one intrinsic PL band at 1.35 eV with a width of 0.3 eV is usually observed in the spectra of pure (undoped) a-Si:H with a defect density $N_D<10^{16}$ cm^{-3}. The luminescence at 1.35 eV is almost always assigned to transitions between states in the band tails. Samples of a-Si:H with a defect concentration $N_D\approx10^{18}$ cm^{-3} typically display the defect PL at 0.9 eV with a width of 0.35 eV. The PL line at 0.9 eV appears as a result of the tunneling of electrons from the conduction-band tail into neutral (paramagnetic) dangling bonds D^0 followed by radiative recombination with holes self-trapped in states in the valence-band tail. The doping of pure a-Si:H supplements and modifies the states in the mobility gap.

Our investigations showed that the doping of a-Si:H with erbium and oxygen leads to an increase in the defect density N_D. The defect concentration, which was determined, as indicated above, by PDS, varied from 10^{18} to 10^{19} cm^{-3} as the level of doping of a-Si:H with erbium and oxygen was increased. Naturally, the defect PL peak is observed at such a defect density, but the intrinsic PL peak of a-Si:H is not observed.

Figure 4 shows the variation of the Er PL intensity (the

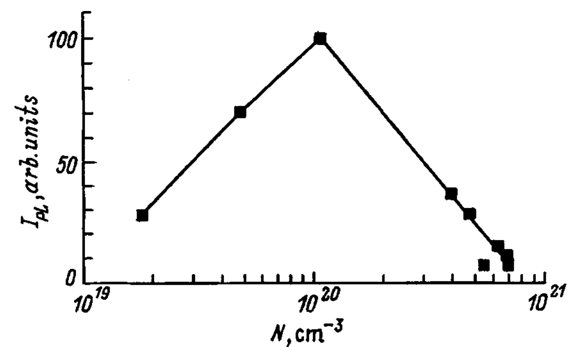

FIG. 4. Dependence of the Er PL intensity (the 1.54 μm band) at $T=300$ K on the erbium concentration N_{Er} at a constant oxygen concentration $N_{\mathrm{O}}=2\times10^{20}$ cm^{-3}.

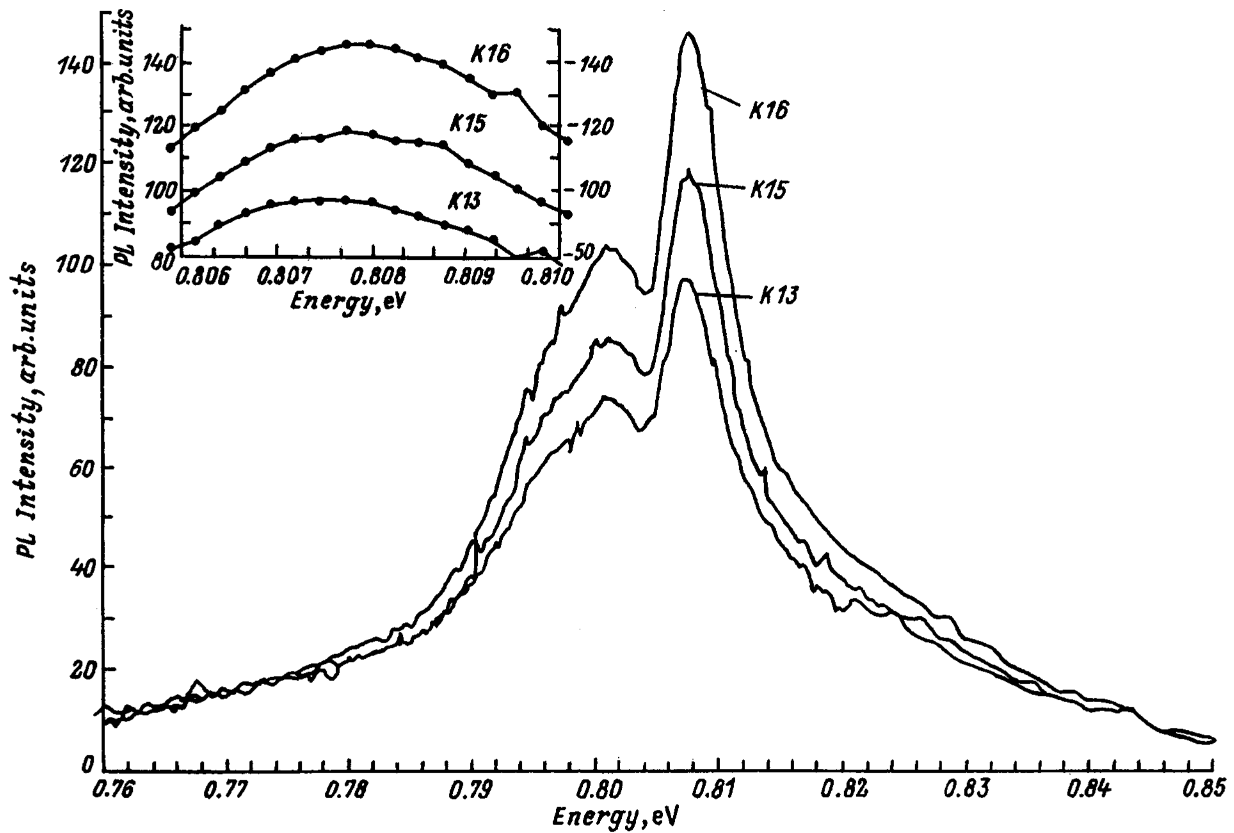

FIG. 5. PL spectra of a-Si:H⟨Er,O⟩ ($T=300$ K) at a constant erbium concentration $N_{Er}=6\times10^{20}$ cm^{-3} and various values of the oxygen concentration N_O, cm^{-3}: K 13 — 2.5×10^{20}, K 15 — 8.2×10^{20}, K 16 — 2.0×10^{21}.

peak at 1.54 μm, 0.804 eV) as a function of the Er concentration in a-Si:H⟨Er,O⟩. The oxygen concentration in the films was constant and equal to 1×10^{20} cm^{-3}. The PL intensity reaches its maximum value at $N_{Er}=1\times10^{20}$ cm^{-3}, and a further increase in the Er concentration leads to a decrease in the PL intensity. This can be attributed to: 1) the formation of clusters at high Er concentrations or 2) an insufficient oxygen concentration if oxygen plays the same important role in amorphous silicon as in crystalline silicon.

In order to test these hypotheses, we investigated the influence of the oxygen concentration in the range from 10^{19} to 10^{21} cm^{-3} on the Er PL intensity. The oxygen concentration in the samples was varied by varying the partial pressure of oxygen in the chamber from 8×10^{-6} to 5×10^{-4} Torr.

Figure 5 shows the PL spectra of Er ($T=300$ K) for samples with various oxygen concentrations. As follows from Fig. 5, the intensity of the 1.54-μm photoluminescence increases with increasing oxygen concentration, and the maximum Er PL intensity is achieved when $N_O/N_{Er}\approx10$ (Fig. 6); the values of the concentrations themselves are two orders of magnitude higher than in crystalline silicon.

The investigations performed point out the important role of oxygen in the optical activation of Er ions in the amorphous matrix of a-Si:H⟨Er⟩ as well. In all likelihood, it can be stated that in the case of a-Si:H⟨Er⟩ a considerable portion of the oxygen is bound in Er-O complexes and just this Er, which is surrounded by oxygen, is optically active and acts as a luminescent center for the $I_{13/2}-I_{15/2}$ transition.

The investigations of the local environment of Er performed by Mössbauer spectroscopy in Ref. 9 showed that some of the Er ions have an environment of Si atoms (an environment similar to $ErSi_2$) and some have an environment of oxygen atoms (an environment similar to Er_2O_3). Wherever there are more of the latter, a higher Er PL intensity is observed.

It is noteworthy that increasing the oxygen concentration by an order of magnitude, i.e., from 10^{20} to 10^{21} cm^{-3}, leads

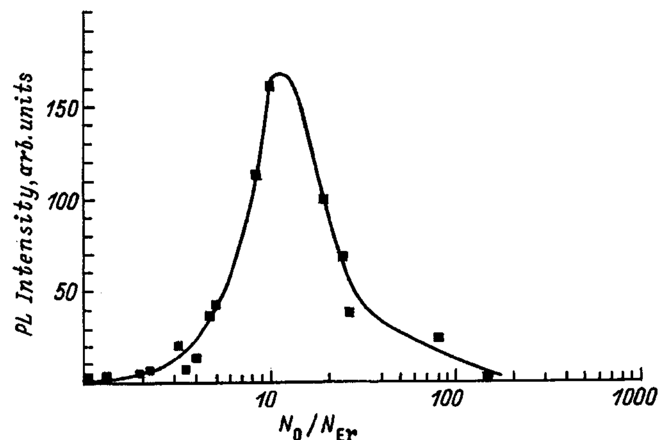

FIG. 6. Variation of the Er PL intensity ($T=300$ K) plotted as a function of the ratio between the oxygen and erbium concentrations in a-Si:H⟨Er,O⟩ films.

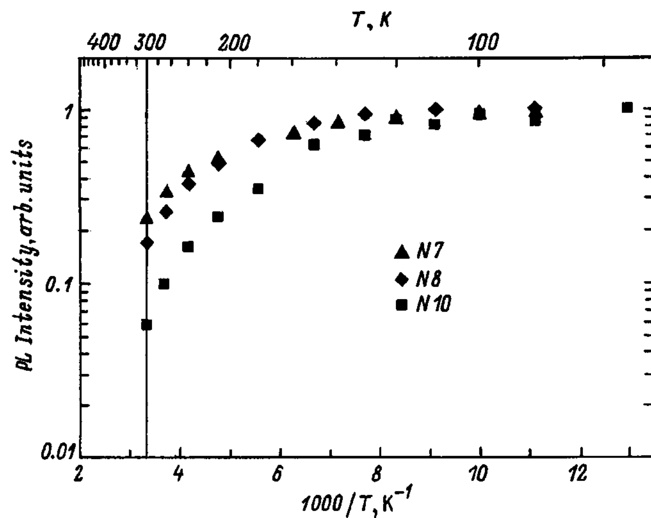

FIG. 7. Temperature dependence of the Er PL intensity in a-Si:H⟨Er,O⟩ samples with various values of the oxygen concentration N_O: N 10 — 2.5×10^{20} cm^{-3}, N 8 — 3.5×10^{20} cm^{-3}, N 7 — 1×10^{21} cm^{-3}.

to displacement of the Er PL band by 0.001 eV. Figure 5 (see the inset) shows the Er PL spectra at $T=300$ K, which were measured with a high resolution, for a-Si:H⟨Er⟩ films with various oxygen concentrations. Distinct differences between the positions of the peaks in the samples, which show that the presence of additional oxygen alters the local environment of the Er ions, are observed. Such displacement of the Er PL band due to the addition of oxygen is observed in c-Si:H⟨Er⟩ (Ref. 10) and a-Si:H with implanted Er and O ions.[11]

In c-Si erbium behaves as a microscopic getter for oxygen,[8] and the effective solubility of Er in the context of the formation of an optically active complex with oxygen is completely determined by the oxygen content. Since the solubility of oxygen in c-Si is $\sim10^{18}$ cm^{-3} [the solubility limit of oxygen in c-Si is $1.5\times10^{17}-2\times10^{18}$ cm^{-3} at 1000–1400 °C (Ref. 7)], the excess Er, which has not formed an Er-O complex, can form precipitates. It has been shown that Er precipitates having the form of disks with a diameter of ~300 Å and a thickness of 10 Å form in c-Si above the concentration $N_{Er}=1.3\times10^{18}$ cm^{-3} at $T_0=900$°C. The structure of these precipitates is similar to that of $ErSi_2$ (Ref. 12).

Apparently, the gettering of oxygen by erbium takes place in a-Si:H⟨Er,O⟩, just as in c-Si⟨Er,O⟩. The only difference is that the solubility of Er and O in a-Si:H is higher, and the formation of Er precipitates, which is observed in c-Si⟨Er⟩, can be observed in a-Si:H⟨Er⟩ at concentrations approximately two orders of magnitude higher than in c-Si ⟨Er⟩.

The investigations of the influence of the oxygen concentration on the temperature dependence of the PL of Er in a-Si:H⟨Er,O⟩ showed that, as in the case of c-Si⟨Er,O⟩, increasing the oxygen content leads to a rise in the Er PL intensity at room temperature and to a weaker temperature dependence (Fig. 7). It is assumed that the increase in the Er PL intensity at room temperature in c-Si⟨Er,O⟩ can be associated both with an increase in the concentration of optically active centers and with a decrease in the lifetime of the excited state of the emitting center.[3] In the case of a-Si:H⟨Er,O⟩, the performance of additional investigations is needed to attribute the increase in the Er PL intensity with increasing oxygen concentration to one of the factors just indicated.

4. CONCLUSIONS

The investigations performed have shown that, as in the case of c-Si⟨Er⟩, oxygen has an effect of the intensity of the 1.54 μm photoluminescence in a-Si:H⟨Er⟩ films. The maximum PL intensity is achieved when $N_O/N_{Er}\approx10$ (i.e., when a local environment of the erbium ions similar to the local environment of the erbium ions in the structure of Er_2O_3 is realized). The values of the erbium and oxygen concentrations at which the maximum PL intensity is observed are two orders of magnitude higher than in crystalline silicon due to the higher solubility of Er and oxygen in the amorphous matrix than in crystalline silicon. The increase in the Er PL intensity at room temperature and its weaker temperature dependence in comparison to c-Si⟨Er,O⟩ attest to the prospect of using a-Si:H⟨Er⟩ films in optoelectronic applications.

This work was supported in part by Volkswagen-Stiftung (Grant No. 1/71 646), the Russian Fund for Fundamental Research (Grant No. 96-02-16931-a), and a Ministry of Science Grant (Grant No. 1S91.11F020).

[1] P. N. Favennec, H. L. Haridon, D. Moutonnet, M. Salvi, and M. Gaunean, Jpn. J. Appl. Phys. **29**, L524 (1990).
[2] P. N. Michel, J. L. Benton, R. F. Ferrante, D. C. Jacobson, D. J. Eaglesham, E. A. Fitzgerald, Y.-H. Xie, J. M. Poate, and L. C. Kimerling, J. Appl. Phys. **70**, 2672 (1991).
[3] S. Coffa, G. Franzo, F. Priolo, A. Polman, and R. Serna, Phys. Rev. B **49**, 16 313 (1994).
[4] M. S. Bresler, O. B. Gusev, V. Kh. Kudoyarova, A. N. Kuznetsov, P. I. Pak, E. I. Terukov, I. N. Yasievich, B. P. Zakharchenya, W. Fuhs, and A. Sturm, Appl. Phys. Lett. **67**, 3599 (1995).
[5] O. B. Gusev, A. N. Kuznetsov, E. I. Terukov, M. S. Bresler, V. Kh. Kudoyarova, I. N. Yassievich, B. P. Zakharchenya, and W. Fuhs, Appl. Phys. Lett. **70**, 240 (1997).
[6] V. Marakhonov, N. Rogachev, J. Ishkalov, J. Makakhonov, E. Terukov, and V. Chelnokov, J. Non-Cryst. Solids **137/138**, 817 (1991).
[7] *VLSI Technology*, S. M. Sze [Ed.] (McGraw-Hill, New York, 1983; Mir, Moscow, 1986, Vol. 1b, p. 286).
[8] A. Polman, G. N. van den Hoven, J. S. Custer, J. H. Shin, R. Serna, and P. F. A. Alkemade, J. Appl. Phys. **77**, 1256 (1995).
[9] V. F. Masterov, F. S. Nasredinov, P. P. Seregin, V. Kh. Kudoyarova, A. N. Kuznetsov, and E. I. Terukov, Pis'ma Zh. Tekh. Fiz. **22**(23), 25 (1996) [Tech. Phys. Lett. **22**(12), 960 (1996)].
[10] F. Priolo, G. Franzo, S. Coffa, A. Polman, S. Libertino, R. Barklie, and D. Carey, J. Appl. Phys. **78**, 3874 (1995).
[11] J. H. Shin, R. Serna, van den Hoven, A. Polman, W. G. H. M. van Sark, and A. M. Vredenberg, Appl. Phys. Lett. **68**, 997 (1996).
[12] D. J. Eaglesham, J. Michel, E. A. Fitzgerald, D. C. Jacobson, J. M. Poate, J. L. Benton, A. Polman, Y.-H. Xie, and L. C. Kimerling, Appl. Phys. Lett. **58**, 2797 (1991).

Translated by P. Shelnitz

Influence of the deposition and annealing conditions on the optical properties of amorphous silicon

A. I. Mashin, A. V. Ershov, and D. A. Khokhlov

N. I. Lobachevskiĭ Nizhniĭ Novgorod State University, 603600 Nizhniĭ Novgorod, Russia

(Submitted September 15, 1997; accepted for publication May 26, 1998)
Fiz. Tekh. Poluprovodn. **32**, 1390–1392 (November 1998)

The refractive index and extinction coefficient in the range 0.6–2.0 eV of amorphous silicon films deposited by electron-beam evaporation with variation of the substrate temperature, deposition rate, and anneal temperature in an air atmosphere are presented. The results are discussed in terms of variation of the Penn energy gap as a function of the deposition and treatment conditions. © *1998 American Institute of Physics.* [S1063-7826(98)01911-5]

The interest in hydrogenated amorphous silicon (a-Si:H) is due mainly to the prospects of using it to fabricate inexpensive film solar cells of large area.[1] At the same time, researchers have been focusing increasingly greater attention on ''hydrogen-free'' amorphous silicon (a-Si) as a promising material with a large refractive index for near-infrared fiber-optic passive interference elements.[2,3]

Figure 1 shows typical spectral curves of the refractive index n and the extinction coefficient k of a-Si films obtained by electron-beam evaporation in vacuum (for the technological details, see, for example, Ref. 4). The optical constants were determined according to the method in Ref. 5. As in the case of most of the literature data,[6] in our case (curve *1*) the values and dispersion of the refractive index of the a-Si films are greater than those of crystalline silicon (c-Si) and a-Si:H in the frequency range investigated. This finding can be explained if it is recalled that amorphous silicon has not only a loss of long-range order, but also a high concentration of matrix defects: dangling bonds, voids, extrinsic impurities, etc. In this communication we examine the influence of voids on the optical properties of a-Si films obtained at various substrate temperatures (T_s) and deposition rates (V_s) and subjected to annealing in air.

Two cases can be considered, depending on the void size.

1. If the voids are fairly large compared to the interatomic distance and slightly exceed or are comparable to the light wavelength, the electromagnetic light wave undergoes repeated scattering, and the optical properties of the material can be described within the effective-medium theory. According to Ref. 7, if there are only voids in the material, it satisfies the equality

$$(1-x_v)[\hat{\varepsilon}_m(\omega)-\hat{\varepsilon}(\omega)]/[\hat{\varepsilon}_m(\omega)+2\hat{\varepsilon}(\omega)] + x_v[\hat{\varepsilon}_v(\omega)-\hat{\varepsilon}(\omega)]/[\hat{\varepsilon}_m(\omega)+2\hat{\varepsilon}(\omega)]=0, \quad (1)$$

where x_v is the relative void volume, $\hat{\varepsilon}_m(\omega)$ and $\hat{\varepsilon}_v(\omega)$ are the complex dielectric constants of the medium and the voids, and $\hat{\varepsilon}(\omega)$ is the effective complex dielectric constant of the system.

2. If the voids are very small (less than 1 nm), they can be treated as accessible elements of a uniform network. Then the overall influence of the voids is confined to decreases in the mean interatomic bonding force and the plasma frequency of the material, and the optical properties can be calculated within the Penn model. According to Ref. 8, the static refractive index n_0 is related to the plasma frequency ω_p and the Penn energy gap $\hbar\omega_g$ in the following manner:

$$n_0^2=1+(2/3)(\omega_p^2/\omega_g^2). \quad (2)$$

In this case the value of $\hbar\omega_g$ coincides to within good accuracy with the maximum of the $k(\omega)$ spectrum, and

$$\omega_p^2=(4\pi e^2/m)(\rho L_A/A)n_v, \quad (3)$$

where e and m are the charge and mass of an electron, ρ is the density of the material, A is the molecular weight, and L_A is Avogadro's number. For c-Si $n_v=4$.

The quantity $\hbar\omega_g$ is called the plasmon energy. A plasmon is a collective excitation of the electron gas that is localized mainly in dense regions of the random network and penetrates only slightly into the voids, which, in turn, create the density deficit in a-Si. Thus, the plasmon energy can serve as a measure of the microscopic density of the amorphous semiconductor.

According to the data in Ref. 9, a-Si films typically have voids with diameters no greater than 0.5 nm. A void can then be regarded as a cluster of atoms separated from the fully coordinated structure, and the expression (2) can be written as[10]

$$n=1+(2/3)(\omega_p^2/\omega_g^2)(\rho/\rho^0)^{1-4f}, \quad (4)$$

where $f=d\ \ln C/d \ln \rho$ is the fraction of cluster bonds on the void surface, C is the mean coordination number, and the superscript 0 denotes the parameter for the completely coordinated material. The value of f varies from 0 to 1 as a function of the void diameter. In the case of small voids (less than $2-3$ coordination spheres) $f>0.25$, and the value of n for such a medium will be greater than the value for the completely coordinated material.

 © 1998 American Institute of Physics

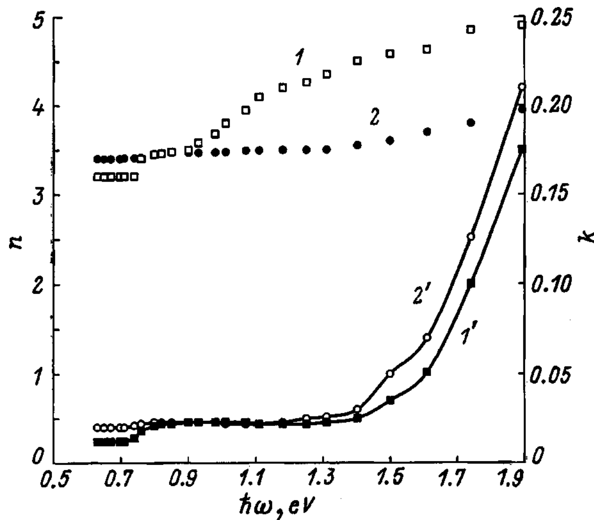

FIG. 1. Spectral curves of the refractive index n (*1*, *2*) and the extinction coefficient k (*1′*, *2′*) of a-Si films obtained by electron-beam evaporation at the substrate temperatures $T_s = 250$ (*1*, *1′*) and 20 °C (*2*, *2′*).

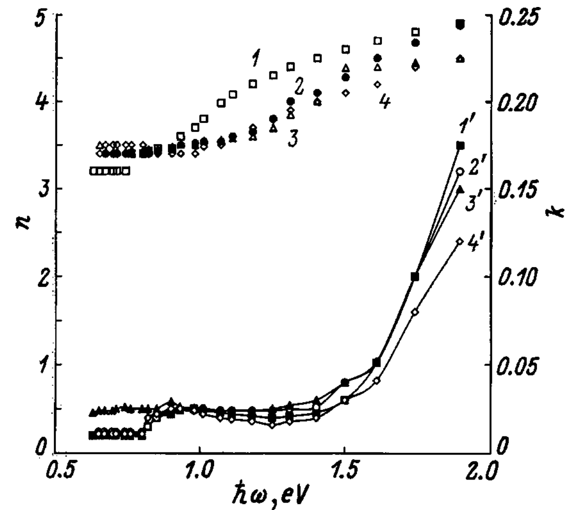

FIG. 3. Spectral curves of the refractive index n (*1–4*) and the extinction coefficient k (*1′–4′*) of a-Si films deposited at $T_s = 250$ °C and annealed in air for 1 h at 20 (*1*, *1′*), 100 (*2*, *2′*), 150 (*3*, *3′*) and 250 °C (*4*, *4′*).

On the basis of these arguments, it can be assumed that in our case the a-Si films obtained by electron-beam evaporation at $T_s = 250°$C (Fig. 1) have voids, whose diameter is comparable to the first or second coordination radius and, accordingly, are characterized by a large refractive index.

Variation of the deposition conditions, or, more specifically, a decrease in the substrate temperature T_s from 250 to 20 °C and the deposition rate V_s by a factor of roughly 2 (Figs. 1 and 2), leads to qualitatively identical variation of n for the films, i.e., to lowering of its value near the absorption edge. The refractive index dispersion also decreases under these conditions. As a result, the difference in the behavior of curves *1* and *2* in both figures is very significant in the short-wavelength region. For example, while the difference between the refractive indices for a photon energy $\hbar\omega \simeq 1.9$ eV is ~ 1 (Fig. 1), the difference for $\hbar\omega \simeq 1.0$ eV amounts to ~ 0.4. When $\hbar\omega < 0.8$ eV, the value of the refractive index scarcely depends on the deposition conditions indicated.

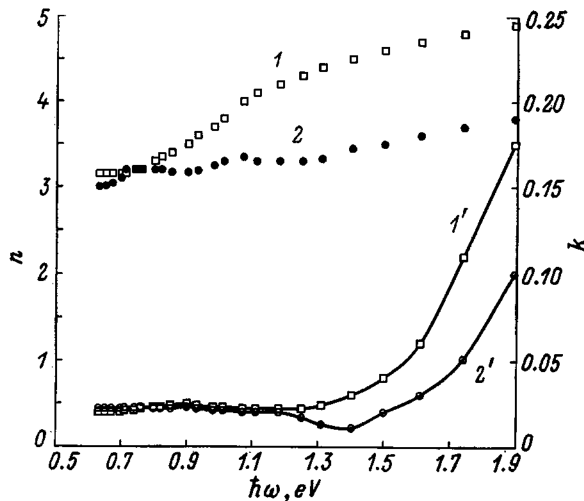

FIG. 2. Influence of the deposition rate on the spectral curve of the refractive index n (*1*, *2*) and the extinction coefficient k (*1′*, *2′*) of a-Si films. Film deposition rate V_s, nm/s: *1*, *1′* — 0.53; *2*, *2′* — 0.30.

Inspection of the spectral curves of the extinction coefficient (Figs. 1 and 2, curves *1′* and *2′*) reveals that variations in T_s and V_s influence the behavior of $k(\omega)$ differently. For example, a decrease in the substrate temperature T_s (Fig. 1) leads to displacement of the absorption edge toward longer wavelengths, while a decrease in V_s (Fig. 2) causes displacement of the absorption edge of amorphous silicon toward higher energies. This finding allows us to assume that the mechanisms for the decreases in the refractive index in response to the lowering of T_s and V_s are different.

Lowering T_s clearly leads to an increase in the diameters of the voids in a-Si. This, in turn, leads to lowering of n, bringing it closer to the values for c-Si, and for very large voids ($\sim 50-100$ nm) it leads to refractive index values that are smaller than in crystalline silicon. Since the width of the Penn gap also decreases in that case, the maximum on the $k(\omega)$ curve and, therefore, the absorption edge shift toward longer wavelengths, as we observe on the experimental curves presented (Fig. 1). The decrease in $\hbar\omega_g$ in this case is attributed to a decrease in the mean coordination number.

A decrease in the deposition rate should lead to a decrease in the film porosity, and in this case, according to (4), there should be an increase in the refractive index. On the other hand, at low deposition rates a large quantity of extrinsic impurities, such as oxygen, hydrogen, carbon, etc., enters the film. If we follow Shevchik and Paul[9] and assume that the diameter of the voids in the original a-Si is ~ 0.5 nm, it is difficult to imagine a further decrease in their diameter as the deposition rate is lowered. Thus, an influence of lowering the deposition rate on the optical characteristics of a-Si through a decrease in the void diameter is unlikely.

In order to reveal the influence of extrinsic impurities, it would be useful to jointly examine the influences of the deposition rate and the subsequent annealing of a-Si in air, since the penetration of extrinsic impurities into the film from the atmosphere should be expected in the latter case.

According to the experimental data, annealing *a*-Si in air, like a decrease in the deposition rate (Figs. 2 and 3), leads to a decrease in the refractive index and displacement of the absorption edge toward higher energies.

Taking into account the foregoing statements, we believe that the character of the variation of the optical properties of *a*-Si in response to variation of the deposition conditions and to heat treatment is described well within the Penn model. The magnitude of the Penn gap is determined both by the presence and character of the behavior of extrinsic impurities in the film and by the short-range structure of amorphous silicon. For example, the diffusion of oxygen into the bulk of the material leads to saturation of the dangling bonds and the formation of Si–O bonds instead of Si–Si bonds. Since a Si–O bond is energetically stronger than a Si–Si bond, the Penn gap $\hbar\omega_g$ increases and the maximum on the $k(\omega)$ curve shifts toward shorter wavelengths. On the other hand, ''lightening'' the network, i.e., lowering the number of dangling bonds, leads to an increase in the coordination number, and relaxation of the already completely connected network (a decrease in the spread of bond lengths, bond angles, and dihedral angles) increases the Penn gap.

[1] A. Madan and M. P. Shaw, *The Physics and Applications of Amorphous Semiconductors* (Academic Press, Boston, 1988; Mir, Moscow, 1991), p. 670.
[2] K. Hamada, M. Wada, H. Shimizu, M. Kume, F. Susa, T. Shibutani, N. Yoshikawa, K. Itoh, G. Kano, and I. Teramoto, IEEE J. Quantum Electron. **QE-21**, 623 (1985).
[3] A. V. Ershov, N. B. Zvonkov, A. I. Mashin, and D. A. Khokhlov, in *Proceedings of the Russian Conference ''Structure and Properties of Crystalline and Amorphous Materials,'' Nizhniĭ Novgorod, 1996* [in Russian], Nizhniĭ Novgorod State University, Nizhniĭ Novgorod (1996), p. 28.
[4] A. V. Ershov, A. I. Mashin, and D. A. Khokhlov, Vysokochist. Veshchestva **2**, 35 (1995).
[5] A. S. Valeev, Opt. Spektrosk. **15**, 500 (1963) [Opt. Spectrosc. (USSR) **15**, 301 (1963)].
[6] M. H. Brodsky, R. S. Title, K. Weiser, and G. D. Pettit, Phys. Rev. B **1**, 2632 (1970).
[7] D. R. Penn, Phys. Rev. **128**, 2093 (1962).
[8] *The Physics of Hydrogenated Amorphous Silicon, Vol. 2: Electronic and Vibrational Properties*, J. D. Joannopoulos and G. Lucovsky [Eds.] (Springer-Verlag, Berlin–New York, 1984; Mir, Moscow, 1987), p. 447.
[9] N. J. Shevchik and W. Paul, J. Non-Cryst. Solids **16**, 55 (1974).
[10] J. C. Philips, Phys. Status Solidi B **44**, K1 (1971).

Translated by P. Shelnitz

PHYSICS OF SEMICONDUCTOR DEVICES

Influence of internal mechanical stresses on the characteristics of GaAs light-emitting diodes

V. G. Sidorov and D. V. Sidorov

St. Petersburg State Technical University, 195251 St. Petersburg, Russia

V. I. Sokolov

A. F. Ioffe Physicotechnical Institute, Russian Academy of Sciences, 194021 St. Petersburg, Russia

(Submitted March 23, 1998; accepted for publication April 20, 1998)
Fiz. Tekh. Poluprovodn. **32**, 1393–1398 (November 1998)

A systematic investigation of the influence of internal mechanical stresses on the characteristics of gallium arsenide light-emitting diodes (LED's) is performed. The LED structures are grown by liquid-phase epitaxy from a confined volume of a melt based on a solution of GaAs in Ga. The melt is doped with silicon or with silicon and tin. It is shown that the magnitude and sign of the internal mechanical stresses in the epitaxial layer are determined by the impurity concentration in the melt. The LED's fabricated from epitaxial structures with the smallest internal mechanical stresses have the greatest quantum efficiency and the slowest rate of degradation of their parameters. A model of the reorganization of the defect structure of gallium arsenide, which describes the observed phenomena, is proposed. © *1998 American Institute of Physics.* [S1063-7826(98)02011-0]

INTRODUCTION

Internal mechanical stresses appear in a solid as a result of local strains of interatomic bonds, which are assigned by the doping level and the conditions under which the solid is formed. For just this reason, internal mechanical stresses are an inherent component of any solid and, accordingly, of every solid-state device.

The local strains of interatomic bonds cause local variation of the band structure of a solid, which can be manifested as broad variation of its electrical properties, i.e., as variation of the parameters of semiconductor devices. The magnitude and distribution of the internal mechanical stresses in the bulk of a semiconductor device are determined to a significant extent by the rates of performance of the production operations. The presence of uncompensated internal mechanical stress gradients in a semiconductor device renders its structure fundamentally unstable and predetermines various degradation effects, which are a consequence of the relaxation of internal mechanical stresses during storage or operation of the device.

In this paper we present the results of an experimental study of the effect of internal mechanical stresses on the efficiency and service life of GaAs light-emitting diodes (LED's).

EXPERIMENTAL METHOD AND RESULTS

The samples investigated were GaAs epitaxial $p-n$ structures. The structures were grown in a single liquid-phase epitaxy cycle from a confined volume of a melt based on a solution of GaAs in Ga on (100) GaAs substrates doped with Sn or Te. The thickness of the substrates was 300–350 μm, and the thicknesses of the n and p regions in the epitaxial layer were approximately identical and varied in the range from 20 to 60 μm. Silicon was added to the melt as a dopant. The silicon concentration in the liquid phase was varied from 0.1 to 1.1 wt %. In the case of double doping, the concentration of silicon in the liquid phase was held constant at a value of 1.1 wt %, while the concentration of tin was varied in the range from 1 to 8 wt %.

The following parameters of each experimental sample were measured: the radius of curvature (R) of the epitaxial structure (which was determined by x-ray methods); the microhardness (H) and the dislocation density (N_d) on a fragment of the structure in the electroluminescence generation region, which is located in the p layer of the structure at a distance of 3–15 μm from the $p-n$ junction;[1] the concentration of deep levels (N_t) in the $p-n$ junction; the external electroluminescence quantum efficiency (β_{ex}) and its dependence on the operating time of the LED; and the internal-friction spectrum at a frequency of 6 Hz.

The measured parameters of the epitaxial structures and LED's are presented in Figs. 1 and 2 as functions of the silicon or tin concentration in the liquid phase. Figure 3 shows typical internal-friction spectra for some of the structures investigated.

As can be seen in Fig. 3, the epitaxial layers investigated are composite materials based on gallium arsenide. In fact, the sharp absorption peaks at the melting points of gallium and tin attest to the presence of microinclusions of the metallic phase of these elements in the bulk of the layer.[2] The amount of gallium trapped in microinclusions by the grow-

 © 1998 American Institute of Physics

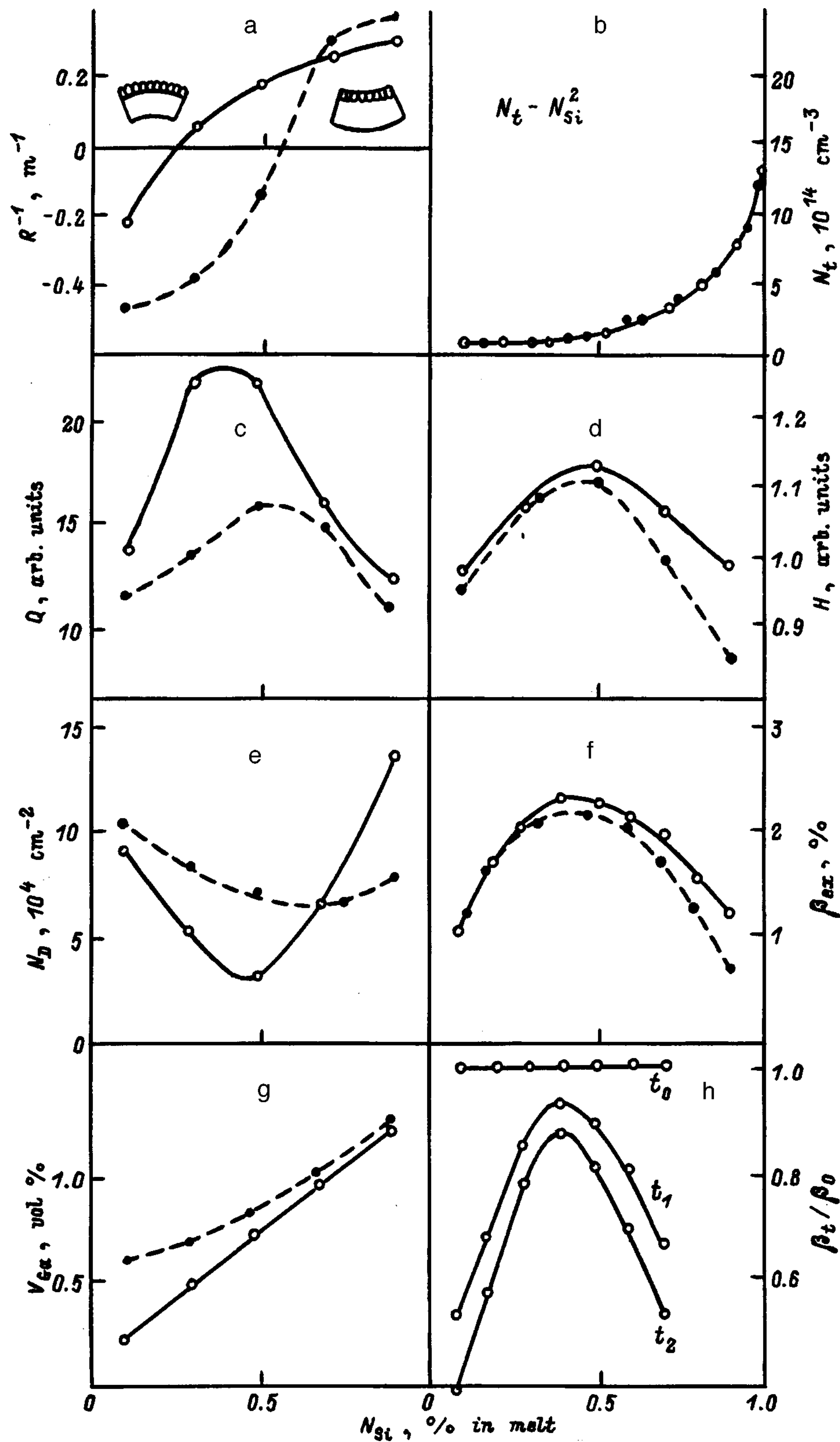

FIG. 1. Parameters of LED structures as a function of the silicon concentration in the melt. Cooling rate of the melt: solid curves — 0.5 °C/min, dashed curves — 7 °C/min. a — Curvature; b — concentration of deep levels; c — mechanical Q factor; d — microhardness; e — dislocation density; f — external quantum efficiency; g — concentration of metallic gallium; h — variation of the external quantum efficiency in accelerated tests.

ing epitaxial layer increases as the silicon concentration, as well as the cooling rate of the melt, are increased (Fig. 1g).

The negative curvature of the epitaxial structures with small silicon concentrations (Fig. 1a) correspond to convex bending of the structures toward the epitaxial layer. As the silicon concentration is increased, the curvature of the structure changes sign at a certain critical value, which is determined by the cooling rate of the melt. This finding is a re-

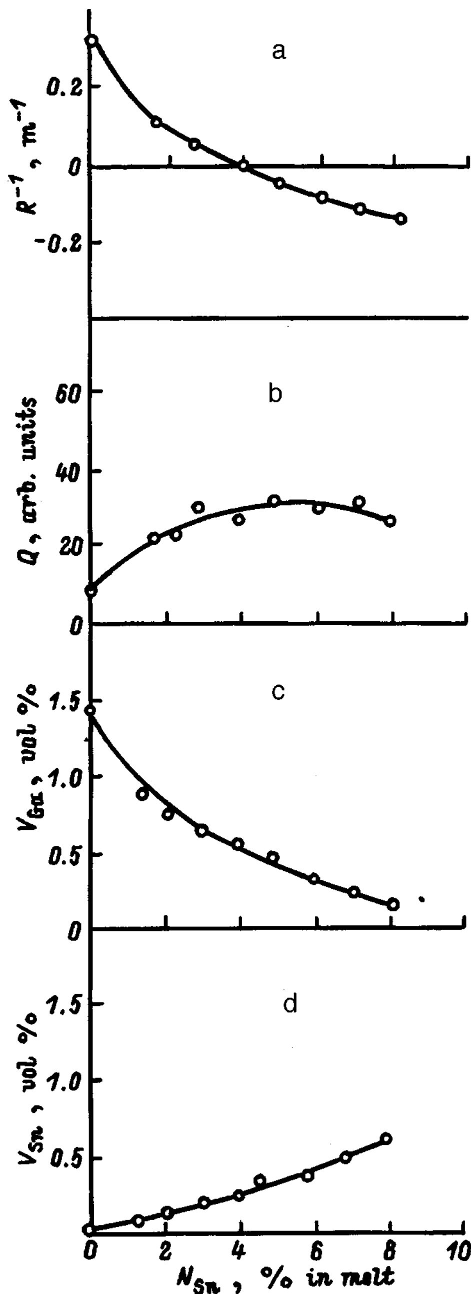

FIG. 2. Parameters of LED structures with various tin concentrations in the melt and a silicon concentration equal to 1.1 wt %: a — curvature; b — mechanical Q factor; c — concentration of metallic gallium; d — concentration of metallic tin.

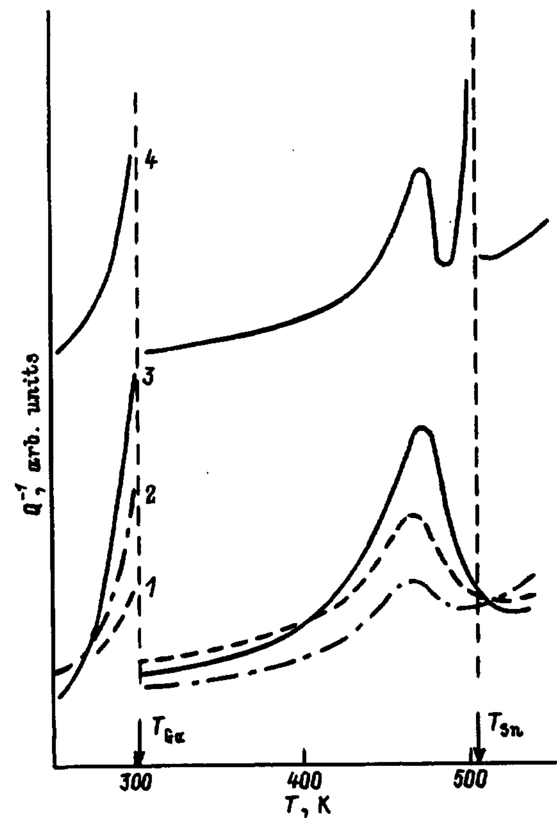

FIG. 3. Internal-friction spectra at various dopant concentrations in the melt: *1*, *2*, *3* — silicon concentrations equal to 0.1, 0.3, and 0.7 wt %, respectively; *4* — silicon concentration equal to 1.1 wt % and tin concentration equal to 3 wt %.

flection of structural reorganization in the crystal lattice. As a result of this restructuring, the magnitude of the internal mechanical stresses in the epitaxial layer drops dramatically, and, as can be seen from Figs. 1e, 1d, 1f, and 1h, the measured value of N_d, H, β_{ex}, and β_{ex}/β_0 reach their extremum values.

It is noteworthy that the intensity of the absorption band observed in the internal-friction spectra at 470 K (Fig. 3) clearly correlates with the magnitude of the mechanical stresses in the epitaxial layer. The Q factor of the oscillator circuit including the sample being measured reaches a maximum (Fig. 1c) at the silicon concentration corresponding to zero curvature of the structure (Fig. 1a). This provides some basis to regard the Q factor of the oscillator circuit at 470 K (when the internal friction is measured at 6 Hz) as a characteristic specifying the level of internal mechanical stresses in the sample.

DISCUSSION OF RESULTS AND MODEL REPRESENTATIONS

When gallium arsenide is grown from a nonstoichiometric silicon-doped melt, the defect structure of the epitaxial layer is shaped by several processes: a) the arsenic deficiency in the melt leads to the formation of excess vacancies in the arsenic sublattice (V_{As}), whose equilibrium concentration is determined by the temperature of the process; b) the growing layer traps excess gallium to a greater extent, the higher is the cooling rate of the melt; c) amphoteric doping of the epitaxial layer by silicon takes place.

Silicon can occupy vacancies in both sublattices in gallium arsenide, creating Si_{Ga} defects (donors) and Si_{As} defects (acceptors). At the same time, silicon always lends preference to vacancies in the gallium sublattice, where its concentration is significantly higher even in p-type crystals,[3] i.e., the acceptor levels in silicon-doped gallium arsenide, which determine the hole conductivity of the crystal, are formed not just by simple Si_{As} defects.

Table I presents the structural characteristics of the elements, which we need in order to analyze the defect-formation processes in the GaAs layers investigated. The lat-

TABLE I. Structural characteristics of elements.

Element	Atomic weight, g/mol	X-ray density, g/cm^3	Atomic volume, cm^3
Ga	69.72	5.908	11.8
Ga in GaAs	–	4.65	15.0
As	74.92	5.77	12.98
As in GaAs	–	6.15	12.2
Si	28.08	2.332	12.04
α-Sn	118.7	5.77	20.5

tice strain appearing upon the formation of a defect can be characterized by the local change in the atomic volume upon the introduction of the defect, i.e., by the increment ($\Delta\Omega$) (Table II). In Table II the increments are listed without allowance for relaxation of the lattice. The sign of the increment indicates the type of strain: a minus sign corresponds to compression, and a plus sign corresponds to expansion.

The interactions of the defects in a growing epitaxial layer can be described by a system of quasichemical reactions, among which the principal reactions are

$$Ga_L \rightleftarrows Ga_s, \qquad (1)$$

$$Ga_i + V_{As} \rightleftarrows Ga_{As}, \qquad (2)$$

$$Si_L \rightleftarrows Si_s, \qquad (3)$$

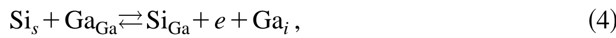
$$Si_s + Ga_{Ga} \rightleftarrows Si_{Ga} + e + Ga_i, \qquad (4)$$

$$Si_s + V_{As} \rightleftarrows Si_{As} + h, \qquad (5)$$

$$Si_{Ga} + Si_{As} \rightleftarrows (Si_{Ga} - Si_{As}), \qquad (6)$$

where the subscripts L and s refer to the liquid and solid phases, e is an electron, h is a hole, and the subscript i labels an interstitial site.

Under the conditions of an arsenic deficiency and, accordingly, the generation of excess vacancies in the arsenic sublattice, the excess gallium and the dopant (Si) not only form Ga_i and Si_{Ga} defects [Eq. (4)], but also tend to occupy arsenic vacancies, creating Ga_{As} [reaction (2)] and Si_{As} defects [reaction (5)], to ensure mechanical stability of the lattice. According to reaction (2), the concentration of antistructure Ga_{As} defects is directly proportional to the concentration of interstitial gallium, i.e., if the cooling rate of the melt is held constant, an increase in the silicon concentration in the GaAs lattice should lead to an increase in the concentration of antistructure defects [reactions (4) and (2)].

TABLE II. Local changes in the atomic volume (increments) upon the introduction of defects in GaAs (without allowance for relaxation of the lattice).

Defect	Increment $\Delta\Omega$, cm^3	Defect	Increment $\Delta\Omega$, cm^3
V_{Ga}	−15.0	Si_{Ga}	−2.96
V_{As}	−12.2	Si_{As}	−0.16
As_{Ga}	−2.8	Sn_{Ga}	+5.5
Ga_{As}	+2.8	Sn_{As}	+8.3
Ga_i	+3.8		

Thus, it can be presumed that at small silicon concentrations the excess gallium trapped by the growing layer and the gallium displaced by silicon from lattice sites occupy Ga_i interstitial positions for the most part. The large positive increment of this defect (Table II) specifies convex bending of the structure toward the epitaxial layer (Fig. 1a). As the Si concentration is increased, the excess Ga increasingly occupies antistructure Ga_{As} positions, where the lattice strain produced is smaller. The concentration of Si_{As} defects, whose formation also diminishes the internal mechanical stresses in the lattice (Table II), increases simultaneously. The decrease in the magnitude of the local strain caused by the formation of Si_{Ga} defects is greater, the closer an antistructure Ga_{As} defect and a Si_{As} acceptor atom are to the Si_{Ga} defect.[4] Therefore, the antistructure Ga_{As} defects and Si_{As} acceptors should be located in the first coordination sphere near a Si_{Ga} donor atom with a high probability. In other words, the general condition that the system tend to the energy minimum should be satisfied, i.e., defects with negative and positive increments should be near one other and form an elastic superlattice in the crystal.[5] Instead of the single cluster for an ideal crystal, viz., $GaAs_4Ga_{12}$, the structural clusters formed in the GaAs lattice in this case can have different forms, depending on the silicon concentration. For example, they can be

$$Ga[V_{As}As_3]Ga_{12}, \qquad (7)$$

$$Si_{Ga}[V_{As}As_3]Ga_{12}, \qquad (8)$$

$$Si_{Ga}[V_{As}Ga_{As}As_2]Ga_{12}, \qquad (9)$$

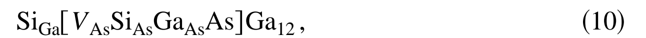
$$Si_{Ga}[V_{As}Si_{As}Ga_{As}As]Ga_{12}, \qquad (10)$$

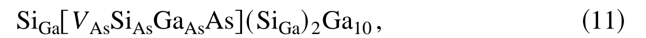
$$Si_{Ga}[V_{As}Si_{As}Ga_{As}As](Si_{Ga})_2Ga_{10}, \qquad (11)$$

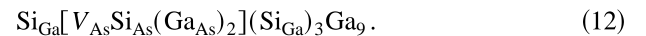
$$Si_{Ga}[V_{As}Si_{As}(Ga_{As})_2](Si_{Ga})_3Ga_9. \qquad (12)$$

Due to the large negative increments, which are equal to −12.2 (7), −15.16 (8), −12.36 (9), −12.52 (10), −18.44 (11), and −18.6 (12), respectively, these clusters create a compressive strain in the lattice, which partially compensates for the expansion caused by interstitial gallium atoms. As can be seen from formulas (7)–(12), these clusters contain not only 2–5 silicon atoms, but also 11–13 gallium atoms with tetrahedral bonds, which are not characteristic of gallium. Therefore, when the local strains are large, these clusters become structurally unstable and can collapse with the formation of tiny precipitates of metallic gallium. Since the atomic volume of gallium is significantly smaller in the metallic phase than in the GaAs lattice (Table I), a collapsed cluster absorbs several interstitial gallium atoms from the local environment. In this case the lattice strain can change sign from positive to negative. This process is shown schematically in Fig. 4 in the example of cluster (12) with six interstitial gallium atoms positioned near it. Upon collapse, the total increment of the cluster under consideration, together with the interstitial gallium atoms, changes from +4.2 in the initial state (*I*) to +1.2 in the final state (*III*) in the case of the absorption of four interstitial gallium atoms by the metallic phase or to −6.8 in the case of the absorption of

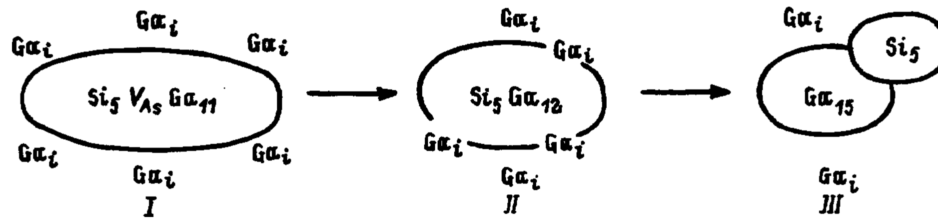

FIG. 4. Scheme of the formation of precipitates in a GaAs(Si) lattice.

three gallium atoms. As follows from the diagram, the collapse of clusters can also lead to the formation of silicon precipitates.

The phenomenon described apparently takes place over the entire range of silicon concentrations investigated, as follows from the internal-friction spectra (Fig. 3) and the variation of the curvature of the epitaxial structures as a function of the silicon concentration and the cooling rate of the melt (Fig. 1a). In fact, the gallium trapped during growth of the epitaxial layer from the melt introduces interstitial defects of two types into the gallium arsenide lattice: pointlike Ga_i centers and tiny metallic precipitates of Ga. At high cooling rates the quantity of gallium trapped by the lattice being formed rises (Fig. 1g). This reflects a general principle in the evolution of systems away from thermodynamic equilibrium: The transition to the equilibrium state takes place through a series of intermediate states, and the residence time of the system in each of them is proportional to the depth of the corresponding potential well, and it decreases with decreasing depth of the well.[6] In addition, for the same reason, at high cooling rates a larger quantity of silicon is trapped by vacancies in the arsenic sublattice [reaction (5)], displacing the formation of collapsed clusters toward larger silicon concentrations in the melt.

Thus, a superstructure of local regions of expansion by interstitial defects and compression by collapsed clusters forms in the crystal lattice of the epitaxial layer. At certain optimum silicon concentrations, at which there is no bending of the epitaxial structure, these local regions mutually balance one another, reducing the gradients of internal mechanical stresses in the structures to a minimum. This situation is conducive to maximum relative perfection of the crystal structure of the epitaxial layers, i.e., the mechanical Q factor of the samples reaches its maximum at these silicon concentrations (Fig. 1c). It is also reflected in the maximum value of the microhardness (Fig. 1d) and the minimum dislocation density (Fig. 1e).

The features of the defect structure formed in the epitaxial layers also determine the properties of the LED's fabricated from them. At the optimum silicon concentrations the external quantum efficiency β_{ex} of the LED's reaches a maximum (Fig. 1f), and the LED's exhibit the slowest rate of degradation of this parameter (Fig. 1h). It is noteworthy that the deep levels responsible for nonradiative recombination in LED's (the activation energy $E_t = E_v + 0.44$ eV, and the trapping cross section for the majority charge carriers $\sigma_t = 10^{-17}$ cm^2 at 300 K) can belong to the $Si_{Ga}-Si_{As}$ complex, whose concentration, like the concentration of deep levels, is proportional to the square of the silicon concentration in the melt (Fig. 1b).

At silicon concentrations greater than 0.8% the structure of the epitaxial layers deteriorates sharply: the mean dislocation density increases, the distribution of dislocations in the layers becomes significantly nonuniform, and they assemble in bunches with a density of $10^7 - 10^8$ cm^{-2}. In addition, impregnations of silicon precipitates appear (Fig. 4, state *III*). At the same time, the mechanical inequivalence of the bonds increases. The intensity of the band at 470 K in the internal-stress spectrum increases, i.e., the mechanical Q factor of the sample decreases (Fig. 1c).

It would be natural to expect that the introduction of an impurity with a large atomic volume into the melt would lead to effective compensation of the mechanical stresses in the epitaxial layers. One example of such an impurity is tin (see Table I), and 4 wt % of it in the melt (according to a calculation) should provide for compensation of the internal mechanical stresses in structures grown at the maximum silicon concentration, which is equal to 1.1 wt %. As the experimental results showed, when the concentration of tin is 4 wt %, there is no bending of the epitaxial structures (Fig. 2a), the amount of gallium trapped by the growing epitaxial layer decreases by a factor of 2 or 3 (Fig. 2c), and the mechanical perfection of the structure increases sharply (Fig. 2b). In addition, the layers contain no silicon precipitates, the dislocation density decreases by two orders of magnitude, and the microhardness increases by 10%, on the average. While the emission wavelength characteristic of a silicon concentration of 1.1 wt % (1 μm) is conserved, the external quantum efficiency of the LED's increases by 20–100%, and the degradation time increases by an order of magnitude.

CONCLUSIONS

This investigation has shown that one of the main reasons for the existence of an optimum doping level for obtaining GaAs(Si) LED structures with the highest consumer characteristics is the compensation of the internal mechanical stresses in these structures.

This work was supported by the Federal Special-Purpose Program ''Integration'' (Project No. 75).

[1] V. L. Korolev and V. G. Sidorov, Fiz. Tekh. Poluprovodn. **22**, 1827 (1988) [Sov. Phys. Semicond. **22**, 1155 (1988)].
[2] N. D. Vasilenko, O. K. Gorodnichenko, I. E. Maronchuk, and É. E.

Maronchuk, Zh. Tekh. Fiz. **50**, 1355 (1980) [Sov. Phys. Tech. Phys. **25**, 783 (1980)].

[3] W. G. Spitzer and M. Panish, J. Appl. Phys. **40**, 4200 (1969).

[4] A. G. Khachaturian, *Theory of Structural Transformations in Solids*, (Wiley, New York 1983; Nauka, Moscow, 1974).

[5] G. Horz and M. Popovic, Acta Metall. **27**, 1453 (1979).

[6] H. Haken, *Information and Self-Organization. A Macroscopic Approach to Complex Systems*, (Spinger-Verlag, Berlin–Heidelberg–New York–Tokyo, 1988; Mir, Moscow, 1974).

Translated by P. Shelnitz

Appearance of negative resistance in $p-n$ junction structures in a microwave field

D. A. Usanov, A. V. Skripal', and N. V. Ugryumova

Saratov State University, 410026 Saratov, Russia
(Submitted September 15, 1997; accepted for publication May 28, 1998)
Fiz. Tekh. Poluprovodn. **32**, 1399–1402 (November 1998)

The results of theoretical and experimental investigations of the appearance of negative differential resistance in $p-n$ junction diode structures in the presence of a high level of microwave power are presented. The theoretical analysis of the influence of a high level of microwave power on the form of the current-voltage characteristic of a diode takes into account the variation of the constant component of the current flowing through the $p-n$ structure due to the heating of the free charge carriers and the rectifier effect. © *1998 American Institute of Physics.* [S1063-7826(98)02111-5]

INTRODUCTION

Strong microwave fields have a significant effect on the current-transfer characteristics of $p-n$ junction structures. For example, the stationary current-voltage characteristics (IVC's) of diodes change significantly under the effect of a high level of microwave power due to the appearance of a considerable thermocurrent of hot charge carriers through the $p-n$ junction.[1]

The comparison of the experimental data with the results of calculations of IVC's with allowance for the appearance of a thermocurrent of hot charge carriers in a $p-n$ junction in Ref. 1 showed that the agreement is fairly good only for germanium $p-n$ junctions. A generation-recombination model of current transfer in the space-charge layer has been used along with allowance for the thermocurrent of hot charge carriers to account for the ''anomalously'' large currents in silicon $p-n$ junctions in a strong microwave field.[2–4]

It has been shown in the presently known experimental studies[3,5] that the application of a strong microwave field can also lead to qualitative alteration of the IVC's of $p-n$ junction diodes. For example, the appearance of segments with negative differential resistance (NDR) on the IVC's of short-base silicon $p-i-n$ diodes for the microwave range with a fairly perfect structure[5] and on the IVC's of silicon $p-n$ junction diodes with a large number of deep levels[3] was observed under the action of a high level of microwave power. No theoretical description of this phenomenon was presented.

In this paper we present the results of theoretical and experimental investigations of the appearance of NDR on the current-voltage characteristics of microwave diode structures based on silicon $p-n$ junctions under the action of a high level of microwave power.

EXPERIMENT

The influence of a high level of microwave power on the form of the stationary IVC's of type 2A604 silicon microwave $p-n$ junction diodes was investigated in the experiments.

A microwave diode was connected in parallel to a microband transmission line with a wave impedance of 59 Ω and a matched load. In contrast to the case considered in Refs. 3 and 4, here the electric-field vector of the microwave field was oriented perpendicularly to the plane of the $p-n$ junction. A signal with a frequency of 1000 MHz was fed through a controllable attenuator to the microwave diode. The microwave power level in the input signal was monitored by a power meter. To minimize the influence of the thermal heating of the diode structure at forward bias voltages, the IVC's were measured using an IVC plotter with a scanning frequency of 100 Hz.

Figure 1 shows the experimental IVC's of a microwave diode for various values of the input signal power P_0 (curves *1–4*). As follows from the experimental results, when the input power is increased to 150 mW, a region of NDR appears on the IVC's of the diodes. The magnitude of the NDR increases with increasing input signal power in the range of values from 150 to 500 mW. When the input signal power is at the 500 mW level, the negative differential resistance on the descending portion of the IVC reaches a value of -20 Ω, and low-frequency oscillations with a frequency of 100–200 kHz appear in the power-supply circuit.

MODEL USED IN THE CALCULATION

The equivalent circuit shown in Fig. 2 was used to simulate the behavior of a microwave diode connected in parallel to a microband transmission line. The elements of the equivalent circuit simulate a semiconductor diode structure in the form of a nonlinear resistance R and a capacitance C connected in parallel. The diode body is simulated by the elements L_k and C_k, and the microband line is simulated by the input conductivity Y_0 in the junction plane of the diode.

It was assumed that the resistance of the base layer of the diode structure does not depend on the value of the current and is considerably smaller than the nonlinear resistance R of the space-charge layer at bias voltages V that are smaller than the contact potential difference V_k. At $V>V_k$ the value of R was assumed to be constant and was defined as

 © 1998 American Institute of Physics

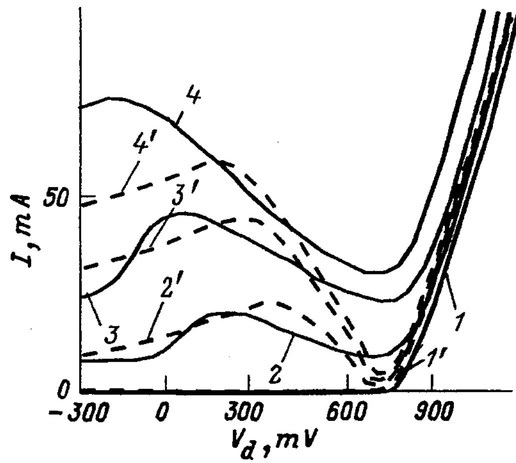

FIG. 1. Experimental (*1–4*) and theoretical (*1′–4′*) current-voltage characteristics $I(V_d)$ of a microwave diode for various values of the input-signal power P_0, mW: *1, 1′* — 0; *2, 2′* — 150; *3, 3′* — 350; *4, 4′* — 500.

$R=\rho l/S$, where ρ, l, and S are the resistivity, thickness, and area of the base layer of the diode structure.

The nonlinear resistance R was defined as the average resistance of the $p-n$ junction for the first harmonic of the microwave current:

$$R=\frac{V^{\sim}}{I_{\sim}}, \quad \text{where} \quad I_{\sim}=\sqrt{A^2+B^2},$$

$$A=\frac{2}{T}\int_0^T I(V)\sin\,\omega t\,dt,$$

$$B=\frac{2}{T}\int_0^T I(V)\cos\,\omega t\,dt,$$

$$V=V_0+V^{\sim}\sin\,\omega t.$$

Here V_0 and $V^{\sim}$ are the value of the constant voltage and the amplitude of the variable voltage on the microwave diode, I is the current flowing through the active resistance R, and $T=2\pi/\omega$ is the period of the microwave oscillations.

The passage of current through the diode was simulated using an expression for the current-voltage characteristic obtained with consideration of the generation-recombination processes in the space-charge layer, which are manifested in the nonideality coefficient n (Ref. 2), and the heating of the free charge carriers:[1]

$$I=\frac{qD_n n_{p0}S}{\sqrt{D_n\tau_n}}\left\{\exp\left[\frac{qV_k}{nkT_0}\left(\frac{T_n-T_0}{T_n}\right)+\frac{qV}{nkT_n}\right]-1\right\}$$
$$+\frac{qD_p p_{n0}S}{\sqrt{D_p\tau_p}}\left\{\exp\left[\frac{qV_k}{nkT_0}\left(\frac{T_p-T_0}{T_p}\right)+\frac{qV}{nkT_p}\right]-1\right\},$$

where D_n, D_p, τ_n, τ_p, T_n, and T_p are the electron and hole diffusion coefficients, lifetimes, and temperatures, respectively, and T_0 is the lattice temperature.

Since a signal from the low-frequency portion of the microwave range (1000 MHz) was used in the experiments, the effects associated with the finite values of the energy and quasimomentum relaxation times of the free charge carriers could be disregarded in the calculations.[6,7]

The capacitance of the semiconductor structure (C) was determined by the sum of the barrier (C_b) and diffuse (C_d) capacitances:

$$C=C_b+C_d.$$

The barrier and diffuse capacitances were determined as the averages for the first harmonic of the microwave current using the relations[8,9]

$$C_b=S\sqrt{\frac{\varepsilon\varepsilon_0 qnp}{2(V_k-V)(n+p)}},$$

$$C_d\approx\tau\frac{dI}{dV},$$

where n and p are the electron and hole concentrations in the n and p regions of the $p-n$ junction, respectively; τ is the effective lifetime of the minority charge carriers, which is determined in short-base structures by the diffusion time of carriers through the base layer and the carrier recombination rate at the contact;[10] ε is the relative dielectric constant; ε_0 is the permittivity of free space; S is the area of the structure; and V_k is the contact potential difference.

The current-voltage characteristic of the diode was calculated with consideration of the rectifier effect using the relation $I_c=\int_0^T I(V)\,dt$. It was taken into account in the calculations that a constant low resistance R_l was connected in series to the microwave diode in the power-supply circuit. The current-voltage characteristic $I(V_d)$ was determined from the solution of the equation

$$V_d=V_0+I_cR_l.$$

The amplitude of the microwave voltage $V^{\sim}$ was determined from the value of the microwave power P absorbed by the diode from the relation

$$P=(V^{\sim})^2/2R.$$

The microwave power absorbed was calculated using the expression[11]

$$P=P_0(1-|N|^2-|T|^2),$$

where P_0 is the microwave power impinging on the diode, $N=-Y/(2Y+Y_0)$ is the reflectivity of the diode for the microwave signal, $T=2Y_0/(Y+2Y_0)$ is the transmission coef-

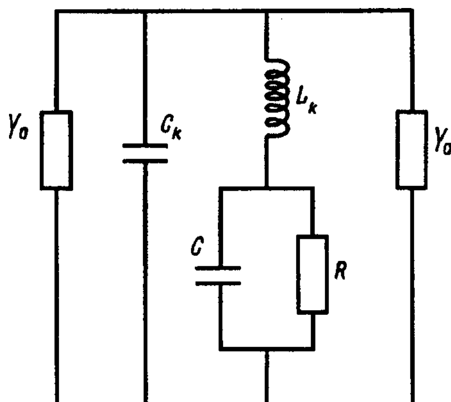

FIG. 2. Equivalent circuit of a microband transmission line with a parallel microwave diode.

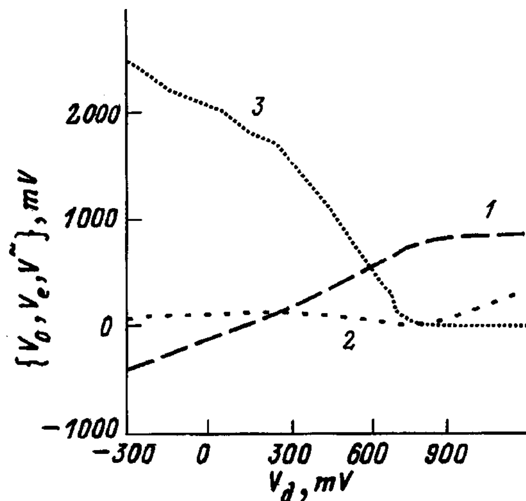

FIG. 3. Plots of the constant bias voltage V_0 (*1*) and V_l (*2*) on the $p-n$ junction and the series resistance, respectively, as well as of the amplitude of the variable voltage $V^{\sim}$ (*3*) on the microwave diode, plotted as functions of the applied voltage V_d.

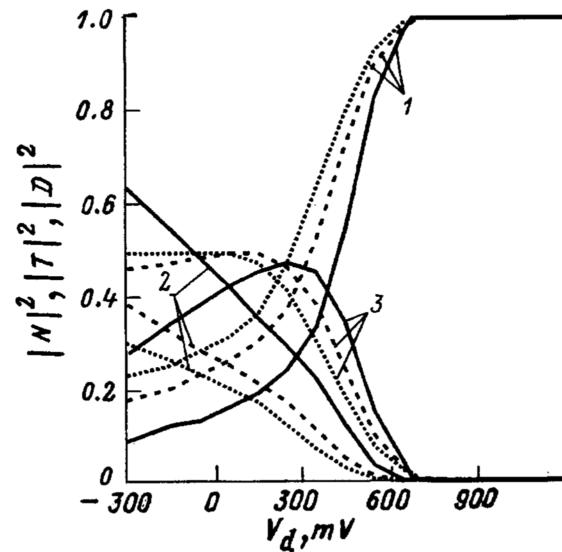

FIG. 4. Dependence of the squares of the moduli of the reflection coefficient N (*1*), the transition coefficient T (*2*), and the absorption coefficient D (*3*) on the fixed bias V_d for various values of the incident microwave power: $P_0 = 100$ (solid lines), 300 (dashed lines), and 500 mW (dotted lines).

ficient for the microwave signal, and $Y = j\omega C_k + [j\omega_k L_k + (j\omega C + 1/R)^{-1}]^{-1}$ is the complex conductivity of the diode.

CALCULATION RESULTS

The calculations performed using the model described above showed that when a microwave signal is supplied to a diode at negative and small positive bias voltages, a considerable portion of the power is absorbed.

Current passes through the $p-n$ junction due to the heating of the charge carriers and the rectification effect, which creates a voltage drop across the series resistance R_l that displaces the $p-n$ junction in the reverse direction. As the forward bias V_d is increased, the bias V_0 on the diode increases (Fig. 3, curve *1*), while the voltage drop V_l on the series resistance R_l remains almost constant (Fig. 3, curve *2*).

The current through the diode increases monotonically in this range of bias voltages. Its value is determined by the injection current under the conditions of heating of the electron gas by the microwave field and by the amplitude of the rectified signal. We note that consideration of the heating of the charge carriers leads to a decrease in the additional constant current component caused by the microwave signal as a result of the decrease in the amplitude of the rectified signal.

As the forward bias on the diode V_0 increases, the decrease in the resistance R of the diode and the increase in the capacitance C of the semiconductor structure produce a significant increase in the reflected microwave signal (Fig. 4, curves *1*) and decreases in the transmitted (Fig. 4, curves *2*) and absorbed (Fig. 4, curves *3*) signals.

This leads to a decrease in the amplitude of the variable voltage on the diode (Fig. 3, curves *3*). Therefore, a decrease in the rectified signal and, consequently, a decrease in the constant current flowing through the $p-n$ junction are observed as the fixed bias applied to the diode is increased. Thus, there is a region of negative differential resistance (Fig. 1, curves *2′–4′*).

At large positive biases the value of the absorbed power becomes insignificant, and the IVC of the diode takes the form which it has in the absence of a microwave signal.

CONCLUSIONS

We have shown, therefore, that a theoretical explanation for the experimentally detected appearance of negative differential resistance on the IVC's of diode structures under the action of a high level of microwave power is possible when the heating of the charge carriers and the rectifier effect are taken into account.

[1] A. I. Veĭnger, A. G. Paritskiĭ, É. A. Akopyan, and N. A. Dadamirzaev, Fiz. Tekh. Poluprovodn. **9**, 216 (1975) [Sov. Phys. Semicond. **9**, 144 (1975)].

[2] C. T. Sah, R. N. Noyse, and W. Shockley, Proc. IRE **45**, 1228 (1957).

[3] N. A. Ablyazimova, A. I. Veĭnger, and V. S. Pitanov, Fiz. Tekh. Poluprovodn. **22**, 2001 (1988) [Sov. Phys. Semicond. **22**, 1267 (1988)].

[4] N. A. Ablyazimova, A. I. Veĭnger, and V. S. Pitanov, Fiz. Tekh. Poluprovodn. **26**, 1041 (1992) [Sov. Phys. Semicond. **26**, 583 (1992)].

[5] V. G. Vinenko, S. V. Krasovskiĭ, and D. A. Usanov, Élektron. Tekh., Ser. 1: Élektron. SVCh **4**, 38 (1987).

[6] K. S. Champlin, D. B. Armstrong, and P. D. Henderson, Proc. IRE **52**, 125 (1964).

[7] V. Denis, Zh. Kantsleris, and Z. Martunas, in *Thermal Electrons* [in Russian], Yu. Pozhela (Ed.), Mokslas, Vil'nyus (1983).

[8] G. I. Veselov, E. N. Egorov, Yu. N. Alekhin *et al.*, in *Microelectronic Microwave Devices* [in Russian], G. I. Veselov (Ed.), Vyssh. Shkola, Moscow (1988).

[9] S. Basu, S. A. Maas, and T. Itoh, IEEE Microwave Guid. Wave Lett. **5**, 293 (1995).

[10] I. M. Vikulin and V. I. Stafeev, *Physics of Semiconductor Devices* [in Russian], Radio i Svyaz', Moscow (1990).

[11] J. Helszajn, *Passive and Active Microwave Circuits* (Wiley, New York, 1978; Radio i Svyaz', Moscow, 1981).

Translated by P. Shelnitz

OBITUARIES

In memory of Yuliĭ Ivanovich Ukhanov

Fiz. Tekh. Poluprovodn. **32**, 1404–1405 (November 1998)
[S1063-7826(98)02211-X]

The renowned physicist and teacher Professor Yuliĭ Ivanovich Ukhanov, who held the title of a Distinguished Man of Science and Technology of the Russian Federation and a degree of Doctor of Physical and Mathematical Sciences, died on March 2, 1998.

A disciple of the ''St. Petersburg School of Physics'' founded by A. F. Ioffe, Yuliĭ Ukhanov devoted more than 40 years of his life to the service of science and higher education. His name is associated with the development of semiconductor optics. His research and the work of his students are widely known.

Yuliĭ Ivanovich Ukhanov was born on October 22, 1925 to the family of a surveyor in the city of Krasnyĭ Kholm. In 1942, after graduating high school, he started working as a mechanic and signal man at the Krasnyĭ Kholm Railroad Station of the Yaroslavl' Railroad. In January 1943 he was drafted into the Red Army. He began his army service as a private and was discharged in June 1946 as an officer.

In 1946 he enrolled in the department of physics and mechanics of the Polytechnic Institute in Leningrad, from which he graduated with honors in 1952. In that year he started working in the Military-Engineering Academy of Communication, where he became chairman of the department of physics in 1959. He set up a scientific laboratory, in which he performed research on the modulation of infrared radiation in germanium as a result of the injection of minority carriers. He defended his Candidate's dissertation on this subject in 1957. This work was carried out in close contact with the semiconductor laboratories of the A. F. Ioffe Physicotechnical Institute.

Beginning in 1964, Yuliĭ Ukhanov was successively a lecturer, professor, chairman of the department of experimental physics, deputy rector for scientific work, and dean of the faculty of physics and mechanics of the Polytechnic Institute. There he also ran a laboratory and guided extensive research on the magneto-optical properties of semiconductors. When he still worked at the Academy of Communication, he built the first system for investigating the Faraday effect in semiconductors in the Soviet Union. A scientific seminar was regularly held in his laboratory in the Leningrad Polytechnic Institute under his tutelage. The research was carried out jointly with scientists from the semiconductor laboratories of the A. F. Ioffe Physicotechnical Institute and the Institute of Semiconductors of the Academy of Sciences of the USSR.

Ukhanov's most important work was his research on the band structure of semiconductor compounds by magneto-optical methods. This work formed the basis of his doctoral dissertation entitled ''Experimental investigation of optical and magneto-optical phenomena in semiconductors,'' which he defended in 1966.

In the nineteen-seventies the department of experimental physics of the Leningrad Polytechnic Institute was transformed into a major scientific and methodical center under the guidance of Yuliĭ Ivanovich Ukhanov. Two conferences were organized by the department: the All-Union Conference on the Physics of III–V Compounds and the All-Union Symposium on the Spectroscopy of Crystals Activated by Ions of Transition and Rare-Earth Metals. In 1975–1978 a new course of general physics was developed in the department, and the laboratory manual was updated. The laboratory manual became one of the best in the Soviet Union, for which it was awarded a First-Class Certificate at the Exhibition of Achievements in the National Economy of the USSR in 1979.

Along with his main activity, Yuliĭ Ukhanov performed considerable scientific administrative work. He participated in the organization, development, and coordination of science and education in institutions of higher learning. As a member of several specialized councils of the Supreme Cer-

 © 1998 American Institute of Physics

tification Commission, he actively participated in the training of highly qualified scientific personnel.

Yuliĭ Ukhanov was the author of more than 150 published papers and the monographs *Optical Properties of Semiconductors* [in Russian] (Nauka, Moscow, 1977) and *Magneto-optical Faraday and Voigt Effects as Applied to Semiconductors* [in Russian] (Naukova Dumka, Kiev, 1979), the latter being coauthored by F. F. Sizov. He was the author of ten scientific textbooks. During the 16 years when he chaired the department, eight of his coworkers defended doctoral dissertations. He trained more than three decades of Candidates of Science.

Yuliĭ Ukhanov's interests were not confined to science and teaching. A frequent visitor to art exhibitions in the Hermitage Museum in St. Petersburg and the Russian Museum, he himself was no stranger to artistic creativity. Both wood and stone were transformed into works of art in his skilled hands.

Yuliĭ Ukhanov exemplified selfless and devoted service to the ideals of science and education until the end of his life. Everyone who was associated with him saw in him a bearer of the finest traditions of the Russian intelligentsia, a wise teacher of young people, a kind and sensitive human being, and a faithful and reliable friend, who was always ready to provide assistance to anyone needing it. Although he held high positions, Yuliĭ Ukhanov always had an unassuming and accessible demeanor. He treated his colleagues with sympathy and respect. Yuliĭ Ukhanov remained such a commendable person until his final days. He will be remembered as such by all who knew him.

Zh. I. Alferov, Yu. S. Vasil'ev, A. G. Zabrodskiĭ,
B. P. Zakharchenya, V. I. Ivanov-Omskiĭ, I. P. Ipatova,
F. P. Kesamanly, and V. F. Masterov
Editorial Board of Fizika i Tekhnika Poluprovodnikov

Translated by P. Shelnitz

In memory of Sergeĭ Ivanovich Radautsan

Fiz. Tekh. Poluprovodn. **32**, 1406–1407 (November 1998)
[S1063-7826(98)02311-4]

We have suffered a heavy loss. The outstanding physicist and member of the Moldovan Academy of Sciences, Sergeĭ Ivanovich Radautsan, passed away unexpectedly on March 6, 1998.

Sergeĭ Radautsan was born on June 17, 1926 in Kishinev and graduated from Kishinev State University in 1955. He studied at the Leningrad Physicotechnical Institute under Prof. N. A. Goryunova. In 1958 Sergeĭ Radautsan defended his Candidate's dissertation "Investigation of several solid solutions based on indium arsenide," and in 1966 he defended his doctoral dissertation "Investigation of diamond-like semiconductors." In 1970 he was elected a corresponding member and in 1973 a full member of the Moldovan Academy of Sciences.

From 1959 Sergeĭ Radautsan worked in the Institute of Applied Physics of the Moldovan Academy of Sciences, where he set up a laboratory for semiconductor compounds. He was the founder and first rector (1964–1973) of the Kishinev Polytechnic Institute, where he organized the Scientific-Research Laboratory of Microelectronics. In 1990–1995 Sergeĭ Radautsan was vice president of the Moldovan Academy of Sciences and director of the Center for Semiconductor Materials Science of the Moldovan Academy of Sciences.

A member of the Moldovan Academy of Sciences and the Romanian Academy of Sciences and a holder of honorary doctoral degrees from several universities, Sergeĭ Radautsan was also the founder of the foremost scientific school in the field of complex semiconductors. The team of scientists which he headed was awarded the State Prize of the USSR in 1983 for their work on the synthesis, investigation, and application of binary semiconductor materials. Sergeĭ Radautsan was a member of the Bureau of the Scientific Council of the Academy of Sciences of the USSR for Physicochemical Problems in Semiconductor Materials Science and chairman of the Scientific Council of the Moldovan Academy of Sciences for the Physics and Chemistry of Semiconductors. The five All-Union Conferences on Complex Semiconductors organized by Sergeĭ Radautsan in Kishinev were widely acknowledged forums for this field of science. For many years Sergeĭ Radautsan was a member of the organizing committee of the International Conferences on Multicomponent Compounds, and the 8th International Conference, which was held in Kishinev in 1990 (and was the only one held on the territory of the USSR), attested to the international recognition of the contribution of Radautsan's school to the science of complex semiconductors.

The main area of Sergeĭ Radautsan's scientific activity was the comprehensive investigation of the physicochemical and physical properties of binary and ternary semiconductor compounds and solid solutions based on them. Sergeĭ Radautsan was the author of ten monographs and the scientific editor of 25 collections of articles on this subject. Among the most important scientific accomplishments of Sergeĭ Radautsan and his closely knit team, the following can be singled out.

- Technologies for growing bulk crystals, films, and multilayer structures based on InP and other binary compounds were developed, and the features of the energy band structure and physical properties of these materials were studied.
- New technologies for obtaining ternary II–IV–V semiconductors were developed, thin films of these compounds were obtained, their optical spectra and the features of their band structure were studied, exciton states were detected, the phenomena of electrical switching and photoelectric memory were discovered, and the influence of nonstoichiometric defects and dopants on the electrical and magnetic properties of these materials was studied.
- Schottky diodes, $p-n$ junctions, and heterojunctions were fabricated on the basis of binary and ternary semiconductors.

 © 1998 American Institute of Physics

Having been trained as a scientist at the A. F. Ioffe Leningrad Physicotechnical Institute, Sergeĭ Radautsan honorably exemplified its best traditions during his life and always maintained scientific and cordial ties with the Institute. He wrote an excellent book entitled *The Wizard of Diamond-like Semiconductors* [in Russian] (1987) about his mentor, Prof. Nina Aleksandrovna Goryunova.

Sergeĭ Radautsan's energy, determination, and skill in selecting the points for applying scientific effects, as well as his personal scientific achievements, promoted the development of semiconductor materials science in the USSR to a great extent. His appearance at any scientific center or symposium, either in Kiev or Minsk or in Strasbourg or Rome, instantly made him the focus of attention of colleagues, prompted fruitful discussions, and initiated joint scientific projects.

For his many colleagues, students, and friends, working with Sergeĭ Radautsan was the highest form of human cooperation. His earnest good will and intelligence, constant readiness to help, and professional sophistication, as well as his vigor and creative genius, gave him a unique personality.

There were many triumphant moments in his life, and there were difficult times, which he endured with rare dignity. Still, the respect and love of his associates and colleagues were probably most important to him.

A benevolent and decent human being, talented scientist, and brilliant administrator, Sergeĭ Ivanovich Radautsan will remain in the hearts of all who knew him.

Zh. I. Alferov, Yu. V. Gulyaev, L. M. Keldysh,
F. A. Kuznetsov, A. M. Prokhorov, V. I. Perel',
V. G. Veselago, A. G. Gurevich, V. D. Prochukhan,
K. G. Nikiforov, and V. I. Ivanov-Omskiĭ

Editorial Board of Fizika i Tekhnika Poluprovodnikov

Translated by P. Shelnitz

ERRATA

Erratum: Radiation emitted by quantum-well InGaAs structures I. Spontaneous emission spectra [Semiconductors 32, 423–427 (April 1998)]

P. G. Eliseev

Temporary Address: Center of High-Technology Materials, University of New Mexico, Albuquerque, New Mexico, USA

I. V. Akimova

P. N. Lebedev Physics Institute, Russian Academy of Sciences, 117924 Moscow, Russia
Fiz. Tekh. Poluprovodn. **32**, 1408 (November 1998)

[S1063-7826(98)02411-9]

The correct figures for this article should read as follows:

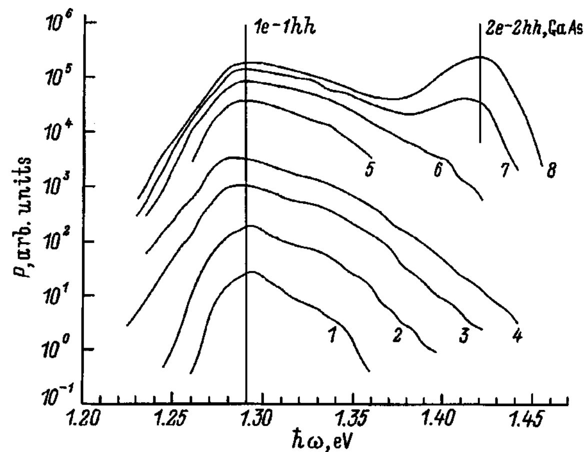

FIG. 1. Relative spectral density P of the radiation of an InGaAs quantum well at 286 K. Pump current I, mA: *1* — 1, *2* — 2, *3* — 5, *4* — 10, *5* — 50, *6* — 100, *7* — 150, *8* — 200. The spectra 3 and 4 were obtained in the direct-current regime.

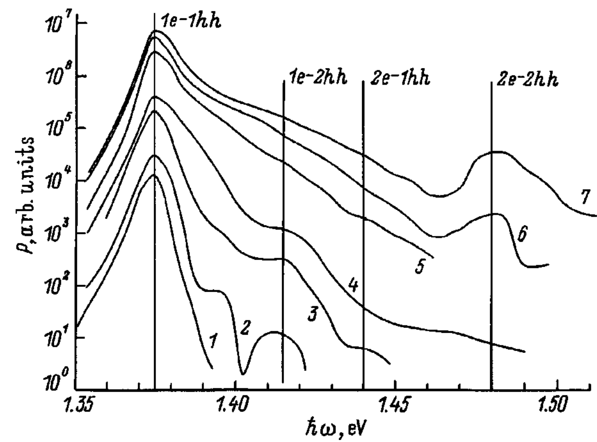

FIG. 2. Relative spectral density P of the radiation of an InGaAs quantum well at 4.2 K. Pump current I, mA: *1* — 1, *2* — 2, *3* — 10, *4* — 20, *5* — 100, *6* — 150, *7* — 200. The spectra 1 and 4 were obtained in the direct current regime.

 © 1998 American Institute of Physics

Erratum: Study of GaN thin layers subjected to high-temperature rapid thermal annealing [Semiconductors 32, No. 10, 1048 (October 1998)]

N. I. Katsavets

ZAO "Semiconductor Devices," 192281 St. Petersburg, Russia

G. M. Laws, I. Harrison, E. C. Larkins, and T. M. Benson

Department of Electrical and Electronic Engineering, University of Nottingham, Nottingham NG7 2RD, England

T. S. Cheng and C. T. Foxon

Department of Physics, University of Nottingham, Nottingham NG7 2RD, England

[S1063-7826(98)02511-3]

The Editorial Board of "Fizika i Tekhnika Poluprovodnikov" informs of the correction that should be made in this article. On page 1048, Section 2, the first sentence of the second paragraph, should read as follows:

"RHTA was performed in a quartz reactor at a temperature of 1000 C for 30 s in a stream of N_2 or Ar."

 © 1998 American Institute of Physics